



HAL
open science

Beam-Beam long-range wire compensation for enhancing CERN LHC performance

Axel Poyet

► **To cite this version:**

Axel Poyet. Beam-Beam long-range wire compensation for enhancing CERN LHC performance. Accelerator Physics [physics.acc-ph]. Université Grenoble Alpes [2020-..], 2021. English. NNT : 2021GRALY034 . tel-03508377

HAL Id: tel-03508377

<https://theses.hal.science/tel-03508377>

Submitted on 3 Jan 2022

HAL is a multi-disciplinary open access archive for the deposit and dissemination of scientific research documents, whether they are published or not. The documents may come from teaching and research institutions in France or abroad, or from public or private research centers.

L'archive ouverte pluridisciplinaire **HAL**, est destinée au dépôt et à la diffusion de documents scientifiques de niveau recherche, publiés ou non, émanant des établissements d'enseignement et de recherche français ou étrangers, des laboratoires publics ou privés.



THÈSE

Pour obtenir le grade de

DOCTEUR DE L'UNIVERSITÉ GRENOBLE ALPES

Spécialité : Physique Subatomique et Astroparticules

Arrêté ministériel : 25 mai 2016

Présentée par

Axel POYET

Thèse dirigée par **Jean-marie DE CONTO**, Université Grenoble Alpes

et codirigée par **Guido STERBINI**, Organisation Européenne pour la Recherche Nucléaire

préparée au sein du **Laboratoire Laboratoire de Physique Subatomique et Cosmologie**
dans l'**École Doctorale Physique**

Compensation des interactions faisceau-faisceau pour l'amélioration des performances du Grand Collisionneur de Hadrons du CERN

Beam-Beam Long-Range Wire Compensation for Enhancing CERN LHC Performance

Thèse soutenue publiquement le **18 mai 2021**,
devant le jury composé de :

Monsieur MAURO MIGLIORATI

PROFESSEUR ASSOCIE, Univ. degli Studi di Roma La Sapienza,
Rapporteur

Monsieur PHILIP BURROWS

PROFESSEUR, University of Oxford, Rapporteur

Madame MAUD BAYLAC

INGENIEUR DE RECHERCHE, CNRS DELEGATION ALPES,
Examinatrice

Monsieur JOHANN COLLOT

PROFESSEUR DES UNIVERSITES, UNIVERSITE GRENOBLE ALPES,
Président

Monsieur BENJAMIN TROCME

DIRECTEUR DE RECHERCHE, CNRS DELEGATION ALPES,
Examineur

Monsieur PATRICK PUZO

PROFESSEUR DES UNIVERSITES, UNIVERSITE PARIS-SACLAY,
Examineur



THÈSE
pour obtenir le grade de
DOCTEUR DE L'UNIVERSITÉ GRENOBLE-ALPES

Présentée par
Axel Poyet

Thèse dirigée par **Jean-Marie De Conto**, Université-Grenoble Alpes,
et codirigée par **Guido Sterbini**, CERN.

Préparée au sein du
Laboratoire de Physique Subatomique et de Cosmologie
et de
l'Organisation Européenne pour la Recherche Nucléaire

École Doctorale de Physique 47
Spécialité : Physique Subatomique et Astroparticules

Compensation des interactions faisceau-faisceau pour améliorer les
performances du Grand Collisionneur de Hadrons du CERN

Beam-Beam Long-Range Wire Compensation For Enhancing CERN
LHC Performance

Thèse soutenue publiquement le 18 Mai 2021, devant le jury composé de:

Monsieur Mauro Migliorati Professeur associé, Università degli Studi di Roma "La Sapienza"	Rapporteur
Monsieur Philip Burrows Professeur des Universités, University of Oxford	Rapporteur
Monsieur Johann Collot Professeur des Universités, Université Grenoble-Alpes	Président
Monsieur Patrick Puzo Professeur des Universités, Université Paris-Saclay	Examineur
Madame Maud Baylac Ingénieure de Recherche, Laboratoire de Physique Subatomique et de Cosmologie	Examineur
Monsieur Benjamin Trocmé Directeur de Recherche, Laboratoire de Physique Subatomique et de Cosmologie	Examineur

Above all, don't fear difficult moments. The best comes from them.

— Rita Levi-Montalcini

REMERCIEMENTS

Il est certain qu'une seule page ne saurait suffire à faire la liste de toutes les personnes que j'aimerais remercier. Amis, famille, collègues, collaborateurs, tant de personnes qui ont été à mes côtés pendant ces dernières années, qui n'ont pas toujours été les plus faciles.

J'aimerais tout d'abord remercier Guido, mon superviseur direct au CERN. Merci pour toutes ces discussions, pour ton enseignement, non seulement de la physique en général, mais de l'approche scientifique à adopter. Ma vision du monde de la recherche s'est forgée durant ces trois dernières années, principalement grâce à toi. J'aimerais également remercier Jean-Marie, mon directeur de thèse, pour sa confiance, dès notre première rencontre en 2016 alors que j'étais encore un étudiant ingénieur. Tu m'as suivi pendant toutes ces années, et pour cette raison je te remercie.

Ces quatre dernières années au CERN, j'ai été accueilli au sein d'une équipe incroyable. Un grand merci à mes deux chefs de section consécutifs, Yannis et Hannes, pour leur confiance, leur soutien, et leur aide. Merci également à tous mes collègues, avec qui j'ai pu soit travailler sur mon sujet de recherche, soit simplement partager tant de discussions passionnantes, ou simplement de bons moments. Stéphane, Ilias, Fanouria, Foteini, Sofia, Nikos, Kyriacos, et tous les autres, merci. Un merci tout particulier à ces collègues qui sont devenus des amis proches, sans qui je n'aurais sûrement pas été capable de surmonter ces années: Michalis, Kostas, Natalia, Tirsi, merci à vous.

Mais également merci aux autres amis, du CERN ou d'ailleurs, qui ont été à mes côtés, pour le meilleur comme pour le pire: Timothée, Zahos, Florentia, Apostolos, Leo, Félix... La liste est beaucoup trop longue pour être exhaustive ici. Merci à vous, de tout mon coeur.

Enfin, un grand merci à toute ma famille, qui a su croire en moi, et m'apporter tout le soutien dont j'avais besoin. Mon doctorat s'est déroulé au milieu d'un contexte particulier, la pandémie de coronavirus, et les différents confinements ont été une réelle épreuve pour moi. Ma famille a toujours été là, merci à eux.

ABSTRACT

In high intensity and high energy colliders such as the CERN Large Hadron Collider and its future luminosity upgrade, interactions between the two beams around the different interaction points are one of the machine performance limitations. In fact, their effect reduces the beam lifetime and therefore the collider's luminosity reach.

In the early 2000's, it was proposed for the first time to use current bearing wires in order to mitigate the effect of those so-called Beam-Beam Long-Range interactions. In 2015, a semi-analytical demonstration of a resonance compensation mechanism motivated the construction and the installation of four demonstrators for the LHC, that took place in 2017 and 2018. A two years long experimental campaign followed.

During this campaign, a proof-of-concept was successfully completed and motivated an additional set of experiments, successfully demonstrating the mitigation of the Beam-Beam Long-Range interactions effects in beam conditions compatible with an operational configuration of the collider.

In this Thesis, we report in details the preparation of the experimental campaign together with its results. This experimental work has been supported by tracking simulations, whose results are also presented in this document. Finally, simulations also allowed to prepare the next LHC Run 3, operating with the wire compensators, and to draw conclusions and perspectives for the future.

RÉSUMÉ

Dans les collisionneurs à haute énergie et à haute intensité, comme le Grand Collisionneur de Hadrons au CERN, ou sa mise à niveau en termes de luminosité, les interactions entre les deux faisceaux autour des différents points d'interactions représentent une des limitations des performances de la machine. Leur effet peut réduire considérablement le temps de vie du faisceau, et donc, le possible niveau de luminosité.

Au début des années 2000, une nouvelle idée fut proposée afin de compenser les effets de ces interactions, appelées interactions faisceau-faisceau à grande échelle. Cette idée consiste à utiliser des fils porteurs d'un courant direct. En 2015, une démonstration semi-analytique d'une possible compensation basée sur les résonances motiva la construction et l'installation de quatre prototypes pour le LHC. Cette installation eut lieu en 2017 et 2018 et une campagne expérimentale de deux ans s'en suivit.

Dans un premier temps, une preuve du concept fut réalisée. Les résultats positifs obtenus motivèrent une autre série d'expériences afin de pouvoir démontrer la possibilité de compenser les interactions faisceau-faisceau à grande échelle dans des conditions proches de l'opération nominale du LHC.

Cette thèse rapporte en détails la préparation de cette campagne expérimentale, ainsi que les résultats obtenus. De plus, ces travaux expérimentaux ont été complétés par un important travail de simulations, dont les résultats sont également présentés dans ce document. Enfin, grâce aux simulations, il fut possible de préparer la prochaine mise en route du LHC. Il est en effet prévu de piloter la machine avec les compensateurs dans les conditions nominales d'opération. Ces simulations ont donc permis de tirer des conclusions sur les possibles scénarios opérationnels, et des perspectives pour le futur.

CONTENTS

1	INTRODUCTION	1
1.1	The CERN Accelerator Complex and its Upgrade	1
1.1.1	An Overview of CERN History	1
1.1.2	The Large Hadron Collider and its Injectors	1
1.1.3	The Concept of Luminosity	6
1.1.4	LHC Performance and HL-LHC	9
1.2	Beam-Beam Long-Range Interactions in the LHC	11
1.2.1	Locate and Enumerate the BBLR Interactions	11
1.2.2	Optics in the LHC	14
1.2.3	Electromagnetic Field Created by a Beam and Linear Optics	17
1.2.4	Multipolar Expansion and Non-Linear Optics	20
1.3	BBLR Compensation Using DC Wires	24
2	WIRE COMPENSATORS SETTINGS IN THE LHC	29
2.1	The Experimental Setup in the LHC	29
2.1.1	Magnetic Field of a DC Wire	29
2.1.2	The LHC Wire Compensators	30
2.2	BBLR Compensation and Tune Footprint	34
2.3	BBLR and Resonance Driving Terms	35
2.3.1	Compensation Principle	35
2.3.2	Wires Settings in an Ideal LHC Case	39
2.3.3	Wire Settings for the LHC	41
2.3.4	Wires Powering Configurations	43
2.4	Conclusions	44
3	COMPENSATION OF THE BBLR INTERACTIONS USING DC WIRES IN THE LHC	45
3.1	Low Intensity Experiment: Proof-of-Concept	45
3.1.1	Experiment Preparation and Procedure	45
3.1.2	Results and Observations	52
3.1.3	Numerical Validation of the Results	54
3.2	BBLR Mitigation with High Intensity Beams	58
3.2.1	Experiment Preparation and Procedure	58
3.2.2	Results and Observations	61
3.2.3	Numerical Validation of the results	64
3.3	Conclusions	68
4	MITIGATION OF THE BBLR WITH LANDAU OCTUPOLES IN THE LHC	71
4.1	The Achromatic Telescopic Squeeze and its By-Products	71
4.2	Mitigation of the BBLR Interactions For Round Optics	73
4.2.1	Objectives of the experiments	73
4.2.2	BBLR mitigation, octupoles and crossing angles	73

Contents

4.2.3	BBLR mitigation at low crossing angle	78
4.3	Mitigation of the BBLR Interactions For Flat Optics	81
4.3.1	Flat optics for (HL)-LHC	81
4.3.2	Mitigation of the BBLR interactions using the Landau octupoles	83
4.4	Conclusions	87
5	TOWARDS OPERATION WITH THE WIRE COMPENSATORS FOR THE LHC RUN 3	89
5.1	Run 3: Foreseen Operational Scenarios and Performances Estimates	89
5.1.1	LHC Run 3: objectives and challenges	89
5.1.2	First performance estimates	90
5.1.3	Wire compensators: change of layout	90
5.2	Numerical Optimization of the Wire Compensators Settings	93
5.3	Wire Compensators in the Nominal Scenario	97
5.3.1	Dynamic Aperture and wire currents	98
5.3.2	Tune scans	101
5.3.3	Wire compensation and Landau octupoles	102
5.3.4	Bunch intensity and crossing angle	108
5.4	Exploring the Potential of the Wire Compensators	108
5.5	Hardware Non-Idealities and Consequences for the HL-LHC Era	111
5.5.1	Effect of a misalignment of the wires on the dynamic aperture	111
5.5.2	Aligning the wires without the use of the BPMs	112
5.6	Conclusions	113
6	CONCLUSIONS AND PERSPECTIVES	115
	APPENDICES	117
A	LUMINOSITY AND CROSSING ANGLE	119
B	LIST OF THE LHC FILLS FOR THE EXPERIMENTAL CAMPAIGN	121
	ACRONYMS	123
	GLOSSARY	125
	BIBLIOGRAPHY	127

LIST OF FIGURES

1.1	The CERN accelerator complex in 2020 (not to scale). The figure indicates the starting year of each accelerator, together with their circumference (if circular).	2
1.2	LHC superconducting dipole magnet cross-section. [10]	3
1.3	One empty bucket and one bucket filled with a bunch, together with the RF voltage.	4
1.4	The LHC ring (not to scale). Beam 1 (B1) is drawn in blue and rotate clockwise while Beam 2 (B2) is in red and rotates anti-clockwise.	5
1.5	A typical LHC cycle (Fills 7239 and 7240). The black solid line shows the evolution of the beams energy in time while the blue and red solid lines represent the intensity of Beam 1 and Beam 2 respectively.	6
1.6	Luminosity as a function of the crossing angle, for the nominal LHC case.	8
1.7	Integrated luminosity in the four experiments of the LHC during the 2017-2018 LHC Run.	9
1.8	Principle of crab crossing, using crab cavities for the HL-LHC.	11
1.9	Beam positions around the two high luminosity Interaction Points during the 2018 LHC Run. The dipoles are represented by blue rectangles while the quadrupoles by red ones.	12
1.10	An example of filling scheme in the LHC.	13
1.11	Zoom on the first 300 bunches of the filling scheme.	13
1.12	Number of BBLR experienced by the bunches of B1 in IR5 as a function of their position within the beam.	14
1.13	Optics layout around IP5 at 6.5 TeV at the end of the pre-squeeze (top plot) and at the end of the tele-squeeze (bottom plot).	15
1.14	Optics layout of the two first FODO cells of an LHC arc (Sector 56). The dipoles and quadrupoles are represented with blue and red squares respectively.	15
1.15	Optics layout around the Interaction Point 5 during the 2018 LHC Run.	16
1.16	Physical and normalized beam-beam separation (horizontal plane) around the IP5.	17
1.17	Kick given by a round bi-Gaussian beam together with its derivative with respect to x	18
1.18	Schematic view of the reference system for the multipolar expansion.	20
1.19	Example of tune footprints in the case of the 2017-2018 LHC Run 2: $\beta^* = 30$ cm, $\theta_c/2 = 150$ μ rad, $N_b = 1.15 \cdot 10^{11}$ p, collisions in all IPs. The amplitude of the particles is represented by the size of the dots.	25
1.20	Schematic view of an electron compression device [82]	25
1.21	Comparison between the beam-beam kick and a DC wire-induced kick.	26
1.22	History of the DC wire compensators: the evolution of their dimensions (active length and radius) and their nominal currents.	26
2.1	Wire collimator currently installed in the LHC tunnel on the left side of IP5 (L5).	30
2.2	Assembly of the wire on its support [95].	31
2.3	3D representations of a wire collimator [95].	31
2.4	Physical beam-wire distances as a function of the collimator opening during the 2018 LHC Run. The black dashed line represents the configurations explored during the experimental campaign.	32
2.5	The LHC ring configuration during the 2017-2018 Run. Beam 1 is represented in blue while Beam 2 in red. Four wire collimators are installed on Beam 2, around IP1 and IP5.	33

List of Figures

2.6	Optics layout in IR5, and wire compensators location.	33
2.7	Tune footprints for three configurations: HO only, HO and BBLR and wire compensation. The size of the markers is proportional to the initial amplitude of the particle. Particles are tracked up to 6σ amplitude.	35
2.8	Phase advances around the IP5.	37
2.9	Principle of the BBLR compensation using DC wires in the weak-strong approximation.	38
2.10	Residual RDT after the compensation of the (4,0)-(6,0) RDTs in the case of the 2017-2018 LHC Run 2 ($\theta_c/2 = 150 \mu\text{rad}$, $\beta^* = 30 \text{ cm}$).	39
2.11	Dynamic aperture in the configuration space for the ideal setup in two different cases: with BBLR interactions only, with BBLR interactions and wire compensation.	40
2.12	DA variation as a function of the beam-wire distances and the wire currents in an ideal case. LHC Run 2 optics is used but the wires are installed at the optimal aspect ratios.	41
2.13	DA variation as a function of the beam-wire distances and the wire currents for the 2017-2018 LHC Run 2.	42
2.14	Optimal currents required in the wires in order to compensate the (4,0)-(0,4) RDTs as a function of the collimators opening. The collimators opening explored during the experimental campaign are shown with black dashed lines.	43
2.15	Two different wire powering configurations.	43
3.1	Filling scheme used for the Low Intensity experiment. Only the first 600 bunch slots are displayed.	46
3.2	Feed-forward system for the Low Intensity experiment. The quadrupoles strengths variation is given as a function of the wires currents.	48
3.3	Residual tunes shifts after powering the wires and their feed-forward as a function of the wires currents, for the Low Intensity experiment.	49
3.4	β -beating induced by the wires and their feed-forward in the Low Intensity experiment.	49
3.5	5^{th} -axis collimator (Wire R1) alignment: BPM signal as a function of the 5^{th} -axis position. The dots represent the measurement while the solid lines are the second order polynomial fits. The maximum of each parabola is indicated by a cross.	50
3.6	Experiment objective: expected evolution of the effective cross-section and burn-off (BO) efficiency.	51
3.7	Overview of the Fill 7169 used for the Low Intensity experiment: beams' intensities and energy, octupoles current and half crossing angle as a function of time.	53
3.8	Low Intensity experiment results: evolution of the effective cross-section (top plot) and the wires currents (bottom plot) in time. The background coloring of the top plot shows the evolution of the half crossing angle.	53
3.9	Dynamic aperture in the configuration space for the Low Intensity experiment.	54
3.10	Tune footprints for the Low Intensity experiment.	55
3.11	Dynamic aperture as a function of the half crossing angle and the bunch population, with and without wire compensation, in the case of the Low Intensity experiment. Iso-DA lines are shown in black.	56
3.12	Evolution of the dynamic aperture as a function of the choice of the tune working point. The red crosses signal missing points. The red star shows the nominal working point while the green one shows the optimal one. The green lines are the iso-DA.	56
3.13	Dynamic aperture variation as a function of the Landau octupoles and wires currents. The red star shows the Low Intensity experiment configuration while the black one shows the operational one. The green box corresponds to the best DA configurations.	57
3.14	Filling scheme used for the High Intensity experiment. Only the first 600 bunches slots are displayed.	58

3.15	Feed-forward system for the High Intensity experiment. The quadrupoles strengths variation is given as a function of the wires currents.	59
3.16	Residual tunes shifts after powering the wires and their feed-forward for the High Intensity experiment.	60
3.17	β -beating induced by the wires and their feed-forward in the High Intensity experiment.	60
3.18	Effect of the Wire R5 on the betatron tunes at injection energy.	61
3.19	Validation of the feed-forward system: quadrupoles and wires currents as a function of time.	61
3.20	Effect of the wires and their feed-forward on the horizontal and vertical tunes.	62
3.21	Overview of the High Intensity experiment in terms of beam intensity, energy, Landau octupoles current (bottom plot, blue and orange solid lines) and half crossing angle (bottom plot, black solid line).	62
3.22	High Intensity experiment results: beams losses, octupoles current (top plot), wires currents and beams' intensities (bottom plot) as a function of time. In the top plot, the top background coloring shows the evolution of the half crossing angle while the bottom part coloring shows the on/off (green/red, respectively) cycles of the wires.	63
3.23	High Intensity experiment results: dBLM bunch-by-bunch losses as a function of time. The top background coloring shows the half crossing angle evolution while the bottom coloring shows the on/off wires cycles.	63
3.24	Dynamic aperture in the configuration space for the High Intensity experiment.	64
3.25	Tune footprint for the High Intensity experiment.	65
3.26	Dynamic aperture as a function of the half crossing angle and the bunch population, in the case of the High Intensity experiment. The plain black lines are iso-DA lines.	66
3.27	Variation of the dynamic aperture as a function of the choice of the tune working point. The red crosses signal missing points. The red star shows the nominal working point while the green star shows the optimal one. The black plain lines are the iso-DA lines.	66
3.28	Dynamic aperture variation as a function of the Landau octupoles and wires currents. The red star shows the High Intensity experiment configuration and the black star the operational one. The best DA configurations are shown in the green box.	67
3.29	Comparison of the tune footprints obtained without wires and without octupoles and the one obtained with wires and negative octupoles currents	68
4.1	β -functions at an octupole, from the arc 45, location, as a function of the tele-index.	72
4.2	Tune spread induced by the Landau octupoles, powered at +350 A, for a tele-index of 1 and 4 (in blue and red respectively).	72
4.3	Filling scheme used for the Fill 6431. Only the first 500 bunch slots are displayed.	74
4.4	Overview of the Fill 6431. Top plot: beams intensities (blue and red lines) and energy (black line) as a function of time. Middle plot: Landau octupoles currents (orange and blue lines) and half crossing angle (black line) as a function of time. Bottom plot: beams' lifetime (in blue for B1 and red for B2) as a function of time. The background coloring shows the different beam modes.	74
4.5	Effective cross-section of a selection of bunches of Beam 1 and Landau octupoles current as a function of time.	75
4.6	Effective cross-section of a selection of bunches of Beam 2 and Landau octupoles current as a function of time.	75
4.7	Filling scheme used for the Fill 6432.	76
4.8	Overview of the Fill 6432. Top plot: beams intensities (blue and red lines) and energy (black line) as a function of time. Middle plot: Landau octupoles currents (orange and blue lines) and half crossing angle (black line) as a function of time. Bottom plot: beams' lifetime (in blue for B1 and red for B2) as a function of time. The background coloring shows the different beam modes.	77

List of Figures

4.9	Evolution of the beams lifetime and of the half crossing angle as a function of time.	77
4.10	Filling scheme used for the Fill 7171.	78
4.11	Overview of the Fill 7171. Top plot: beams intensities (blue and red lines) and energy (black line) as a function of time. Middle plot: Landau octupoles currents (orange and blue lines) and half crossing angle (black line) as a function of time. Bottom plot: beams' lifetime (in blue for B1 and red for B2) as a function of time. The background coloring shows the different beam modes.	79
4.12	Evolution of the beams lifetime as a function of time. The half crossing angle evolution is shown with the background coloring.	79
4.13	Effective cross-section of a collection of Beam 1 bunches and Landau octupoles current as a function of time.	80
4.14	Effective cross-section of a collection of Beam 2 bunches and Landau octupoles current as a function of time.	80
4.15	Schematic view of the beam footprint in the vacuum chamber of the Inner Triplet for round optics (on the left) and flat optics (on the right). Both IR1 (top plots) and IR5 (bottom plots) are illustrated. Courtesy of S. Fartoukh.	82
4.16	Filling scheme used for the Fill 6995. Only the first 500 bunch slots are displayed.	83
4.17	Overview of the Fill 6995. Top plot: beams intensities (blue and red lines) and energy (black line) as a function of time. Middle plot: Landau octupoles currents (orange and blue lines) as a function of time. Bottom plot: beams' lifetime (in blue for B1 and red for B2) as a function of time. The background coloring shows the different beam modes.	84
4.18	Beam 1 and Beam 2 lifetimes together with the Landau octupoles current as a function of time, at $\theta_c/2 = 130 \mu\text{rad}$	84
4.19	Evolution, in time, of the effective cross-section of a collection of bunches included in the BCMS train of Beam 1, during the octupoles current scan at $\theta_c/2 = 130 \mu\text{rad}$	85
4.20	Evolution, in time, of the effective cross-section of a collection of bunches included in the BCMS train of Beam 2, during the octupoles current scan at $\theta_c/2 = 130 \mu\text{rad}$	85
4.21	Beam 1 and Beam 2 lifetimes together with the Landau octupoles current as a function of time, at $\theta_c/2 = 100 \mu\text{rad}$	86
4.22	Evolution, in time, of the effective cross-section of a collection of bunches included in the BCMS train of Beam 1, during the octupoles current scan at $\theta_c/2 = 100 \mu\text{rad}$	86
4.23	Evolution, in time, of the effective cross-section of a collection of bunches included in the BCMS train of Beam 2, during the octupoles current scan at $\theta_c/2 = 100 \mu\text{rad}$	87
5.1	First performance estimates for the LHC operation during the next LHC Run 3. From left to right, and from top to bottom: evolution of the beam intensity, horizontal and vertical emittances, bunch length, half crossing angle, β^* , pileup, instantaneous luminosity, integrated luminosity and integrated luminosity per 24 h, as a function of time.	91
5.2	Schematic view of the LHC ring configuration during the LHC Run 3. Beam 1 is represented in blue while Beam 2 in red. Two out of the four B2 wire compensators are now installed on B1.	92
5.3	Comparison of the β -functions around IP5 for B1, between Run 2 and Run 3.	94
5.4	Tune feed-forward implementation using the two Q4 quadrupoles in the case of Beam 1: quadrupoles strengths variation as a function of the wires current.	95
5.5	Effect of the wire compensators and their feed-forward system for the next LHC Run 3: residual tune shifts as a function of the wires current.	95
5.6	Maximum β -beating induced by the wires and their feed-forward system, as a function of the wires current, in the case of Beam 2.	96
5.7	Residual tune shifts with the wires on as a function of the tele-index (Beam 1 case).	97

5.8	Proposal for the wires ramping time.	97
5.9	DA variation as a function of the wire currents for the LHC Run 3. The wire collimators are opened at 8.5σ	98
5.10	Sanity checks for the tracking simulations in the context of the LHC Run 3: tunes and chromaticities as a function of the wires currents.	99
5.11	Dynamic aperture in the configuration space, for different configurations (no wires, wires in IR1 or IR5 only, and wires in both IRs).	100
5.12	Tune footprints, for different configurations (no wires, wires in IR1 or IR5 only, and wires in both IRs).	101
5.13	Dynamic aperture as a function of the horizontal and vertical tunes, with and without wire compensation, for the LHC Run 3.	102
5.14	Sanity checks for the tracking simulations in the context of the LHC Run 3: computed tunes and chromaticities as a function of the chosen horizontal and vertical tunes.	103
5.15	DA variation as a function of the wires and the Landau octupoles currents. Iso-detuning lines are also displayed in red (horizontal), blue (vertical) and green (cross anharmonicities). The red star shows the best DA configuration while the green star shows the configuration where both horizontal and vertical detuning cancel out.	104
5.16	Tune footprints without compensation, for the linear detuning cancellation, and for the best DA configuration.	106
5.17	RMS-like detuning due to the wires and the Landau octupoles.	107
5.18	Knob proposal to maintain the detuning constant while inverting the octupoles polarity: wires and Landau octupoles currents as a function of time.	107
5.19	Residual RMS-like while inverting the octupoles polarity, with the use of the wires.	108
5.20	Dynamic aperture as a function of the half the crossing angle and the bunch population, at the end of the β -leveling, without the use of the wire compensation.	109
5.21	Dynamic aperture as a function of the half the crossing angle and the bunch population, at the end of the β -leveling, with the use of the wire compensators.	109
5.22	Dynamic aperture variation as a function of the wire currents, with negatives octupoles and reduced wire collimators gap.	110
5.23	Dynamic aperture as a function of the half the crossing angle and the bunch population, at the end of the β -leveling, with negative octupoles, and reduced wire collimators gap.	111
5.24	Dynamic aperture as a function of a horizontal and vertical 5^{th} -axis misalignment.	112
5.25	Effect of a misalignment of the 5^{th} -axis on the horizontal (in blue) and the vertical (in red) tunes (2-jaws powering configurations, collimators opened at 8.5σ).	113
A.1	Rotated reference system for collisions in presence of a crossing angle.	119

LIST OF TABLES

1.1	List of the LHC injectors and their main parameters during the 2017-2018 LHC Run. The given energies are the kinetic ones.	4
1.2	Comparison of the LHC and HL-LHC baseline parameters.	10
1.3	BBES of different bunches of B1. The number of BBLR encounters is given per side of IP (left/right).	13
2.1	Longitudinal positions of the wires with respect to the IPs.	32
3.1	Wire settings during the Low Intensity experiment. The beam-wire distance is algebraic and given with respect to the Beam 2 reference system.	45
3.2	Expected wire induced tune shifts for the Low Intensity experiment.	47
3.3	Wire settings during the High Intensity experiment. The mention “x 2” indicates that the 2-jaw powering configuration is used.	58
3.4	Expected wire induced tune shifts for the High Intensity experiment.	59
5.1	Wires settings for the next LHC Run 3.	93
5.2	Maximum expected wire induced tune shifts during the next LHC Run 3.	93
5.3	Simulations parameters for the nominal operation of the wire compensators in the LHC Run 3	98
5.4	Beam-wire distances as a function of the collimator opening.	110
B.1	List of the LHC fills considered for the experimental campaign	121

1 INTRODUCTION

The idea of a European Organization for Nuclear Research - or CERN - originates back at the end of the 1940's, in a Europe devastated by the Second World War. At that time, numerous international organizations started to be created in view of a more peaceful world. Following these examples, a group of European scientists imagined the creation of a European laboratory focused on nuclear physics research. In 1952, an agreement was signed between 11 countries, and the CERN acronym (Conseil Européen pour la Recherche Nucléaire) was officially born. This acronym was kept, even after "Conseil" was replaced by "Organisation". The Council then chose Geneva as building site, and soon after the construction of two new particles accelerators began.

1.1 THE CERN ACCELERATOR COMPLEX AND ITS UPGRADE

1.1.1 AN OVERVIEW OF CERN HISTORY

The first particle accelerator built at CERN was the Synchrocyclotron (SC) [1]. It accelerated its first proton beam in 1957 up to a kinetic energy of 600 MeV. In the meantime, another machine was under construction: the Proton Synchrotron (PS) [2]. In 1959 it accelerated its first proton beam. While the SC was stopped and decommissioned in 1990, the PS is still running, more than 60 years later. It is now part of a long chain of different accelerators called the CERN Accelerator Complex. The latter is presented - as in 2020 - on Figure 1.1 [3].

In the meantime, physicists started to develop machines that could not only accelerate beams, but also produce collisions between particles. Thus in the early 1960's the conception of a first collider at CERN, that would be fed by the PS, began. In 1971, the first collisions between two proton beams occurred in the Intersecting Storage Rings (ISR) [4]. The ISR has been operated for 13 years before being dismantled.

During the operation of the ISR, CERN physicists decided to keep exploring the outcome of particle collisions. For that reason, a new synchrotron was built: the Super Proton Synchrotron (SPS) [5]. It was first turned on in 1976 and was able to accelerate proton beams up to a kinetic energy of 400 GeV. Five years later, the SPS was turned into a proton-antiproton collider: the $Spp\bar{S}$ [6]. The proton and antiproton beams were accelerated up to a kinetic energy of 315 GeV and brought into collisions. This led to the discovery in 1983 of the W and Z particles [7]. However, when operating as an accelerator for fixed-target experiment, the SPS can accelerate a proton beam up to a kinetic energy of 450 GeV before being extracted.

The year 1988 was also a turning point for CERN, as the 27 km long and about 100 m deep tunnel built to house the new Large Electron-Positron collider (LEP) [8] was achieved. The LEP was and still remains the largest electron-positron collider ever built. During its first stage, it could operate at a beam energy of 45.5 GeV, producing millions of Z bosons. It was then upgraded and reached center of mass collision energies up to 209 GeV. In 2000, the LEP was stopped and dismantled as the tunnel had to be freed in order to house a brand new and innovative machine: the Large Hadron Collider (LHC) [9].

1.1.2 THE LARGE HADRON COLLIDER AND ITS INJECTORS

The CERN LHC is a 27 km long collider, buried around 100 m below the ground surface. It accelerates two counter-rotating hadron beams denoted Beam 1 (B1) and Beam 2 (B2) from an energy of 450 GeV to a final energy

1 Introduction

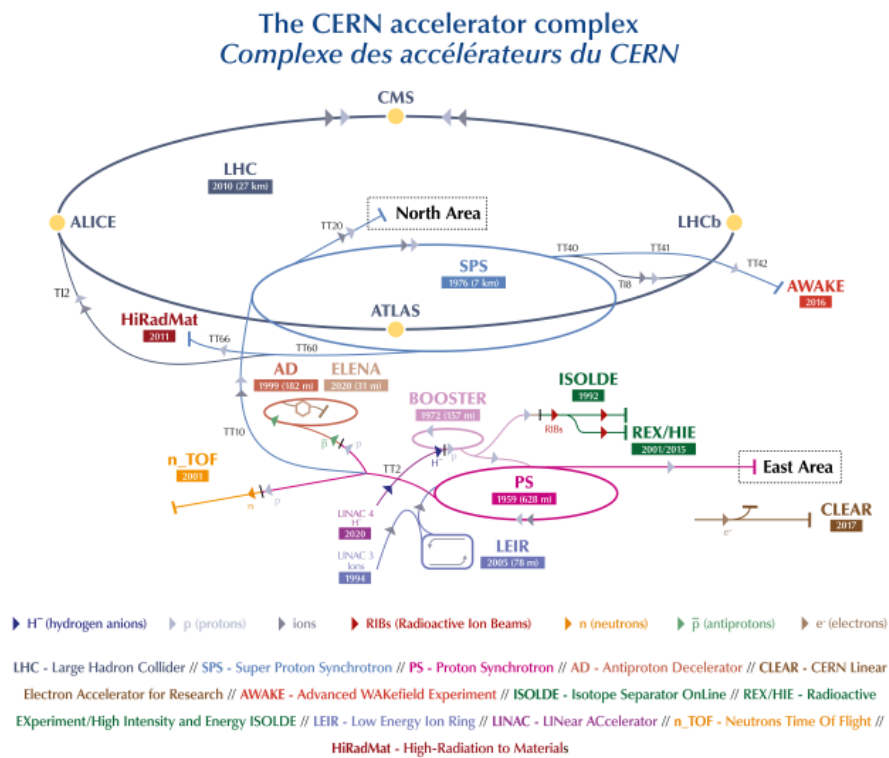


Figure 1.1: The CERN accelerator complex in 2020 (not to scale). The figure indicates the starting year of each accelerator, together with their circumference (if circular).

of 6.5 TeV¹. It is composed of 1232, 15 m long, dipole magnets used to bend the beams and 392, 5 to 7 m long, quadrupole magnets used to focus them. Most of these magnets are superconducting and are maintained at a temperature of about 2 K. The two beams circulate into different vacuum pipes, sharing the same magnets. Figure 1.2 shows the cross-section of an LHC dipole magnet, where the two different vacuum pipes are visible.

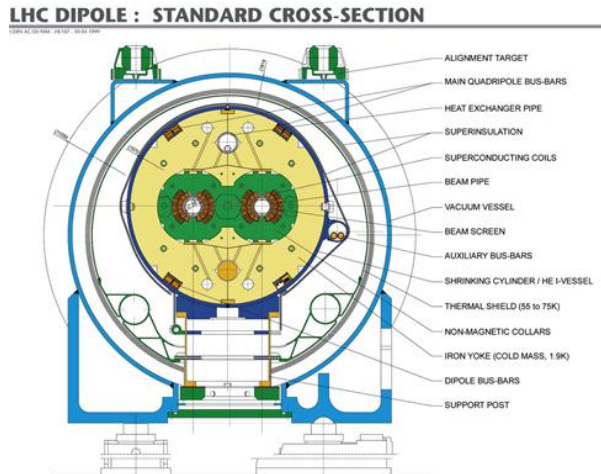


Figure 1.2: LHC superconducting dipole magnet cross-section. [10]

A current of about 11 kA circulates in the superconducting coils, producing the needed dipolar magnetic field of about 8 T in order to bend the trajectory of the particles when they reach their maximum energy. Inside the beam chambers, the vacuum is maintained at a level between about 10^{-10} and 10^{-11} mbar [11].

Beams are accelerated using 16 Radio Frequency (RF) cavities (8 per beam) [12]. Each of those cavities can reach a maximum voltage of 2 MV and is tuned to oscillate at about 400 MHz. Those cavities are embedded in four different cryomodules, in order to work in a superconducting state. As a particle shall always see an accelerating voltage in the RF cavity gap, the RF frequency of the cavity, f_{RF} , must be an integer multiple of the revolution frequency f_{rev} :

$$f_{RF} = h \cdot f_{rev}, \quad (1.1)$$

where h is known as the harmonic number. In the ultra-relativistic approximation, and considering proton beams (which will be the case in the following of this Thesis), the velocity of a particle can be approximated to $\beta_r c \approx c$ and the LHC harmonic number is equal to 35640.

The LHC circumference can be divided in h virtual points, and the areas of stable longitudinal motion around those points are called buckets. They define the longitudinal acceptance of the machine. A particle exactly synchronized with the RF cavity frequency is called synchronous particle. All the other protons will oscillate around this synchronous particle and form a group of protons called bunch. Figure 1.3 illustrates qualitatively the definition of buckets and bunches.

In the LHC, only one out of ten buckets is filled with a bunch so that the bunch time spacing remains 25 ns. In fact, the bucket configuration determines where and how many times the different bunches of the two beams will collide. Depending on the chosen beam structure - also called filling scheme - the LHC can house up to 2808 bunches [13]. Another reason for leaving some empty buckets is the need for a so-called abort gap [14]: when a beam dump is triggered, the rising time of the extraction kickers is not zero and therefore one shall make sure that no proton is kicked during that time in order not to damage machine elements located downstream those kickers. The bunch length in the LHC is about 1 ns. This parameter is set from the injectors chain as presented on Figure 1.1.

¹In the 2017-2018 run. The possibility of running the LHC at 7 TeV (nominal design energy) during the next run is - at the moment of writing (2021) - under investigation.

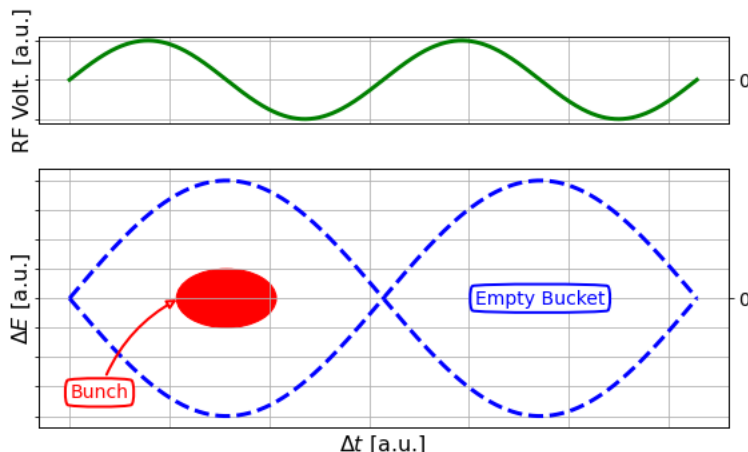


Figure 1.3: One empty bucket and one bucket filled with a bunch, together with the RF voltage.

From the hydrogen bottle to the LHC, there are in fact four different accelerators whose role is to accelerate the proton beam up to 450 GeV (the LHC injection energy) with the correct bunch length and the desired emittances. Table 1.1 summarizes the characteristics of the LHC injectors during the 2017-2018 LHC Run [15].

Machine	Year	Type	Length	Inj. Energy	Ext. Energy
LINAC 2	1978	Linear	36 m	90 keV	50 MeV
PS Booster	1972	Circular	157 m	50 MeV	1.4 GeV
PS	1959	Circular	628 m	1.4 GeV	25 GeV
SPS	1976	Circular	7 km	25 GeV	450 GeV

Table 1.1: List of the LHC injectors and their main parameters during the 2017-2018 LHC Run. The given energies are the kinetic ones.

In view of the next LHC luminosity upgrade, the High-Luminosity LHC (HL-LHC) [16], the injector chain has been upgraded after the 2017-2018 LHC Run in order to be ready to inject more intense beams with smaller emittances. The LHC Injector Upgrade (LIU) [17] consisted in modifying all the injectors to be ready for HL-LHC, and building a new LINAC, LINAC 4 [18], in order to replace the existing LINAC 2. LINAC 4 is 86 m and, in 2020, it started accelerating H^- ions up to 160 MeV. The two electrons of each ion are then stripped, and the remaining protons are injected into the PS Booster. The protons then circulate through the four rings of the latter before being injected into the PS, where they will be stored for a few seconds before being extracted. The protons are finally injected into the SPS where they reach the LHC injection energy of 450 GeV.

Once the two beams are injected in the LHC according to the chosen filling scheme, the energy of both beams is ramped from 450 GeV to 6.5 TeV. The currents of the different magnets are ramped up synchronously. The beams are then focused (squeezed) and brought into collisions at four so-called Interaction Points (IP), housing four different experiments. Two of these experiments were assigned to the primary goal of observing the Higgs boson, using different technologies, but ensuring the consistency of the observation. These are ATLAS (A Toroidal LHC Apparatus) [19] and CMS (Compact Muon Solenoid) [20]. These IPs are referred to as high luminosity experiments, as they require a high statistical precision for their physics search. On the other hand, the two other experiments require a reduced number of collisions as they are optimized for a different physics search. These are ALICE (A Large Ion Collider Experiment) [21] and LHCb (Large Hadron Collider beauty) [22].

The LHC consists in different sections with different purposes. It is divided in eight sectors which are composed of an arc where the beams' trajectories are bent and of a straight section that can house different types of instruments and devices. Figure 1.4 shows a schematic overview of the LHC ring.

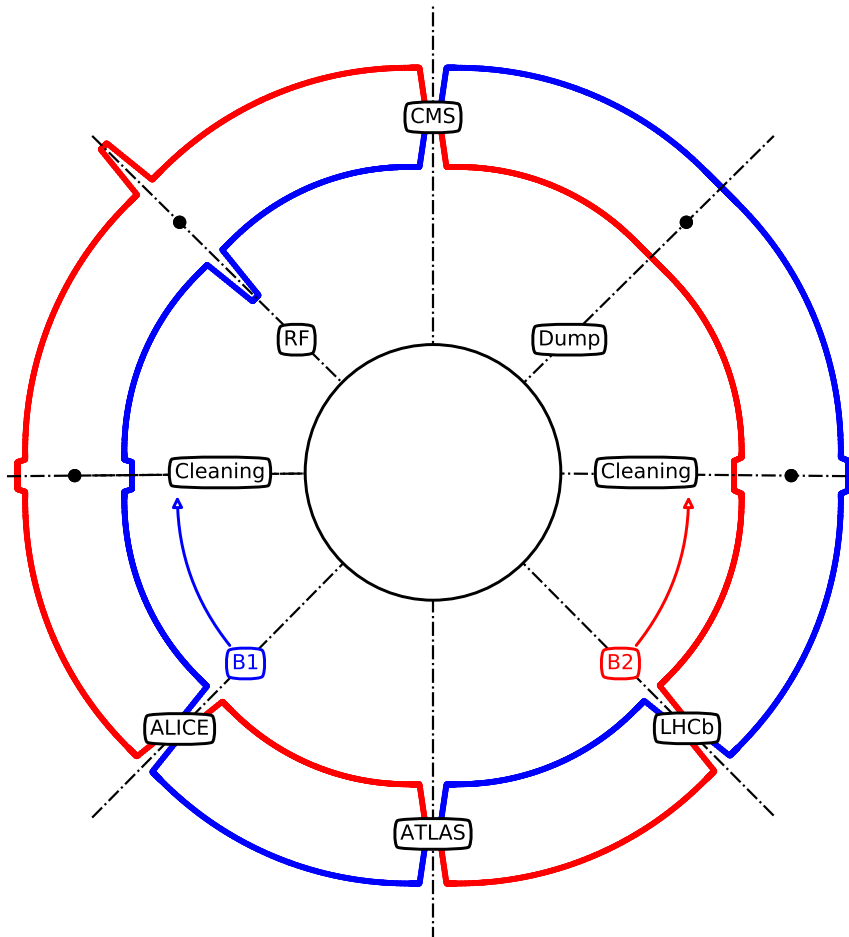


Figure 1.4: The LHC ring (not to scale). Beam 1 (B1) is drawn in blue and rotate clockwise wise Beam 2 (B2) is in red and rotates anti-clockwise.

As mentioned, each Insertion Region is separated from the previous one by an arc and has its own purpose:

- IR1 houses the ATLAS experiment
- IR2 houses the ALICE experiment and the injection of Beam 1
- IR3 houses the off-momentum collimation cleaning [23] (see later in Section 2.1.2)
- IR4 houses the RF cavities to accelerate the beams (see Section 1.1.2)
- IR5 houses the CMS experiment
- IR6 houses the beams extraction to the dumps [24]
- IR7 houses the betatronic collimation cleaning [25]

1 Introduction

- IR8 houses the LHCb experiment and the injection of Beam 2

After about ten hours of collisions, the decision of extracting and dumping the beams is made. This decision has to take into consideration many different factors, such as the remaining intensity, and therefore the efficiency of the on-going collisions, the availability of the injectors or possible foreseen incoming technical issues. Figure 1.5 shows a typical LHC cycle in terms of beam energy and intensities.

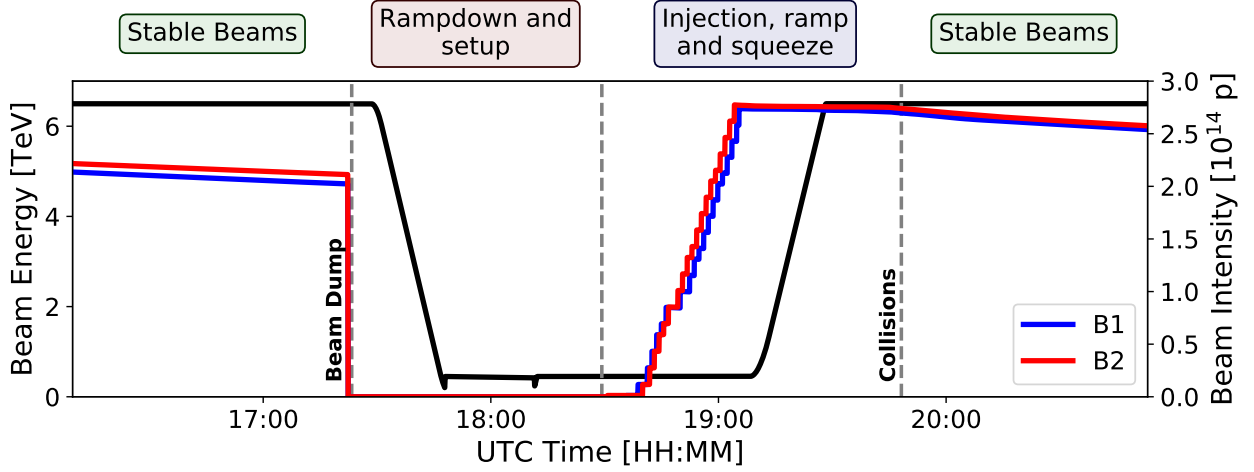


Figure 1.5: A typical LHC cycle (Fills 7239 and 7240). The black solid line shows the evolution of the beams energy in time while the blue and red solid lines represent the intensity of Beam 1 and Beam 2 respectively.

The main purpose of the LHC is to deliver collisions into the four detectors that require the best statistics for their physics search. The corresponding performance indicator is called luminosity and is of prime importance in the design of a collider.

1.1.3 THE CONCEPT OF LUMINOSITY

Nowadays, particle physics experiments aim to understand our universe, its origin, and to explain the observations concerning its expansion. Reproducing conditions similar to the ones of the first instants after the big-bang is challenging and requires to collide two high energy particles. From these collisions, the detectors can observe new particles. In the case of the LHC, the colliding particles are protons (or ions, but this is not covered in this Thesis), but other colliders have been using different species. As an example, the American collider Tevatron at FermiLab [26] was colliding protons with antiprotons. In the future, one of the considered options for the Future Circular Collider (FCC) is to collide electrons and positrons [27].

The frequency of apparition of a given event from the collisions is called event rate (or number of event per second), and the luminosity is thus defined as the proportionality factor between this even rate, denoted dR/dt , and the cross-section of this event, denoted σ_p , as in Eq. 1.2 [28]:

$$\frac{dR}{dt} = \mathcal{L} \cdot \sigma_p. \quad (1.2)$$

The luminosity has the dimension of a frequency divided by a surface and is measured in $\text{cm}^{-2} \cdot \text{s}^{-1}$, or in Hz/cm^2 . Following the approach of [29], we consider two bunches with densities $\rho_1(\mathbf{x}, t)$ and $\rho_2(\mathbf{x}, t)$, normalized such as:

$$\int_{-\infty}^{+\infty} d^3\mathbf{x} \rho_i(\mathbf{x}, t) = N_i, \quad (1.3)$$

where $\mathbf{x} = (x, y, s)$ is the vector coordinates of a considered particle in the laboratory frame and N_i is the number of particles in the bunch $i = 1, 2$. The so-called single bunch luminosity \mathcal{L}_{SB} can be defined as the integral over the luminous region (denoted $S_{\mathcal{L}}$) [30] of the product of the two 3-dimensions density distributions, multiplied by a kinematic factor K , the bunches intensities N_i ($i = 1, 2$), and by the revolution frequency f_{rev} :

$$\mathcal{L}_{SB} = N_1 N_2 f_{rev} K \int_{S_{\mathcal{L}}} \rho_1(\mathbf{x}, t) \rho_2(\mathbf{x}, t) d^3 \mathbf{x} dt, \quad (1.4)$$

where K is defined as:

$$K = \sqrt{(\mathbf{v}_1 - \mathbf{v}_2)^2 - \frac{(\mathbf{v}_1 \times \mathbf{v}_2)^2}{c^2}}. \quad (1.5)$$

The derivation of this integral can always be done numerically, even though it might require high computing resources. In order to obtain a closed form, some approximations have to be made. In the context of this Introduction, we propose to express the luminosity in a simple case, neglecting in particular the hour glass [30, 31, 32] or the crossing angle [33, 34] effects.

The vectors \mathbf{v}_1 and \mathbf{v}_2 represent the velocity of the two bunches in the laboratory frame. In the ultra-relativistic approximation, and assuming no crossing angle between the two bunches (that is a pure head-on collision), one can define the two velocity vectors as $\mathbf{v}_1 = (0, 0, c)$ and $\mathbf{v}_2 = (0, 0, -c)$. With these definitions, the kinematic factor becomes $K = 2c$.

For our integration purpose, we use the longitudinal distance s of the two bunches from the central point of collision s_0 , as often in accelerator physics, by replacing the time variable $t = s/c$. Besides, we assume all the densities to be uncorrelated in all planes so that we can write:

$$\mathcal{L}_{SB} = 2N_1 N_2 f_{rev} \iiint \int_{S_{\mathcal{L}}} \rho_{1x}(x) \rho_{1y}(y) \rho_{1s}(s - s_0) \rho_{2x}(x) \rho_{2y}(y) \rho_{2s}(s + s_0) dx dy ds ds_0. \quad (1.6)$$

Let us now consider a collision between two bunches with Gaussian profiles in all dimensions. This is a valid assumption for the LHC case [35, 36], and the densities can be written:

$$\begin{aligned} \rho_{iu}(u) &= \frac{1}{\sigma_{iu} \sqrt{2\pi}} \exp\left(-\frac{u^2}{2\sigma_{iu}^2}\right) \\ \rho_{is}(s \pm s_0) &= \frac{1}{\sigma_{is} \sqrt{2\pi}} \exp\left(-\frac{(s \pm s_0)^2}{2\sigma_{is}^2}\right), \end{aligned} \quad (1.7)$$

where $i = 1, 2$ and $u = x, y$. We also assume that the two beams are equal in terms of size so that $\sigma_{1u} = \sigma_{2u}$ with $u = x, y, s$. Eq. 1.6 thus becomes:

$$\mathcal{L}_{SB} = \frac{2N_1 N_2 f_{rev}}{(\sqrt{2\pi})^6 \sigma_s^2 \sigma_x^2 \sigma_y^2} \iiint \int_{S_{\mathcal{L}}} e^{-\frac{x^2}{\sigma_x^2}} e^{-\frac{y^2}{\sigma_y^2}} e^{-\frac{s^2}{\sigma_s^2}} e^{-\frac{s_0^2}{\sigma_s^2}} dx dy ds ds_0. \quad (1.8)$$

It is now possible to integrate using:

$$\int_{-\infty}^{+\infty} e^{-ax^2} dx = \sqrt{\frac{\pi}{a}}, \quad \forall a > 0, \quad (1.9)$$

and so we obtain finally:

$$\mathcal{L}_{SB} = \frac{N_1 N_2 f_{rev}}{4\pi\sigma_x\sigma_y}. \quad (1.10)$$

However, we described the case of two single bunches colliding. The LHC is in general filled with n_b bunches, producing N_b collisions at a given IP and we therefore have to multiply Eq. 1.10 by this factor to obtain the expression of the luminosity produced by the collision of two equal beams, assuming Gaussian profiles and no crossing angle:

$$\mathcal{L} = \frac{N_1 N_2 f_{rev} N_b}{4\pi\sigma_x\sigma_y}. \quad (1.11)$$

Nonetheless, colliders such as the LHC do not collide bunches directly head-on but with a crossing angle. The motivation for the presence of a crossing angle is two-fold [37]. The first reason is related to the detectors. They have a limited number of channels and trackers. If the number of events becomes too high, some of them will not be measured. Moreover, one has to isolate the track of each created particle. Each tracker and channel thus cannot be saturated. The second reason is related to the collider itself as when approaching the IP, the two beams share the same vacuum chamber and become close from each other. As composed of charged particles in motion, each beam produces a strong and non-linear electromagnetic field influencing the other one. These effects are called *beam-beam* effects and can limit the performance of the machine.

In order to compute the integral reported in Eq. 1.6 in presence of a crossing angle, a change of variable is needed and the full derivation is reported in Appendix A. Eq. 1.12 gives the luminosity of Gaussian bunches colliding with a horizontal crossing angle θ_c :

$$\mathcal{L} = \frac{N_1 N_2 f_{rev} N_b}{4\pi\sigma_x\sigma_y} \frac{1}{\sqrt{1 + \left(\frac{\sigma_s}{\sigma_x} \tan\left(\frac{\theta_c}{2}\right)\right)^2}}. \quad (1.12)$$

Using the baseline parameters of the nominal LHC, reported in Table 1.2 [13, 38], Figure 1.6 shows the variation of the luminosity with the crossing angle.

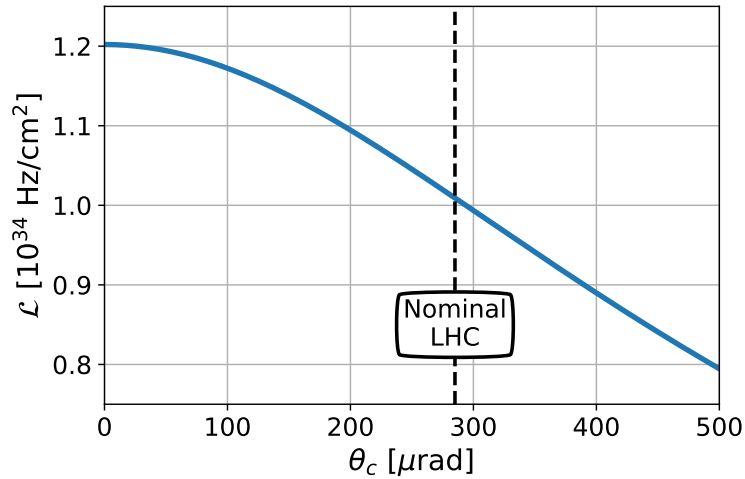


Figure 1.6: Luminosity as a function of the crossing angle, for the nominal LHC case.

From Eq. 1.12 and Figure 1.6 one can see that increasing the crossing angle would reduce the luminosity. However, reducing this crossing angle brings the two beams closer in a region where they share the same vacuum pipe, thus enhancing the beam-beam effects. A trade-off has to be found in order to guarantee the best machine performance.

1.1.4 LHC PERFORMANCE AND HL-LHC

The LHC performance is described through the integrated luminosity, measured in inverse barns², or more conveniently in fb^{-1} , and defined as the time integral over a given interval of the luminosity as defined from Eq. 1.12:

$$\mathcal{L}_{int} = \int_{t_0}^{t_1} \mathcal{L} dt, \quad (1.13)$$

where t_0 and t_1 are generally taken as the beginning and the end of a yearly run.

Figure 1.7 shows the evolution of the integrated luminosity along the 2017 and 2018 LHC runs, for the different experiments.

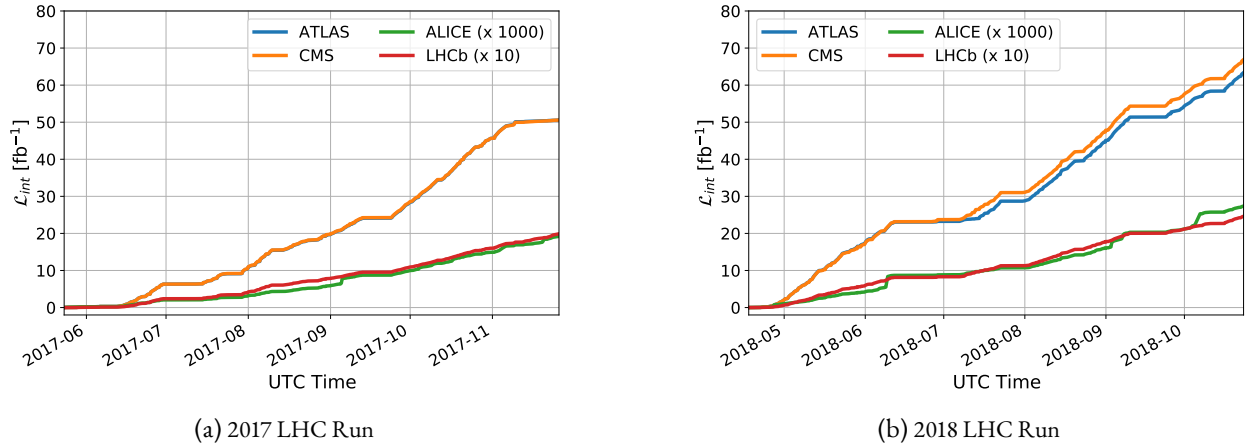


Figure 1.7: Integrated luminosity in the four experiments of the LHC during the 2017-2018 LHC Run.

Optimizing the integrated luminosity consists in reaching a high peak luminosity at the start of the collisions (within the tolerances of the detectors) together with maintaining a high beam lifetime during the fill and a high machine availability. The peak luminosity in the LHC was foreseen to be $1 \cdot 10^{34} \text{ Hz/cm}^2$, which has been overcome, reaching more than $2 \cdot 10^{34} \text{ Hz/cm}^2$. However, the foreseen yearly 60 fb^{-1} [9] in each high luminosity IP were not reached before the 2018 run.

After announcing the discovery of the Higgs boson by ATLAS and CMS [39, 40] in 2012, fulfilling one of the primary purposes of the LHC, the latter continued to provide data to the experiments, allowing new measurements of the Higgs boson's properties, along with the potential discovery of new particles or phenomena by the ALICE and LHCb collaborations [41, 42].

However, in order to keep increasing knowledge while reducing the statistical errors in the measurements, a major upgrade is needed in terms of luminosity production capacities. Moreover, the magnets located close to the IP1 and IP5 are highly exposed to energy deposition due to the collisions occurring nearby and must be replaced as no spare piece was produced in case of damage [43, 44]. This major luminosity upgrade is called HL-LHC and is foreseen to start operating around 2026 [45]. In order to fully exploit the potential of the LHC, the HL-LHC project aims to determine a set of beam parameters allowing to reach two main luminosity objectives: a peak luminosity of $8 \cdot 10^{34} \text{ Hz/cm}^2$ (compared to the nominal design of $1 \cdot 10^{34} \text{ Hz/cm}^2$ for the LHC), leveled along the fill, in order to reach 250 fb^{-1} per year and therefore about 3000 fb^{-1} within a decade of operation. This corresponds to ten times the luminosity LHC has produced over 12 years of operation. Table 1.2 compares the baselines of the LHC and the HL-LHC [13].

Reaching such objectives implies different and various challenges [46]. Two of the main concerns are worth noting here. The first challenge consists in providing much brighter beams than in the LHC: the HL-LHC beams will be

²1 barn = 10^{-24} cm^2

Parameters	Nominal LHC (design)	HL-LHC (standard)
Energy [TeV]	7	7
Bunch spacing (ns)	25	25
Nb. of bunches	2808	2760
Nb. of collisions (IP1/5)	2808	2748
Bunch charge [10^{11}]	1.15	2.2
Total current [A]	0.58	1.11
β^* [cm]	55	15
Crossing angle [μ rad]	285	500
Beam separation [σ]	9.4	10.5
Norm. transverse emittance [μ m.rad]	3.75	2.5
Peak luminosity (w/o crab cavities) [10^{34} Hz/cm $^{-2}$]	1.0	8.1
Leveled luminosity [10^{34} Hz/cm $^{-2}$]	NA	5.0
Leveling time [h]	NA	7.2

Table 1.2: Comparison of the LHC and HL-LHC baseline parameters.

twice as intense, with smaller emittances. Such beams need to be prepared by the injector complex which has been upgraded in the LIU project. Such brightnesses might rise stability issues, or enhance detrimental effects such as beam-beam interactions or electron cloud effects, already present in the LHC. Secondly, and as a direct consequence, the separation between the two beams around the IP has to be increased in order to limit strong beam-beam effects. As one can see in Table 1.2, the foreseen crossing angle for HL-LHC is twice as large as in the LHC case. Increasing the crossing angle directly affects the so-called Piwinski angle, denoted Φ_w . This angle characterizes the overlap of the two bunches while colliding and thus the luminosity in presence of a crossing angle. It can be defined as [47, 48]:

$$\Phi_w = \frac{\theta_c \sigma_s}{2\sigma^*}, \quad (1.14)$$

where θ_c is the crossing angle, σ_s is the RMS bunch length and $\sigma^* = \sqrt{\varepsilon_g \beta^*}$ is the RMS spot size at the IP, defined as the square root of the product between the β -function at the IP and the geometrical emittance.

The baseline scenario for HL-LHC in order to cope with the enlarged crossing angle is the use of the so-called crab cavities [49, 50] that would maintain a low Piwinski angle. A crab cavity is a superconducting RF dipole used in order to recover the inefficient overlap of two colliding bunches due to a large crossing angle. A cavity located before the IP would tilt longitudinally the considered bunch by imposing a kick whose amplitude varies as the bunch passes through the cavity: the head and the tail of the bunch experience the same kick, with opposite sign, while the center of the bunch does not experience any kick. That way, the collision is achieved with an optimized overlap. After the IP (and a phase advance of π), another cavity will kick back the bunch in order to give it back its original angle. This process is called crab crossing and is illustrated in Figure 1.8.

In the present HL-LHC baseline, it is foreseen to install two cavities per beam and per IP side [51], for a total of 16 cavities in the machine. Each cavity is powered with a voltage of 3.4 MV. However, for a full compensation of the baseline crossing angle, four cavities per beam and per IP side would be required. Consequently, the normalized crossing angle (with respect to the beam size σ) was reduced from 12.5 σ down to 10.5 σ . Such a separation is not enough to neglect the interactions between the two beams [52]. Moreover, keeping the crossing angle at a lower level would also be beneficial for different reasons. Firstly, it would allow for a reduction of the orbit corrector strengths, used to control the orbit bumps in the IR. Secondly, it would reduce the physical aperture needed by the beams in the IR, especially in the final focusing quadrupoles, called Inner Triplet (IT), where the available aperture is limited

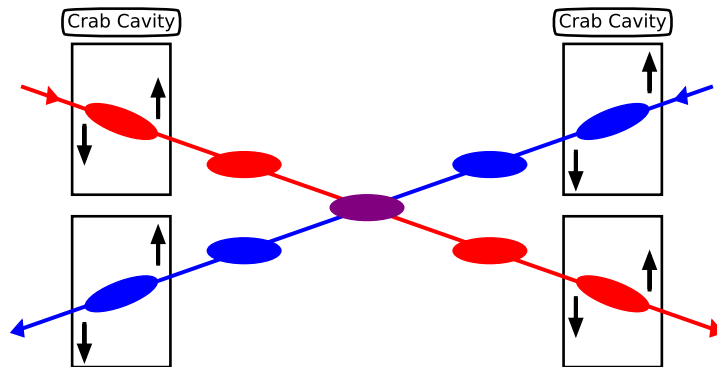


Figure 1.8: Principle of crab crossing, using crab cavities for the HL-LHC.

[53]. Finally, it would reduce the heat load [54] and the integrated radiation dose deposited on the IT [43] due to the debris coming from the collisions at the IP.

In the (HL)-LHC, the transverse separation of the two beams in the IR is small, and the two beams thus interact with each other with a longitudinal offset with respect to the IP. These interactions are called Beam-Beam Long-Range (BBLR) interactions and have a detrimental effect on the beam lifetime. Moreover, a high number of bunches is required in the machine in order to optimize the luminosity. Consequently, the number of BBLR interactions around the IPs is high too. The study of these effects and their possible compensation is of prime importance in a collider such as LHC or HL-LHC where the crossing angle is maintained at a level at which such effects cannot be neglected.

1.2 BEAM-BEAM LONG-RANGE INTERACTIONS IN THE LHC

In this Section, we develop in more details the effects of the BBLR interactions, in the case of the LHC. In a first part, we describe the location of those interactions along the machine, together with the way we can enumerate them. In a second part, we evaluate their effect from a beam dynamics point of view and draw conclusions about possible solutions in order to compensate them. In the next Sections, we introduce several useful concepts of beam dynamics. The reader is assumed to be familiar with the basic concepts of linear optics.

1.2.1 LOCATE AND ENUMERATE THE BBLR INTERACTIONS

At first, we study the longitudinal location of the BBLR interactions, together with a way to count the different encounters a given bunch would experience.

BEAMS' POSITION IN THE INTERACTION REGION

The IR is the straight section of a sector in which the two beams will cross at the IP (in the case of the IR housing an experiment: IR1/2/5/8). At the IP, the two beams collide with a crossing angle so that they can be separated after the collision. This crossing angle is vertical in IR1 and horizontal in IR5. In order to control this crossing, orbit bumps are created using horizontal or vertical orbit correctors. A first dipolar kick is given to the beam on the non-IP side of the IT, and the orbit bump is closed on the other side of the IP by another corrector whose phase advance with respect to the first one is equal to π . Figures 1.9a and 1.9b show the position of the beams in the horizontal and vertical planes around IP1 and IP5 respectively.

1 Introduction

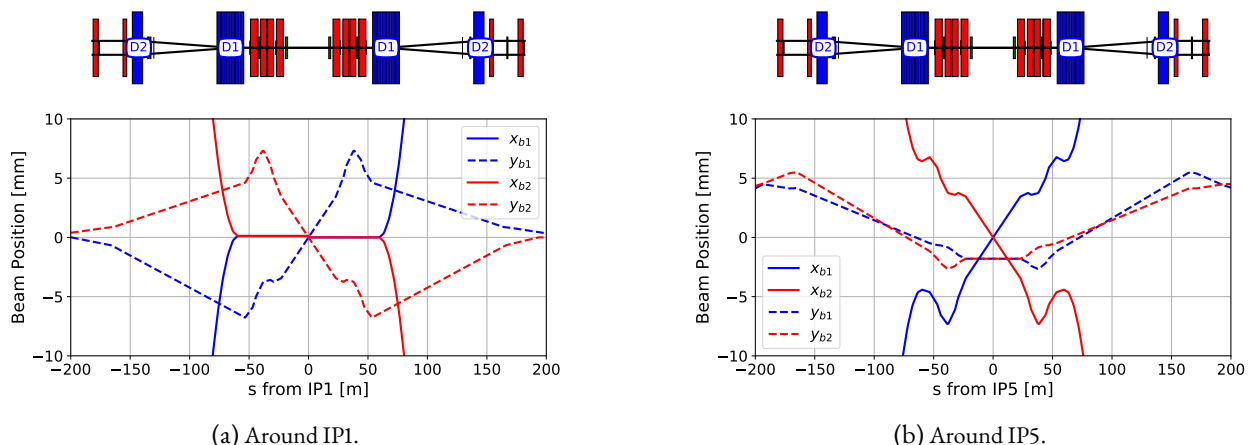


Figure 1.9: Beam positions around the two high luminosity Interaction Points during the 2018 LHC Run. The dipoles are represented by blue rectangles while the quadrupoles by red ones.

The positions are given with respect to the laboratory frame. From the IP, the beams share the same vacuum chamber and go through the IT before entering the separation dipoles, noted D1. These are normal conducting magnets [55]. After the D1, the vacuum chamber splits into two in a Y-shape. The nominal separation of 19.4 cm between the two beams is reached in the superconducting recombination dipole, denoted D2.

Around IP1, the horizontal separation is brought to zero at the D1 locations, while a vertical bump allows for the crossing of the two beams. Around IP5, the crossing is done in the horizontal plane, as one can see on Figure 1.9b. The presence of a vertical bump and of a non-zero vertical position at the IP location is due to a misalignment of the CMS detector that has been corrected in view of the next LHC Run 3 [56]. In between the two D1, where the beam-beam separation is the smallest one, the interactions between the two beams can be treated in the horizontal or the vertical plane while neglecting the other. After the D1, the beam-beam separation increases rapidly and the interactions between the two beams become negligible. The exit of the two D1 are located at approximately 80 m from the IP. Above this limit, the interactions between the two beams are neglected. The bunches are separated in time by 25 ns, which corresponds to a distance of 7.5 m. A bunch from a given beam thus interacts with a bunch from the other beam every 3.75 m. This gives a total of 21 interactions per IP and per side. However, this number is not constant, and depends on the beam structure.

BEAM-BEAM COLLISION SCHEDULE

Depending on the injected filling scheme in the collider, the number of interactions between the bunches of B1 and B2 can vary. The beam structure is defined by a succession of filled buckets separated by empty ones. Bunches are generally grouped in trains of 48 or 72 bunches and several trains can be injected in the machine. For a given number of bunches, the number of Head-On (HO) collisions depends on the considered IP. IP1 and IP5 are diametrically separated and the number of HO collisions is the same for both of them. However, this is not the case for IP2 and IP8. Not only they are closer to IP1 than to IP5, but the distances between IP1 and IP2, and between IP1 and IP8, are not exactly the same. When the two beams interact in an IR, each bunch might encounter one or none partner bunch from the other beam at the IP, producing, or not, a HO collision. As for the HO, the number of BBLR interactions it experiences depends on its position in the train, and on the structure of this train. This is the concept of beam-beam collision schedule. A bunch located in the middle of the train experiences more BBLR interactions than a bunch located at the extremity of this train. Figure 1.10 gives an example of a LHC Run 2 filling scheme.

Many trains are visible, some of them close to each other while some others are more separated. The large gap at the end of the beam corresponds to the previously mentioned abort gap. From this filling scheme, it is possible to

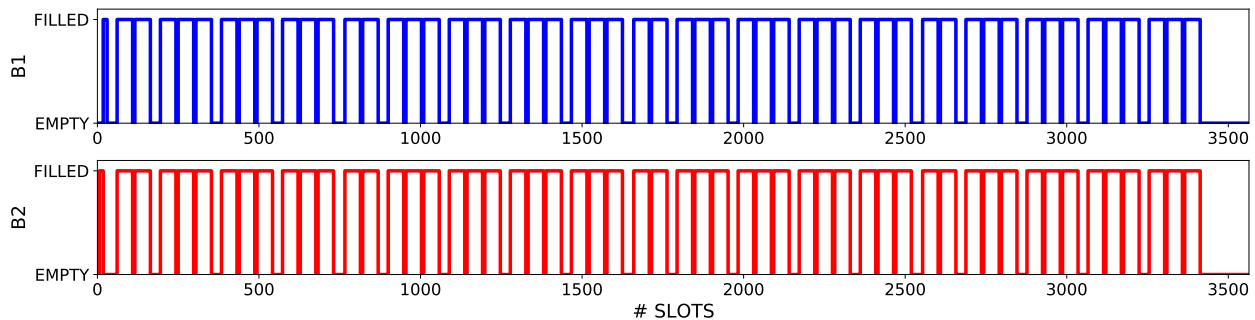


Figure 1.10: An example of filling scheme in the LHC.

determine the beam-beam collision schedule or Beam-Beam Encounter Schedule (BBES). With the filling scheme presented in Figure 1.10, each beam is composed of 2556 bunches, producing 2544 HO collisions in IP1/5, 2215 in IP2, and 2332 in IP8. But one can also obtain the beam-beam collision schedule of each individual bunch. A zoom on the first 300 bunches of the same filling scheme is given in Figure 1.11.

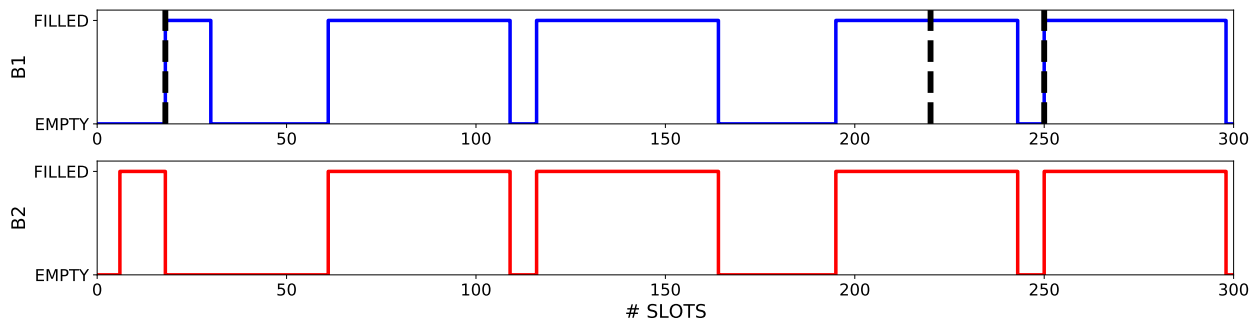


Figure 1.11: Zoom on the first 300 bunches of the filling scheme.

Given this filling scheme, Table 1.3 gives the BBES of three different bunches of B1, represented by black dashed lines on Figure 1.11. We consider only 21 BBLR interactions per IP and per side.

Bunch	HO IP1	HO IP2	HO IP5	HO IP8	LR IR1	LR IR2	LR IR5	LR IR8
18	0	1	0	0	12/0	9/21	12/0	0/21
220	1	1	1	1	21/21	21/21	21/21	21/21
250	1	0	1	1	14/21	17/19	14/21	21/14

Table 1.3: BBES of different bunches of B1. The number of BBLR encounters is given per side of IP (left/right).

All the bunches do not collide HO in all IPs, and the number of BBLR interactions they experience in fact depends on their position within the train. One can count the number of BBLR interactions a bunch would experience in a given IP. Figure 1.12 thus shows the number of BBLR interactions experienced by the bunches of Beam 1 in the IR5 as a function of their position within the beam.

A bunch experiencing less or no BBLR interactions is often referred in the literature as a PACMAN bunch. The PACMAN effects for LHC or HL-LHC were largely studied and are described, for instance, in [57, 58]. During the early design phase of the LHC, such effects were expected to be of prime importance. However, after operating the machine for more than a decade, it seems that the LHC is eventually not dominated by PACMAN effects.

1 Introduction

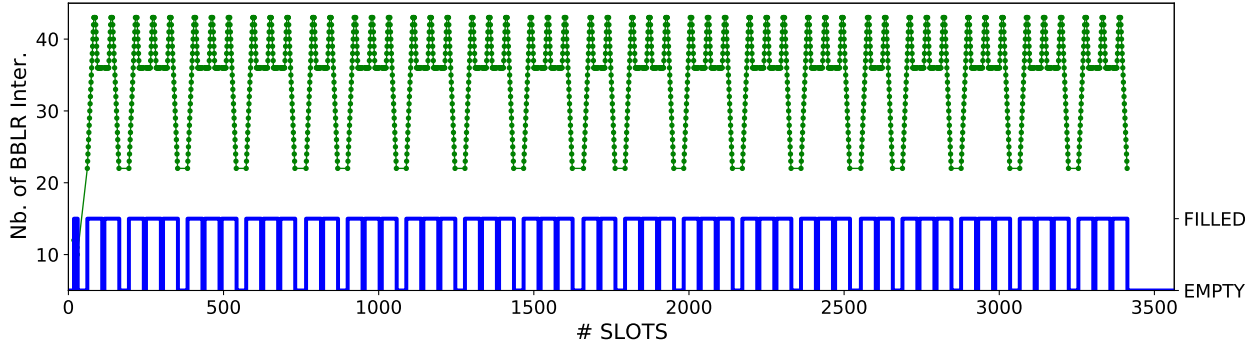


Figure 1.12: Number of BBLR experienced by the bunches of B1 in IR5 as a function of their position within the beam.

We showed where the BBLR interactions are located, and how to enumerate them. In order to study the impact of such interactions on the beams dynamics, it is now necessary to describe the optics of the LHC.

1.2.2 OPTICS IN THE LHC

In this Section we describe the main features of the LHC optics, focusing on the IR, which is the location of the BBLR interactions.

THE ACHROMATIC TELESCOPIC SQUEEZE

Since the beginning of the Run 2 in 2016, a new optics scheme was developed and implemented in the LHC: the Achromatic Telescopic Squeeze (ATS) [59, 60, 61]. The LHC uses the so-called round optics. Both β^* are equal at the collision point. The ATS scheme consists in splitting the reduction of β^* in two stages. The first one, called *pre-squeeze*, uses the matching quadrupoles of a given IR in order to reduce β^* at an intermediate level ranging from 1 m to 40 cm depending on the machine configuration. However, using those matching quadrupoles has several limits (quadrupole strength, chromaticity correction, orbit control...). Consequently, by using only the pre-squeeze, one can reach $\beta^* = 36$ cm for the LHC and $\beta^* = 48$ cm for the HL-LHC. The ATS is therefore needed for the HL-LHC in order to reach the foreseen β^* of 15 cm. The second step consists in a so-called *tele-squeeze*. Reduced β^* values are reached using the matching quadrupoles located in the nearby IRs, namely IR2 and IR8 for the tele-squeeze in IR1, and IR4 and IR6 for the tele-squeeze in IR5. The sectors 81, 12, 45 and 56 are denoted ATS sectors. This configuration results in the propagation of β -beating waves along the arcs, leading - with the correct choice of phase advances - to the desired reduced β -function at the IP. Those β -beating waves are designed in order to preserve the chromatic correction of the Inner Triplet, using the sextupoles located in the ATS sectors. The design and the convenience of such a scheme is, in fact, based on the fact that the peaks of the β -functions occur in specific locations, typically where the arc sextupoles, or the arc octupoles are located, increasing consequently their efficiency. The ratio between β_{Pre}^* , the β^* at the end of the pre-squeeze, and β_{Tele}^* , the β^* at the considered tele-squeeze is called tele-index and is denoted r^{Tele} :

$$r^{Tele} \equiv \frac{\beta_{Pre}^*}{\beta_{Tele}^*}. \quad (1.15)$$

Figure 1.13 shows the β -functions at 6.5 TeV around the IP5 in both planes, together with the corresponding ATS sectors.

The example given in Figure 1.13 (bottom plot) shows a β^* equals to 10 cm, which is in practice not reachable in the LHC. However, this example is chosen for the sake of graphical evidence. One can see the β -beating wave propagating from the ATS sectors towards the IP to be squeezed.

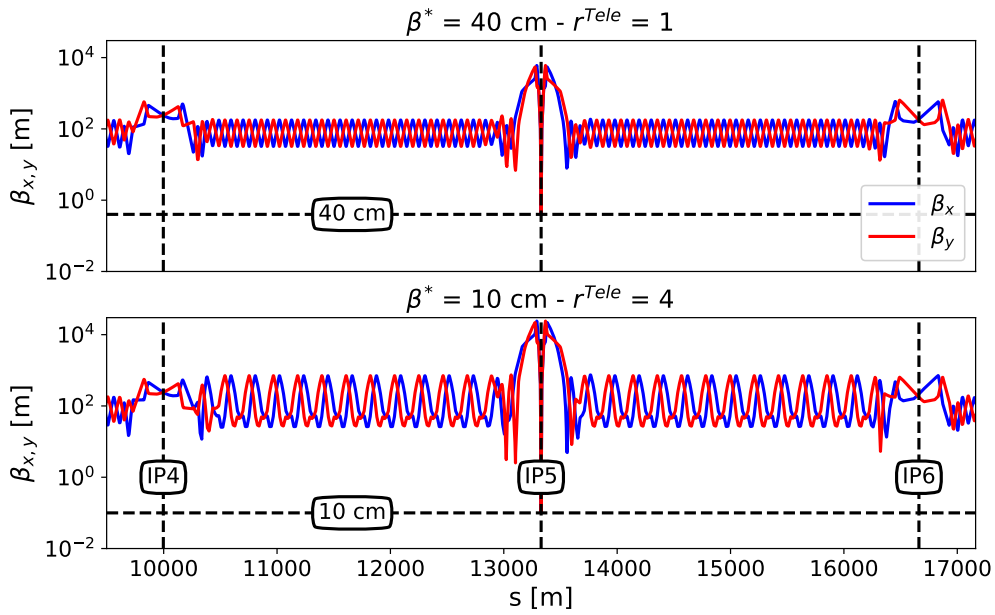


Figure 1.13: Optics layout around IP5 at 6.5 TeV at the end of the pre-squeeze (top plot) and at the end of the tele-squeeze (bottom plot).

Each arc is composed of 23 standard FODO cells [62]. The phase advance of each arc is close to $\pi/2$ and chosen such as the sextupoles and octupoles installed in the arcs are correctly in phase. The sextupoles are used to correct the chromaticity of the machine while the octupoles (so-called Landau octupoles) are used in order to produce enough Landau damping to provide beam stability [63, 64]. Figure 1.14 shows the main optics features on the 56 LHC arc. The two first FODO cells are shown.

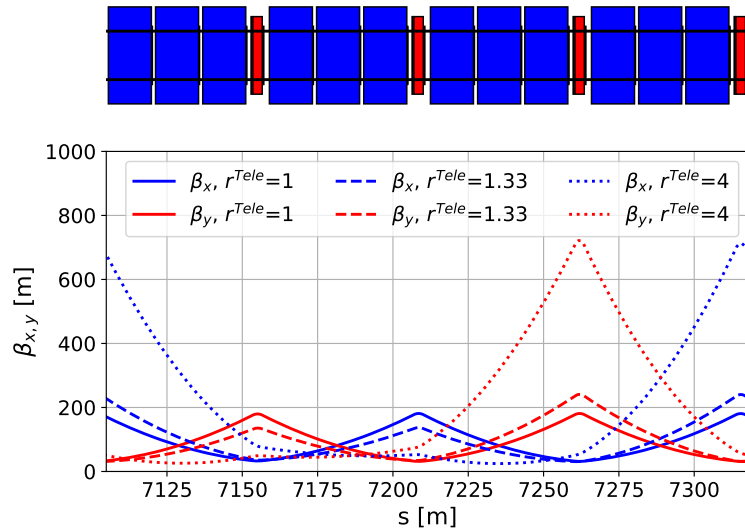


Figure 1.14: Optics layout of the two first FODO cells of an LHC arc (Sector 56). The dipoles and quadrupoles are represented with blue and red squares respectively.

The propagation of the β -beating wave in the arc is visible, and the β -functions are in fact increased or decreased significantly when reaching high tele-indexes.

1 Introduction

As a result, Figure 1.15 shows the β -functions around IP5, for B1, and for a β^* equals to 30 cm ($r^{Tele} = 1.33$).

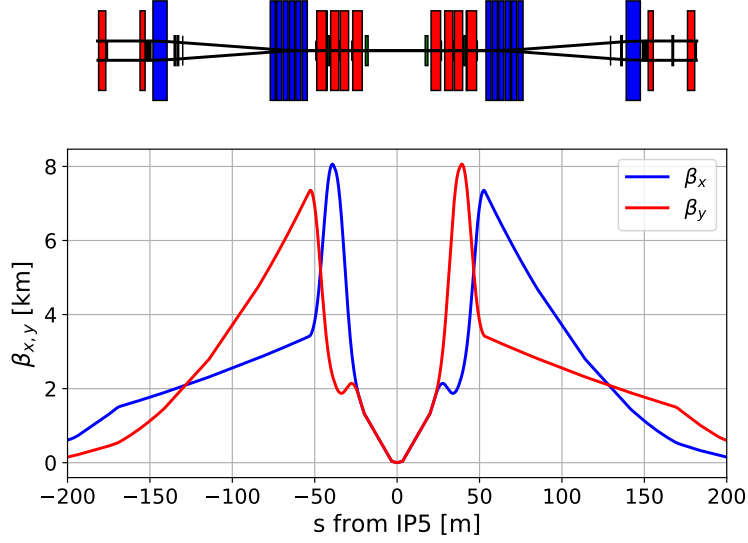


Figure 1.15: Optics layout around the Interaction Point 5 during the 2018 LHC Run.

It is worth noting some interesting properties of the optics around the IP:

- The optics are antisymmetric for a given beam with respect to the IP for both transverse planes, namely: $\beta_x^R = \beta_y^L$ and $\beta_x^L = \beta_y^R$, where L and R stand for left and right respectively.
- The optics are antisymmetric for a given IP side with respect to other beam, namely: $\beta_x^{B1} = \beta_y^{B2}$ and $\beta_x^{B2} = \beta_y^{B1}$.
- The optics are identical for the two beams between the two high-luminosity IP, with a horizontal crossing in IP5 and a vertical in IP1 (at least for the LHC).

BEAM-BEAM SEPARATION

For the study of the BBLR interactions, the distance between the two beams is of prime importance. This distance is called beam-beam separation and denoted d_{bb} . This physical separation can be computed from the beam positions in the laboratory frame as displayed in Figure 1.9. One can normalize this beam-beam separation by the transverse beam size. The normalized beam-beam separation is denoted Δ_{bb} and is given in unit of $\sigma_{x,y}$. Moreover, one can also define the inner normalized beam-beam separation, denoted Δ_{in} and defined as the normalized beam-beam separation in the region between the two ITs, which is a constant, as in Eq. 1.16 [37]:

$$\Delta_{in} = \theta_c \sqrt{\frac{\beta^*}{\epsilon_g}}, \quad (1.16)$$

where θ_c is the full crossing angle given in rad, β^* is the β -function at the IP and ϵ_g is the geometrical emittance. During the 2017-2018 LHC Run, the normalized emittance ϵ_N was equal, in both planes, to about $2.5 \mu\text{m}\cdot\text{rad}$ [65]. The relation between the normalized and geometrical emittance is given by:

$$\epsilon_N = \beta_r \gamma_r \epsilon_g, \quad (1.17)$$

where β_r and γ_r are the relativistic Lorentz factors. During the LHC Run 2, the inner normalized beam-beam separation, assuming a β^* of 30 cm and a half crossing angle of 160 μrad was therefore equal to about $9.2 \sigma_{x,y}$. To compare, the inner normalized beam-beam separation in HL-LHC is foreseen to be set to about $10.5 \sigma_{x,y}$. Moreover, in the case of HL-LHC, the bunch intensity is foreseen to be multiplied by two, while the number of BBLR interactions remains unchanged. The inner beam-beam separation is thus larger than in the LHC case, but not enough to neglect the interactions between the two beams [52].

Figure 1.16 shows the horizontal physical and normalized beam-beam separations around the IP5.

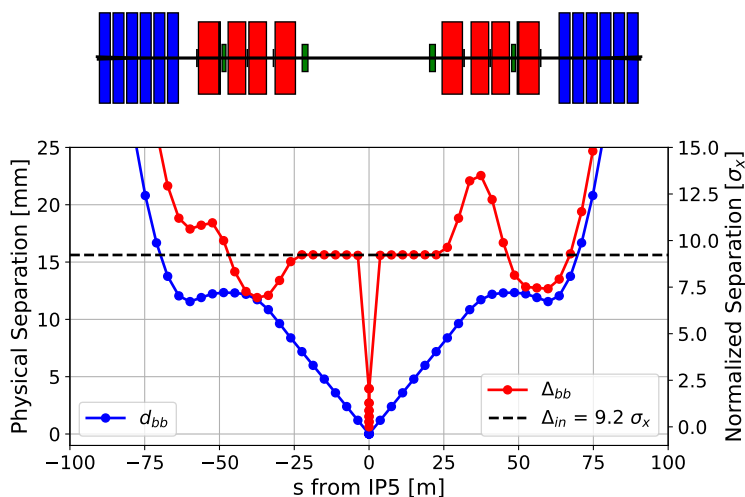


Figure 1.16: Physical and normalized beam-beam separation (horizontal plane) around the IP5.

As we saw on Figure 1.9b, the beam-beam separation increases drastically after the separation dipole, and the interactions between the two beams become negligible.

1.2.3 ELECTROMAGNETIC FIELD CREATED BY A BEAM AND LINEAR OPTICS

At this stage, we are capable of giving the location of the BBLR interactions around the machine and to enumerate the different encounters. We have described the optics at these locations, and we can now evaluate the effect of the BBLR interactions on the beam dynamics. Let us first compute the electromagnetic field created by a beam.

In the following, we assume to be in the weak-strong approximation [66]. This model assumes that a single particle (weak beam) is perturbed by a strong beam (that is not affected by the weak beam). With such an approximation, the beam-beam interactions can be treated as static lenses. However, if the beam-beam interactions become important, the hypothesis of a strong unperturbed beam is not valid anymore. The corresponding model is called strong-strong conditions and the study of the effect of one beam on the other has to be done iteratively.

Let us now assume a bunch of the strong beam in its own rest reference system. The density distribution of this bunch is assumed to be bi-Gaussian as it usually verify in the LHC case [35, 36] and given in Eq. 1.18:

$$\rho(x, y) = \frac{Q}{2\pi\sigma_x\sigma_y} e^{-\left(\frac{x^2}{2\sigma_x^2} + \frac{y^2}{2\sigma_y^2}\right)}, \quad (1.18)$$

where Q is the total charge of the bunch, (x, y) the coordinates of the evaluation point with respect to the center of the bunch and $\sigma_{x,y}$ the RMS transverse bunch size. The bunch length (order of centimeter) is much larger than the transverse size (order of micrometer), so that we neglect the longitudinal dependency of the distribution.

From this distribution, it is possible to derive the field created by the bunch as the associated potential $\phi(x, y)$ follows the Poisson equation:

1 Introduction

$$\nabla^2 \phi(x, y) = \frac{\rho(x, y)}{\varepsilon_0}, \quad (1.19)$$

where ε_0 is the vacuum permittivity.

In 1980, M. Bassetti and G. A. Erskine derived the closed expression for the electric field components E_x and E_y in this particular configuration, using the complex error function and integrating in the complex plane [67]. From these expressions, one can then obtain the formula for the Lorentz forces experienced by a particle of coordinates (x, y) , of charge q and of velocity \mathbf{v} from the general definition of the Lorentz force:

$$\mathbf{F} = q(\mathbf{E} + \mathbf{v} \times \mathbf{B}), \quad (1.20)$$

where (\mathbf{E}, \mathbf{B}) represents the electromagnetic field created by the bunch, in the laboratory frame. In the bunch rest reference system, the field is purely electrostatic and is enough in order to compute the associated force.

In the hypothesis of a round beam ($\sigma_x = \sigma_y = \sigma$), the closed form obtained in [67] can be simplified and one can obtain the force created by a bunch of N protons, as defined in Eq. 1.21 [68]:

$$\begin{aligned} F_x &= -\frac{Ne^2(1 + \beta_r^2)}{2\pi\varepsilon_0} \frac{x}{r^2} \left[1 - e^{-\frac{r^2}{2\sigma^2}} \right] \\ F_y &= -\frac{Ne^2(1 + \beta_r^2)}{2\pi\varepsilon_0} \frac{y}{r^2} \left[1 - e^{-\frac{r^2}{2\sigma^2}} \right], \end{aligned} \quad (1.21)$$

where $r = \sqrt{x^2 + y^2}$ and e is the elementary charge.

The associated kick $(\Delta x', \Delta y')$ experienced by a test particle is given by Eqs. 1.22 and illustrated in Figure 1.17 in the particular example of two beams crossing in the horizontal plane, still in the hypothesis of round beams:

$$\begin{aligned} \Delta x' &= \frac{2r_p N}{\gamma_r} \frac{x}{r^2} \left[1 - e^{-\frac{r^2}{2\sigma^2}} \right] \\ \Delta y' &= \frac{2r_p N}{\gamma_r} \frac{y}{r^2} \left[1 - e^{-\frac{r^2}{2\sigma^2}} \right], \end{aligned} \quad (1.22)$$

where r_p is the classical proton radius. In Figure 1.17 one can see the kick corresponding to a HO interaction for x very close to zero and the one induced by a BBLR interaction for larger x .

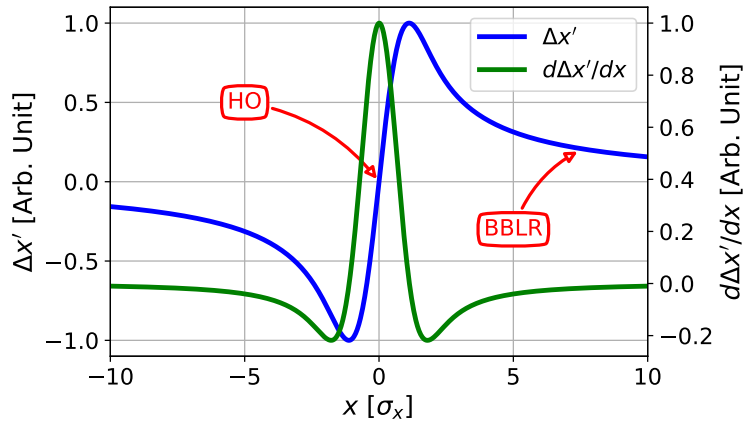


Figure 1.17: Kick given by a round bi-Gaussian beam together with its derivative with respect to x .

For particles located at a large distance from the strong beam ($r \gg \sigma$), the kick defined in Eqs. 1.22 can be written:

$$\begin{aligned}\Delta x' &= \frac{2r_p N x}{\gamma_r r^2} \\ \Delta y' &= \frac{2r_p N y}{\gamma_r r^2}.\end{aligned}\tag{1.23}$$

From the obtained kick or its derivative, it is possible to estimate the effect of the strong beam on the weak one in terms of orbit distortion or betatron tune shift.

For x equals to zero, that is a HO collision, a particle does not experience any force by symmetry. The kick also vanishes for infinite distances, that is a BBLR interaction with a large beam-beam separation. Assuming only a dipolar kick, the effect of the closed orbit at a longitudinal position s due to a given kick $\Delta u'$ located in s_i , where $u = x, y$, is denoted Δu_{co} and can be derived from [69]:

$$\Delta u_{co}(s) = \frac{\sqrt{\beta_u(s_i)\beta_u(s)}}{2 \sin(\pi Q_u)} \cos(\pi Q_u - |\mu_u(s) - \mu_u(s_i)|) \Delta u'(s_i),\tag{1.24}$$

where β is the betatron function, Q the betatron tune and μ the phase advance. One can therefore evaluate the closed orbit distortion at the kick location and obtain:

$$\Delta u_{co}(s_i) = \frac{\beta_u(s_i)}{2 \sin(\pi Q_u)} \cos(\pi Q_u) \Delta u'(s_i).\tag{1.25}$$

Concentrating now on the first order derivative of the obtained kick, one can obtain the betatron tune shift induced by the beam-beam interactions. For distance very close to zero (HO collision), the tune shift is linear and proportional to the first order derivative of the force, as shown in Figure 1.17. The strength of a HO collision can be quantified by this tune shift - also sometimes called beam-beam parameter in the literature - defined for a round beam as [68]:

$$\Delta Q_{x,y}^{HO} = \frac{N r_p \beta_{x,y}^*}{4\pi \gamma_r \sigma^2}.\tag{1.26}$$

In the LHC, the HO interactions in the high-luminosity IPs are strong and the choice of the betatron tunes to operate the machine is important as the HO will shift this working point [70]. From Eqs. 1.22 it is possible to compute the BBLR induced kick as for the HO interaction and to get the associated linear tune shift. However, the symmetry of the crossing between the two high-luminosity IPs (crossing plane rotated by $\pi/2$) allows for the self compensation of the quadrupolar and more generally the $4k+2$ order components induced by the BBLR interactions. This means that the BBLR induced linear tune shift, as well higher order tune spread (see next Section), self-compensates between IP1 and IP5. This idea of designing IPs such as BBLR induced tune shifts would self-compensate dates back to the early design of the Superconducting Super Collider (SSC) [71].

To conclude, HO interactions shift the betatron tunes by a value that depends on the beam intensity and the β^* . However, HO interactions do not induce an orbit distortion at the first order approximation. Secondly, the BBLR interactions induce both a linear tune shift and an orbit distortion. The latter is compensated in average in the machine by design [72] while the first one is self-compensated by the symmetry of the crossing plane in the two high-luminosity IRs. Compensating the linear components of the BBLR interactions is therefore not needed. Nonetheless, beam-beam interactions also drive higher order components, as we will see in the next Section.

1.2.4 MULTIPOLAR EXPANSION AND NON-LINEAR OPTICS

In the previous Section, we derived the kick induced by the beam-beam interactions, and focused on the first orders effects, that are the orbit distortion and the betatron tune shift. In this Section, we propose to expand into multipoles the electromagnetic field induced by the strong beam, and to study the impact of higher order components on the dynamics of the weak beam.

We now consider two bunches interacting at a longitudinal position $s = s_0$, taken as the time origin $t = 0$, in the laboratory frame. One of the two bunches is assumed to be the strong beam, while the other is the weak one. The charge distribution of the strong beam is assumed to be bi-Gaussian, truncated in both horizontal and vertical plane. This assumption is valid in presence of the collimators in the LHC, that clean the beam halo. The total surface charge of the strong bunch in the considered transverse plane is Q_0 and the characteristic radius of the distribution is denoted r_0 . The center of the strong bunch is taken as the reference system origin. The strong beam is assumed to travel towards positive z direction and the weak beam toward negative z . We construct a circle, called expansion circle, of radius r_c (radius of convergence) and centered on z_0 , that is the center of the weak beam with respect to the center of the strong one, that does not include any material or current sources, so that the assumption of free space stands. Finally, we consider a test particle of the weak beam located at a transverse position $z = x + iy$ with respect to the strong beam. Figure 1.18 shows a schematic view of the reference system.

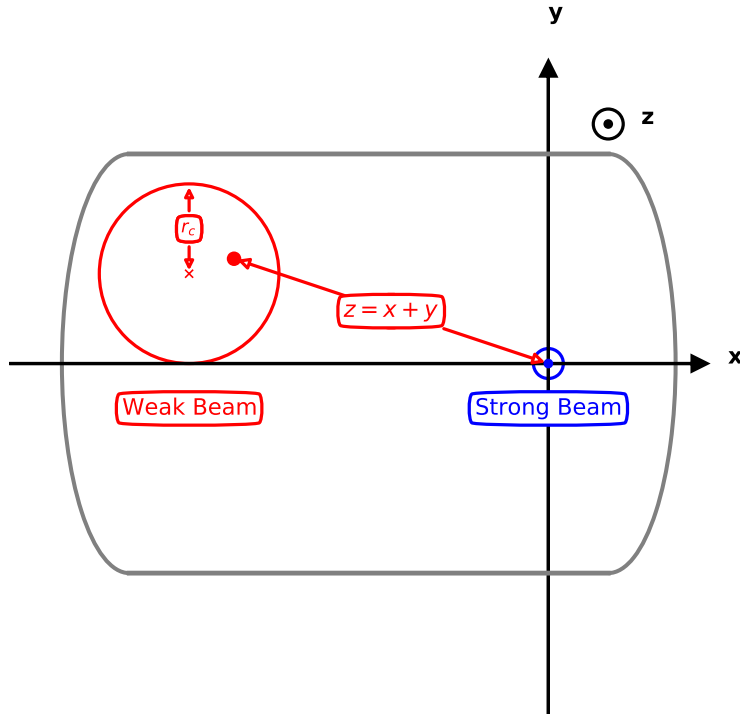


Figure 1.18: Schematic view of the reference system for the multipolar expansion.

We assume here to be in a straight section, so the curvature is zero. The curl of the magnetic field is zero and so is the derivative of all the field components with respect to the z -direction:

$$\begin{aligned} \nabla \times \mathbf{B} &= 0 \\ \frac{\partial B_x}{\partial z} &= \frac{\partial B_y}{\partial z} = 0. \end{aligned} \tag{1.27}$$

Moreover, we have that $\nabla \cdot \mathbf{B} = 0$, so that finally we can write:

$$\begin{aligned}\frac{\partial B_x}{\partial x} &= -\frac{\partial B_y}{\partial y} \\ \frac{\partial B_x}{\partial y} &= \frac{\partial B_y}{\partial x},\end{aligned}\tag{1.28}$$

which are the Cauchy-Riemann conditions. The magnetic field induced by the strong beam and seen by the test particle can thus be written under the form of a Taylor expansion as in Eq. 1.29 [73, 74, 75]:

$$B_y + iB_x = \sum_{n=0}^{\infty} C_n (x + iy)^n,\tag{1.29}$$

where C_n is a complex constant, dependent on the relative position of the two beams. The C_n coefficients characterize the strength and the orientation of each multipole in the transverse complex plane. One can distinguish the normal and skew component of a multipole n , and define C_n as:

$$C_n = b_n + ia_n,\tag{1.30}$$

where b_n and a_n represent the normal and skew components respectively. So we get the general multipolar expansion in Cartesian coordinates:

$$B_y + iB_x = \sum_{n=0}^{\infty} (b_n + ia_n)(x + iy)^n.\tag{1.31}$$

For the sake of consistency with numerical computations, we choose to follow the multipole numbering convention used in the MAD-X software [76], where $n = 0$ corresponds to the dipolar component.

It is sometimes more convenient to use the polar coordinates (r, θ) . Using these coordinates, the magnetic field can be written:

$$B_y + iB_x = \sum_{n=0}^{\infty} (b_n + ia_n)r^n e^{in\theta},\tag{1.32}$$

where the polar coordinates are obtained using:

$$\begin{aligned}x &= r \cos \theta \\ y &= r \sin \theta \\ z &= x + iy = r e^{i\theta}.\end{aligned}\tag{1.33}$$

One can express the magnetic field in terms of radial B_r and azimuthal B_θ components as:

$$B_y + iB_x = (B_\theta + iB_r)e^{-i\theta}.\tag{1.34}$$

Hamiltonian formalism is commonly used in accelerator physics as it allows us to obtain the equations of motion without the need for integrating, which can be difficult. The goal of this Section is not to develop this formalism but simply to recall some results that can be retrieved from [77, 78]. The Hamiltonian formalism will be particularly useful when studying the resonances driven by the BBLR interactions in the next Chapter.

1 Introduction

We write the general expression of the Hamiltonian for an ultra-relativistic particle ($\beta_r \approx 1, \gamma_r \gg 1$) traveling in an electromagnetic field represented by the vector potential $\mathbf{A}(\mathbf{x}, t)$ and the scalar potential $\Phi(\mathbf{x}, t)$:

$$\mathcal{H}(\mathbf{x}, \mathbf{P}, t) = c\sqrt{(\mathbf{P} - q\mathbf{A}(\mathbf{x}, t))^2 + m^2c^2} + q\Phi(\mathbf{x}, t), \quad (1.35)$$

where \mathbf{x} and \mathbf{P} are the conjugate variables, e the elementary charge and m the mass of the particle. It is in general more convenient to use the canonical variables $(x, p_x; y, p_y)$ and the longitudinal position s as independent variable. Assuming a straight section of the accelerator (zero curvature), and no electric field, the Hamiltonian 1.35 can be written [79] in the ultra-relativistic approximation ($\beta_r \approx 1, 1/\gamma_r \approx 0$):

$$\mathcal{H}(x, p_x, y, p_y; s) = \delta - \sqrt{(\delta + 1)^2 - p_x^2 - p_y^2} - a_s(x, y), \quad (1.36)$$

where $\delta = \Delta p/p_0$ is the relative momentum deviation and p_0 the reference momentum. The vector potential is taken to have only a longitudinal component A_s with an appropriate choice of gauge. a_s represents thus this longitudinal component of the vector potential, normalized by the beam rigidity $a_s(x, y) = A_s(x, y)/B\rho$. This choice of gauge is possible assuming only transverse magnetic fields such as $\mathbf{B} = (B_x, B_y, 0)$.

Each multipole from 1.31 has a component in the Hamiltonian 1.36 so that one can expand it under the form:

$$\begin{aligned} \mathcal{H}(x, p_x, y, p_y; s) &= \sum_{n=0}^{\infty} \mathcal{H}_n + \frac{p_x^2 + p_y^2}{2(\delta + 1)} \\ &= \sum_{n=0}^{\infty} \frac{1}{1+n} \Re \left[(k_n(s) + ik_n^{(s)}(s))(x + iy)^{n+1} \right] + \frac{p_x^2 + p_y^2}{2(\delta + 1)}, \end{aligned} \quad (1.37)$$

where k_n and $k_n^{(s)}$ are the strength corresponding to the normal and skew components of the n^{th} -multipole, defined as:

$$\begin{aligned} k_n &= \frac{1}{B\rho} \frac{\partial^n B_y}{\partial x^n} = \frac{b_n}{B\rho} \\ k_n^{(s)} &= \frac{1}{B\rho} \frac{\partial^n B_x}{\partial y^n} = \frac{a_n}{B\rho}. \end{aligned} \quad (1.38)$$

As an example, one can study the effect of a normal octupole component ($n = 3$) on the weak beam. The corresponding Hamiltonian can be written:

$$\begin{aligned} \mathcal{H}_3 &= \frac{1}{4} k_3(s) \Re[(x + iy)^4] \\ &= \frac{1}{4} k_3(s) (x^4 - 6x^2y^2 + y^4), \end{aligned} \quad (1.39)$$

where the (x, y) coordinates can be written, in the perturbation approximation, in terms of action-angle variables $(J_x, \mu_x; J_y, \mu_y)$:

$$\begin{aligned} x &= \sqrt{2J_x\beta_x} \cos(\mu_x) \\ y &= \sqrt{2J_y\beta_y} \cos(\mu_y), \end{aligned} \quad (1.40)$$

where $\beta_{x,y}$ are the β -functions and the actions $J_{x,y}$ are defined positive. So the Hamiltonian can be written:

$$\mathcal{H}_3 = k_3 [J_x^2 \beta_x^2 \cos^4(\mu_x) - 6J_x J_y \beta_x \beta_y \cos^2(\mu_x) \cos^2(\mu_y) + J_y^2 \beta_y^2 \cos^4(\mu_y)] \quad (1.41)$$

The corresponding tune shift can be computed using [80]:

$$\Delta Q_{x,y} = \frac{1}{2\pi} \frac{d\langle \mathcal{H}_3 \rangle}{dJ_{x,y}}, \quad (1.42)$$

where $\langle \mathcal{H}_3 \rangle$ is the average of the Hamiltonian over the betatron phase $\mu_{x,y}$. Finally, the obtained tune shift can be written:

$$\begin{aligned} \Delta Q_x &= \frac{3}{8\pi} k_3 [\beta_x^2 J_x - 2\beta_x \beta_y J_y] \\ \Delta Q_y &= \frac{3}{8\pi} k_3 [\beta_y^2 J_y - 2\beta_x \beta_y J_x]. \end{aligned} \quad (1.43)$$

The detuning induced by the normal octupolar component of the BBLR interactions depends on the amplitude of the test particle. The resulting effect on the beam will thus be a tune spread, or detuning with amplitude. The remaining question is now to evaluate the strength of the normal octupolar component k_3 . To do so, let us consider the rest reference frame of the weak beam. The electric and magnetic field seen by the test particle are purely radial and azimuthal respectively and are related by [48]:

$$\begin{aligned} E_r &= -cB_\theta \\ &= \frac{Q_0}{2\pi\epsilon_0|z|} \delta(s - s_0 + ct), \end{aligned} \quad (1.44)$$

where ϵ_0 is the free space permittivity and δ is the Dirac function. The time variable t can be substituted as $t = (s - s_0)/c$ so that we get:

$$\begin{aligned} B_\theta &= -\frac{Q_0}{2\pi\epsilon_0 c|z|} \delta(2(s - s_0)) \\ &= -\frac{Q_0}{4\pi\epsilon_0 c|z|} \delta(s - s_0). \end{aligned} \quad (1.45)$$

In order to obtain the integrated Lorentz force seen by the test particle, one has to change reference frame and choose the laboratory frame as described in Figure 1.18. In this reference frame, one can integrate the azimuthal magnetic field seen by the particle to obtain the effective magnetic field corresponding to the integrated Lorentz force. Denoting $\theta = \arg(z)$:

$$\begin{aligned}
 \int_{\text{bunch}} (B_y + iB_x) ds &= 2 \int_{\text{bunch}} (B_\theta + iB_r) e^{-i\theta} ds \\
 &= -\frac{Q_0}{2\pi\epsilon_0 c |z|} e^{-i\theta} \\
 &= -\frac{Q_0}{2\pi\epsilon_0 c} \frac{|z| e^{-i\theta}}{|z|^2} \\
 &= -\frac{Q_0}{2\pi\epsilon_0 c} \frac{1}{z}.
 \end{aligned} \tag{1.46}$$

It is worth noting that a factor two was added in comparison to Eq. 1.34 due to the change of reference system: in the two laboratory frame, the two bunches are moving in opposite directions. Finally, we obtain, by using $\epsilon_0 = 1/(\mu_0 c^2)$ and by defining an equivalent integrated current $(IL)_{eq} \equiv Q_0 c$:

$$\int_{\text{bunch}} (B_y + iB_x) ds = -\frac{\mu_0 (IL)_{eq}}{2\pi} \frac{1}{z}. \tag{1.47}$$

We recognize the integrated magnetic field of a Direct Current (DC) wire, carrying a current I , of finite length L and located at a distance d from the observation point. We thus identify the multipolar expansion from Eq. 1.31 to obtain the octupolar strength needed to complete Eq. 1.43 and obtain:

$$\begin{aligned}
 \Delta Q_x &= -\frac{3\mu_0 (IL)_{eq}}{16\pi^2 B\rho} \frac{1}{d^4} [\beta_x^2 J_x - 2\beta_x \beta_y J_y] \\
 \Delta Q_y &= -\frac{3\mu_0 (IL)_{eq}}{16\pi^2 B\rho} \frac{1}{d^4} [\beta_y^2 J_y - 2\beta_x \beta_y J_x].
 \end{aligned} \tag{1.48}$$

The usual way to study numerically the detuning with amplitude induced by the BBLR interactions is to plot a so-called tune footprint. In the LHC, the nominal working point in terms of betatron tunes is ($Q_x = 62.31, Q_y = 60.32$). However, in presence of HO interaction, this working point is shifted as mentioned in the previous section. Moreover, the BBLR interactions induce an additional amplitude detuning as we just showed. Figure 1.19 compares the tune footprints obtained considering only HO collisions and considering both HO and BBLR interactions.

One can observe that the BBLR interactions enlarge the tune footprint. Consequently, some particles are more likely to cross resonances lines, leading to beam losses.

In the derivation of the linear detuning with amplitude, an important observation was made. For large enough beam-beam separations, the force experienced by a test particle from the weak beam is equivalent to the one produced by a DC wire. This observation raises the question of a possible mitigation of the BBLR interactions using DC wires. This method is the topic of this Thesis.

1.3 BBLR COMPENSATION USING DC WIRES

In this Introduction, we saw that each bunch will have a different beam-beam collision schedule. This variety of beam-beam schedule would call for a bunch-by-bunch device for the compensation of the BBLR interactions. In 1997, V. Shiltsev proposed for the first time a possible compensation of the BBLR induced tune spread using an electron lens [81]. The aim was to compensate beam-beam effects in the Tevatron proton-antiproton collider using electron beams. Having an opposite charge, an electron beam should be able to counteract the effect induced by the proton beam on the antiproton one. In [81], V. Shiltsev proved that it was possible to reduce the tune variation

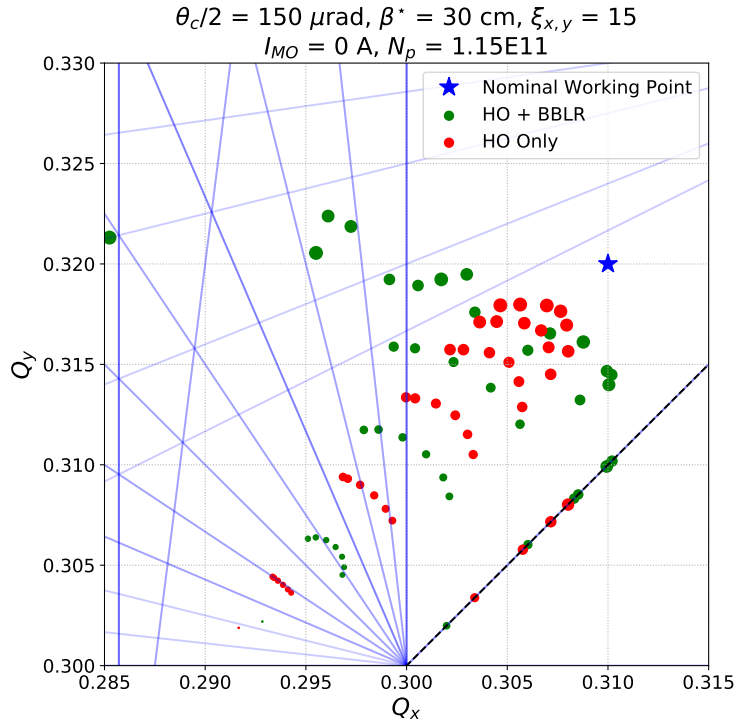


Figure 1.19: Example of tune footprints in the case of the 2017-2018 LHC Run 2: $\beta^* = 30 \text{ cm}$, $\theta_c/2 = 150 \mu\text{rad}$, $N_b = 1.15 \cdot 10^{11}$ p, collisions in all IPs. The amplitude of the particles is represented by the size of the dots.

between two bunches using time-dependent electron currents. These beams are provided by an electron compression device mainly consisting in a cathode, a collector and a solenoid, as shown on Figure 1.20.

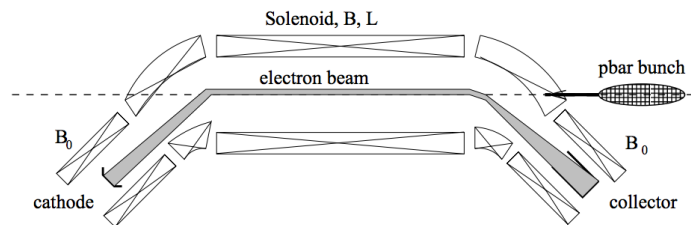


Figure 1.20: Schematic view of an electron compression device [82]

After some years of experiments, FermiLab deployed operational devices and installed them in the Tevatron collider, demonstrating their beneficial effect on the proton beam lifetime [83]. Moreover, U. Dorda, in his PhD thesis, also studied the possibility of compensating the BBLR interactions using RF wires [68]. Those devices are technologically more challenging than the option studied in this Thesis, that is the compensation of the BBLR interactions using DC wires.

The idea of the compensation of the BBLR interactions using DC wires dates back from the early 2000's by observing the similarity of the BBLR kick with the $1/r$ shape of the kick given by a DC wire [84, 85]. Figure 1.21 illustrates this fact by adding the wire-induced kick to the Figure 1.17.

For large enough separations (typically for $\sigma > 2$), corresponding the BBLR interactions, the kicks induced by a DC wire or beam-beam interactions are similar. Consequently, the approximation between a beam and a wire is even better in the case of HL-LHC, where the normalized crossing angle is larger than in the case of the LHC.

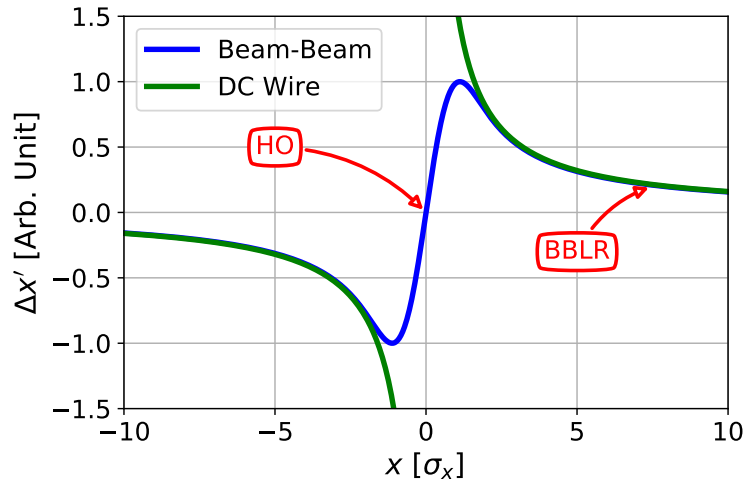


Figure 1.21: Comparison between the beam-beam kick and a DC wire-induced kick.

Since then, several experiments have been carried out, installing and testing different types of wires in different machines such as the Relativistic Heavy Ion Collider (RHIC) [86] at the Brookhaven National Laboratory (BNL), DAFNE (Double Annular Factory for Nice Experiments) [87] at the INFN (Istituto Nazionale di Fisica Nucleare) in Frascati, Italy or in the SPS at CERN [88, 89]. The main characteristics of these wires are reported on Figure 1.22 where one can observe the evolution of the active length and the radius of the wires with respect to the nominal currents expected to be carried.

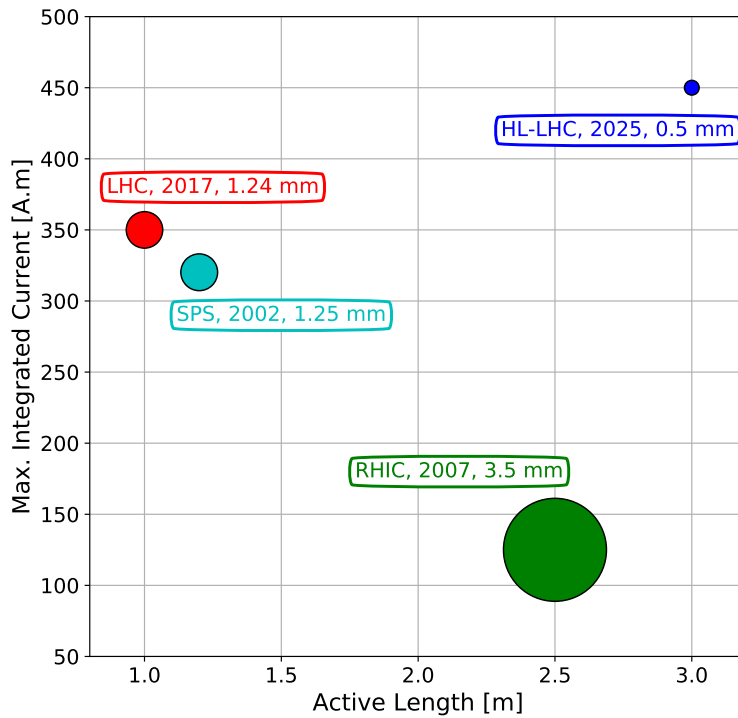


Figure 1.22: History of the DC wire compensators: the evolution of their dimensions (active length and radius) and their nominal currents.

Those different experiments have successfully demonstrated the potential beneficial effect of the wires on the beam lifetime. However, no rigorous analytical treatment was carried out. In 2015, in the framework of the HL-LHC project, it was shown that two wires per IP, correctly located, could compensate or minimize all the so-called Resonance Driving Terms (RDT) [48]. Different approaches to choose the wire settings - including this one - are described in Chapter 2 and used in order to choose at best the wire compensators settings in the LHC as the results obtained in [48] motivated the construction and the installation of demonstrators for the LHC. A two years long experimental campaign followed and the obtained results are reported in Chapter 3. Those experimental results are accompanied by numerical results from tracking simulations. The goal was to demonstrate the possibility of compensating the BBLR interactions in the LHC during the 2017-2018 LHC Run, and to prepare the use of such devices for the future LHC Run 3 and the HL-LHC era. In Chapter 4, we report the results of another set of experiments, consisting in mitigating the BBLR interactions using the Landau octupoles present in the LHC. Finally, in Chapter 5, we report the numerical results obtained in order to prepare the operation of the LHC with the BBLR compensators during the next LHC Run 3. The positive experimental and numerical results obtained and presented in this Thesis turned the wires into operational devices, foreseen to be used systemically at the end of each fill, in order to gain operational experience in view of the HL-LHC era.

2 WIRE COMPENSATORS SETTINGS IN THE LHC

During the 2016-2017 winter technical stop, wire compensators were installed in the LHC, around IP5. The compensators in IR1 were installed the following year, during the 2017-2018 winter technical stop. The installed devices are proof-of-concept demonstrators, intended to show the possibility of mitigating the BBLR interactions using DC wires. In this Chapter, we describe the experimental hardware as installed in the LHC in 2018, together with the different methods used to chose the operational settings of the compensators. Finally, we validate the choice of settings using tracking simulations, and discuss the differences between an ideal setup without any constraint, and the setup used during the experimental campaign.

2.1 THE EXPERIMENTAL SETUP IN THE LHC

2.1.1 MAGNETIC FIELD OF A DC WIRE

We assume a DC wire in free space. As in Section 1.2.3, the Cauchy-Riemann conditions are verified and the magnetic field created by a wire can be written under the form of a Taylor expansion:

$$B_y + iB_x = \sum_{n=0}^{\infty} (b_n + ia_n)(x + iy)^n, \quad (2.1)$$

where b_n and a_n are the normal and skew components of the n^{th} -multipole, respectively. We assume the center of expansion $(0, 0)$ to be the reference orbit of the weak beam. The integrated normal and skew components, denoted B_n and A_n respectively, can be derived from Eq. 2.2 [48]:

$$\begin{aligned} B_n + iA_n &= \int_{Wire} (b_n + ia_n) ds \\ &= -\frac{\mu_0(IL)_w}{2\pi} \frac{n!}{(-x_w - iy_w)^{n+1}}, \end{aligned} \quad (2.2)$$

where $(IL)_w$ is the integrated current of the wire expressed in A.m, and (x_w, y_w) give the position of the wire with respect to the reference orbit of the weak beam. In MAD-X [76], as in the experiment, the weak beam is assumed to be Beam 2, while Beam 1 is the strong beam. A positive integrated current $(IL)_w > 0$ corresponds to a current flowing in the positive s-direction, which corresponds to the Beam 1 direction.

Using Eq. 2.2, one can get an expression for the normal and skew coefficients using the MAD-X conventions. In MAD-X, multipoles coefficients are normalized by the beam rigidity $B\rho$ to obtain the integrated normalized strength of each normal and skew multipole (KN_n and KS_n respectively) as shown in Eqs. 2.3:

$$\left\{ \begin{aligned} KN_n &= \frac{B_n}{B\rho} \\ KS_n &= \frac{A_n}{B\rho}. \end{aligned} \right. \quad (2.3a)$$

$$\left\{ \begin{aligned} KN_n &= \frac{B_n}{B\rho} \\ KS_n &= \frac{A_n}{B\rho}. \end{aligned} \right. \quad (2.3b)$$

2 Wire Compensators Settings in the LHC

Eqs. 2.4 finally give the expression of the n^{th} -multipole strength for a DC wire, using the previous equations.

$$\begin{cases} KN_n = -\frac{n!}{B\rho} \frac{\mu_0(IL)_w}{2\pi} \Re \left[\frac{1}{(-x_w - iy_w)^{n+1}} \right] \\ KS_n = -\frac{n!}{B\rho} \frac{\mu_0(IL)_w}{2\pi} \Im \left[\frac{1}{(-x_w - iy_w)^{n+1}} \right]. \end{cases} \quad (2.4a)$$

$$(2.4b)$$

2.1.2 THE LHC WIRE COMPENSATORS

The wires installed in the LHC are made of copper [90] and covered with a thin silicon dioxide insulator. They are 984 mm long and are placed parallel to the beam, in the horizontal (in IR5) or the vertical (in IR1) plane. Differently from the other wire experiments described in the Introduction, the wire demonstrators installed in the LHC are embedded in collimators [90]. Collimators are devices used in the LHC in order to clean the beams halo and protect the machine against possible beam losses that would damage it [91, 92]. The collimation system of the LHC is designed on a three stages hierarchy. The primary collimators intercept the beam halo, while secondary and tertiary collimators - more widely open - clean the secondary and tertiary emissions. Primary and secondary collimators are located in both IR3 and IR7 of the machine, while tertiary collimators are also located around the different IPs in order to intercept debris from the collisions. The wires are housed inside the tungsten jaws of tertiary collimators in the Insertion Regions 1 and 5 and are installed on Beam 2 only, as it was the only beam foreseen to operate with a coronagraph [93]. Figure 2.1 shows one of the four wire collimators currently installed in the LHC tunnel.

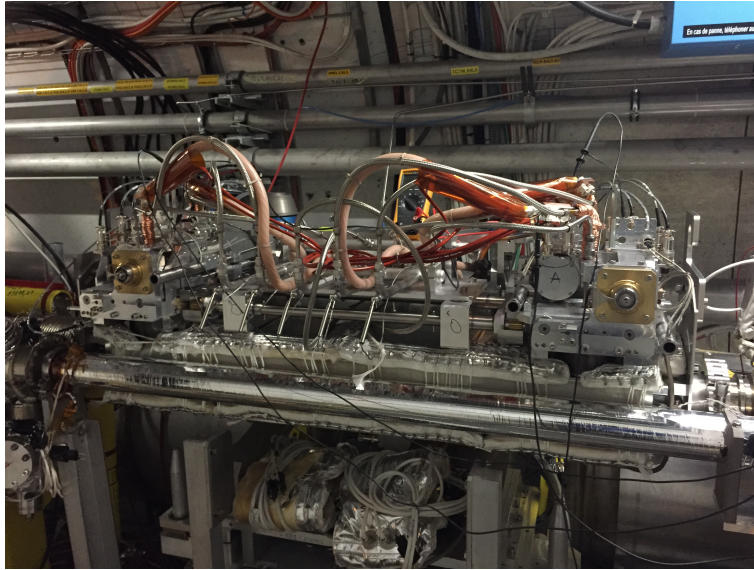


Figure 2.1: Wire collimator currently installed in the LHC tunnel on the left side of IP5 (L5).

The wires can carry a DC current up to 350 A, which is the design and operational value, even if higher currents have been reached during the thermo-mechanical tests of the prototypes. When powered to their nominal power, the wires can produce a thermal load of about 1 kW by Joule effect. This thermal load is then absorbed by the jaw. The design of the wires has therefore to take into consideration those effects since the presence of a wire shall not jeopardize the main purposes of the collimator which are to clean the beam and to protect the machine. Consequently the wires are brazed to a Glidcop[®] T-shaped support [94]. This support is then connected to the tungsten block by means of screws. This brazing maximizes the thermal dissipation and consequently the cooling of the wire itself. At the extremities of the collimator, where the wire is not in direct contact with the jaw, and where the dimension of the

wire is not an issue anymore from a beam dynamics point of view, the wire diameter is increased from 2.48 mm to 3.45 mm in order to decrease the Joule effect induced losses. A section view of the wire in its support is shown on Figure 2.2.

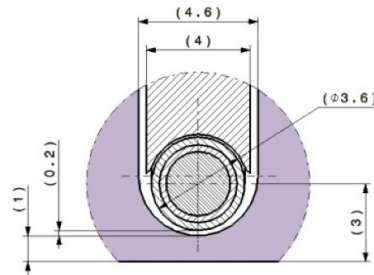
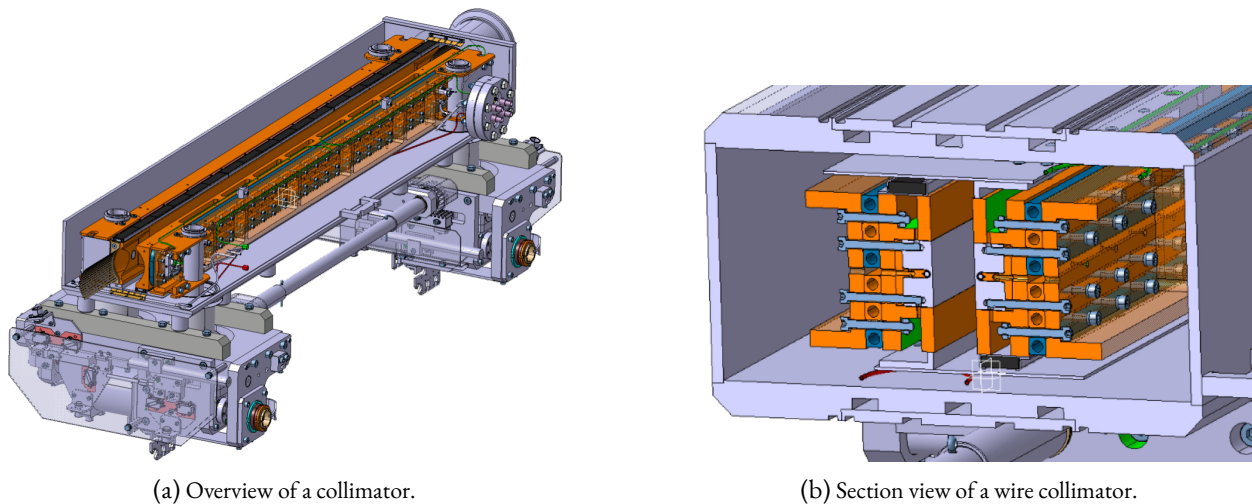


Figure 2.2: Assembly of the wire on its support [95].

Each wire collimator contains two wires, one in each jaw. In Figure 2.3, one can see a 3D representation of a standard tertiary collimator (2.3a) and a section view of a wire collimator (2.3b). In this specific example, an horizontal collimator is shown.



(a) Overview of a collimator.

(b) Section view of a wire collimator.

Figure 2.3: 3D representations of a wire collimator [95].

Each jaw is equipped with two motors allowing a lateral movement of each extremity. These motors are used to open or close the collimator gap, or to introduce a tilt in order to align the collimator with the beam. Moreover the collimator is equipped with an additional motor, enabling the overall tank to be displaced in the plane orthogonal to the one of collimation (in the case of Figure 2.3a, in the vertical plane). The presence of this so-called 5th-axis is motivated by the necessity to offset damaged portions of the jaw by an undamaged one by a simple translation of the collimator, in case of beam impact. On Figure 2.3b one can see the jaws equipped with a wire, visible in the center of each jaw.

The jaws are water cooled in order to minimize the impact of the beam induced heating on the overall mechanical structure. The wire moves, together with the housing jaw, inside the vacuum chamber, with an accuracy of about 20 μm . Its transverse position is thus constrained by the collimation hierarchy. The wires should therefore always sit not only in the shadow of the primary and secondary collimators but also under the protection of the housing tertiary collimator. Consequently, the wires' center is installed 3 mm behind the jaw of their collimator. The corresponding

physical beam-wire transverse distances, as a function of the collimator opening are illustrated in Figure 2.4, in the case of the 2018 LHC Run ($\beta^* = 30$ cm, $\theta_c/2 = 150$ μ rad). The jaw position is given in unit of σ_{coll} ¹.

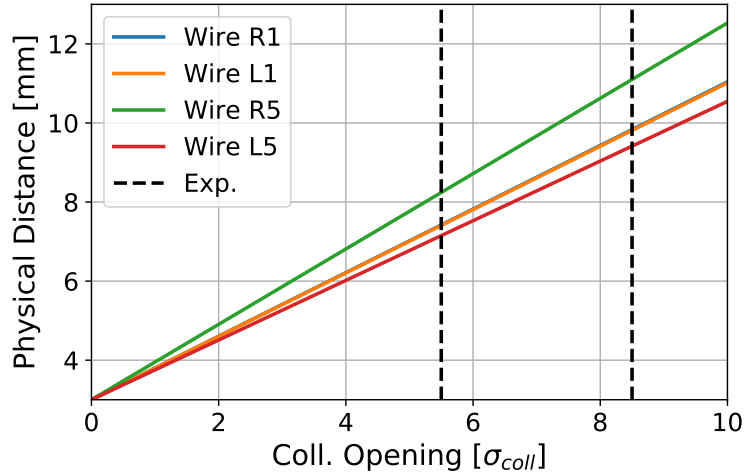


Figure 2.4: Physical beam-wire distances as a function of the collimator opening during the 2018 LHC Run. The black dashed line represents the configurations explored during the experimental campaign.

Each collimator houses two Beam Position Monitors (BPM), one at its entrance (up-stream) and one at its exit (down-stream) [96, 97]. These devices are made of two pick-ups (PU) - one on each jaw - that record the position of the beam within the gap that separates them.

The LHC layout during the 2018 Run including the wire compensators (denoted R1, L1, R5, L5) is presented schematically in Figure 2.5. The naming of the wire compensators corresponds to the IP side (Left or Right) and number (IP1 and 5).

The longitudinal position of the wire collimators with respect to the close-by IP is given in Table 2.1.

Wire Compensator	Dist. from IP [m]	Plane
Wire L1	-176.17	V
Wire R1	145.94	V
Wire L5	-150.03	H
Wire R5	147.94	H

Table 2.1: Longitudinal positions of the wires with respect to the IPs.

Finally, Figure 2.6 shows the location of the two wires in IR5 together with the optics layout. The wire collimators are located in a region where the two vacuum chambers are separated, right after the recombination dipole D2, and close to the Q4 quadrupole. At the wires location, the β -functions are not equal in both planes. In the case of IR1, as one can see from Table 2.1, one of the wires (Wire L1) is located further away from the IP, and is close to the Q5 quadrupole.

We saw in this Section that the wires settings are constrained by the hardware, and the machine layout. In the following Sections, we shall describe different approaches in order to determine the remaining free settings of the wires, namely their current and, to some extent, the beam-wire distance.

¹The mention *coll* refers to the collimation sigma, assuming a normalized emittance of 3.5 mm.mrad.

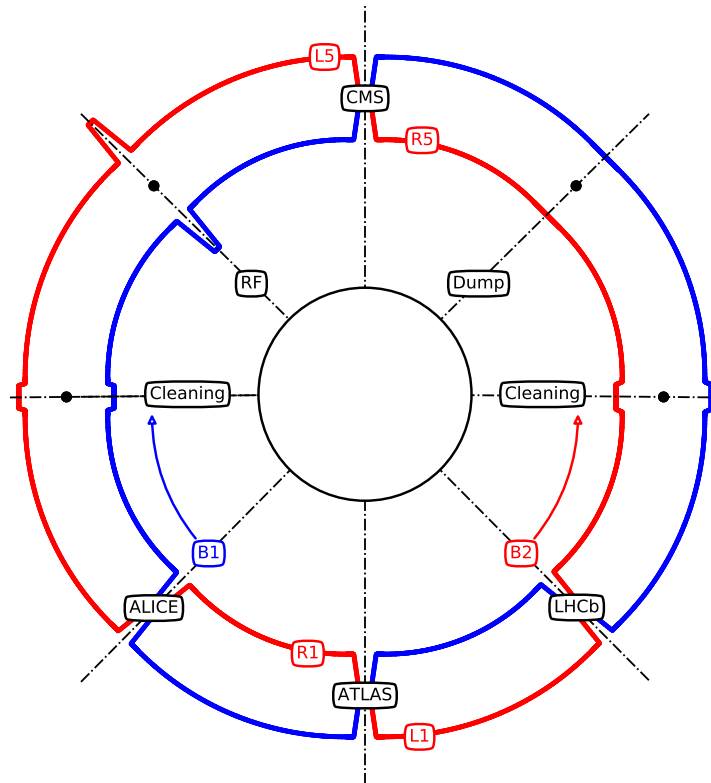


Figure 2.5: The LHC ring configuration during the 2017-2018 Run. Beam 1 is represented in blue while Beam 2 in red. Four wire collimators are installed on Beam 2, around IP1 and IP5.

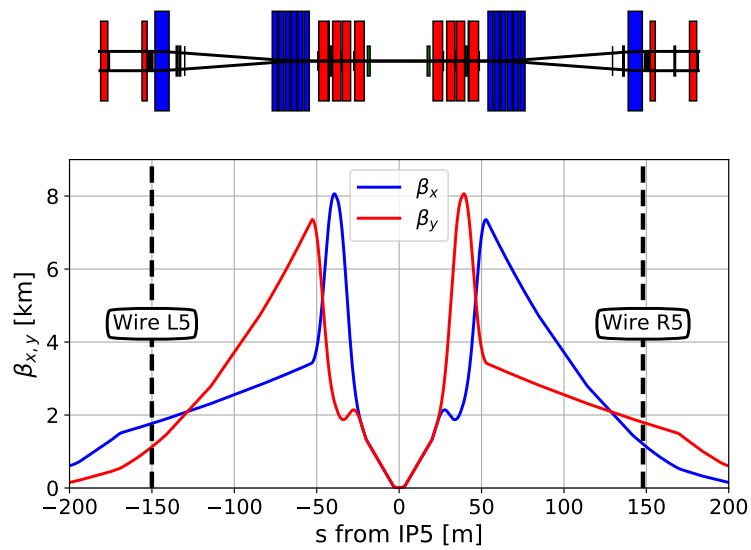


Figure 2.6: Optics layout in IR5, and wire compensators location.

2.2 BBLR COMPENSATION AND TUNE FOOTPRINT

The first proposal for the compensation of the BBLR interactions using electromagnetic lenses in the LHC was done in 2000, by J.-P. Koutchouk in [85]. The main outcome of this report was the determination of the wires' settings, based on a rough scaling of the beam current. The observable of interest for the compensation is the tune footprint, as discussed in the Introduction. It was in fact shown that the use of DC wires can compensate the tune spread induced by the BBLR interactions.

In [85], the choice of the wires' settings is done without considering the hardware constraints formerly mentioned in the previous Section. The study is based on the observation that most of the BBLR interaction occur in between the IT, where the β -functions are equal in both planes, and the normalized beam-beam separation is constant. The proposal of J.-P. Koutchouk in order to compensate the BBLR interactions is thus to install a DC wire where $\beta_x = \beta_y$ (that is between D1 and D2, see Figure 2.6), at a transverse distance equals to the average beam-beam separation over the 15 first encounters, and powered with a current equal to 15 times the current of one bunch:

$$(IL)_{eq} = N_{LR}Q_0c, \quad (2.5)$$

where N_{LR} corresponds to the considered number of BBLR encounters (15 in the described approach). $(IL)_{eq}$ is thus given in A.m. In [85], it is assumed to use one wire per IP and per side.

In this example, we study the 2018 LHC nominal configuration ($\theta_c/2 = 150 \mu\text{rad}$, $\beta^* = 30 \text{ cm}$). In nominal operation, the Landau octupoles current is set to +350 A. Figure 2.7 shows the tune footprint of three different cases. In the first one, only HO collisions occur in the high luminosity IPs. In the second one, we add BBLR interactions in the corresponding IRs. Finally, we add the wire compensation in the third case. In order to follow the approach described in [85], the longitudinal position of the wires is set such as $\beta_x = \beta_y$ at the wire location, which occurs at about 130 m from the IP. The transverse beam-wire distance is equal for each wire, and is set to the normalized inner separation (9.2σ with this specific configuration). The β -functions at the wires' location are equal to about 2000 m, giving a final physical transverse beam-wire distance of about 7.8 mm. In terms of currents, the above estimation is used, and all the wires are powered with:

$$\begin{aligned} I_w &= N_{LR}Q_0c \\ &= 15 \times Q_0c \\ &\approx 83\text{A}, \end{aligned} \quad (2.6)$$

where we assumed a bunch population of $1.15 \cdot 10^{11}$ protons.

In Figure 2.7 one can see that, as observed in the Introduction, the BBLR interactions significantly enlarge the tune footprint. High amplitude particles are the most affected, and cross several resonances. In the LHC, this would lead to beam losses. The use of the wire compensators (green dots) allows us to *compress* back the tune footprint to a situation much closer to the one with HO collisions only (red dots). As for the BBLR interactions, the wire compensators act mostly on the high amplitude particles.

However, this configuration is unrealistic for several reasons in the case of the LHC:

- Longitudinal position of the wires: in this example, we installed the wires at about 130 m from the IP. In the LHC, this corresponds to a location before the D2 recombination dipole (see Figure 2.6). At this specific location, the two vacuum chambers are not parallel, and the nominal separation of 19.4 cm is not reached yet. Since the wires are installed in between the two beams, it would be wiser to install them after the D2.
- Transverse beam-wire distance: the wires are installed at a distance from the beam equals to the inner normalized distance. In this specific example, this correspond to a physical distance of about 7.8 mm. However, the wire

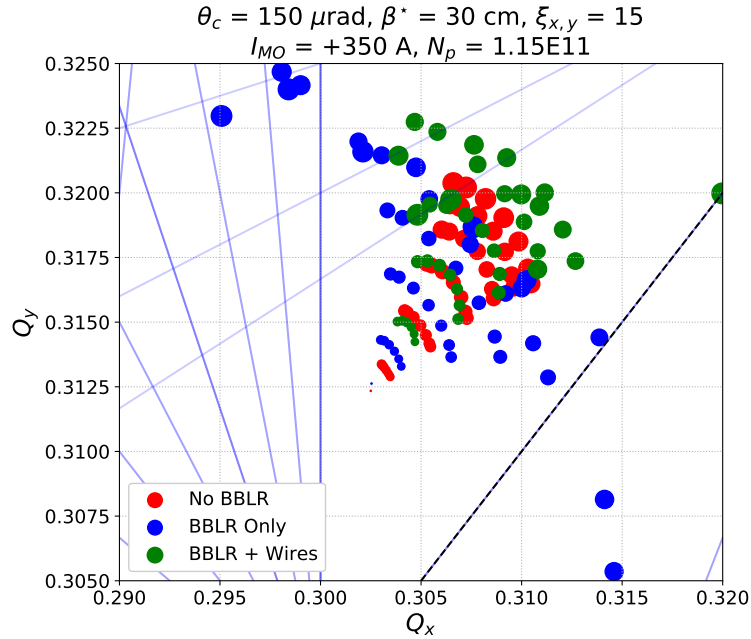


Figure 2.7: Tune footprints for three configurations: HO only, HO and BBLR and wire compensation. The size of the markers is proportional to the initial amplitude of the particle. Particles are tracked up to 6σ amplitude.

compensators have to be installed in the shadow of the tertiary collimators, which might not be the case in this configuration.

Nevertheless, the proposed solution provides a good improvement of the tune footprint, which could lead to a significant reduction of the beam losses in operation. This proposal was not retained for the choice of the wires' settings in the LHC. However, the tune footprint will remain an observable of interest in the next Sections and Chapters.

2.3 BBLR AND RESONANCE DRIVING TERMS

In 2015, S. Fartoukh, in [48], proposed an alternative and more general approach for choosing the wires settings in order to compensate perfectly the BBLR interactions, in the frame of the HL-LHC project. This approach is based on the compensation of the so-called Resonance Driving Terms (RDTs). This Section presents the main outcome of this work. Then we propose an adaptation to the LHC case, first in an ideal configuration without any technical constraint and thus in a realistic configuration compatible with the hardware described in the previous Sections.

2.3.1 COMPENSATION PRINCIPLE

As discussed previously, both a beam and a DC wire produce an electromagnetic field containing all the multipole components, therefore exciting all orders of resonances. This resonances excitation mechanism can be quantified by the Resonance Driving Terms (RDT) that depend - in our situation - on the intensity of the source (either the beam intensity or the wire current), the β -functions at the location of the excitation source, and the transverse distance between the source and the evaluation point of the perturbation. The goal of this Section is therefore to find an expression for these RDTs, both for the wire compensators and for the BBLR interactions in order to see a compensation mechanism emerging from these expressions.

In the Hamiltonian perturbation theory, the goal is to construct a generating function allowing us to re-write our Hamiltonian into a simpler form. Let us write the Hamiltonian of our system under the form of a sum of an unperturbed Hamiltonian \mathcal{H}_0 and a perturbation V [98]²:

$$\mathcal{H} = \mathcal{H}_0(J_x, J_y; s) + \epsilon V(J_x, \phi_x, J_y, \phi_y; s), \quad (2.7)$$

where J and ϕ are the action-angle variables, s - the longitudinal position - is the independent variable and ϵ is a parameter introduced in order to evaluate the order of the perturbation V . \mathcal{H}_0 can be written under a normal form (hence, no dependency on the phases). However, this is not the case of the added perturbation. The goal is now to determine a new way to express this Hamiltonian so that we can integrate it. Let us assume a new set of variables (J_{1x}, ϕ_{1x}) and (J_{1y}, ϕ_{1y}) defining the system (two degrees of freedom) in which the new Hamiltonian \mathcal{H}_1 is obtained under a simpler form. In order to transform our system into the new variables system, we can construct a generating function of second type F_2 such as:

$$F_2 = \phi_x J_{1x} + \phi_y J_{1y} + \epsilon G(\phi_x, J_{1x}, \phi_y, J_{1y}; s), \quad (2.8)$$

where G is our function of interest. F_2 represents our transformation from one set of coordinates, to another. In this latter, the new Hamiltonian does not depend on the phases (ϕ_{1x}, ϕ_{1y}) . The G function can be constructed from the first order perturbation theory. Writing:

$$\mathcal{H}_1 = \mathcal{H}_0(J_{1x}, J_{1y}; s) + \mathcal{O}(\epsilon^2), \quad (2.9)$$

and neglecting the terms of order ϵ^2 , the new Hamiltonian \mathcal{H}_1 is integrable and can be obtained analytically. In the case of a storage ring - or in our case, a collider - with a circumference C , the function G is of the form [98] (only the real part - related to normal multipoles components k_n - is taken into consideration here):

$$G \sim \int_s^{s+C} \frac{(\beta_x(s') J_{1x})^{|m_x|/2} (\beta_y(s') J_{1y})^{|m_y|/2}}{\sin(\pi(m_x Q_x + m_y Q_y))} \times k_n(s') \sin(m_x \theta_x + m_x \phi_x + m_y \theta_y + m_y \phi_y) ds', \quad (2.10)$$

where m_x and m_y are integers, k_n is a n^{th} -multipole component, Q_x and Q_y are the horizontal and vertical betatronic tunes, respectively and $\theta_{x,y}$ are functions of the phase advances $\mu_{x,y}$ and defined as:

$$\begin{aligned} \theta_x &= \mu_x(s') - \mu_x(s) - \pi Q_x \\ \theta_y &= \mu_y(s') - \mu_y(s) - \pi Q_y. \end{aligned} \quad (2.11)$$

If G is small, the generating function F_2 in Eq. 2.8 is close to the identity. However, G can be infinite if the tunes are such that:

$$m_x Q_x + m_y Q_y = l, \quad (2.12)$$

where l is an integer. This condition corresponds to a resonance of order $|m_x| + |m_y|$. If a collider is tuned on a resonance, the perturbation that a particle would experience at some point of the machine would add coherently from turn to turn, leading to the possible loss of this particle. However, the proximity of the tunes form a given resonance is not enough in order to quantify its effect. The strength of this resonance has also to be quantified, and

²In the following, we neglect the synchrotron motion and work with only two degrees of freedom

this is the physical meaning of the RDTs of interest. The strength of a given resonance can be characterized by a factor r that can be defined, from 2.10 as:

$$r e^{i\chi} = \int_s^{s+C} \beta_x(s')^{|m_x|/2} \beta_y(s')^{|m_y|/2} k_n^c(s') e^{i(m_x \theta_x + m_y \theta_y)} ds', \quad (2.13)$$

where χ is a parameter characterizing the contribution of the phase advance between the source of the perturbation and the observation point, $k_n^c = k_n + i k_n^{(s)}$ is a complex sum of the normal and skew components of the n^{th} -multipole.

From the perturbation theory and the expressions developed below, S. Fartoukh, in [48], proposed an expression for the leading orders RDTs driven by the BBLR interactions, assuming the beam-wire equivalence showed in the Introduction. Those RDTs are denoted c_{pq}^{LR} and defined as:

$$c_{pq}^{LR} \equiv \sum_{i \in LR} \frac{\beta_x^{|p|/2}(s_i) \beta_y^{|q|/2}(s_i)}{d_{bb}^{|p|+|q|}(s_i)} e^{i[p\mu_x(s_i) + q\mu_y(s_i)]}, \quad (2.14)$$

where p and q can directly be identified as m_x and m_y . By removing the rotation terms, one can fix p and q to be positive and so the absolute value can be ignored. Figure 2.8 shows, as an example, the horizontal and vertical phase advances around IP5.

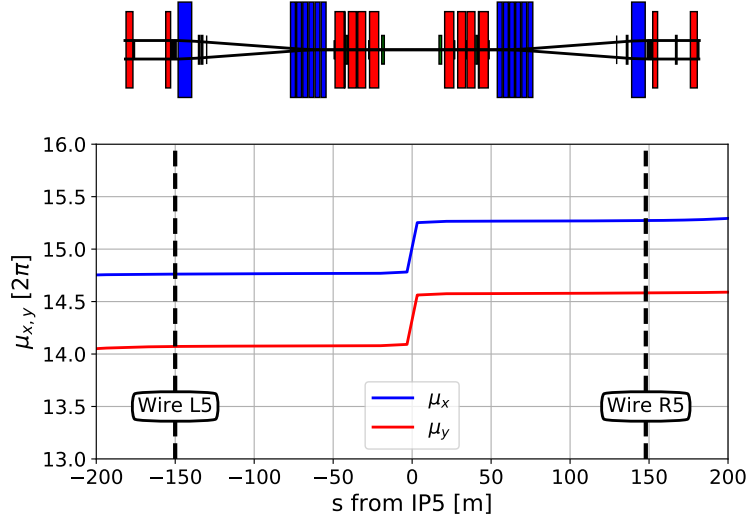


Figure 2.8: Phase advances around the IP5.

One can see that the phase is constant along the IR (in between the two Q5 quadrupoles), in both planes, with a jump of π at the IP. This allows us to neglect the phasing term in the RDTs expression, so that we get, for the BBLR-driven RDTs:

$$c_{pq}^{LR} = \sum_{i \in LR} \frac{\beta_x^{p/2}(s_i) \beta_y^{q/2}(s_i)}{d_{bb}^{p+q}(s_i)}. \quad (2.15)$$

Similarly, the (p, q) RDT driven by a DC wire can be written:

$$c_{pq}^w = N_w \times \frac{\beta_{x,w}^{p/2} \beta_{y,w}^{q/2}}{d_w^{p+q}}, \quad (2.16)$$

where N_w is the integrated current of the wire, expressed in terms of equivalent number of BBLR interactions (as in Section 1.2.3).

If one considers a single BBLR encounter at a given location, the electromagnetic equivalence between beam and wire guarantees that this interaction can be compensated by installing a wire at this exact location. The same is true for several interactions, by placing a wire at the location of each of them. However, installing a single wire for each BBLR interaction is not reasonable, as the beam-beam separation keeps reducing until the IP, and it would not make sense to install such wires inside the particle detectors. The question is therefore: is it possible to compensate a distributed non-linear kick locally with a single wire? The answer to this question is presented by S. Fartoukh in [48]. The rationale of the compensation mechanism is illustrated on Figure 2.9. In the weak-strong approximation [99, 100] where one beam (strong, illustrated with the yellow dots) is assumed to be unperturbed by the other one (weak, experiencing kicks illustrated by the red arrows), S. Fartoukh showed that it was possible to compensate the non-linear distributed kick by computing two equivalent kicks to be compensated locally by a wire.

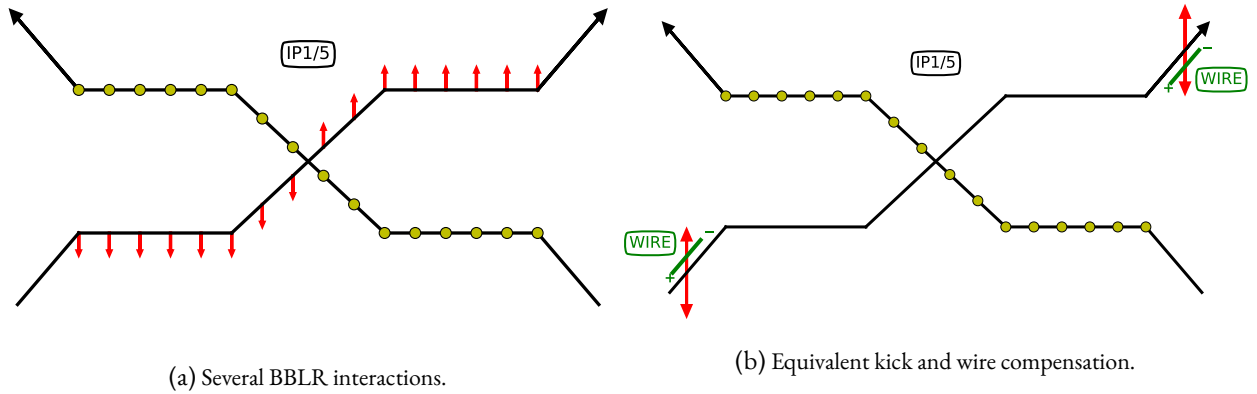


Figure 2.9: Principle of the BBLR compensation using DC wires in the weak-strong approximation.

In an unconstrained situation, where the wires could be installed wherever brings the best results, one can use Eqs. 2.16 and 2.15 in order to determine the current, the transverse position and the longitudinal position of the wires, required to compensate the BBLR interactions. The longitudinal position of the wires is taken into account in the RDT expression by the dependency on the β -functions at the wires' location.

In [48], it is shown, without analytical proof, that by installing one wire on each side of the IP at a specific aspect ratio $r_w = \beta_{x,w}/\beta_{y,w}$, at the same physical transverse distance and by dimensioning them such as they compensate two chosen RDTs (p_1, q_1) and (p_2, q_2) , then all the other RDTs are compensated or minimized. As the (HL)-LHC optics are symmetric, this aspect ratio can be equal to either ~ 2 or ~ 0.5 . This is the main difference with the approach of J. P. Koutchouk described in Section 2.2 where the aspect ratio at the wires' location was equal to one.

As an example, Figure 2.10 shows the normalized residual RDT after compensation of the $(4,0)$ - $(6,0)$ RDTs as a function of the β aspect ratio at the wires location, assuming a perfect left/right symmetry with respect to the IP for the installation of the wires, namely, for each IP $i = 1,5$:

$$r_w^{Ri} = 1/r_w^{Li}. \quad (2.17)$$

One can see that all the high-order RDTs are minimized or compensated for the two mentioned aspect ratios. The lower order RDTs as the dipolar or quadrupolar components are not. However, as explained in the Introduction, these components are already optimized in the machine during nominal operation. Nevertheless, it is worth noting that even by choosing the *worse* possible aspect ratio in terms of residual RDTs (typically, one), we can still compensate at least 70 % of all the RDTs, which would have a significant impact on the beam performances.

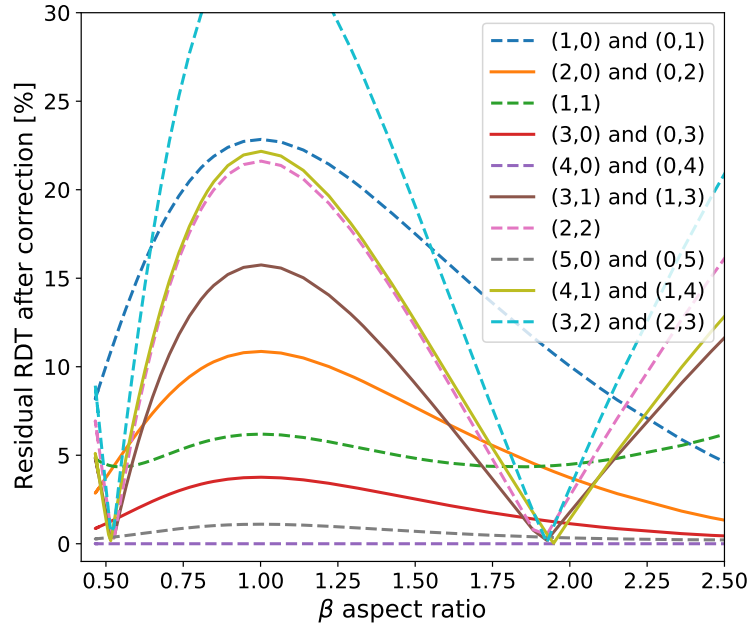


Figure 2.10: Residual RDT after the compensation of the $(4,0)$ - $(6,0)$ RDTs in the case of the 2017-2018 LHC Run 2 ($\theta_c/2 = 150 \mu\text{rad}$, $\beta^* = 30 \text{ cm}$).

The question now is to choose the settings of the wires in order to compensate two RDTs (p_1, q_1) and (p_2, q_2) . As mentioned previously, this depends on the location of the wires (both transverse and longitudinal positions) and their currents.

2.3.2 WIRES SETTINGS IN AN IDEAL LHC CASE

Let us start by an *ideal* case, where there are no technical constraints on the wires installation or hardware limitations. As, of course, no experimental data can be exploited for such a case, this study is done using tracking simulation and this Section is thus an opportunity to introduce useful concepts used in all numerical simulations presented in this Thesis.

Particle tracking is done using both MAD-X [76] and SixTrack [101] codes. SixTrack is a 6D single particle symplectic tracking code used for long term tracking in high energy rings such as (HL)-LHC. The main output provided by SixTrack and used in this thesis is the so-called Dynamic Aperture (DA). The dynamic aperture of a machine is the maximum amplitude of a particle in the phase space for which its motion remains stable [102]. The goal is to set an initial amplitude grid and to track the particles for N turns, monitoring the moment particles are lost. One therefore gets the amplitude below which all the particles survived, which is defined as the DA of the machine, that depends on N . This observable is motivated by the fact that even with nowadays computers, it remains impossible to track billions of particles for hours. In the following, and unless mentioned differently, particles are tracked in the LHC for one million turns, corresponding to about 90 seconds in the actual (HL)-LHC.

Assuming that one can install the wires at the previously described aspect ratios, one can find analytically the optimal beam-wire distance and currents needed to compensate two given RDT (p_1, q_1) and (p_2, q_2) and, in this particular ideal case, minimize all the others. The analytical optimum is defined in [48] as:

2 Wire Compensators Settings in the LHC

$$d_w = \sqrt{\beta_{eq}^w} \times \left[\frac{C_{p1,q1}^{LR} \frac{p2-q2}{r_w^4} + \frac{q2-p2}{r_w^4}}{C_{p2,q2}^{LR} \frac{p1-q1}{r_w^4} + \frac{q1-p1}{r_w^4}} \right]^{\frac{1}{p2+q2-p1-q1}}$$

$$N_w = \left[\frac{(C_{p1,q1}^{LR})^{p2+q2} \left(\frac{p2-q2}{r_w^4} + \frac{q2-p2}{r_w^4} \right)^{p1+q1}}{(C_{p2,q2}^{LR})^{p1+q1} \left(\frac{p1-q1}{r_w^4} + \frac{q1-p1}{r_w^4} \right)^{p2+q2}} \right]^{\frac{1}{p2+q2-p1-q1}}, \quad (2.18)$$

where $\beta_{eq}^w = \sqrt{\beta_x^w \beta_y^w}$. All the wires are assumed to be installed at the same physical transverse distance from the beam and powered with the same current.

Figure 2.11 shows the DA in the configuration space in two different cases: with BBLR interactions only and with BBLR interactions and wire compensation. In the following, we consider HO collisions and BBLR interactions only in the two high luminosity IPs.

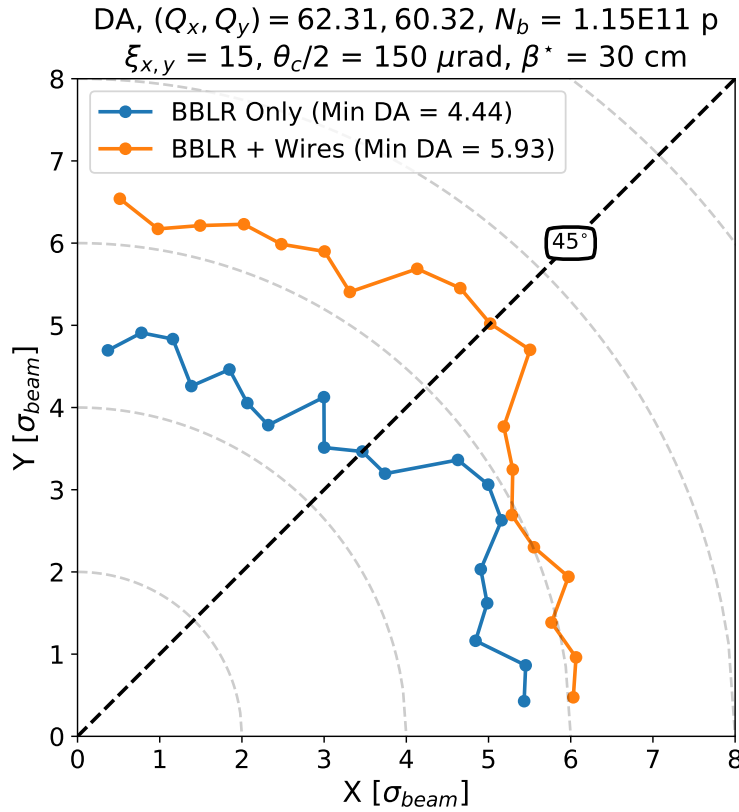


Figure 2.11: Dynamic aperture in the configuration space for the ideal setup in two different cases: with BBLR interactions only, with BBLR interactions and wire compensation.

The DA in a configuration without BBLR interactions is not displayed here but the impact of those interactions on the DA in the (HL)-LHC has been largely studied [103, 104], and is known to be detrimental. From Figure 2.11, we can see that the wires can recover the DA up to about 6σ , which is above the acceptable limit of 5σ , below which beam losses are expected to be observed in the machine.

One can also study the impact of different wire currents and beam-wire distances (always assuming that all the wires have the same settings). Figure 2.12 shows the evolution of the DA as a function of these parameters.

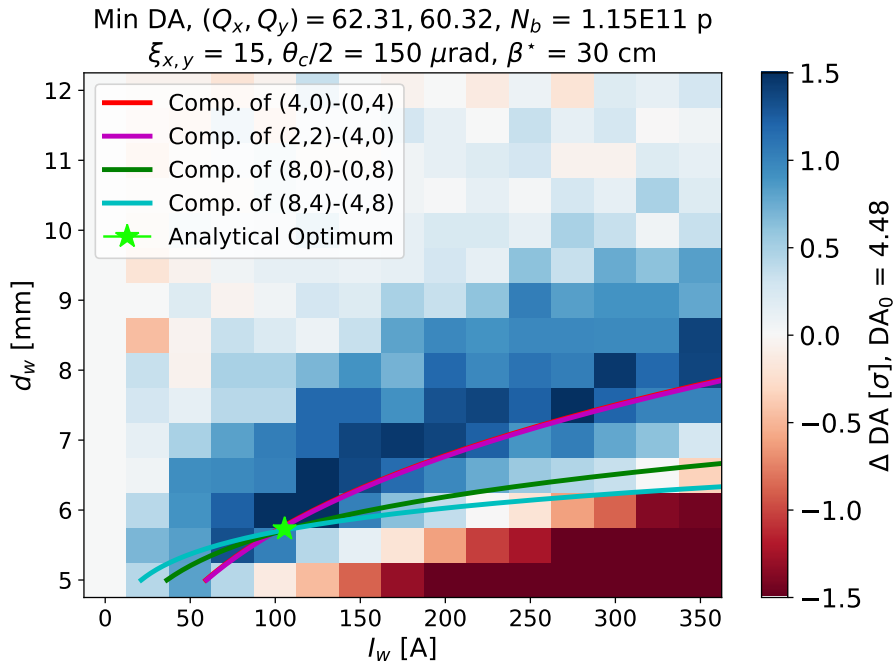


Figure 2.12: DA variation as a function of the beam-wire distances and the wire currents in an ideal case. LHC Run 2 optics is used but the wires are installed at the optimal aspect ratios.

The mention *Min DA* in the title indicates that among all the DA values for the different angles in the configuration space (see Figure 2.11), only the minimal value is retained as it is considered to be the limiting one. The color scale on the figure corresponds to the DA variation with respect to a situation without wires ($I_w = 0$ A). Red corresponds to a degradation of the DA while blue to an improvement. The green star corresponds to the analytical optimum. On top of the DA color map, the (I_w, d_w) combinations compensating two given RDTs are displayed. Being in an optimal situation, all the lines cross at the analytical optimum green star, showing that there is a configuration of the wires that compensate all the RDTs excited by the BBLR interactions. This analytical optimum is obtained for a wire current of about 100 A and a transverse beam-wire distance of about 5.5 mm (which is not realistic in terms of collimation constraints, as we saw previously). However, many other *good* DA points are observed, especially along the line corresponding to the compensation of the (4,0)-(0,4) or (2,2)-(4,0) RDTs, which are the octupolar resonances. This observation yields two conclusions. Firstly, those RDTs are important in the BBLR compensation mechanism. This is consistent with Section 2.2, where the observable was the detuning with amplitude, directly related to the octupolar component of the electromagnetic fields. Secondly, the setup does not have to be so *ideal* to provide satisfactory results, as we will see in the next Section.

2.3.3 WIRE SETTINGS FOR THE LHC

In the current LHC, the wires locations are constrained by the installation of the collimators where the aspect ratio is not optimal anymore. Moreover one can see from Table 2.1 that the left/right symmetry is broken in the case of IR1. Figure 2.13 shows the same study as Figure 2.12 but with the actual longitudinal position of the wires.

In this case, the compensation lines do not all cross at the same point and a minimization of all the RDTs is not possible. However, the figure shows several good configurations that could improve the DA up to $\sim 1.5 \sigma$, which is quite similar to the improvements observed in Figure 2.12. These good DA configurations follow, as in Figure 2.12, the (4,0)-(0,4) RDT compensation line. One has thus to determine the remaining wire settings that are the currents and the beam-wire distance, required in order to compensate these octupolar resonances.

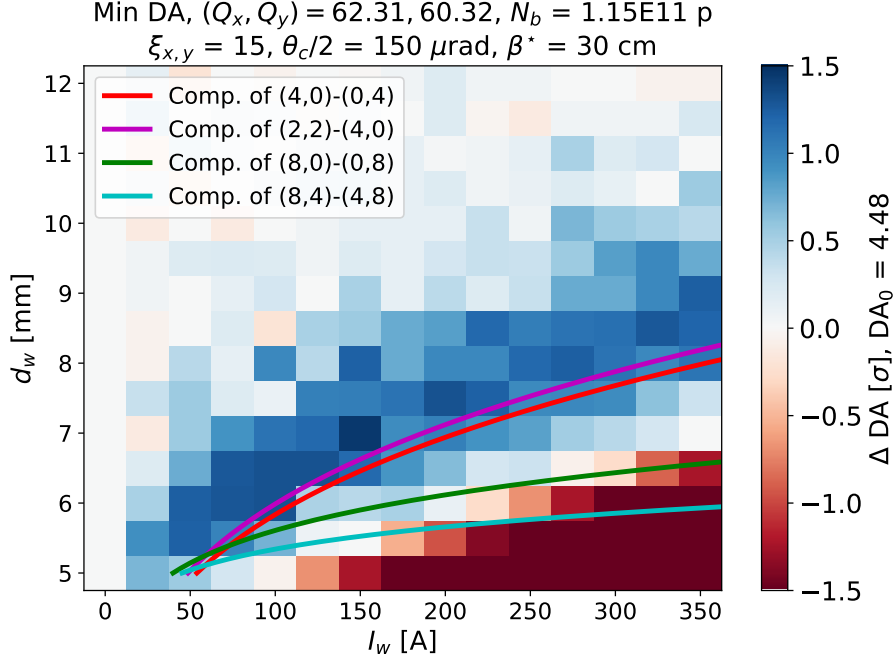


Figure 2.13: DA variation as a function of the beam-wire distances and the wire currents for the 2017-2018 LHC Run 2.

Considering each IP independently, and adding the subscripts L and R for the left and right wires respectively, one has to solve the system of Eq. 2.19 in order to determine the current required in each wire to compensate the (p_1, q_1) - (p_2, q_2) RDTs:

$$\begin{cases} c_{p_1, q_1}^{w,L} + c_{p_1, q_1}^{w,R} = -c_{p_1, q_1}^{LR} & (2.19a) \\ c_{p_2, q_2}^{w,L} + c_{p_2, q_2}^{w,R} = -c_{p_2, q_2}^{LR} & (2.19b) \end{cases}$$

In the ideal case, the wires are assumed to be installed at the same physical transverse distance from the beam. In the LHC, this is not possible, as the wires are installed inside collimators. The collimator opening is given in terms of normalized jaw-beam distance (the center of the wires being installed 3 mm behind the jaw of their housing collimator). Consequently, the wires can only be located at the same normalized transverse distance from the beam. One can thus solve the system of Eqs. 2.19 assuming known (fixed by the collimators opening, assumed to be the same) the distances d_R and d_L for the right and left wires respectively, as reported on Figure 2.4. Denoting $N_{w,L}$ and $N_{w,R}$ the left and right wire current respectively, one can finally obtain:

$$\begin{aligned} N_{w,L} &= \frac{d_L^{p_1+q_1+p_2+q_2} (c_{p_1, q_1}^{LR} d_R^{p_1+q_1} \beta_{x,R}^{p_2/2} \beta_{y,R}^{q_2/2} - c_{p_2, q_2}^{LR} d_R^{p_2+q_2} \beta_{x,R}^{p_1/2} \beta_{y,R}^{q_1/2})}{d_L^{p_2+q_2} d_R^{p_1+q_1} \beta_{x,L}^{p_1/2} \beta_{x,R}^{p_2/2} \beta_{y,L}^{q_1/2} \beta_{y,R}^{q_2/2} - d_L^{p_1+q_1} d_R^{p_2+q_2} \beta_{x,L}^{p_2/2} \beta_{x,R}^{p_1/2} \beta_{y,L}^{q_2/2} \beta_{y,R}^{q_1/2}} & (2.20) \\ N_{w,R} &= \frac{d_R^{p_1+q_1+p_2+q_2} (c_{p_1, q_1}^{LR} d_L^{p_1+q_1} \beta_{x,L}^{p_2/2} \beta_{y,L}^{q_2/2} - c_{p_2, q_2}^{LR} d_L^{p_2+q_2} \beta_{x,L}^{p_1/2} \beta_{y,L}^{q_1/2})}{d_L^{p_1+q_1} d_R^{p_2+q_2} \beta_{x,L}^{p_2/2} \beta_{x,R}^{p_1/2} \beta_{y,L}^{q_2/2} \beta_{y,R}^{q_1/2} - d_L^{p_2+q_2} d_R^{p_1+q_1} \beta_{x,L}^{p_1/2} \beta_{x,R}^{p_2/2} \beta_{y,L}^{q_1/2} \beta_{y,R}^{q_2/2}} \end{aligned}$$

As previously discussed, the goal is to target the compensation of the $(4,0)$ - $(0,4)$ RDTs. Figure 2.14 shows the currents required in the wires in order to compensate these RDTs as a function of the collimators opening.

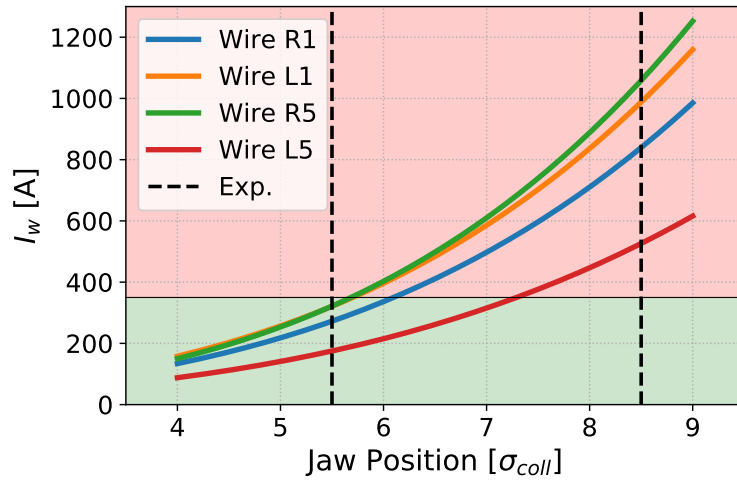


Figure 2.14: Optimal currents required in the wires in order to compensate the (4,0)-(0,4) RDTs as a function of the collimators opening. The collimators opening explored during the experimental campaign are shown with black dashed lines.

The green background coloring corresponds to the currents that are reachable with the present hardware while the red corresponds to those out of reach. The black dash line corresponds to the collimators opening explored during the experimental campaign.

2.3.4 WIRES POWERING CONFIGURATIONS

From Figure 2.14 it is clear that if the jaws of the collimators are opened at $8.5 \sigma_{coll}$, the required currents in order to compensate the (4,0)-(0,4) RDTs are out of reach. In order to cope with this issue, the flexibility brought by the in-jaw installation was used. As mentioned in Section 2.1.2, both collimator jaws contain a wire. A solution consists in recabling the two wires of a collimator in series such as they have the same polarity. By doing so, the quadrupolar, octupolar, etc, strengths are doubled while the others cancel out. This choice is motivated by the need for a compensation of the octupolar resonances as discussed in the previous Section. The two possible configurations are summarized in Figure 2.15.

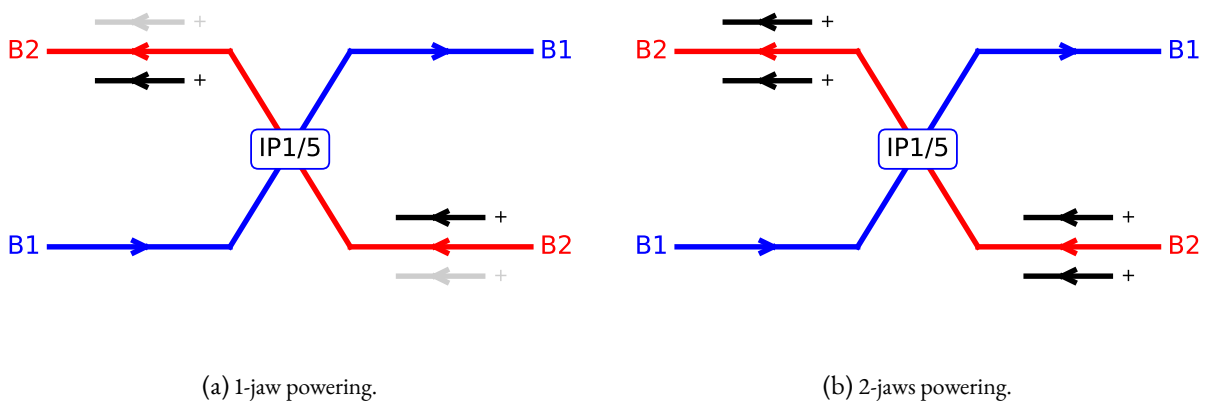


Figure 2.15: Two different wire powering configurations.

2.4 CONCLUSIONS

In this Chapter, we described first the wire demonstrators that were built and installed in the LHC in 2017 and 2018. We thus showed two different approaches that could possibly be used in order to choose the settings of the wire compensators so that they compensate, in the most efficient way, the BBLR interactions in the LHC.

The first approach was the original one, proposed by J. P. Koutchouk and consisted in installing the wires at a location where the β -aspect ratio is equal to one and to set the transverse beam-wire distance equal to the inner normalized beam-beam separation. The observable was the tune footprint and we showed that such a choice of settings would, in fact, compensate the tune spread induced by the BBLR interactions. However, such longitudinal positions are not reasonable in the case of the LHC with the 2018 optics, as an aspect ratio of one is reached before the D2 recombination dipole.

The second approach was the one of S. Fartoukh, proposed in 2015 and based on the compensation of the so-called Resonance Driving Terms. The idea is to minimize all the RDTs driven by the BBLR interactions by computing two equivalent kicks per IP, to be compensated locally by the wires. This approach showed very good results in terms of dynamic aperture. Even if the original proposal suggests precise wire settings, the DA studies showed that it was possible to adapt these settings to the technical constraints of the LHC, while maintaining a satisfactory DA improvement. This approach is the one chosen for the choice of the wire compensators settings in the LHC, adapting it to the constraints in terms of longitudinal and transverse positions, as well as wire currents.

Finally, it is worth noting that a last approach was recently proposed by D. Kaltchev [105]. This approach is similar to the one of S. Fartoukh and proposed to compute the Fourier coefficients of the BBLR Hamiltonian with the use of special Bessel functions. The same work is done with the wires, and, assuming a locality of the compensation, settings are determined.

3 COMPENSATION OF THE BBLR INTERACTIONS USING DC WIRES IN THE LHC

The wire demonstrators used in the LHC have been installed during two different winter technical stops. A first set of wire collimators have been installed in the Interaction Region 5 during the 2016-2017 winter technical stop. In 2017, a first year of experiments took place in order to commission and test these demonstrators in the LHC. The results obtained during this first part of the experimental campaign are reported in [106, 107]. During the 2017-2018 winter technical stop, another set of wire collimators have been installed in the LHC, in the Interaction Region 1. Differently from the experiments carried out in other machines as described in the Introduction, the LHC wire compensators are the first to be installed close to the BBLR interactions: the compensation is in phase with the perturbation. As discussed in Chapter 2, this allows to target Resonance Driving Terms in an almost perfect way and to choose the wire settings accordingly.

The 2018 experimental campaign following the wires installation was organized in two parts. The first part consisted in a proof-of-concept, using a low intensity beam. This first part of the experimental campaign is referred in the following as Low Intensity experiment. The second part of the experimental campaign consisted in testing the BBLR mitigation using DC wires with settings compatible with the nominal operation of the LHC. In the following, this part of the campaign is referred as High Intensity experiment. In this Chapter, we report the preparation and the results of these experiments, together with the corresponding tracking studies. Detailed experimental results are also reported in [108, 109].

3.1 LOW INTENSITY EXPERIMENT: PROOF-OF-CONCEPT

3.1.1 EXPERIMENT PREPARATION AND PROCEDURE

REQUIREMENTS AND WIRE SETTINGS

The goal of the first part of the 2018 experimental campaign was to demonstrate the possibility of compensating the BBLR interactions using DC wires. From Eq. 2.2, one gets the dependency of the wire strength on its transverse distance from the beam. During the Low Intensity experiment, it was requested to move the wire collimators jaws closer to the beam, at $5.5 \sigma_{coll}$, so that the wires effective strength is increased. The corresponding physical beam-wire distances are given in Figure 2.4 and reported in Table 3.1.

Wire	Beam-Wire Distance [mm]	Current [A]
L1	-7.41	350
R1	7.42	320
L5	-7.15	190
R5	8.24	340

Table 3.1: Wire settings during the Low Intensity experiment. The beam-wire distance is algebraic and given with respect to the Beam 2 reference system.

3 Compensation of the BBLR Interactions Using DC Wires in the LHC

This setting is not operational and it was therefore required to lower the intensity of the beam to be compensated, namely Beam 2, in order to satisfy machine protection requirements. The total beam intensity limit imposed by those requirements is $3 \cdot 10^{11}$ protons. Consequently, it was decided to use the simplest filling scheme providing the required collision schedule and only two bunches (with respective intensities of about $1.2 \cdot 10^{11}$ p) were used for Beam 2 while Beam 1 could be composed of several trains. Figure 3.1 shows the filling scheme used for the Low Intensity experiment, where the LHC Fill 7169 is taken as an example. The list of the LHC fills used for the BBLR compensation experiments is reported in Appendix B.

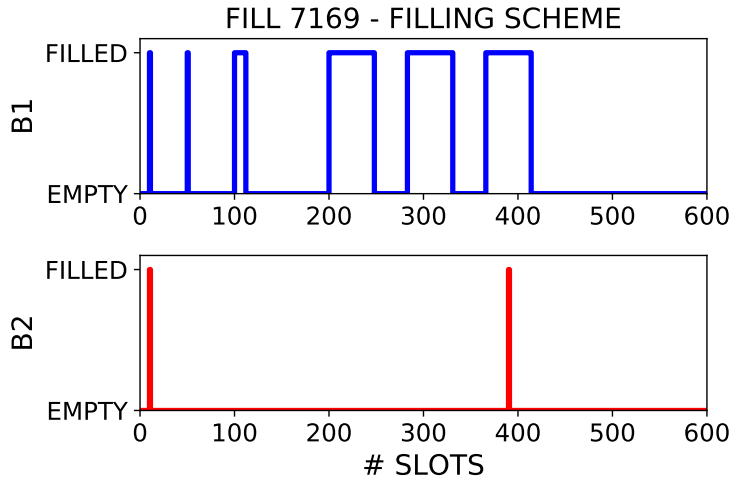


Figure 3.1: Filling scheme used for the Low Intensity experiment. Only the first 600 bunch slots are displayed.

Using this filling scheme, the first bunch of Beam 2 encounters only one partner bunch from Beam 1 (HO collision at the IP1/5). In the following, this bunch will be denoted *HO* bunch. The second bunch collides HO at the IP as well but, additionally, experiences some BBLR interactions. In the following, it is denoted *HO+BBLR* bunch.

The wire currents are chosen such as the (4,0)-(0,4) RDTs are compensated, as detailed in Chapter 2. For the Low Intensity experiment, these currents are reported in Table 3.1. They are within the 350 A limit of the wires power supplies and the 1-jaw powering configuration was therefore used.

COMPENSATION OF THE LINEAR EFFECTS OF THE WIRES

As discussed in the Introduction, in the (HL)-LHC, the linear effects of the BBLR interactions, averaged along the different bunches of the beam, are taken into account and corrected for the overall optimization during machine operation. The wire compensation thus only has to address the non-linear effect due to the BBLR interactions. Moreover, we saw in Chapter 2, and especially in Figure 2.10, that the wire compensators cannot address the lower order RDTs induced by the BBLR interactions. The wires linear effects have then to be compensated.

The LHC closed orbit feedback [110] is routinely active during the operation of the machine at top energy. The role of the closed orbit feedback is to monitor closed orbit distortions and to correct them. It is therefore assumed to compensate the wire dipolar effect if the 1-jaw powering configuration is used. This assumption has been verified experimentally [106]. However, the LHC tune feedback [110] is not active while the beams are colliding. The expected horizontal and vertical tune shifts $\Delta Q_{x,y}$ induced by the wires in the Low Intensity experiment are reported in Table 3.2.

It is therefore needed to implement a dedicated tune feed-forward to compensate the tune shift induced by the wires. It is, in fact, known that tune variations of the order of 10^{-3} can influence significantly the dynamic aperture of the machine, and therefore, the beam lifetime [111]. As we saw in the Introduction, the beam lifetime is an important

Wire	ΔQ_x [10^{-3}]	ΔQ_y [10^{-3}]
L1	2.03	-5.92
R1	7.79	-5.46
L5	-3.08	4.83
R5	-6.61	4.43

Table 3.2: Expected wire induced tune shifts for the Low Intensity experiment.

figure for optimizing the integrated luminosity and the performance of the machine. Losses of beam lifetime shall thus be avoided.

In order to avoid the propagation of a β -beating wave along the machine, the feed-forward of the tunes is implemented using the nearby quadrupoles for each wires, named Q4 and Q5, such as we have, for each wire:

$$\begin{cases} \Delta Q_{x,w} = -\Delta Q_{x,Q4} - \Delta Q_{x,Q5} \\ \Delta Q_{y,w} = -\Delta Q_{y,Q4} - \Delta Q_{y,Q5}, \end{cases} \quad (3.1a)$$

$$(3.1b)$$

where $\Delta Q_{x,y}$ represent the horizontal or vertical tune shift induced by the wires (subscript w) and by the nearby quadrupoles Q4 or Q5. Those quantities can be expressed as [112]:

$$\begin{aligned} \Delta Q_{xy,w} &= \mp \frac{\mu_0 (IL)_w}{8\pi^2 B\rho} \frac{\beta_{x,y}^w}{d_w^2} \cos(2\phi_w) \\ \Delta Q_{xy,Qi} &= \pm \frac{\beta_{x,y}^{Qi} (\Delta KL)_{Qi}}{4\pi}, \end{aligned} \quad (3.2)$$

where $B\rho$ is the beam rigidity, $d_w = \sqrt{x_w^2 + y_w^2}$ is the beam-wire distance, ϕ_w gives the position of the wire in the (x, y) plane (assuming a correct alignment of the wires, $\phi_w = 0, \pi$ or $\pm\pi/2$) and $(\Delta KL)_{Qi}$ is the variation of the integrated strength of the quadrupole Qi as defined in the MAD-X code¹.

As discussed in the Introduction, in the (HL)-LHC, the luminosity is leveled by reducing the β^* along the fill. Taking advantage of the use of ATS optics (see Section 1.2.2), the feed-forward system implemented for a given β^* does not have to be changed in case of a further ATS squeeze down to lower β^* values as the product between β^* and the β -functions at any point of the considered IR in between the two Q5 quadrupoles remains almost constant:

$$\beta_i^* \beta(s) \sim Cst, \quad \forall s \in [Q5.Li, Q5.Ri], \quad (3.3)$$

where $i = 1, 5$ is the IR number. Since the wires and the feed-forward system are well within these limits, the dynamic of the problem does not change in case of a telescopic β^* -leveling.

The set of Eqs. 3.1 can be applied to each wire installed in the machine and its nearby Q4/5 quadrupoles. Assuming that we can profit from each wire independently, we can express the linear relation between the variation of the integrated strength $(\Delta KL)_{Qi}$ of each quadrupole and the wire settings $((IL)_w, d_w)$. We have for each wire:

$$\begin{aligned} (\Delta KL)_{Q4} &= \alpha_{Q4} \cdot \frac{(IL)_w}{d_w^2} \\ (\Delta KL)_{Q5} &= \alpha_{Q5} \cdot \frac{(IL)_w}{d_w^2}. \end{aligned} \quad (3.4)$$

¹In MAD-X, the strength is normalized by the beam rigidity.

3 Compensation of the BBLR Interactions Using DC Wires in the LHC

In the perturbative approximation, one can solve analytically this system and obtain the α coefficients:

$$\alpha_{Q4} = \frac{\mu_0}{2\pi B\rho} \frac{\beta_x^w \beta_y^{Q5} - \beta_y^w \beta_x^{Q5}}{\beta_x^{Q4} \beta_y^{Q5} - \beta_x^{Q5} \beta_y^{Q4}} \quad (3.5)$$

$$\alpha_{Q5} = \frac{\mu_0}{2\pi B\rho} \frac{\beta_y^w \beta_x^{Q4} - \beta_x^w \beta_y^{Q4}}{\beta_x^{Q4} \beta_y^{Q5} - \beta_x^{Q5} \beta_y^{Q4}}.$$

These coefficients can also be retrieved using MAD-X and the corresponding feed-forward system is presented on Figure 3.2.

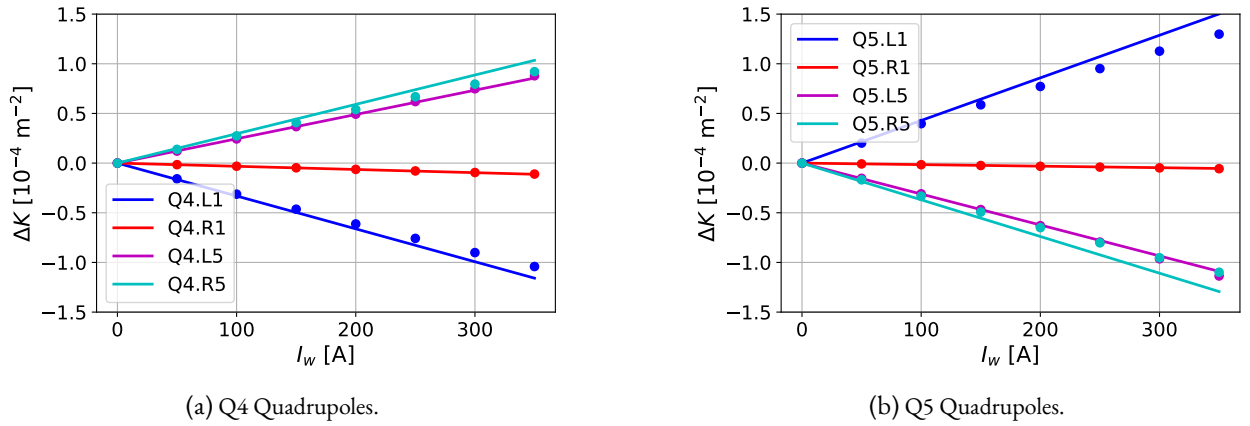


Figure 3.2: Feed-forward system for the Low Intensity experiment. The quadrupoles strengths variation is given as a function of the wires currents.

The solid lines represent the analytical computation while the dots give the numerical results obtained with MAD-X. The slight discrepancy is due to the resulting β -beating that can be quantified using MAD-X. Implementing this feed-forward, one can thus see that the final obtained tune shift (compared to the desired value) is not zero, as illustrated in Figure 3.3.

A maximum residual tune shift of the order of 10^{-5} is observed, which is acceptable for our purposes. The β -beating induced by the wires and their feed-forward is illustrated in Figure 3.4.

The induced β -beating stays below the 2% level all along the machine, which is negligible in comparison to the β -beating induced by the beam-beam effects as it can reach up to 10%.

BEAM-WIRE ALIGNMENT

The alignment of the wires relies on the alignment of the collimators they are housed in. The alignment of the jaw with the beam is done with the nominal operation settings. However, the 5th-axis alignment is not operational and has to be carried out as a misalignment of a wire would result in a modification of the required magnetic field (see Eq. 2.1).

Differently from the jaw alignment, the 5th-axis alignment requires a scan of its position. The BPMs embedded in the collimators give the absolute position of the beam in between the jaws, but there is not an equivalent BPM for the 5th-axis. To proceed with this alignment one can monitor the signal of those BPMs while moving the jaws of the collimator. If the 5th-axis is misaligned, the signal recorded by the BPMs becomes weaker. The intensity of this signal is linear with the beam intensity (a normalization of the signal by the beam intensity might therefore be needed) while the misalignment is a second order effect with respect to the jaw position. Thus for small variations around the

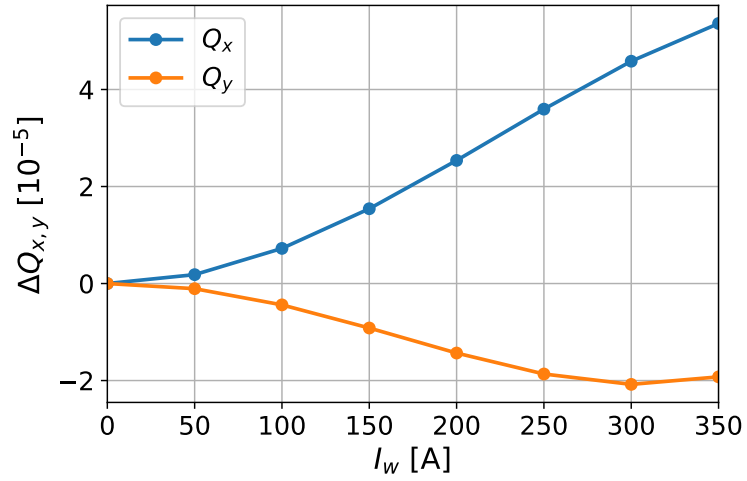


Figure 3.3: Residual tunes shifts after powering the wires and their feed-forward as a function of the wires currents, for the Low Intensity experiment.

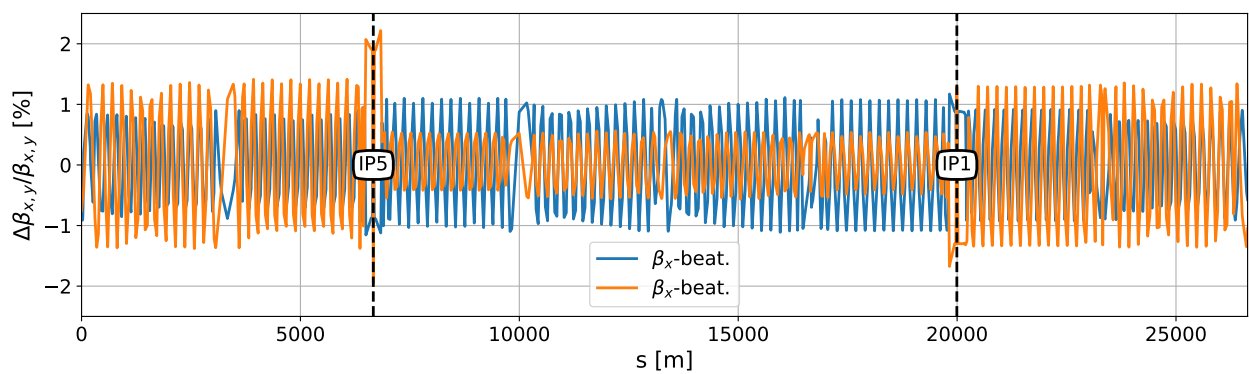


Figure 3.4: β -beating induced by the wires and their feed-forward in the Low Intensity experiment.

aligned position, the BPM reading as a function of the 5th-axis position is expected to be a parabola whose maximum corresponds to the position of the motors that aligns the collimator - and the wire - to the beam.

The alignment of the wires has to be carried out before starting powering the wires for the compensation experiment. In the first part of the Low Intensity experiment, an issue was encountered with one of them in terms of alignment and the example is shown in Figure 3.5.

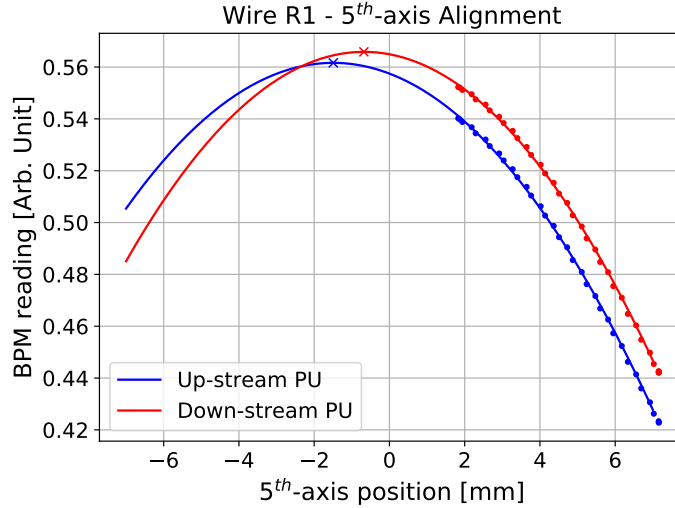


Figure 3.5: 5th-axis collimator (Wire R1) alignment: BPM signal as a function of the 5th-axis position. The dots represent the measurement while the solid lines are the second order polynomial fits. The maximum of each parabola is indicated by a cross.

Figure 3.5 shows the reading of each pick-up (PU) of the BPMs as a function of the 5th-axis position in this particular example. The 5th-axis of the collimator installed on the right side of the IP1 was blocked by the vacuum chamber of the opposite beam since the 5th-axis direction of the collimators installed around IP1 is horizontal. While moving its motor and recording the BPM signal it was then impossible to reach the maximum of the parabola. An intervention in the tunnel was therefore required and took place during a technical stop. The 5th-axis misalignment was almost fully recovered. However, this example showed that the use of bulky collimator jaws to house a wire might not be ideal in the future since their motion can be limited. Moreover, this illustrates the importance of having local beam diagnosis for a precise and fast wire alignment.

Finally, Figure 3.5 raises the question of a need for an additional axis. The 5th-axis is responsible for the motion of the overall tank, without any upstream/downstream distinction. As a result, the maxima of the two parabolas are not the same. However, this difference is below the 1 mm order and averaging the two values is generally enough for our purposes.

OBSERVABLES AND OBJECTIVES OF THE EXPERIMENT

In an ideal collider, the main mechanism responsible for the beam losses during the collision is the luminosity burn-off: particles are lost while producing head-on collisions at the interaction point. Considering one IP, the burn-off decay time constant is given by [113]:

$$\tau_{b0} = \frac{N_0}{\mathcal{L}_0 \sigma_{tot}}, \quad (3.6)$$

where N_0 and \mathcal{L}_0 are the initial bunch intensity and luminosity, respectively, and σ_{tot} is the total proton-proton effective cross-section, defined, for an ideal collider, as:

$$\sigma_{tot} = \sigma_{inel} + \sigma_{el}. \quad (3.7)$$

σ_{el} and σ_{inel} are the elastic and inelastic cross-section respectively. At 6.5 TeV, $\sigma_{el} \sim 30$ mb and $\sigma_{inel} \sim 80$ mb [114, 115]. In the LHC, due to the small beam sizes at the IP, only the inelastic part of the proton-proton collisions is expected to contribute to the luminosity losses, the second part being mostly responsible for the emittance blow-up. The intensity decay of the considered proton beam can then be expressed, in the case of an ideal collider, as:

$$N(t) = \frac{N_0}{1 + t/\tau_{bo}}. \quad (3.8)$$

However, in a real machine, beam losses can be caused by different mechanisms, other than the luminosity production. BBLR interactions, electron cloud effects or beam-gas interactions are some example of possible direct or indirect causes of beam losses.

In the LHC, beam losses can be quantified by the use of the Beam Losses Monitors (BLM) [116]. These devices give both a spatial and a time resolution of the beam losses. Depending on their bandwidth, one can distinguish between ionization chamber BLMs [117] which are slow devices and give the losses averaged along the bunches, and diamond BLMs (dBLM) [118], faster, and giving the losses with a bunch-by-bunch resolution. Another way to measure the beam losses integrated along the full machine is to monitor the beam intensity's evolution. This can be done using the Beam Current Transformers (BCT) [119] or the Fast BCT (FBCT) [120], which provide a bunch-by-bunch intensity evolution. By differentiating in time the FBCT signal, one can obtain directly the beam intensity loss rate dN/dt while the use of BLMs requires a non-trivial calibration [121].

In order to disentangle the luminosity losses from the loss rate of all other sources, one can normalize the loss rate dN/dt to the luminosity \mathcal{L}_n measured in detector n to obtain the so-called effective cross-section [113], denoted σ_{eff} . As for the physical cross-section, it has the dimension of a surface and can be defined as:

$$\sigma_{eff} = \frac{1}{\sum_{n \in IP} \mathcal{L}_n} \frac{dN}{dt}, \quad (3.9)$$

which can be measured bunch-by-bunch, using the FBCT and the bunch-by-bunch luminosity data provided by the experiments. This observable can be defined only in collisions, with a non-zero luminosity. The drawback of this observable lies on the fact that it requires a differentiation of the FBCT data. This can yield a noisy signal and calls for integration periods of several minutes.

Figure 3.6 shows then the objective for the BBLR compensation experiment in terms of effective cross section.

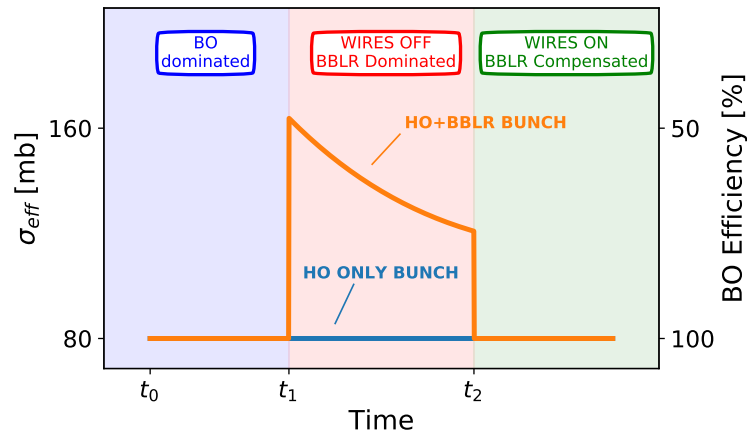


Figure 3.6: Experiment objective: expected evolution of the effective cross-section and burn-off (BO) efficiency.

In the case of an ideal collider, the effective cross-section is equal to the cross-section of the proton-proton inelastic collisions. However, in presence of other beam losses processes, the beam lifetime decreases, and therefore the effective cross-section increases. This allows us to define a burn-off efficiency, defined as the ratio between the physical and the effective cross-sections, as illustrated in Figure 3.6. If the effective cross-section is ~ 80 mb, the beam losses are due exclusively to the luminosity burn-off and the corresponding efficiency reaches 100 %. However, if the effective cross-section increases due to additional losses, the efficiency is reduced. As shown in Figure 3.6, a cross-section of 160 mb corresponds in fact to a burn-off efficiency of 50 %.

The objective of the experiments consists in comparing the effective cross-section of two bunches with two different collision schedules: one bunch encountering a partner bunch via a HO collision only (denoted *HO* bunch in Figure 3.6) and one bunch encountering additional partner bunches through BBLR interactions (denoted *HO+BBLR* bunch in Figure 3.6).

The experiments start in a burn-off dominated regime where the effect of the BBLR interactions is negligible. At this stage, the effective cross-section of the two bunches are the same and equal to ~ 80 mb. The effect of BBLR interactions is thus enhanced by reducing the crossing-angle or by increasing the transverse beam size by a controlled transverse emittance blow-up [122]. Only an effect on the effective cross-section of the bunch experiencing the BBLR interactions should be observed under the form of a losses spike followed by a transient. Two diffusion mechanisms are at the origin of this phenomena. The first one consists in interactions between the opposite beam and the high amplitude particles (halo) of the considered one. The BBLR interactions act like a slow beam scraper, inducing losses at first. After some time, as the halo is fully depopulated, the losses decrease and the effective cross-section would return to the 80 mb level. However, and as we will see later on with the experimental results, the equilibrium reached after the transient is not 80 mb but a higher value. This indicates a second mechanism in which the BBLR interactions induce a diffusion of the low amplitude particles (core). In this case, the particles diffuse from the core to the halo before being lost. As the core concentrates most of the beam intensity, this explains why the transient does not end at the 80 mb level. Even if these mechanisms are well understood, they are still difficult to quantify and predict.

Once the BBLR interactions signature is identified, the wires are turned on. If the proof-of-concept is valid, the effective cross-section of the bunch experiencing the BBLR interactions is expected to return to the burn-off level, successfully demonstrating the possibility of mitigating BBLR interactions effects using DC wires.

3.1.2 RESULTS AND OBSERVATIONS

Using the settings reported in Table 3.1, the Low Intensity experiment was carried out following the previously described procedure. The polarity of the wires was checked, together with their correct alignment with the beam. The starting point in collisions was chosen at a crossing angle of $150 \mu\text{rad}$ (corresponding to a normalized crossing angle of about 8.6σ) and a β^* of 30 cm. Figure 3.7 gives an overview of the Low Intensity experiment, in terms of beam intensities, energy, half crossing angle (bottom plot, black solid line) and Landau octupoles current (bottom plot, orange and blue solid lines).

In order to identify the BBLR interactions signature, the transverse beam size of Beam 2 was increased by a controlled transverse emittance blow-up. A spike of beam losses was observed on the *HO+BBLR* indicating that the BBLR interactions have been enhanced. The wire compensators were thus turned on and off repeatedly in cycles, and the results are reported in Figure 3.8.

The top plot in Figure 3.8 shows the evolution of the effective cross-section for both the *HO* and *HO+BBLR* bunches (blue and orange solid lines respectively). The spike observed around 10:20 corresponds to the transverse emittance blow-up. The *HO* bunch also experienced a spike of a smaller amplitude. By powering on and off the wires, the losses of the *HO+BBLR* bunch reduced and increased respectively, showing, with a crossing angle of $150 \mu\text{rad}$, a possible mitigation of the BBLR interactions with the wires. At around 11:10, the crossing angle was reduced down to $140 \mu\text{rad}$ (8.1σ), with the wires on, enhancing again the BBLR interactions. Nevertheless, no spike of losses was observed for the *HO+BBLR* bunch, showing that even with a reduced crossing angle, the wire compensators could

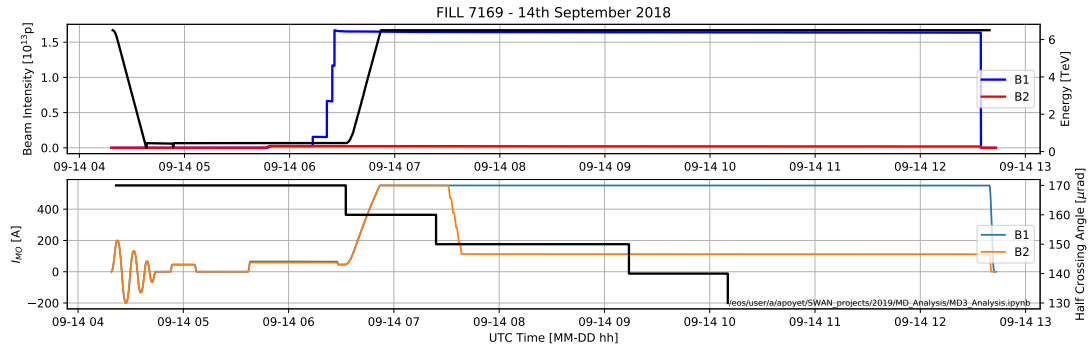


Figure 3.7: Overview of the Fill 7169 used for the Low Intensity experiment: beams' intensities and energy, octupoles current and half crossing angle as a function of time.

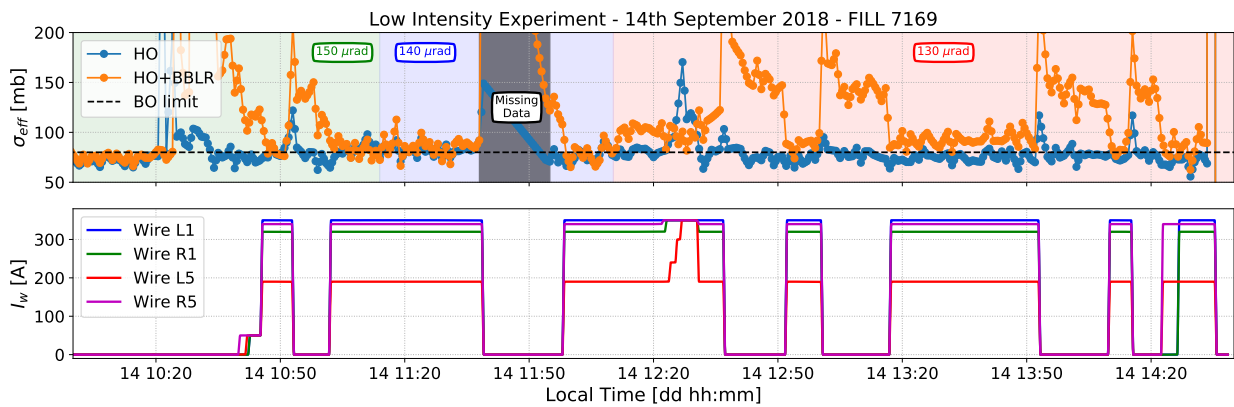


Figure 3.8: Low Intensity experiment results: evolution of the effective cross-section (top plot) and the wires currents (bottom plot) in time. The background coloring of the top plot shows the evolution of the half crossing angle.

still be effective. The crossing angle was finally decreased further down to $130 \mu\text{rad}$ (7.5σ). A slight increase of losses was observed for the *HO+BBLR* bunch but the effective cross-section remained closed to the burn-off limit. Eventually, some on and off cycles with the wires were performed in order to demonstrate the reproducibility of the observations, even in a more aggressive configuration with a lower crossing angle. At around 11:50, data was partially lost due to an issue with the CMS data logging system.

The Low Intensity experiment was therefore very conclusive, showing a clear effect of the wire compensators on the BBLR interactions. It has been observed that the BBLR-induced losses could be reduced or cancelled by powering the wires, without any negative impact on the bunch experiencing no or less BBLR interactions.

3.1.3 NUMERICAL VALIDATION OF THE RESULTS

In parallel to this experiment, tracking simulations have also been carried out in order to benchmark the numerical setup, both in MAD-X and SixTrack. Although the wires are installed on Beam 2 in the LHC, only Beam 1 can be tracked in SixTrack at the time of writing. All the results and numerical computations are adapted to Beam 1 using the symmetries between the two beams presented in the Introduction. It is especially worth mentioning the inversion left/right in the naming of the wires. The wire R1 installed on Beam 2 corresponds therefore to the wire L1 in the tracking simulations.

In Figure 3.9 one can see the DA in the configuration space for the two cases, with and without wires. The wires settings are the ones used in the Low Intensity experiment.

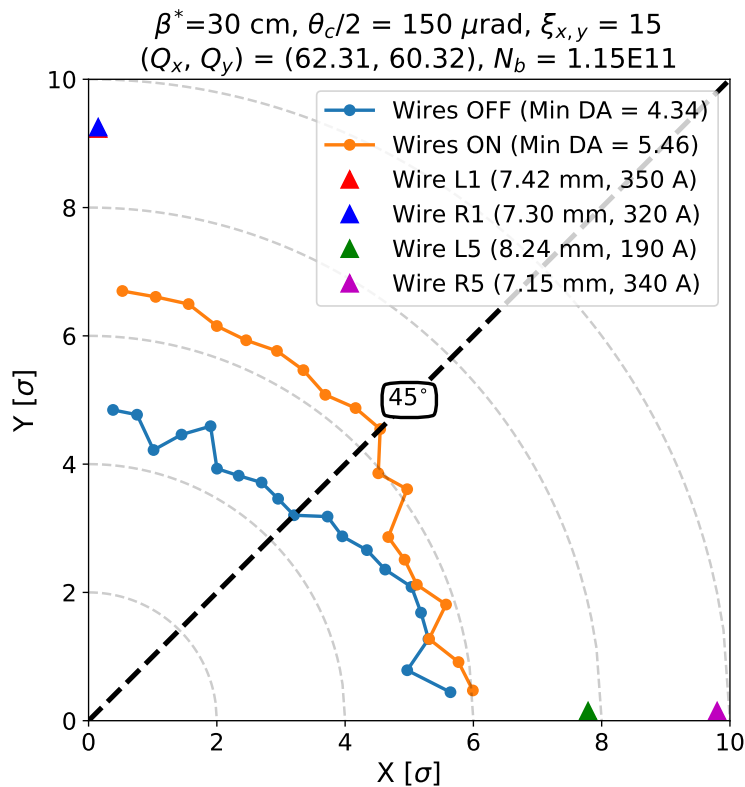


Figure 3.9: Dynamic aperture in the configuration space for the Low Intensity experiment.

In terms of minimum dynamic aperture, an improvement of 1.12σ by using the wires is observed. This result agrees qualitatively with the improvement observed experimentally in terms of beam losses. The transverse position of the wires with respect to the beam is shown in Figure 3.9 by triangular markers. The DA is mostly improved in

the vertical plane (improvement of about 2σ), while almost no improvement is observed in the horizontal plane. Without the wires, the DA is not symmetric and is higher in the horizontal plane (about 6σ) than in the vertical (about $4\text{-}5\sigma$). This asymmetry could explain the difference of improvement in the two planes.

In Figure 3.10 one can see the tune footprint for the two cases with (in red) and without (in blue) wires, still using the Low Intensity experiment configuration.

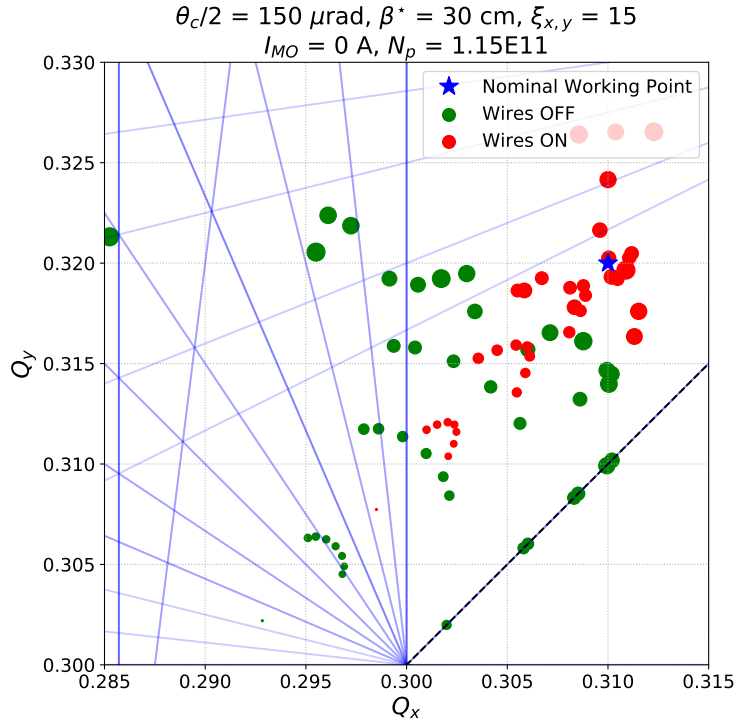


Figure 3.10: Tune footprints for the Low Intensity experiment.

One can observe an efficient compression of the tune footprint (the red footprint looks like a footprint with HO collisions only) thanks to the use of the wires. The most important part of this improvement is the fact that some particles are moving away from the diagonal which is an important resonance. This study shows again a good agreement with the DA studies and the experimental data.

As done experimentally, one can repeat the study varying the crossing angle. In that respect, Figure 3.11 shows the evolution of the DA as a function of the half crossing angle and the bunch population.

In Figure 3.11a, we show the evolution of the DA as a function of the half crossing angle and the bunch population in the case without the wire compensation. One can see that for a bunch intensity of about 1.1 or $1.2 \cdot 10^{11}$ p, a reduction of crossing angle below $150\ \mu\text{rad}$ yields a reduction of DA below the 5σ limit. In particular, a crossing angle of $130\ \mu\text{rad}$ is reachable only for very low bunch intensities. Nevertheless, turning on the wire compensation as shown in Figure 3.11b improves the situation in terms of DA. For the same bunch intensities - which are the ones used in the Low Intensity experiment - a reduction of the crossing angle down to $130\ \mu\text{rad}$ is now possible without reducing the DA below the 5σ limit. This numerical result is consistent with the experimental observations as the crossing angle was in fact reduced down to this value without observing significant additional beam losses. The mitigation of the BBLR interactions using DC wires is therefore also observed in DA studies.

Moreover one can study the impact of the tunes on the DA. It is in fact known that the dynamic aperture, and the beam lifetime, are sensitive to the choice of the working point [99, 111]. Consequently, during the nominal LHC operation in Run 2, the tunes were moved from the nominal working point (62.31, 60.32) to an optimal working

3 Compensation of the BBLR Interactions Using DC Wires in the LHC

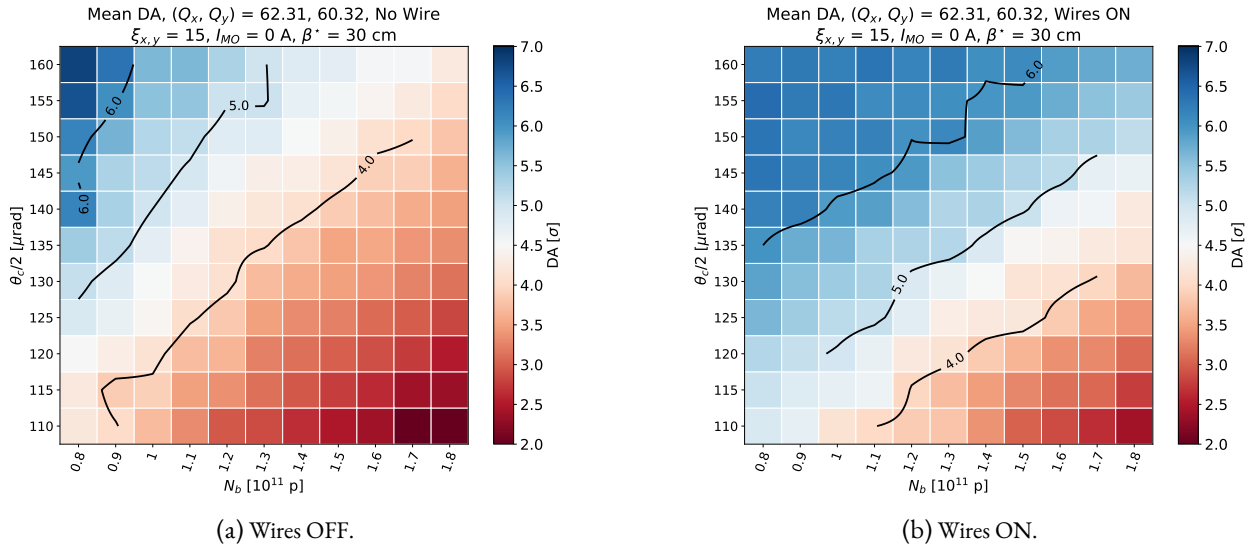


Figure 3.11: Dynamic aperture as a function of the half crossing angle and the bunch population, with and without wire compensation, in the case of the Low Intensity experiment. Iso-DA lines are shown in black.

point (62.313, 60.317). Figure 3.12 shows the impact of the choice of the working point on the DA, with or without the wires.

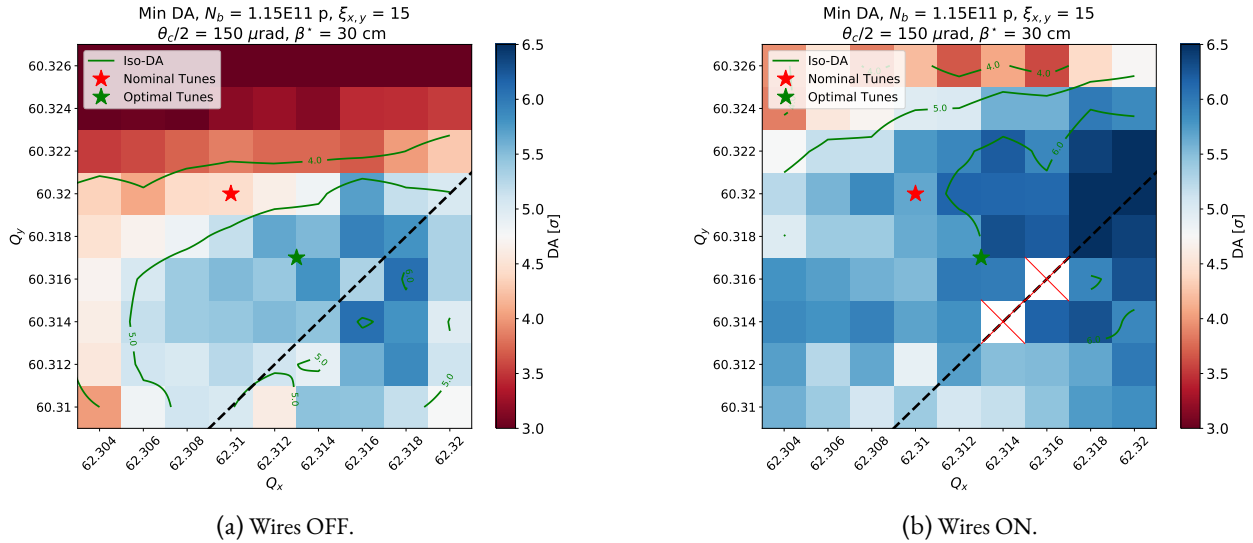


Figure 3.12: Evolution of the dynamic aperture as a function of the choice of the tune working point. The red crosses signal missing points. The red star shows the nominal working point while the green one shows the optimal one. The green lines are the iso-DA.

The absolute minimum DA is displayed, going from lower values in red to higher values in blue. The nominal and optimal working points are illustrated by a red and green star respectively. The black dashed line represent the diagonal $Q_x = Q_y$. Finally the green solid lines represent iso-DA lines. One can observe that the region where the DA is acceptable without the wires - that is a DA greater than 5σ - is quite narrow and close to the diagonal. Moreover all the tune values below the diagonal are not acceptable: the bunches are injected in the LHC with tunes above the diagonal and it is then impossible to cross it later on. The use of the wires significantly enlarges the tune space

where the DA is acceptable, not only towards the diagonal but also towards the third integer resonance ($Q_y = 0.33$). The consequence is that a particle with a tune different from the nominal working point due - for instance - to an enhanced tune spread from non-linear effects, can still be accommodated in the region with a DA greater than 5σ .

Finally, even if this parameter was not modified during the Low Intensity experiment, we study the impact of the Landau octupoles current, together with the wires current, on the DA. Figure 3.13 shows the impact of the octupoles and the wires currents on the DA.

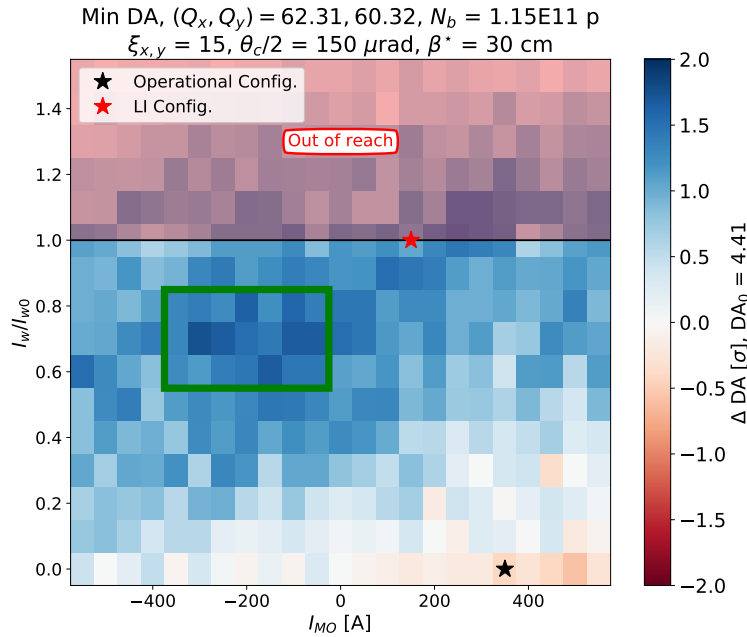


Figure 3.13: Dynamic aperture variation as a function of the Landau octupoles and wires currents. The red star shows the Low Intensity experiment configuration while the black one shows the operational one. The green box corresponds to the best DA configurations.

The reference point DA_0 corresponds to the case where both the wires and the octupoles are turned off. The wires currents are given relatively to their nominal values I_{w0} (see Table 3.1) chosen during the Low Intensity experiment. The black star shows the operational LHC configuration in 2018 (no wire compensators, and octupoles powered at +350 A) while the red one shows the Low Intensity (LI) experiment settings (wires powered at their nominal current I_{w0} and octupoles powered at +150 A). The choice for the value of the Landau octupoles current during the Low Intensity experiment was motivated by two main points. Firstly, in order to disentangle the effect of the wires and the one of the octupoles, it was decided to reduce the octupoles current. Secondly it was observed that setting the octupoles current to 0 A could lead to beam instabilities. A trade-off was therefore made. In Figure 3.13 one can see an improvement of DA using only the octupoles and setting them to a negative polarity. This effect can be further enhanced by powering the wires. The region with the best DA values (up to 2σ improvement) is highlighted with the green rectangle. Negative octupoles could therefore contribute to the BBLR compensation, lowering the required wire currents. Mitigating the BBLR interactions using only the Landau octupoles in the LHC, with different optics configurations, has also been done experimentally, and the results are reported later on, in Chapter 4.

The positive experimental results, together with the numerical benchmark motivated the High Intensity experiment, moving towards beam conditions compatible with the nominal operation configuration. The preparation of the High Intensity experiment, its results and the corresponding numerical benchmark are reported in Section 3.2.

3.2 BBLR MITIGATION WITH HIGH INTENSITY BEAMS

After having achieved the proof-of-concept, it was decided to carry out a new set of experiments, using settings closer to the ones used in the nominal operation of the LHC. This Section recalls these settings and their implications, and describes the preparation of the experiment together with the obtained results. As in the case of the Low Intensity experiment, the approach is supported by tracking simulations whose results are reported in Section 3.2.3.

3.2.1 EXPERIMENT PREPARATION AND PROCEDURE

REQUIREMENTS AND WIRE SETTINGS

Compared to the Low Intensity experiment, the goal of this new experiment was to demonstrate the possibility to mitigate the BBLR interactions in a nominal configuration. During the nominal LHC operation, the tertiary collimator jaws are opened at $8.5 \sigma_{coll}$. The corresponding physical beam-wire distances are reported in Table 3.3.

Wire	Beam-Wire Distance [mm]	Current [A]
R1	9.83	350 x 2
R5	11.10	350 x 2

Table 3.3: Wire settings during the High Intensity experiment. The mention “x 2” indicates that the 2-jaw powering configuration is used.

With such collimator settings, it was possible, from a machine protection point of view, to use a higher intensity for Beam 2, injecting several trains of bunches as for Beam 1.

Only three out of the four wire collimators are operational. The collimator L1 is, in fact, not a tertiary collimator. During the nominal operation of the LHC, its jaws have to sit at a normalized distance larger than $15 \sigma_{coll}$. It was decided not to use it as the expected effect of wires located at such distance is weak. The L5 wire collimator is a tertiary collimator and is therefore operational. However, in order to maintain the symmetry between the two IPs, it was decided not to use the corresponding wires.

Figure 3.14 shows the filling scheme used for the High Intensity experiment, where the LHC Fill 7386 is taken as an example (see Appendix B for the complete list of fills considered for this experiment).

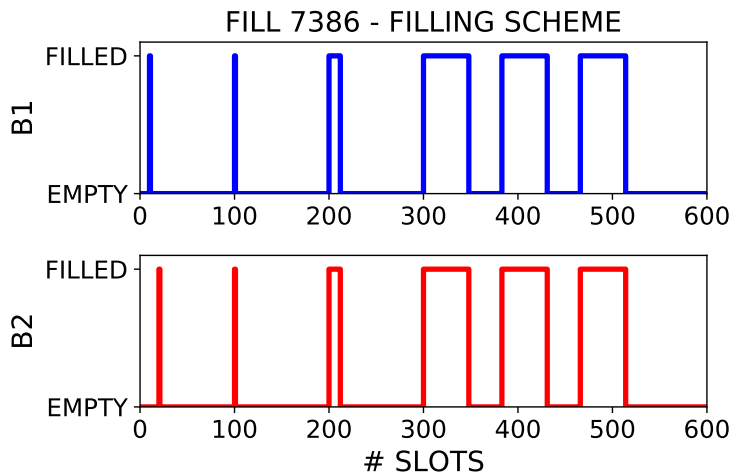


Figure 3.14: Filling scheme used for the High Intensity experiment. Only the first 600 bunches slots are displayed.

Using this filling scheme, the two beams are the same and composed of several trains. As discussed in Section 1.2.1, such a filling scheme yields a variety of beam-beam collision schedules, although collisions occur only in IP1 and IP5. Bunches at the extremity of a train are expected to experience less beam losses due to BBLR interactions than the bunches located in the center of the train.

The choice of the wire currents follows again the rationale described in Chapter 2 in order to compensate the (4,0)-(0,4) RDTs. As one can see in Figure 2.14, with the collimators opened at $8.5 \sigma_{coll}$, the required wire currents are not within the hardware limit of 350 A. Consequently the 2-jaws powering configuration was used and all the wires were powered with the maximum allowed current, as reported in Table 3.3.

FEED-FORWARD AND WIRES ALIGNMENT

As in the case of the Low Intensity experiment, it was necessary to compensate the linear effects induced by the wires. Assuming a correct alignment of the two wires housed in one collimator, the overall dipolar components of the wires cancels out. The remaining possible effect due to a small alignment error is assumed to be corrected by the LHC orbit feedback system. However, the quadrupolar contribution of the wires is doubled and must be compensated. The expected tune shifts from the wires in the High Intensity experiment are reported in Table 3.4.

Wire	$\Delta Q_x [10^{-3}]$	$\Delta Q_y [10^{-3}]$
R1	9.71	-6.81
R5	-7.50	5.02

Table 3.4: Expected wire induced tune shifts for the High Intensity experiment.

During the High Intensity experiment, the same feed-forward system using the Q4 and Q5 quadrupoles was used. As both the wires present in a wire collimator are used, the analytical formulas expressed in Chapter 3 are still valid but a factor two must be considered. Figure 3.15 shows the implementation of the tunes feed-forward for the High Intensity experiment.

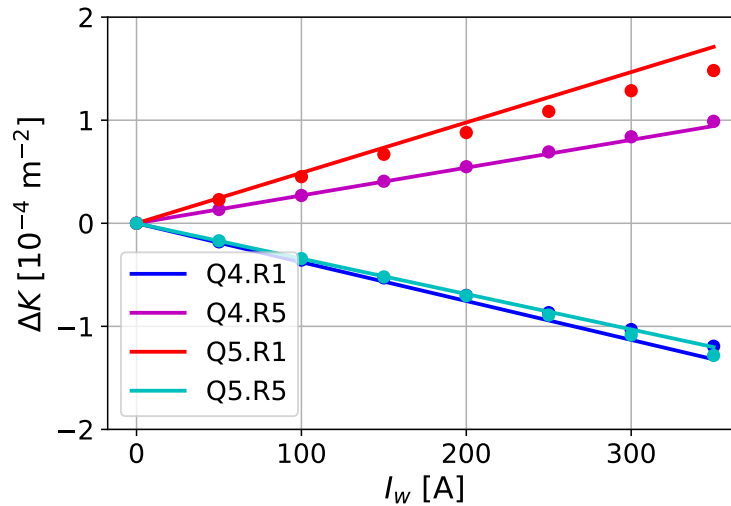


Figure 3.15: Feed-forward system for the High Intensity experiment. The quadrupoles strengths variation is given as a function of the wires currents.

Using this tune feed-forward, the residual tune shifts are - at a level of 10^{-5} - negligible for our purposes, as shown in Figure 3.16.

3 Compensation of the BBLR Interactions Using DC Wires in the LHC

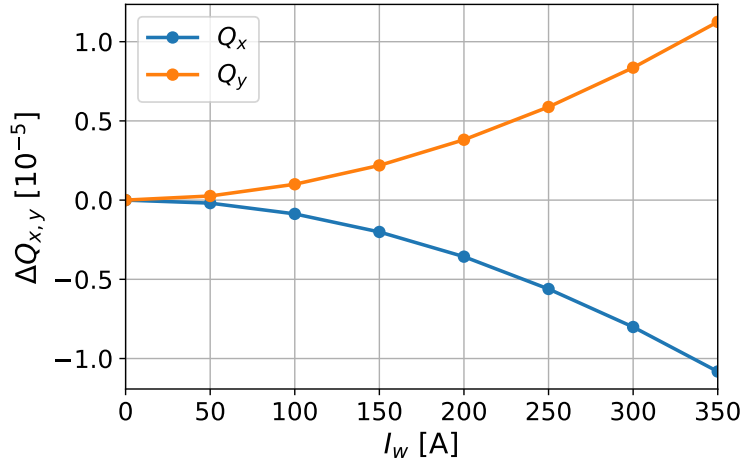


Figure 3.16: Residual tunes shifts after powering the wires and their feed-forward for the High Intensity experiment.

Finally, Figure 3.17 shows the β -beating induced by the wire compensation and its feed-forward system in the case of the High Intensity experiment.

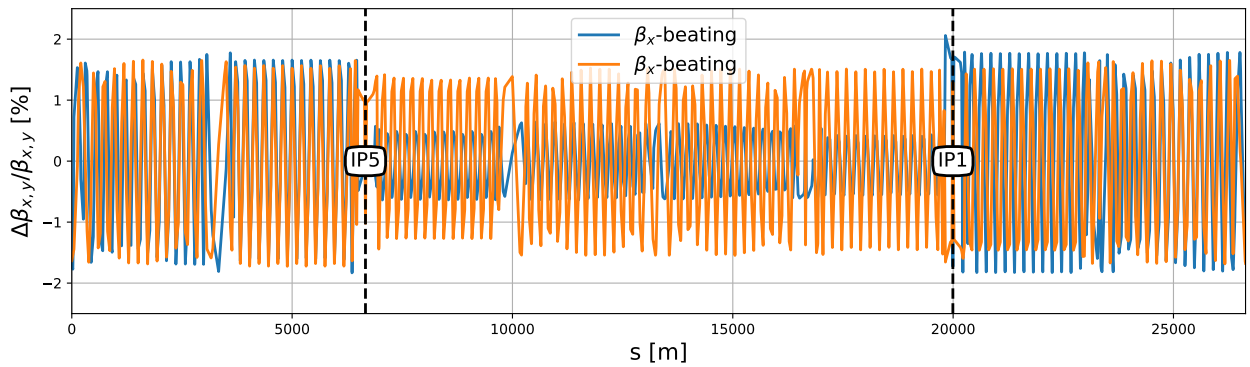


Figure 3.17: β -beating induced by the wires and their feed-forward in the High Intensity experiment.

The β -beating, although slightly increased compared to the Low Intensity experiment (see Figure 3.4), is still under control and negligible in comparison to the beam-beam induced β -beating.

In terms of wire collimators alignment, the procedure remains the same as the one of the Low Intensity experiment, as described in Chapter 3.

OBSERVABLES AND OBJECTIVES OF THE EXPERIMENT

During the Low Intensity experiment, the main observable was the bunch-by-bunch effective cross-section. However, in the case of the High Intensity experiment, the beneficial effect of the wires is reduced as they are located further away from the beam. It was therefore decided to monitor directly the signal coming from the BLMs and to compare Beam 2 (which has the wire compensators) to Beam 1. Nevertheless, the procedure of the experiment remains the same. The BBLR signature is identified by observing the losses of Beam 2 and enhanced by a controlled emittance blow-up and a reduction of the crossing angle. By powering the wires on and off, it is expected to see a decrease or increase respectively of the beam losses on B2 while B1 remains unaffected by the wires.

3.2.2 RESULTS AND OBSERVATIONS

VALIDATION AT INJECTION AND FLAT-TOP ENERGIES

From a machine protection point view, the use of non operational devices requires a validation at both injection and flat-top energies. The validation consists in powering the wires - 2-jaws powering configuration - first with a low intensity beam at injection energy. This setup allows to observe the wires effect on the tunes to check the polarity of the wires at injection energy and the correct implementation of the feed-forward system at flat-top energy.

At first, only one individual bunch was injected per beam. The individual bunch injected as B2 was used to check the polarity of the wires. To do so, all the wires - even though only two were used later - were powered, using the 2-jaw powering configuration and the betatron tunes were monitored, as shown in Figure 3.18 for the example of the Wire R5.

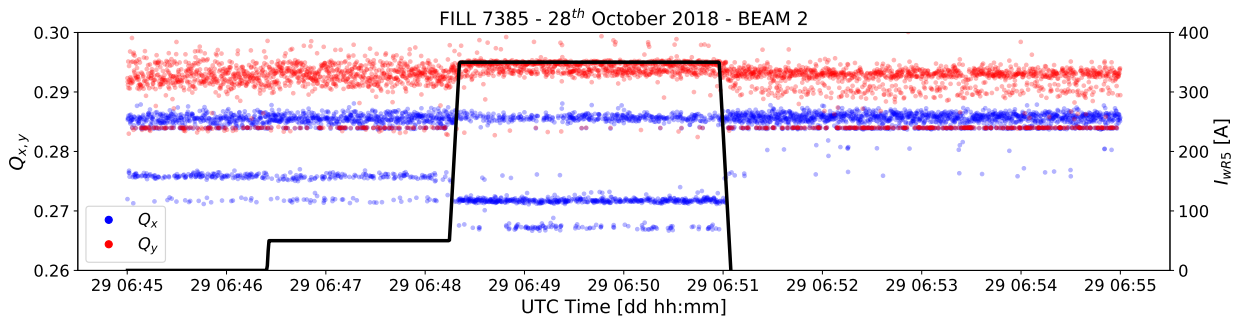


Figure 3.18: Effect of the Wire R5 on the betatron tunes at injection energy.

As expected from the analytical formulas, the horizontal tune shift induced by the wires in IR1 is positive and the one induced by the wires in IR5 negative. The opposite is also true for the vertical tune shift. This check confirms that the cabling of the wires is correct and that the chosen polarity corresponds, in fact, to a compensation mode.

The other bunches were then injected according to the same filling scheme chosen for the Low Intensity experiment. Beam 1 was composed of several trains while Beam 2 was composed of two bunches only. The energy was thus ramped up to the nominal 6.5 TeV in order to check the feed-forward system. The latter is in fact energy and optics dependent and could not be checked at injection energy. Figure 3.19 shows the evolution of the currents in the Q4 and Q5 quadrupoles together with the wire currents in time.

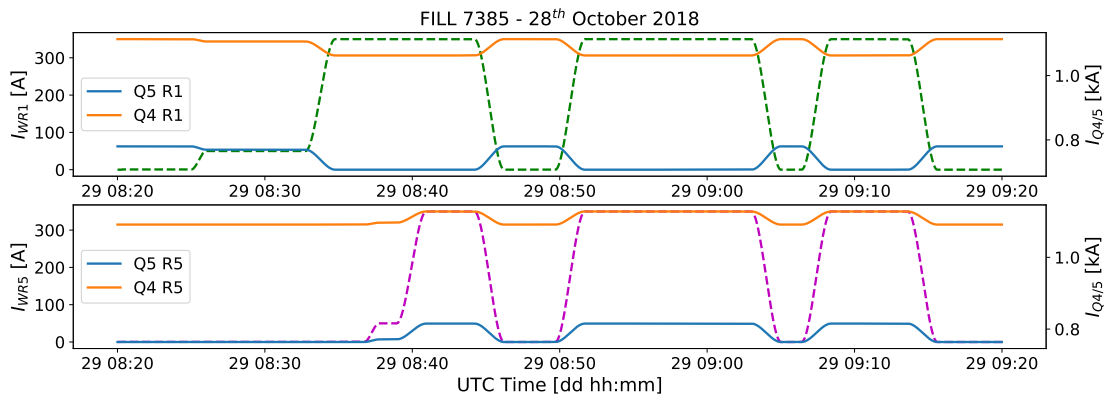


Figure 3.19: Validation of the feed-forward system: quadrupoles and wires currents as a function of time.

3 Compensation of the BBLR Interactions Using DC Wires in the LHC

Each quadrupole reacts to the powering of the corresponding wire as expected and the tunes are presented in Figure 3.20.

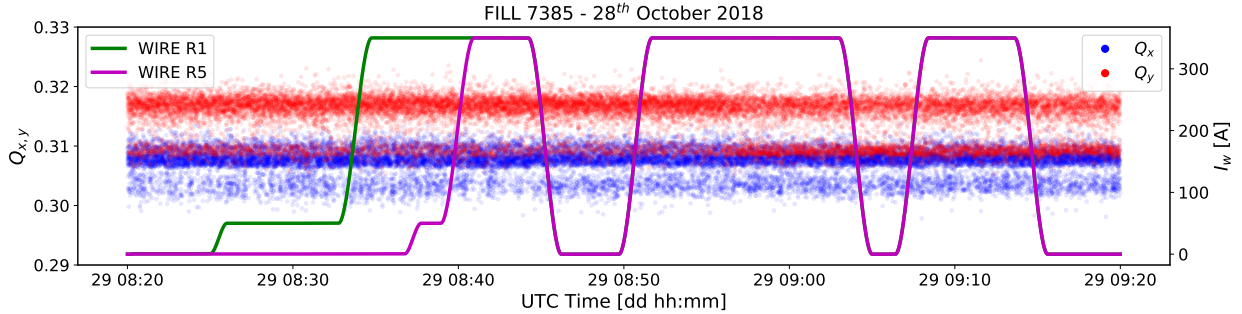


Figure 3.20: Effect of the wires and their feed-forward on the horizontal and vertical tunes.

The tune measurement was done without exciting the beam and is, consequently, noisy. However, we can see that the powering of the wires does not affect the horizontal and vertical tunes. The two beams were then dumped and the machine was set up to get ready for a new injection.

EVIDENCE OF A POSSIBLE BBLR MITIGATION

An overview of the High Intensity experiment is given in Figure 3.21. It is worth noting that unlike the Low Intensity experiment that was carried out using chromaticities of 15 (in order to avoid instabilities encountered in the first fill), the High Intensity experiment was carried out with chromaticities of 7 (nominal operation settings at that time).

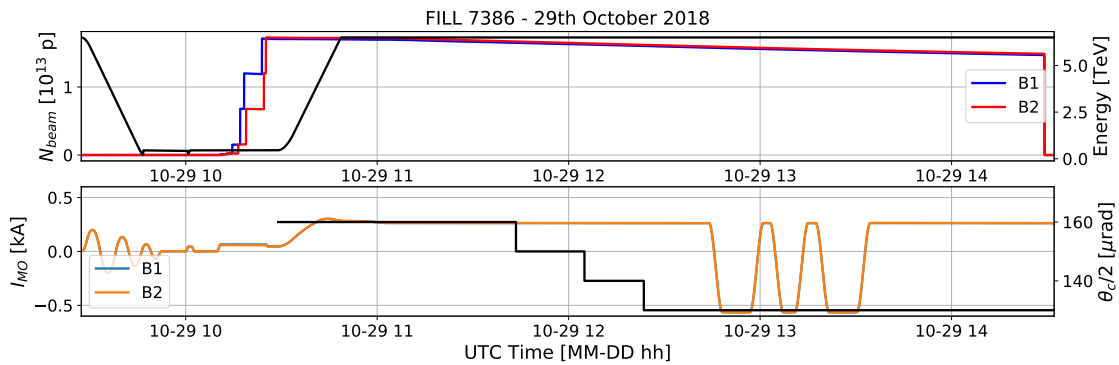


Figure 3.21: Overview of the High Intensity experiment in terms of beam intensity, energy, Landau octupoles current (bottom plot, blue and orange solid lines) and half crossing angle (bottom plot, black solid line).

The starting crossing angle for the collision was $160 \mu\text{rad}$ (9.2σ) with a β^* of 30 cm. Once the BBLR interactions signature was identified, the wires were powered on and off repeatedly in cycles. Figure 3.22 shows the results of the High Intensity experiment in terms of beam losses.

The top plot shows the evolution of the BLM losses from B1 (blue dots) and B2 (red dots), together with the current of the Landau octupoles (black solid line). On this top plot one can also see the evolution of the crossing angle on the top background coloring while the bottom background coloring represents the ON (green) and OFF (red) cycles of the wires. On the bottom plot, one can see the intensity evolution for B1 (in blue) and B2 (in red), together with the currents circulating in the wire R1 (green) and the wire R5 (purple).

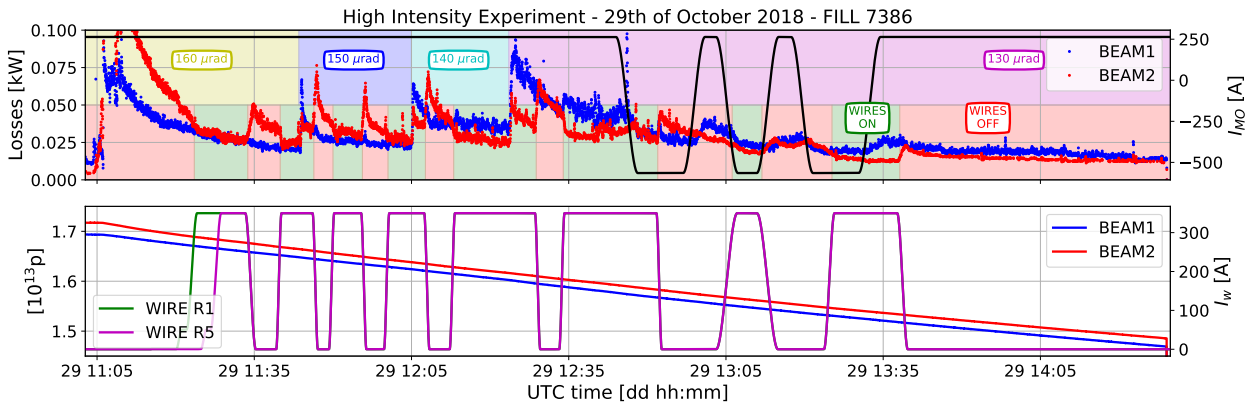


Figure 3.22: High Intensity experiment results: beams losses, octupoles current (top plot), wires currents and beams' intensities (bottom plot) as a function of time. In the top plot, the top background coloring shows the evolution of the half crossing angle while the bottom part coloring shows the on/off (green/red, respectively) cycles of the wires.

As in the Low Intensity experiment, the crossing angle was progressively reduced during the fill, from 160 μ rad down to 130 μ rad. At 11:35, the wires were turned off and a spike of losses was immediately observed on B2. When powering back the wires, the losses decreased to reach the same level as B1, showing that with a crossing angle of 160 μ rad the wire compensators were efficient. As during the Low Intensity experiment, the crossing angle was reduced with the wires on. On every step, one can observe a slight spike of losses on B2. Nevertheless this spike is smaller than the one observed on B1, bringing an evidence of the efficiency of the wire compensators with a configuration compatible with the nominal operating LHC. BBLR interactions mitigation using wires could reduce the beam losses by about 20 %.

Moreover, another parameter was adjusted during the experiment: the current of the Landau octupoles present all along the machine was modified in order to invert their polarity. With this particular optics (low telescopic index of 1.33), no clear evidence of a possible BBLR interactions mitigation using the octupoles could be highlighted. However, other experiments using different optics have shown that the polarity of the Landau octupoles can indeed influence the BBLR detrimental effect and the corresponding results are reported in Chapter 4.

Finally one can also look at the signal provided by the diamond BLMs as those devices provide bunch-by-bunch losses. Figure 3.23 shows the evolution of bunch-by-bunch losses in time, together with the wire currents.

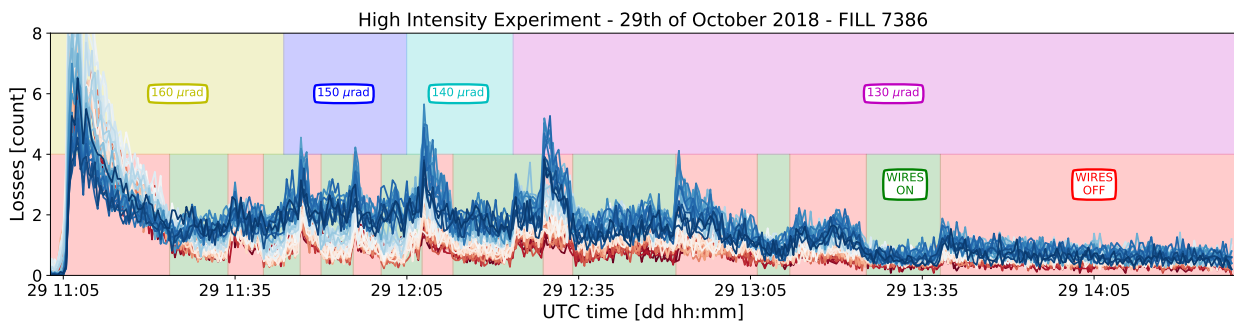


Figure 3.23: High Intensity experiment results: dBLM bunch-by-bunch losses as a function of time. The top background coloring shows the half crossing angle evolution while the bottom coloring shows the on/off wires cycles.

The background of the plot is colored to show the evolution of the crossing angle and the on/off cycle of the wires. Only the losses from the first train are represented (48 bunches). The color corresponds to the position of the bunch within the train: from red for the first bunch of the train, to blue for the last.

The beam losses pattern is quite similar to the one observed on the BLMs: a spike of losses appears when the wires are turned off and can be partially recovered when powering the wires on. Nonetheless, one can extract an additional information from the diamond BLMs: a pattern in the beam losses with respect to the bunch position within the train is observed. Figure 3.23 illustrates that the first bunch of the train always loses less than the last. This cannot be identified as a signature of the BBLR interactions as in that case the central bunch would be the one losing the most. Most likely, this pattern is related to the interplay with electron cloud effects. It is, in fact, known that the LHC is currently dominated by such effects [123, 124]. The wires still reduce the losses by extending the available tune space, therefore increasing the margins to accommodate extra non-linear effects such as electron cloud. This is confirmed by tracking simulations, whose results are reported in the next Section.

3.2.3 NUMERICAL VALIDATION OF THE RESULTS

As in the case of the Low Intensity experiment, tracking simulations have been carried out in order to validate the beneficial effect of the wire compensators observed during the experiment. In Figure 3.24 one can see the DA in the configuration parameter space for the cases with and without wires. The wires settings are the ones used in the High Intensity experiment. In the following, the Landau octupoles current is set to 0 A, unless specified otherwise. During the experiment, this was not the case, as octupoles are needed in order to provide beam stability. However, in the tracking simulations, we want to disentangle the effects of the wires from the ones of the octupoles.

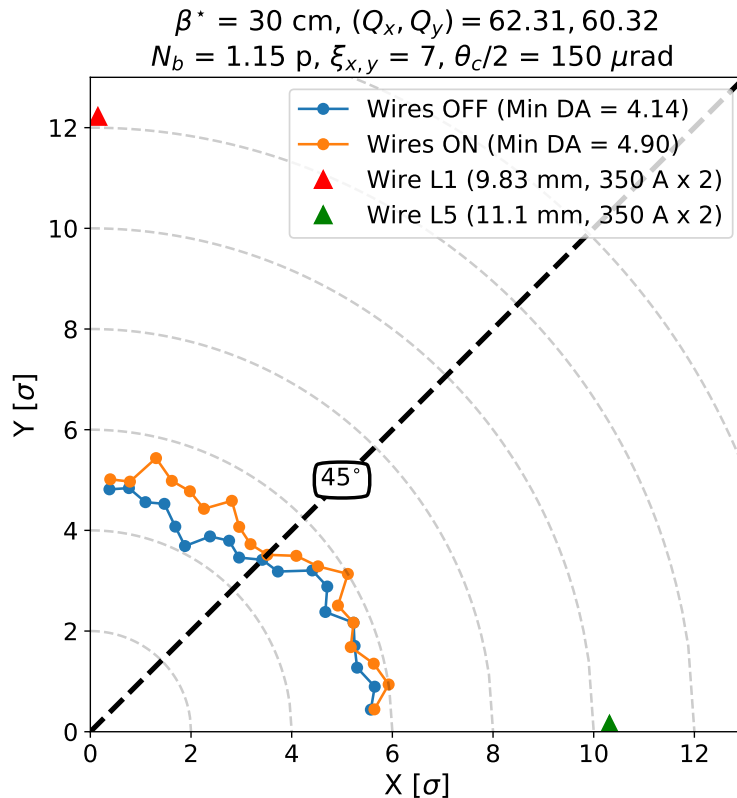


Figure 3.24: Dynamic aperture in the configuration space for the High Intensity experiment.

An improvement of 0.8σ in terms of minimum DA is observed, which is reduced compared to the Low Intensity experiment. This result agrees qualitatively with the improvement observed in the experiment (reduction of the beam losses). The transverse position of the wires with respect to the beam is shown in Figure 3.24 with the use of triangular markers. It is worth noting that, in terms of normalized distance, the jaws are in fact located at $8.5 \sigma_{coll}$

while the wires sit at distances larger than 10σ . The additional 3 mm due to the in-jaw configuration of the wires adds a significant beam-wire distance. As in the Low Intensity experiment case, an asymmetry is observed between the two planes: most of the DA improvement is observed in the vertical plane (above the 45° line).

In Figure 3.25 one can see the tune footprint for the two cases with (in red) and without (in green) wires, still using the High Intensity experiment configuration.

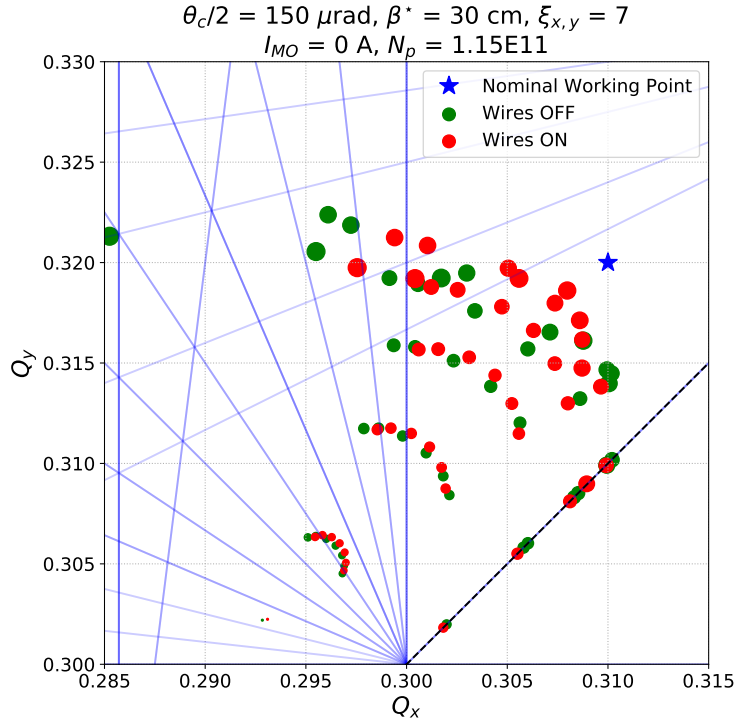


Figure 3.25: Tune footprint for the High Intensity experiment.

The footprint compression is less evident than in the Low Intensity experiment case. We observe that the particles are moving away from the diagonal, as well as from the 3^{rd} integer resonance ($Q_y=0.33$). This is in agreement with the reduction of the beam losses observed experimentally.

As in the case of the Low Intensity experiment, the crossing angle was also reduced during the High Intensity one. Figure 3.26a shows the DA evolution as a function of the half crossing angle and the bunch population. This plot is similar to Figure 3.11a (wires off) as the only difference corresponds to the chosen chromaticity (7 instead of 15).

Nevertheless, the improvement of the DA from the wire compensators can be seen in Figure 3.26b. One can, in fact, see that the area with a DA greater than 5σ is slightly enlarged, allowing for crossing angle down to $140 \mu\text{rad}$ for intensities above $1 \cdot 10^{11}$ protons per bunch. This numerical result is consistent with the experimental observation. Beam 1 - which was not equipped with wire compensators - shows larger beam losses than Beam 2. Once again, the efficiency of the BBLR mitigation using DC wires is confirmed by the tracking simulations.

Tune scans were also performed numerically. Figure 3.27 shows the same tune scan with and without the wire compensators.

As observed in the previous chapter, the tune scan without wires shows that the acceptable area in terms of DA is narrow and centered around the optimal tunes working point. The use of the wires enlarges this acceptable area, although the effect is marginal compared to the Low Experiment case. Nevertheless, small tune variations around the working point can be accommodated without any beam lifetime deterioration. However, one cannot conclude on the possibility to accommodate additional non linear effects as mentioned in the previous Section.

3 Compensation of the BBLR Interactions Using DC Wires in the LHC

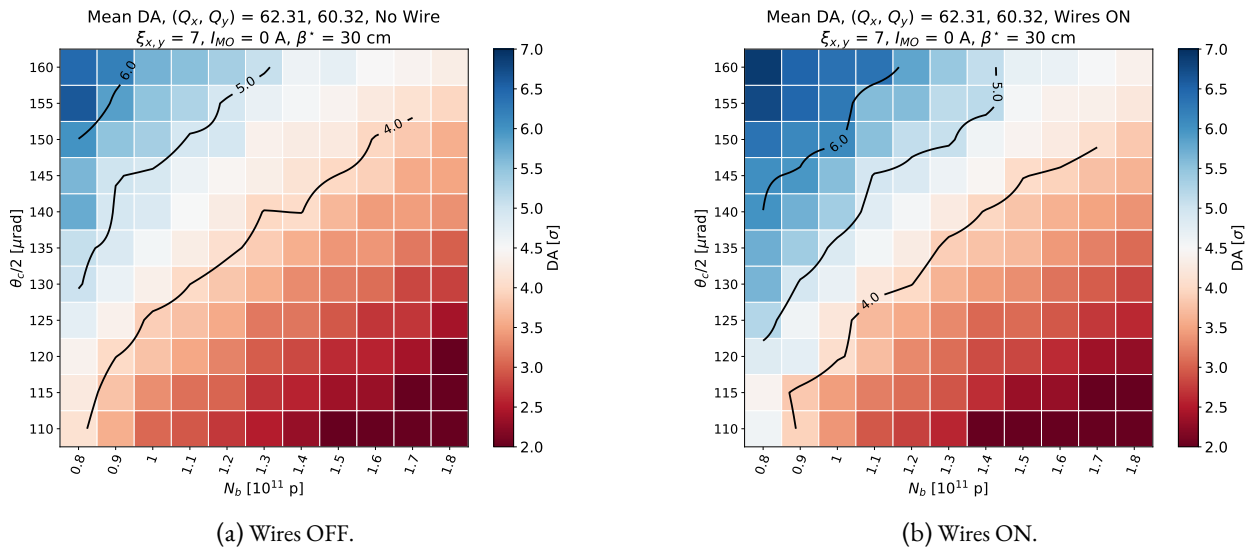


Figure 3.26: Dynamic aperture as a function of the half crossing angle and the bunch population, in the case of the High Intensity experiment. The plain black lines are iso-DA lines.

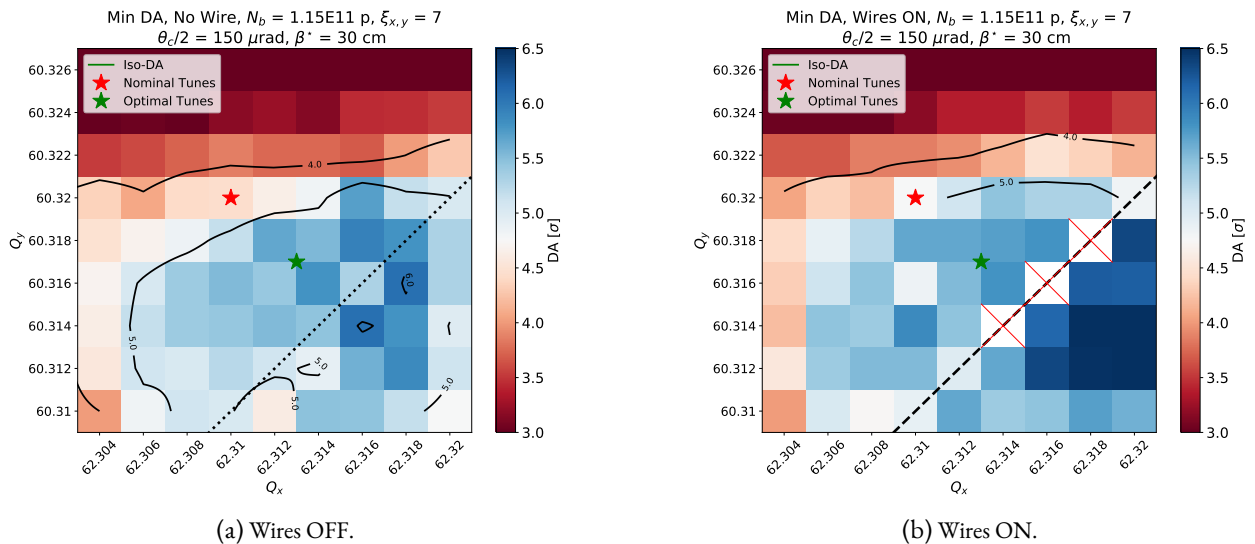


Figure 3.27: Variation of the dynamic aperture as a function of the choice of the tune working point. The red crosses signal missing points. The red star shows the nominal working point while the green star shows the optimal one. The black plain lines are the iso-DA lines.

Finally one can study the optimal wire currents, varying the Landau octupoles currents. Figure 3.28 shows the variation of DA as a function of the octupoles currents and the wires currents, given in terms of fraction of the nominal ones.

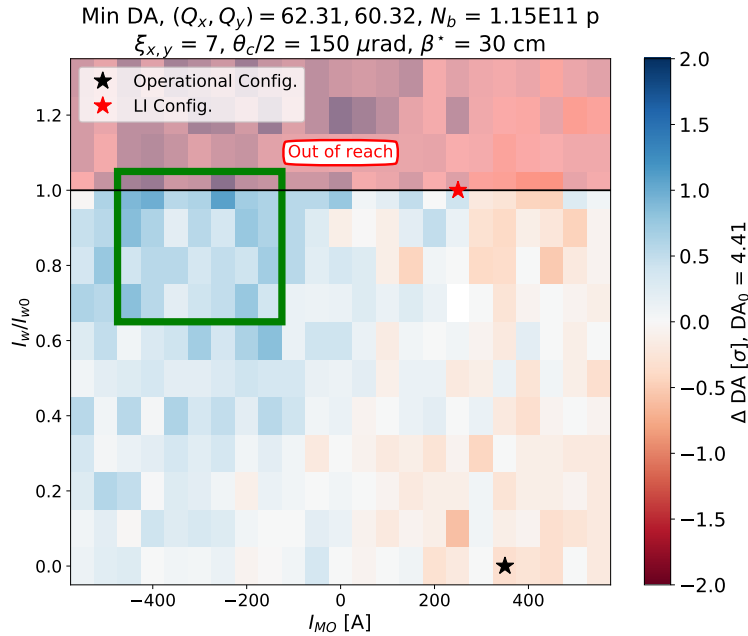


Figure 3.28: Dynamic aperture variation as a function of the Landau octupoles and wires currents. The red star shows the High Intensity experiment configuration and the black star the operational one. The best DA configurations are shown in the green box.

The reference DA, DA_0 , corresponds to the case where both the wires and the octupoles are turned off. The black star shows the nominal operational configuration during the LHC Run 2 while the red one shows the configuration adopted during the High Intensity experiment. During the latter, the octupoles were set to a higher value than in the Low Intensity experiment in order to use settings more compatible with the nominal LHC operational configuration. With the wires off, one can see from Figure 3.28 that reverting the polarity of the octupoles improves the DA. The improvement is then enhanced by the use of the wires, reaching increases of more than 1σ in the area shown in the green box.

As an example one can consider a Landau octupoles current of -250 A and set the wires current to their nominal values ($I_w/I_{w0} = 1$). From Figure 3.28 one can observe a DA improvement of about 1.3σ . The resulting tune footprint is shown on Figure 3.29.

Once again, the footprint compression is clear and validates qualitatively the DA gain. The footprint compression is slightly improved, compared to the Figure 3.25, by the use of negative octupoles. Compensating the linear detuning with amplitude instead of the RDTs could therefore be a possible option for the dimensioning of future devices, in case the technical constraints are such as the RDT compensation is not possible. It is worth noting that by targeting the detuning, the necessity for a local compensation does not hold anymore and the longitudinal positioning of the wires can therefore be relaxed (one could for instance consider installing the wires in the collimation IRs such as IR3 or IR7). However, no studies have been led in this direction yet.

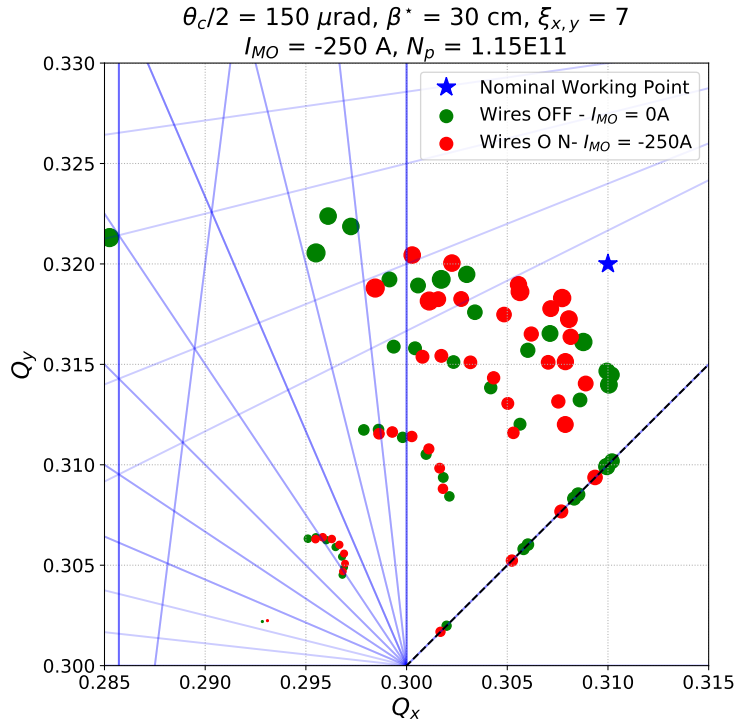


Figure 3.29: Comparison of the tune footprints obtained without wires and without octupoles and the one obtained with wires and negative octupoles currents

3.3 CONCLUSIONS

This Chapter reported the experimental and numerical results of the BBLR compensation using DC wires in the LHC. In Section 3.1, we presented the procedure of the Low Intensity experiment, together with the obtained results. During this experiment, it has been shown that DC wires can mitigate the BBLR interactions. The wire currents were set such as they compensate the octupolar resonances, namely the (4,0) and (0,4) RDTs. Using a low intensity beam, we were allowed from a machine protection point of view to reduce the transverse beam-wire distance and hence, enhance the effect of the compensators. During the experiment, the wires were powered on and off repeatedly, and the crossing angle was reduced in steps from 150 down to 130 μrad . Despite the stronger BBLR interactions in the latter case, the wire compensators showed a clear beneficial impact.

These experimental results were systemically supported by tracking simulations. The impact of several parameters on the dynamic aperture of the LHC was studied. At first, the beneficial effect of the wires in the Low Intensity experiment was validated in terms of DA in the configuration space. Secondly, a slight compression of the tune footprint using the wires was also observed. Finally, the impact of the bunch population, the crossing angle and the Landau octupoles current was also studied, always showing the beneficial effect of the wire compensators.

These positive results motivated another set of experiments using settings compatible with the nominal operation of the LHC. The High Intensity experiment confirmed the good results obtained during the Low Intensity one. It was in fact shown that the BBLR interactions effect can be mitigated even with higher intensity beams and - therefore - larger beam-wire distances. These results are important for the operation of the LHC in the next Run 3, and for the HL-LHC era. Following these results, the wire compensators will no longer be considered as demonstrators but as operational devices. Consequently, it is foreseen to operate the LHC with the wires compensators in the next LHC Run 3. The two unused wire collimators (L1, L5) are currently being removed from Beam 2 and are planned to be

installed on Beam 1 in order to operate with the two beams in the same configuration. The preparation of the next LHC Run 3, through tracking simulation, is described in Chapter 5.

Finally, we observed in this Chapter the role of the octupoles for the BBLR compensation. No clear evidence was shown in the experiments with such a low telescopic index. However, other experiments have been carried out using higher tele-indexes and the mitigation of the BBLR interactions using the Landau octupoles was studied. The results of these studies are reported in the next Chapter 4.

4 MITIGATION OF THE BBLR WITH LANDAU OCTUPOLES IN THE LHC

In the previous Chapters, we showed the importance on the beam performance of the octupolar component of the beam-beam interactions. It is, in fact, the first high order component that is not compensated or self-compensated, in the LHC. As a matter a fact, the wire compensators settings were chosen such as they could compensate the octupolar RDTs, proving to be of great efficiency both in the experiments and in numerical simulations. In the case of the High Intensity experiment, where the currents and beam-wire distances requirements could not be met, we showed through the study of tune footprints, that the compensation of the linear detuning with amplitude - directly linked to the octupolar component of the beam-beam field - could reduce the beam losses. This raises the question of the possibility of mitigating the BBLR interactions only with the use of the Landau octupoles present in the machine.

In this Chapter we intend to answer such a question question through a set of experiments. In the first Section, we describe in more detail the new optics scheme developed in view of the HL-LHC era and on which the BBLR mitigation using octupoles is based on: the Achromatic Telescopic Squeeze. After describing the two types of possible optics (flat or round) provided by such a scheme, we report the experimental results obtained for both cases.

4.1 THE ACHROMATIC TELESCOPIC SQUEEZE AND ITS BY-PRODUCTS

The ATS optics scheme has been described in the Introduction (see, Section 1.2.2). We recall here its main features and develop its by-products. We consider first the case of round optics, where $\beta_x^* = \beta_y^*$. As explained in the Introduction and in more detail in [59, 61], the key principle of the ATS scheme is to first *pre-squeeze* the beams using the conventional methods, trimming the matching quadrupoles of the considered IR. The second step consists in a so-called *tele-squeeze*. Reduced β^* values are reached using the matching quadrupoles located in the nearby ATS sectors.

The key point for this Chapter is the fact that by trimming the matching quadrupoles in the ATS sectors, the β -beating waves propagating along the arcs will reach their peaks at the sextupoles or octupoles locations. The consequent increased sextupoles efficiency is used in order to correct the chromaticity induced by the IT. Additionally, we can take advantage of the increased octupoles efficiency to use them for the BBLR mitigation. Figure 4.1 shows the relative increase of the β -functions at the location of an octupole from an ATS sector as a function of the tele-index r^{Tele} .

The horizontal β -function is increased by 300 % by increasing the tele-index from 1 to 4 while the vertical by 100 %. In this arbitrary example, the pre-squeeze is assumed to end with a β^* equals to 40 cm.

The tune spread induced by an octupole depends on the square of the β -function at its location, as shown in Eqs. 4.1 [63]:

$$\begin{aligned}\Delta Q_x &= \left[\frac{3}{8\pi} \int_{Oct} \beta_x^2 \frac{O_3}{B\rho} ds \right] J_x - \left[\frac{3}{8\pi} \int_{Oct} 2\beta_x\beta_y \frac{O_3}{B\rho} ds \right] J_y \\ \Delta Q_y &= \left[\frac{3}{8\pi} \int_{Oct} \beta_x^2 \frac{O_3}{B\rho} ds \right] J_y - \left[\frac{3}{8\pi} \int_{Oct} 2\beta_x\beta_y \frac{O_3}{B\rho} ds \right] J_x,\end{aligned}\tag{4.1}$$

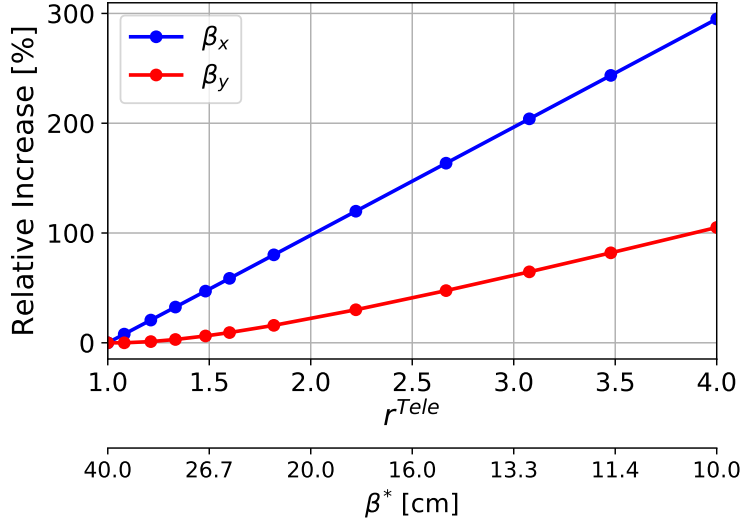


Figure 4.1: β -functions at an octupole, from the arc 45, location, as a function of the tele-index.

where O_3 is defined from the multipolar expansion given in Eq. 1.31 as $O_3 = C_3/3!$. The octupole used as an example in Figure 4.1 would therefore gain a factor 16 in terms of horizontal tune spread, and a factor 4 in the vertical plane, by tele-squeezing down to 10 cm. This effect is illustrated in Figure 4.2.

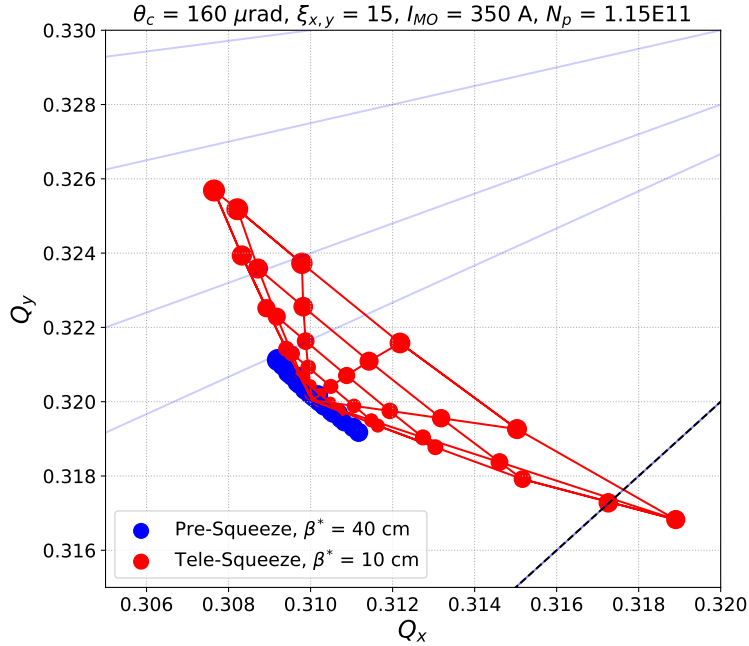


Figure 4.2: Tune spread induced by the Landau octupoles, powered at +350 A, for a tele-index of 1 and 4 (in blue and red respectively).

The two presented footprints show the tune spread induced only by the Landau octupoles in the machine, powered at 350 A, at the end of the pre-squeeze (in blue) and at the end of the tele-squeeze (in red). One can clearly observe the increase of the tune spread by decreasing further down the β -functions at the IPs. We can compare this result to the footprint obtained from the BBLR interactions and presented in Figure 1.19. Both tune footprints are similar in

terms of spread. With such a feature, the octupoles become powerful enough to mitigate the BBLR interactions effect, as we will see in the next Sections.

4.2 MITIGATION OF THE BBLR INTERACTIONS FOR ROUND OPTICS

This Section reports the experimental results obtained during the 2017 and 2018 Machine Development (MD) programs carried out in order to validate the use of the ATS scheme with high tele-index. The implementation of these experiments and the detailed results can be found in [125, 126]. In the following, we assume round optics ($\beta_x^* = \beta_y^*$)

4.2.1 OBJECTIVES OF THE EXPERIMENTS

The first part of the ATS MD program was carried out in 2017 and aimed to answer several questions such as the suitability of the LHC arcs for the ATS optics in terms of field quality and power supplies, the possibility to operate with negative octupoles (which is, at the time being, the foreseen baseline for HL-LHC) and the possibility to use those octupoles to mitigate the BBLR interactions. The second part of the MD program was carried out in 2018 and was a logical continuation of the experiments led in 2017. The first goal of this second part was to converge towards conditions similar to the next LHC Run 3 in terms of beam brightness. Using this new machine configuration, it was attempted to inject several hundred of bunches, grouped in different types of trains. The first type is the so-called BCMS (Batch Compression Merging and Splitting) [127], which is the typical train configuration injected in the LHC, consisting in trains of several bunches all separated by 25 ns. The second type of trains is called 8b4e train [128]. This type of trains has been developed to inject shorter trains in the LHC in order to minimize the heat load produced by electron cloud effects, leading to beam instabilities [129], beam losses and emittance blow-up [130]. These trains consists in series of eight bunches followed by four empty buckets. Finally, the last goal of this experiment was also to validate the combination of the tele-squeeze during the ramp in order to reduce the duration of the squeezing process. The technicalities of this implementation can be found in the previously cited reports.

In Section 4.1, we showed an example of high tele-index up to 4, using an optics squeezing the β^* down to 10 cm, which is not reachable in the LHC (aperture limitation). However, it is still possible to reach high tele-indexes by stopping the pre-squeeze at higher β^* values. As an example, we can choose $\beta_{pre}^* = 1$ m and tele-squeeze down to 25 cm to obtain the same tele-index of 4. This feature is the one explored in the following sections, using a β_{Tele}^* ranging from 35 cm to 65 cm, starting from a β_{pre}^* ranging from 1 to 2 m, corresponding to a tele-index ranging from 2 to 4.

As for the implementation of the Combined Ramp and Double Squeeze (CRDS), the details of the validation of the ATS scheme using pilot bunches [131] or individual bunches¹, together with the corresponding optics corrections, collimation setup and beam losses maps can be found in [125, 126].

4.2.2 BBLR MITIGATION, OCTUPOLES AND CROSSING ANGLES

The first set of ATS experiments was carried out during 2017. After several fills with a single bunch to validate the new optics scheme, it was possible to inject trains, and to bring the beams into collisions. In this set of experiments, β^* was reduced down from 1 m at the end of the pre-squeeze to 35 cm at the end of the tele-squeeze, giving a tele-index r^{Tele} of 2.86. Collisions occurred only in IP1 and IP5. The results reported in this section concern two LHC fills, namely Fill 6431 and Fill 6432, during which the mitigation of the BBLR interactions using the lattice octupoles was studied, together with the impact of the crossing angle.

¹Pilot bunches are low intensity bunches (typically with a bunch population of around 10^9 protons) injected first in the machine in order to detect any possible anomaly. An individual bunch is a bunch with the nominal intensity, but injected individually (in opposition to a train injection).

4 Mitigation of the BBLR with Landau Octupoles in the LHC

During the first fill (6431), 173 nominal bunches per beam were injected and the corresponding scheme is displayed in Figure 4.3.

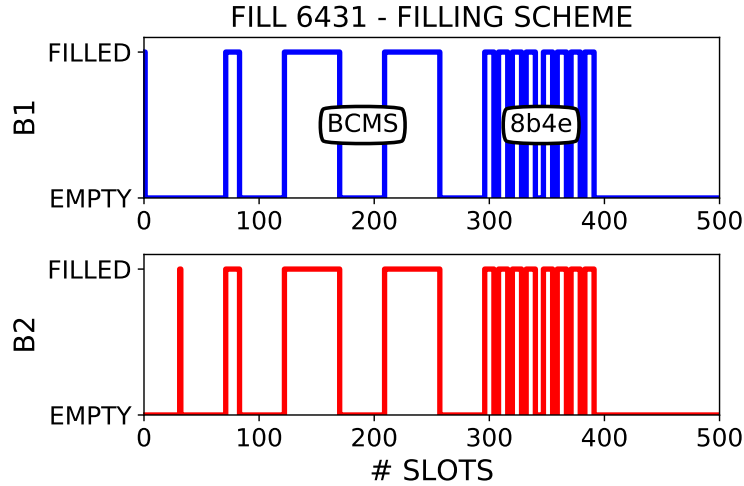


Figure 4.3: Filling scheme used for the Fill 6431. Only the first 500 bunch slots are displayed.

The beams were composed of a single, non colliding, individual bunch, reserved for tune monitoring, a first train of 12 bunches needed for machine validation before injecting the full filling scheme, two BCMS trains of 48 bunches each and two 8b4e trains of 32 bunches each.

After the injection, the energy was ramped up to 6.5 TeV and the β^* was tele-squeezed down to 35 cm. Figure 4.4 gives an overview of the fill in terms of energy, beam intensity, octupoles currents, half crossing angle and beam lifetime.

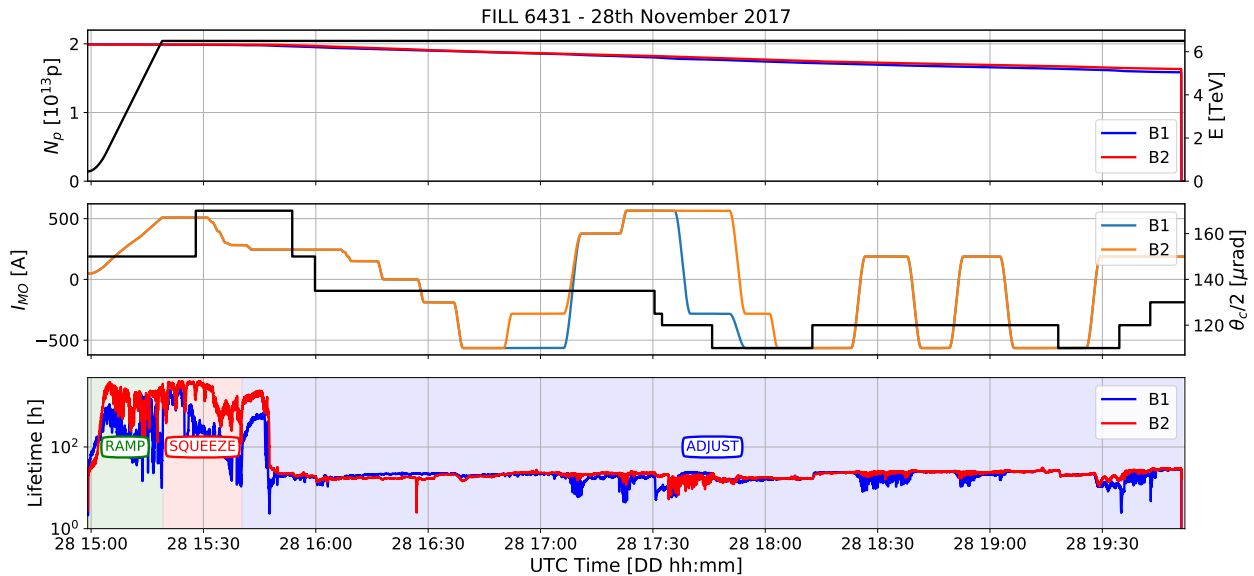


Figure 4.4: Overview of the Fill 6431. Top plot: beams intensities (blue and red lines) and energy (black line) as a function of time. Middle plot: Landau octupoles currents (orange and blue lines) and half crossing angle (black line) as a function of time. Bottom plot: beams' lifetime (in blue for B1 and red for B2) as a function of time. The background coloring shows the different beam modes.

The top plot shows the evolution of the beam intensities (blue and red solid lines for B1 and B2 respectively), together with their energy. The middle plot shows the variation of the Landau octupole current (blue and orange solid lines for B1 and B2, respectively) together with the half crossing angle (black solid line). Finally, the bottom plot shows the evolution of the beam lifetime (burn-off corrected, which means that the luminosity losses are taken into account [121, 132]) in hours, given in a logarithmic scale (blue and red solid lines for B1 and B2 respectively) together with the different beam modes as background coloring. The drop of lifetime observed at 15:45 corresponds to the moment the two beams were brought into collisions. The normalized emittances were measured before the start of the collisions. For B1, the emittances of the BCMS bunches were of about $3 \mu\text{m}\cdot\text{rad}$, while the 8b4e bunches had an emittance of about $2.5 \mu\text{m}\cdot\text{rad}$, in both planes. For B2, these values were reduced ($2.5 \mu\text{m}\cdot\text{rad}$ for the BCMS bunches, $2 \mu\text{m}\cdot\text{rad}$ for the 8b4e bunches, in both planes). The major parameters of interest were the octupoles current and the half crossing angle. The collisions were reached with a positive current of 270 A in the octupoles and a half crossing angle of $170 \mu\text{rad}$ (10.5σ). Several crossing angle and octupole scans took place in order to demonstrate that the beam lifetime was not affected too much and stayed above the expected 20-25 h. The half crossing angle was then successfully reduced down to $120 \mu\text{rad}$ (7.5σ), value for which the octupole scans were carried out. The corresponding results are reported in Figure 4.5 for B1, and in Figure 4.6 for B2.

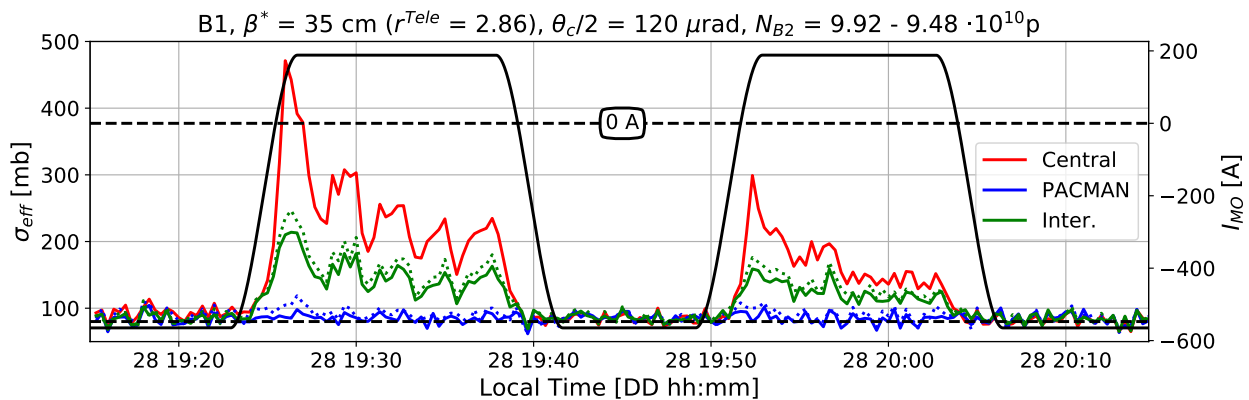


Figure 4.5: Effective cross-section of a selection of bunches of Beam 1 and Landau octupoles current as a function of time.

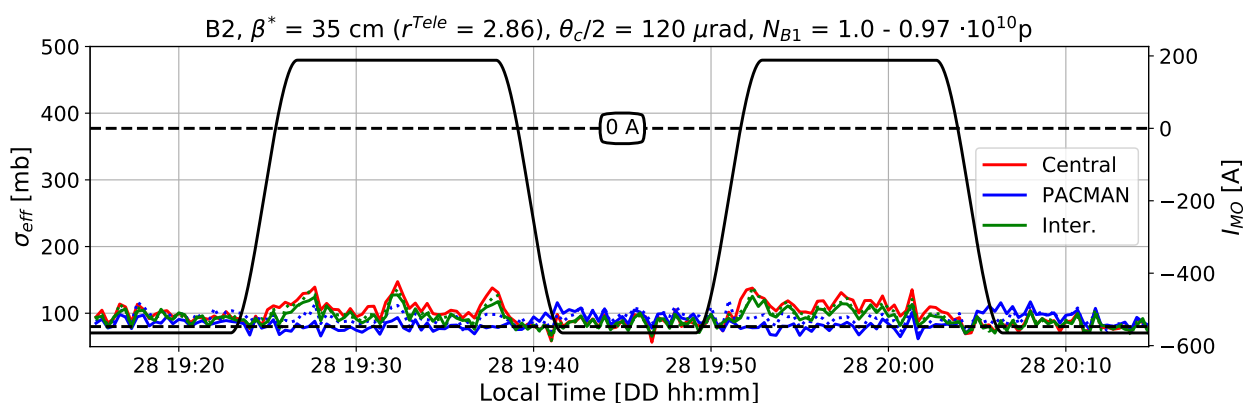


Figure 4.6: Effective cross-section of a selection of bunches of Beam 2 and Landau octupoles current as a function of time.

The average bunch luminosity in both ATLAS and CMS was measured at about $6 \cdot 10^{30} \text{ Hz/cm}^2$. The luminosity and emittances values are important if one wants to compare the obtained effective cross-section with the wire compensation experiments reported in Chapter 3. Figures 4.5 and 4.6 show the evolution of the effective cross-

section - as defined in Chapter 3 - for a collection of bunches, depending on their location within a BCMS train. Three families of bunches were identified. The central bunch, located at equal distance from both extremities of the train and experiencing the most BBLR interactions, the PACMAN bunches, located at the extremities of each train, and the intermediate bunches, located in between the PACMAN and the central bunches, therefore experiencing an intermediate number of BBLR interactions. With these definitions, each of the two BCMS trains has one central bunch (red solid line), two PACMAN bunches (blue solid and dotted lines), and two intermediate ones (green solid and dotted lines). In order to improve the statistics, the two Figures display the average between two bunches having the same position within their respective train.

The first striking observation is the difference of behavior between the two beams. B2 seems in fact insensitive to the BBLR interactions, and therefore, their compensation. This can be explained by the fact that the emittances of the bunches of B2 were smaller during the Fill 6431. It is also known that B2 lifetime is always better than the one of B1 in nominal operation, for a reason that is not yet understood.

Focusing on the clearer results of B1, in Figure 4.5, one can see that strong negative octupoles as set before the beginning of the scan, can bring the effective cross-section of all the bunches almost to the burn-off level (80 mb, see Chapter 3). The half crossing angle is set to 120 μrad (7.5σ). Despite the reduced bunch intensity (less than 10^{11} protons), this crossing angle is reduced enough to observe the impact of the BBLR interactions on the effective cross-section. This shows that the negative octupoles seem to mitigate their effect. This observation is confirmed by the following scans. Around 19:25, the polarity of the octupoles was reversed and their current was set to 200 A. Immediately, a spike of losses was observed on most of the bunches. The observed losses pattern is clearly BBLR dominated: the central bunch experiences more losses than the intermediate bunch, and the effective cross-section of the PACMAN bunch stays almost to the burn-off level. This observation was reproduced once more at 19:50, showing similar results.

These results show the possibility to mitigate the BBLR interactions using the Landau octupoles with a high tele-index. Fill 6431 was dumped in order to inject new beams as the intensities of the previous beams were reduced and the experiment therefore continued with Fill 6432. In terms of filling scheme, Fill 6432 differs from the previous one by the replacement of the 8b4e trains by an additional BCMS train. This filling scheme is reported in Figure 4.7.

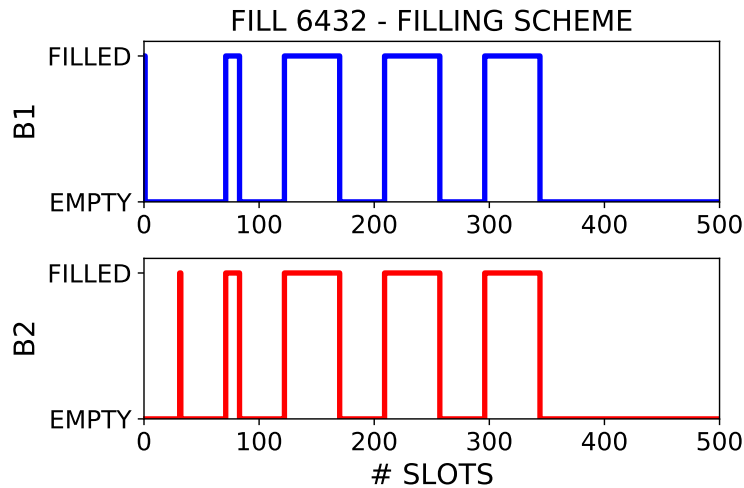


Figure 4.7: Filling scheme used for the Fill 6432.

The starting point of the collisions was the same as for the Fill 6431, with a half crossing angle of 170 μrad (10.6σ), the octupoles set to 250 A and β^* squeezed down to 35 cm. Figure 4.8 shows an overview of this fill.

As for the Fill 6431, Figure 4.8 shows the evolution of the beam intensities and energy (top plot), of the half crossing angle and Landau octupoles (middle plot) and of the beams lifetime (bottom plot). Quickly after collisions

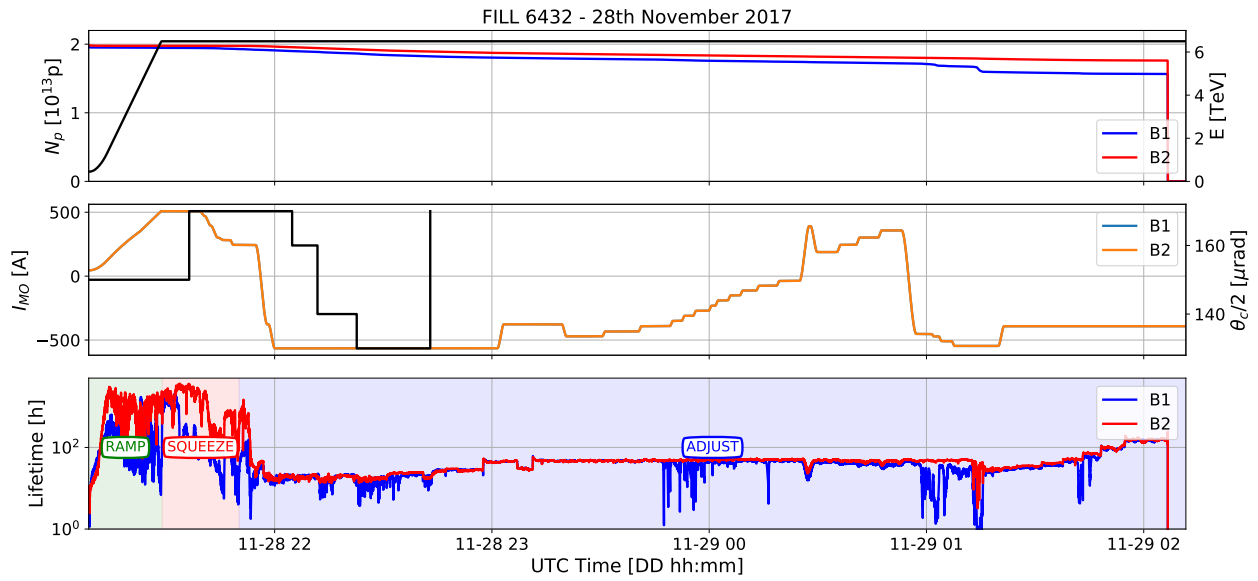


Figure 4.8: Overview of the Fill 6432. Top plot: beams intensities (blue and red lines) and energy (black line) as a function of time. Middle plot: Landau octupoles currents (orange and blue lines) and half crossing angle (black line) as a function of time. Bottom plot: beams' lifetime (in blue for B1 and red for B2) as a function of time. The background coloring shows the different beam modes.

were reached, the octupoles polarity was reversed and their current was set to the maximum value of -570 A. The lifetime of Beam 1 has been deteriorated several times during the fill. The first drops of lifetime observed around 22:30 are due to the reduction of crossing angle. The second part of this fill was used in order to determine instabilities threshold, by changing the octupoles current, hence the sudden and drastic lifetime reductions observed around midnight and 01:00.

A crossing angle scan was performed right after reaching the collisions, and the results in terms of beam lifetime are reported in Figure 4.9.

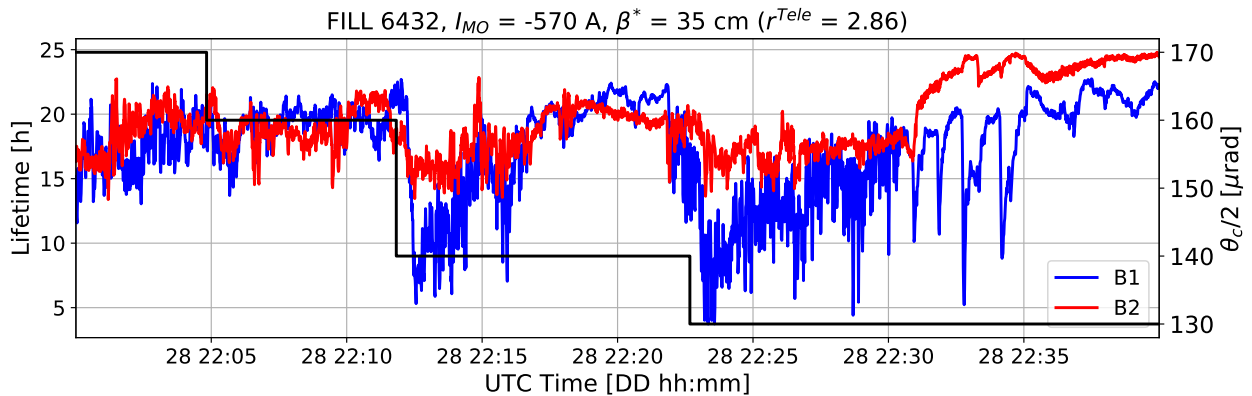


Figure 4.9: Evolution of the beams lifetime and of the half crossing angle as a function of time.

In this Figure, one can see the evolution of the half crossing angle (black solid line) in time, together with the beams lifetime (blue and red solid lines for B1 and B2, respectively). The crossing angle was reduced in several steps from 170 μrad down to 130 μrad (8σ). After each step, an expected drop of lifetime occurred for both beams. However, this drop was recovered after a short time (less than 5 min), reaching again about 20 h lifetime, considered

as a good enough lifetime in collisions. This confirmed the potential of operating with strong negative octupoles at low crossing angle.

This set of experiment, as part of the 2017 ATS MD program, motivated to pursue these studies during the 2018 ATS MD Program.

4.2.3 BBLR MITIGATION AT LOW CROSSING ANGLE

The second set of experiment was carried out in 2018 and its main objective was to ramp up the intensity to several hundred bunches and to validate the ATS scheme for higher intensity beams, but also for brighter bunches, in view of the next LHC Run 3. The other main objective of this program was to confirm the implementation of the combined ramp and squeeze mentioned in the previous Section 4.2.2. In terms of BBLR mitigation using the octupoles, the goal was to demonstrate the possibility of such a compensation in the case of a very low crossing angle. The chosen β^* was 65 cm. However, the value of β^* at the end of the pre-squeeze was changed and set to 2 m. By doing so, the tele-index was further increased, up to 3.08, increasing again the efficiency of the Landau octupole.

This Section reports the experimental results obtained with the Fill 7171, carried on the 14th of September 2018, but more detailed results can be found in [126]. Fill 7171 was the first step of the intensity ramp up, and the beams were therefore composed of an individual bunch for the tunes monitoring, a first train of 12 bunches and one BCMS train of 48 bunches, for a total of 61 nominal bunches. As in the 2017 experimental program, the collisions occurred only in IP1 and IP5. Figure 4.10 shows the chosen filling scheme for the Fill 7171.

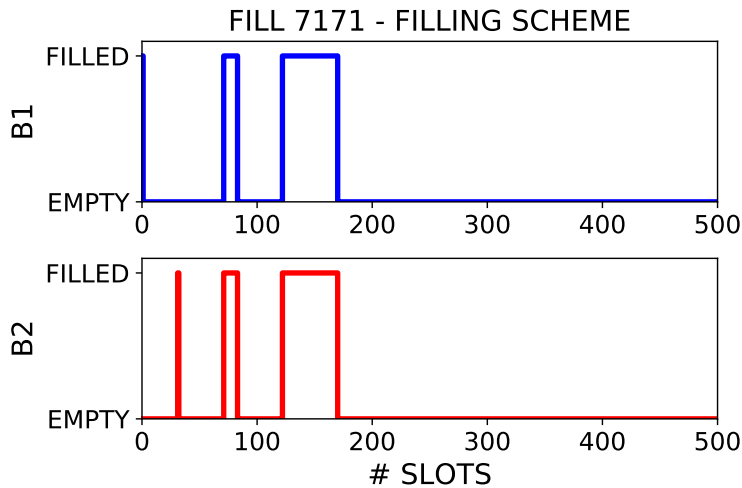


Figure 4.10: Filling scheme used for the Fill 7171.

As for the previous fills, Figure 4.11 gives an overview of the Fill 7171 in terms of beam intensities, energy, half crossing angle, Landau octupoles currents, and beam lifetime.

The emittances were preserved during the ramp, reaching around $2.2 \mu\text{m}\cdot\text{rad}$ for B1 in both planes, and slightly higher values for B2. The goal of this fill was two-fold: perform a crossing angle scan down to lower values with strong negative octupoles, validating this possibility in terms of beam lifetime, and perform an octupole current scan at the chosen crossing angle value. Figure 4.12 shows the evolution of the two beams lifetime during the crossing angle scan.

The starting point of the crossing angle was $120 \mu\text{rad}$ (10.2σ), with the octupoles set to their maximal value of -570 A . The crossing angle was thus reduced down to the value of $90 \mu\text{rad}$, corresponding, in this configuration, to a normalized crossing angle of 7.6σ . In order to restore a good lifetime, the betatron tunes were adjusted when required. However, at this value, the lifetime was too low and the crossing angle was finally tuned to $95 \mu\text{rad}$ (8.1σ),

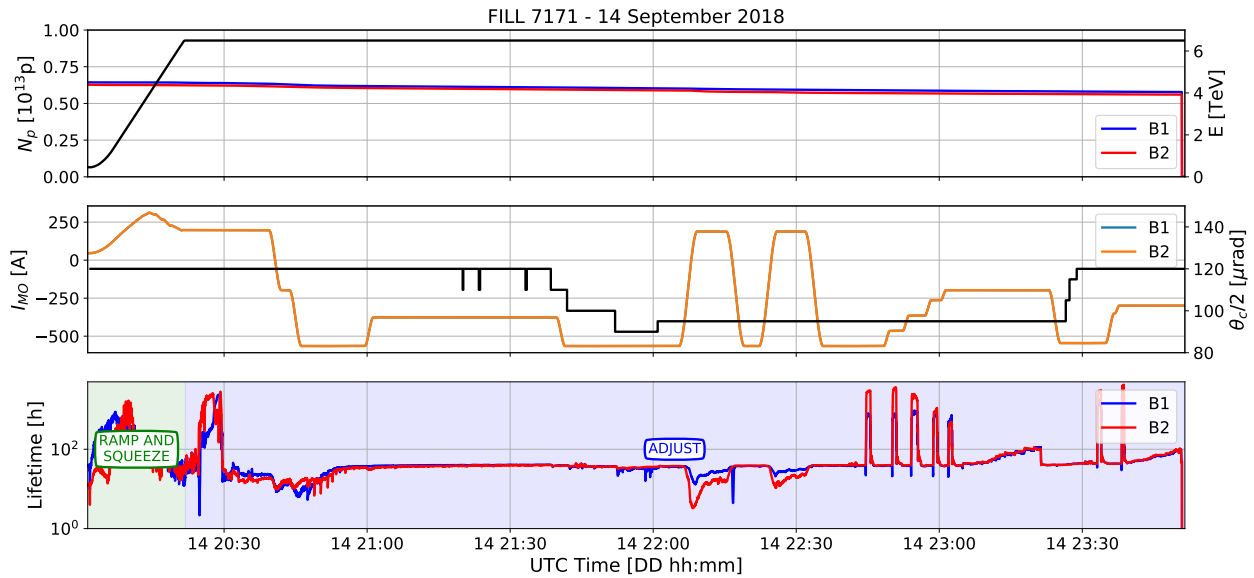


Figure 4.11: Overview of the Fill 7171. Top plot: beams intensities (blue and red lines) and energy (black line) as a function of time. Middle plot: Landau octupoles currents (orange and blue lines) and half crossing angle (black line) as a function of time. Bottom plot: beams' lifetime (in blue for B1 and red for B2) as a function of time. The background coloring shows the different beam modes.

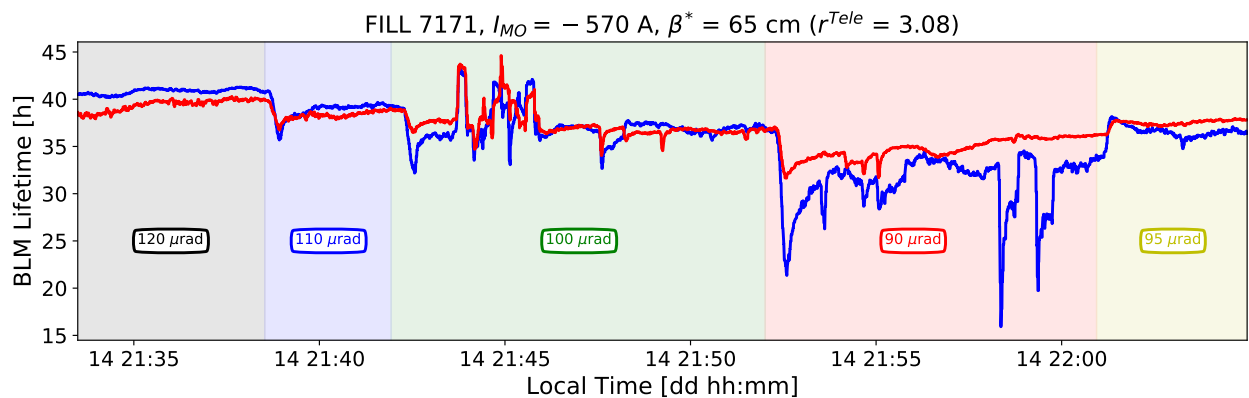


Figure 4.12: Evolution of the beams lifetime as a function of time. The half crossing angle evolution is shown with the background coloring.

4 Mitigation of the BBLR with Landau Octupoles in the LHC

where a typical lifetime of about 35 h was reached. This scan showed that with such tele-index, the octupoles were powerful enough to compensate strong BBLR interactions.

With the half crossing angle set to $95 \mu\text{rad}$, the octupoles current was scanned, monitoring the effect on the effective cross-section of several bunches. The obtained results are presented in Figure 4.13 and 4.14 for B1 and B2 respectively.

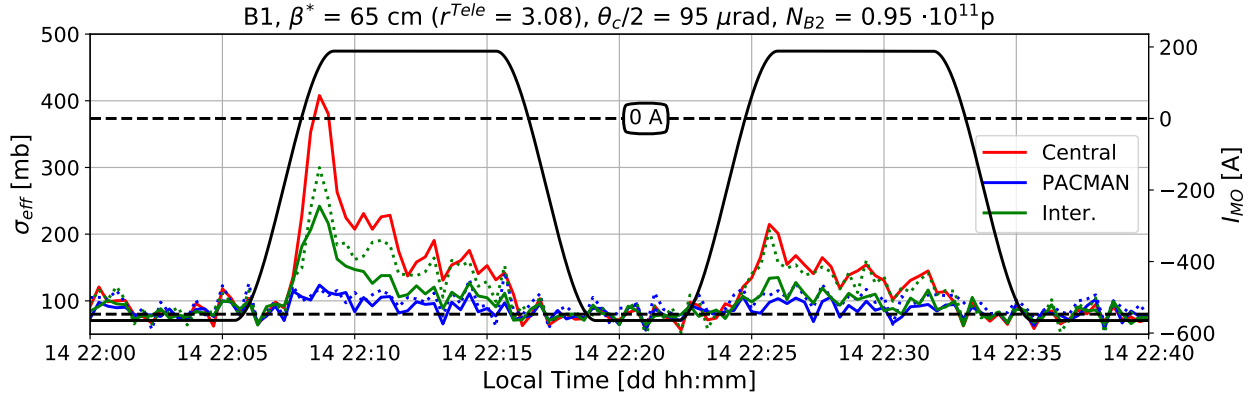


Figure 4.13: Effective cross-section of a collection of Beam 1 bunches and Landau octupoles current as a function of time.

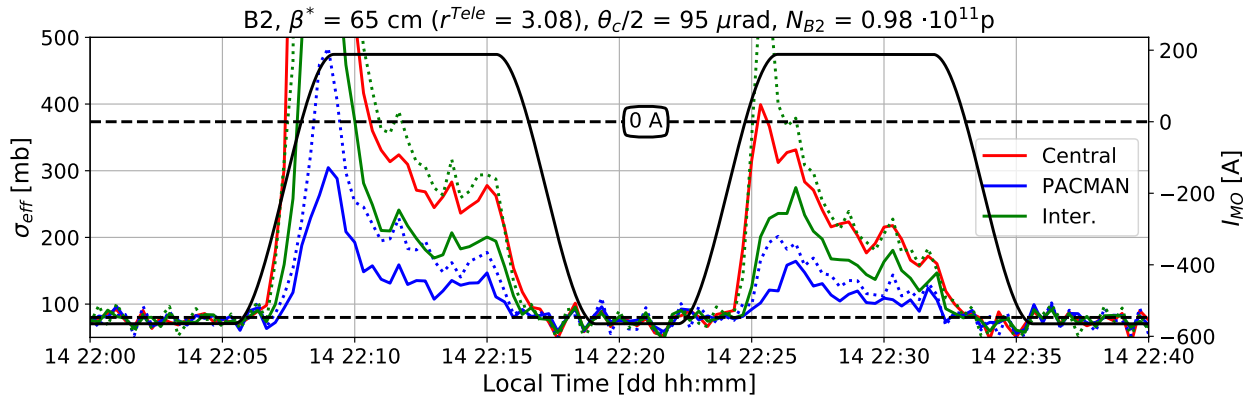


Figure 4.14: Effective cross-section of a collection of Beam 2 bunches and Landau octupoles current as a function of time.

Compared to the experiment presented in Section 4.2.2, the average bunch luminosity was about $4 \cdot 10^{30} \text{ Hz/cm}^2$. Unlike the results described in the previous section, B2 seemed to be more affected than B1 by the BBLR interactions in this configuration. This could be explained by the slightly higher intensity of the B1 bunches, and their slightly smaller emittances. When the octupoles polarity is reverted to positive, the very high values of the different effective cross-sections attest the aggressivity of this configuration in terms of BBLR interactions. In fact, reaching an effective cross-section of more than 400 mb corresponds to a very low burn-off efficiency, and most of the beam losses can therefore be attributed to the BBLR interactions. Moreover, the BBLR pattern can again be identified as the central bunch experiences more beam losses than the intermediate one and than the PACMAN bunch. However it is also observed that the intermediate and PACMAN bunches located in the second half of the train tend to experience slightly more beam losses than their associated bunch from the first part of the train. As discussed in Chapter 3, this could be identified as a consequence of electron clouds effect, where the end of a train always experiences more beam losses than the head of the same train.

However, Figures 4.13 and 4.14 also show the strong capability of the octupoles to mitigate those BBLR interactions. One can observe that by setting their current to -570 A, the effective cross-section of all the bunches shrinks back to the burn-off limit of 80 mb.

To conclude, these sets of experiments successfully demonstrated the possibility to mitigate the BBLR interactions with the Landau octupoles in configurations with high tele-index and rounds optics. Nevertheless, during the 2017-2018 experimental program, the possibility to provide flat optics collision was also explored, and similar BBLR experiments were carried out in that context. These experiments are reported in the next section.

4.3 MITIGATION OF THE BBLR INTERACTIONS FOR FLAT OPTICS

4.3.1 FLAT OPTICS FOR (HL)-LHC

Until now, and in general in the LHC, collisions optics are considered as round: the β -functions at the IP are equal in both planes. However, the ATS scheme was firstly developed in order to deliver flat collision optics at the high luminosity IPs [133], with a more reduced β^* in one of the two planes. Flat optics correspond in fact to an optic scheme where $\beta_x^* \neq \beta_y^*$. The β -functions at the IP could then be brought to lower level in one plane while the one in the other plane is kept to a higher level in order to restore the luminosity geometric factor. The crossing angle is therefore set in the plane of larger β^* . One can thus define a β^* aspect ratio, denoted r^* and defined as [134]:

$$r^* = \frac{\beta_X^*}{\beta_{\parallel}^*}, \quad (4.2)$$

where β_X^* and β_{\parallel}^* represent the β^* values in the crossing and the parallel separation plane respectively. In order not to lose in terms of luminosity performance, the geometric average of the two values should remain unchanged while flattening the optics. One can therefore define an equivalent β_{eq}^* defined as:

$$\beta_{eq}^* \equiv \sqrt{\beta_X^* \beta_{\parallel}^*} \sim \text{Cst.} \quad (4.3)$$

The peak luminosity for flat optics can be expressed as a function of the peak luminosity using round optics, and the geometrical luminosity loss factor $F(r^*, \beta_{eq})$:

$$\mathcal{L}_{flat}(\beta_{eq}, r^*) = \mathcal{L}_{round}(\beta_{eq}) \times F(r^*, \beta_{eq}), \quad (4.4)$$

where the luminosity loss factor can be written:

$$F(r^*, \beta_{eq})^{-1} \equiv \sqrt{1 + \frac{1}{r^*} \left(\frac{\Theta_c \sigma_z}{2\beta_{eq}^2} \right)^2}, \quad (4.5)$$

where Θ_c is the normalized crossing angle and σ_z the RMS bunch length. The normalization of the crossing angle is done with the beam divergence in the plane of larger β^* . Consequently, the physical crossing is reduced by a factor $(r^*)^{1/4}$ when going from round to flat optics. In principle, the peak luminosity could be fully recovered by choosing an infinite aspect ratio at the IP:

$$\lim_{r^* \rightarrow \infty} \mathcal{L}_{flat} = \mathcal{L}_{round}. \quad (4.6)$$

However, the aspect ratio cannot be set to infinite values in practice because of aperture restriction in the IT. As the crossing angle has to be set in the plane of larger β^* , and due to the shape of the LHC beam screens, oriented vertically in IR1 and horizontally in IR5, the crossing should be done accordingly when colliding with flat optics. This is the exact opposite configuration than with round optics, as exposed in Figure 4.15 [134].

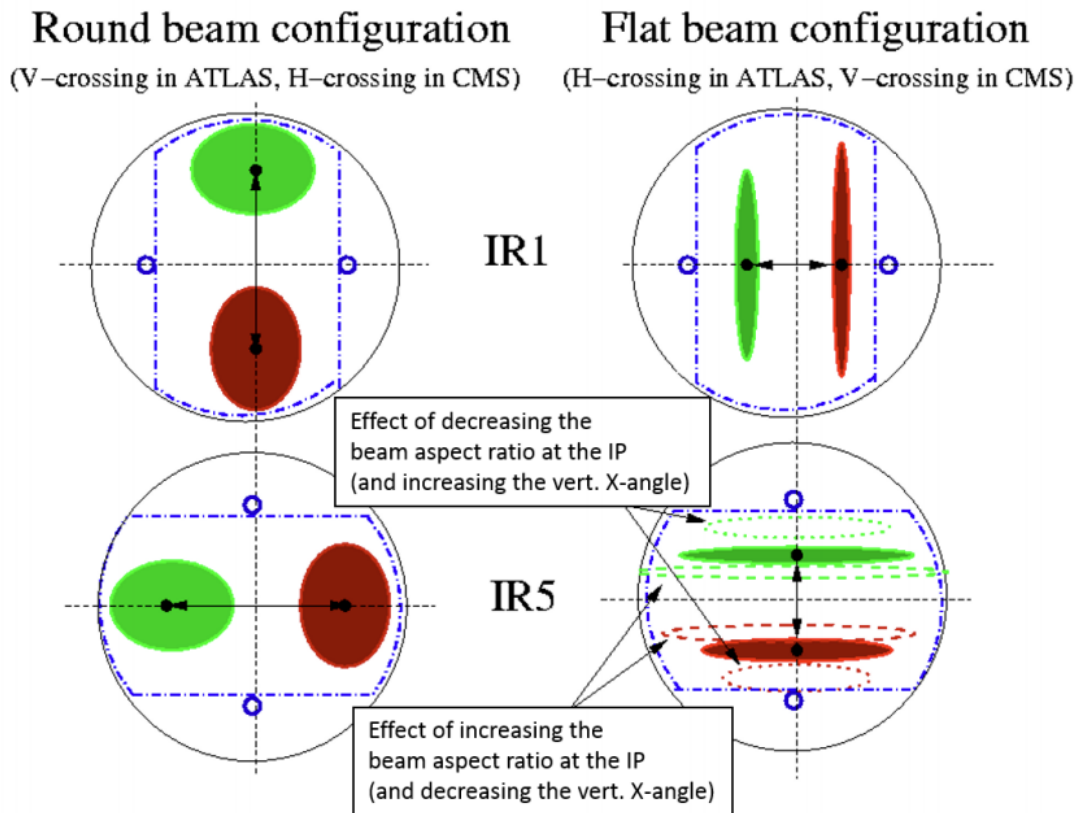


Figure 4.15: Schematic view of the beam footprint in the vacuum chamber of the Inner Triplet for round optics (on the left) and flat optics (on the right). Both IR1 (top plots) and IR5 (bottom plots) are illustrated. Courtesy of S. Fartoukh.

Aspect ratios ranging from 3 to 4 would match the available aperture in the LHC triplet, with the aforementioned configuration (crossing plane inversion). In [134], it is shown that the luminosity performance using flat optics could be similar to the one obtained with round optics. However, only some experiments (some of them reported in the following Sections) have been carried out so far, and no experience with flat optics in nominal operation has been gained during the LHC Run 2. Flat optics are also considered for the LHC Run 3 as they could have a beneficial effect on the triplet luminosity lifetime (the rotation of the crossing angle would induce radiation damages in other regions than the one already affected by the previous LHC runs) [61] and for HL-LHC [48, 135]

The first tests of colliding beams with flat optics were successfully carried out in 2017 with low intensity beams [136], although some challenging steps were met in terms of optics correction. Those studies were continued in 2018 with higher intensity beams, and the next Section reports the corresponding results, especially in terms of BBLR compensation.

4.3.2 MITIGATION OF THE BBLR INTERACTIONS USING THE LANDAU OCTUPOLES

On the 28th of July 2018, the first high intensity tests using flat optics took place. The detailed results of this experimental campaign are reported in [137]. 61 nominal bunches were injected in the LHC, using the following structure: one individual bunch, non-colliding, for tune monitoring, a train of 12 bunches and a BCMS train of 48 bunches. The corresponding filling scheme is reported in Figure 4.16.

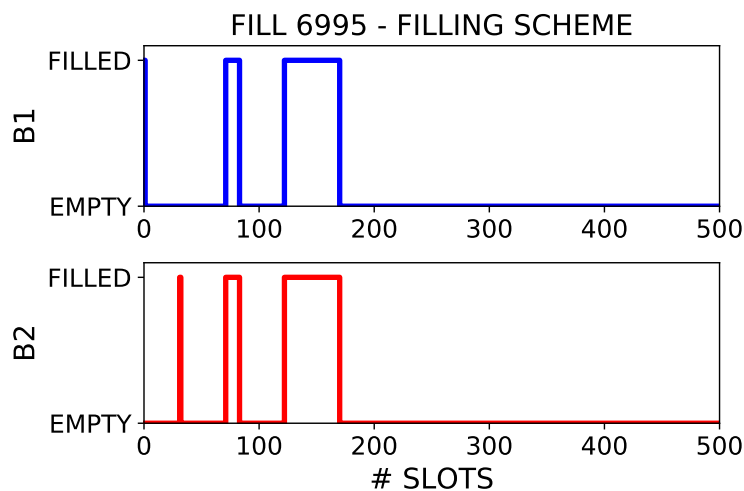


Figure 4.16: Filling scheme used for the Fill 6995. Only the first 500 bunch slots are displayed.

The nominal energy ramp followed the beams injection. At the end of the ramp, the crossing bumps in IR1 and IR5 were rotated. Large lifetime fluctuations were observed for both beams during this rotation, as illustrated in Figure 4.17.

At the end of the tele-squeeze, the final flat optics with $\beta_{X/\parallel}^* = 60/15$ cm were reached. A very poor lifetime was observed immediately after the beams were brought into collisions at a crossing angle of $130 \mu\text{rad}$ (10.6σ). The octupoles polarity was inverted and the tunes were optimized in order to retrieve a lifetime of about 20 h. The emittances measurements revealed some instabilities in B2 (emittances reaching about $8 \mu\text{m}\cdot\text{rad}$ for some bunches in the horizontal plane) while the others had an emittance of about $2\text{-}2.5 \mu\text{m}\cdot\text{rad}$. At the same crossing angle of $130 \mu\text{rad}$, the octupoles current was scanned and the corresponding evolution of the beams lifetime is displayed in Figure 4.18.

The effect of the octupole polarity on the lifetime is very clear as we observe a significant drop of about 5 h for B1 and about 15 h for B2 when the polarity turns positive. The difference of behavior between the two beams (which is

4 Mitigation of the BBLR with Landau Octupoles in the LHC

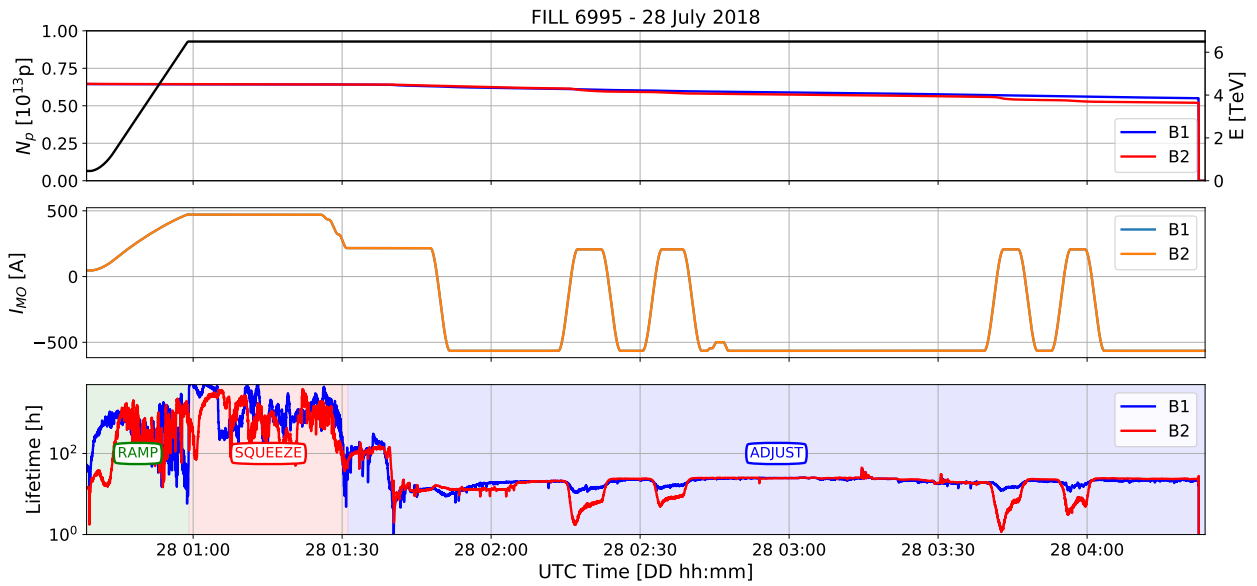


Figure 4.17: Overview of the Fill 6995. Top plot: beams intensities (blue and red lines) and energy (black line) as a function of time. Middle plot: Landau octupoles currents (orange and blue lines) as a function of time. Bottom plot: beams' lifetime (in blue for B1 and red for B2) as a function of time. The background coloring shows the different beam modes.

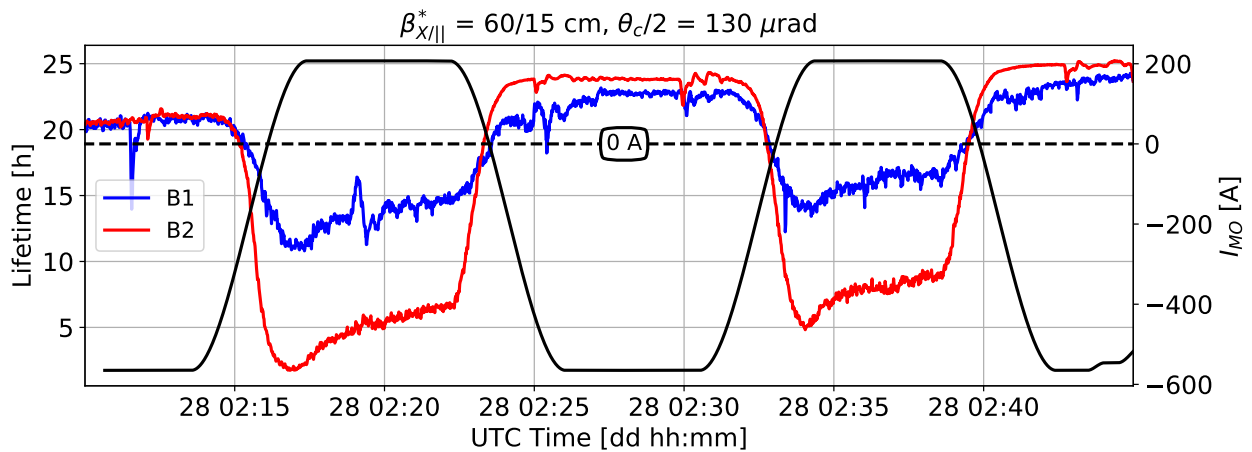


Figure 4.18: Beam 1 and Beam 2 lifetimes together with the Landau octupoles current as a function of time, at $\theta_c/2 = 130 \mu\text{rad}$.

again, the opposite of what we observe during the nominal operation of the LHC) can be explained by the increased emittances of B2 due to the instability that occurred during the squeezing process and, possibly, by the inversion of the crossing planes with flat optics.

Similar results can be observed in terms of bunch-by-bunch effective cross-sections, as shown in Figure 4.19 for B1 and 4.20 for B2. For reference, and comparison to similar plots from the previous Sections and Chapters, the average bunch luminosity at this stage of the experiment was about $7 \cdot 10^{30}$ Hz/cm².

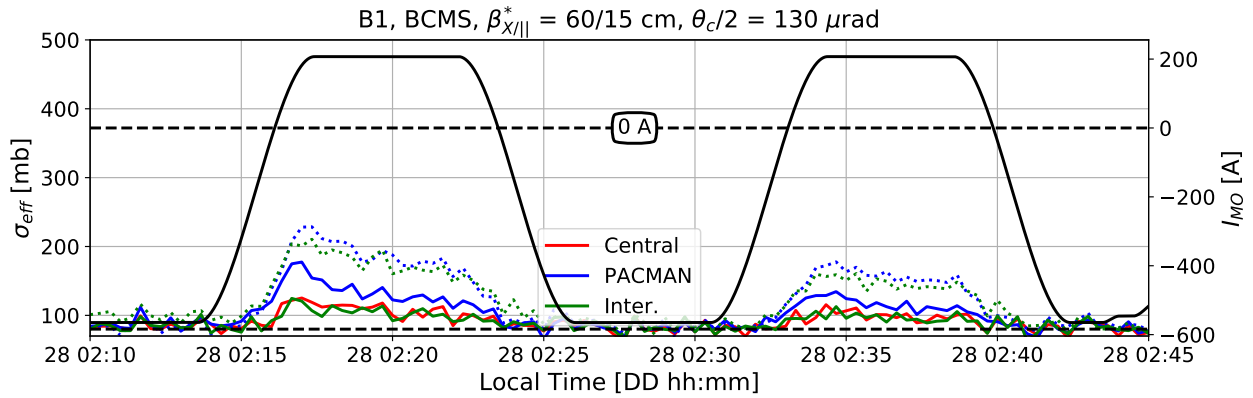


Figure 4.19: Evolution, in time, of the effective cross-section of a collection of bunches included in the BCMS train of Beam 1, during the octupoles current scan at $\theta_c/2 = 130$ μ rad.

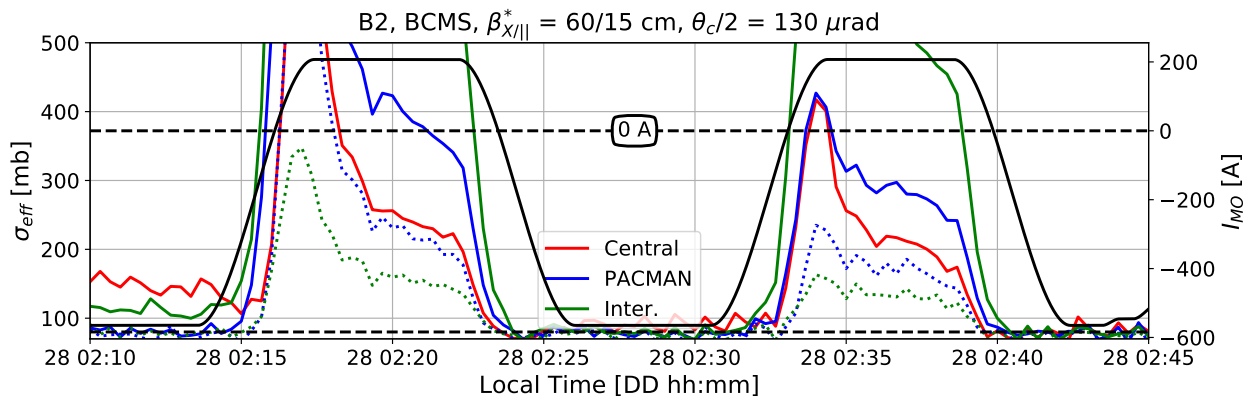


Figure 4.20: Evolution, in time, of the effective cross-section of a collection of bunches included in the BCMS train of Beam 2, during the octupoles current scan at $\theta_c/2 = 130$ μ rad.

The unbalanced effect on the bunches lifetime already observed at the beam level is confirmed, as the effective cross-section of the B2 bunches drastically increases, more than the one of B1 bunches, when reverting the octupoles polarity. In the case of B1, the octupoles seem to be powerful enough, in the explored crossing angle range, to mitigate the strong BBLR interactions while in the case of B2, the effective cross-section of the bunches seems to stay slightly above the burn-off limit, indicating additional beam losses due to BBLR effects. Moreover, in comparison to the previously described experiment, the BBLR losses pattern could not be identified here, as the PACMAN bunches seems to experience more beam losses than the central bunch. This could also be related to the emittances of each bunches, especially after the observed instability during the squeeze.

The half crossing angle was further reduced down to 100 μ rad (8.15σ) and another octupoles current scan was performed. The effect of this scan on the beams lifetime is illustrated in Figure 4.21.

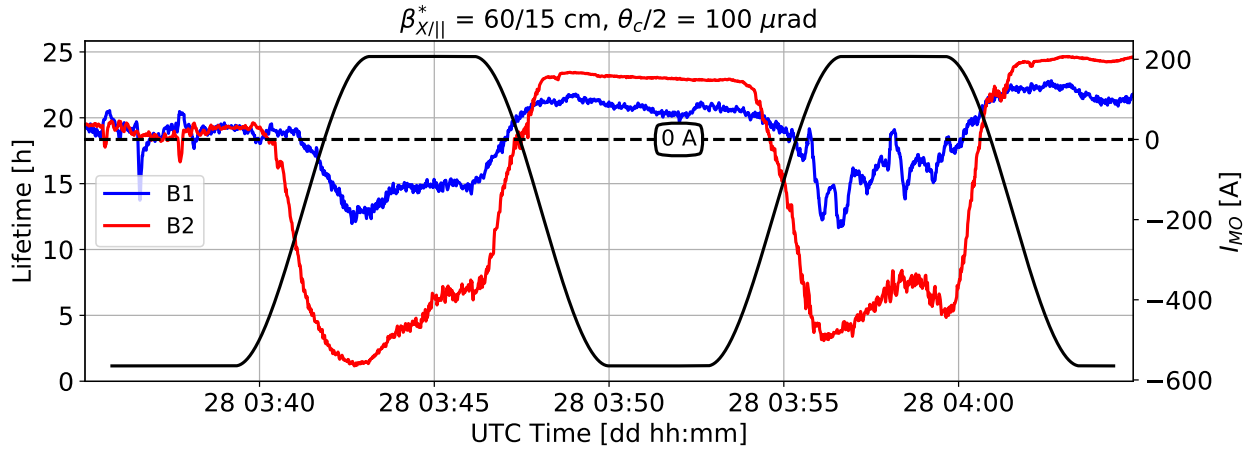


Figure 4.21: Beam 1 and Beam 2 lifetimes together with the Landau octupoles current as a function of time, at $\theta_c/2 = 100 \mu\text{rad}$.

This confirms the unbalanced effect between the two beams. When reverting the polarity of the octupoles, the lifetime of B2 reached very low levels but could be retrieved by switching back to negative octupoles.

The bunch-by-bunch evolution of the effective cross-section of bunches from B1 and B2 as a function of the octupoles current is illustrated in Figure 4.22 and 4.23 respectively. At this stage of the experiment, the average bunch luminosity was reduced to about $6 \cdot 10^{30} \text{ Hz/cm}^2$.

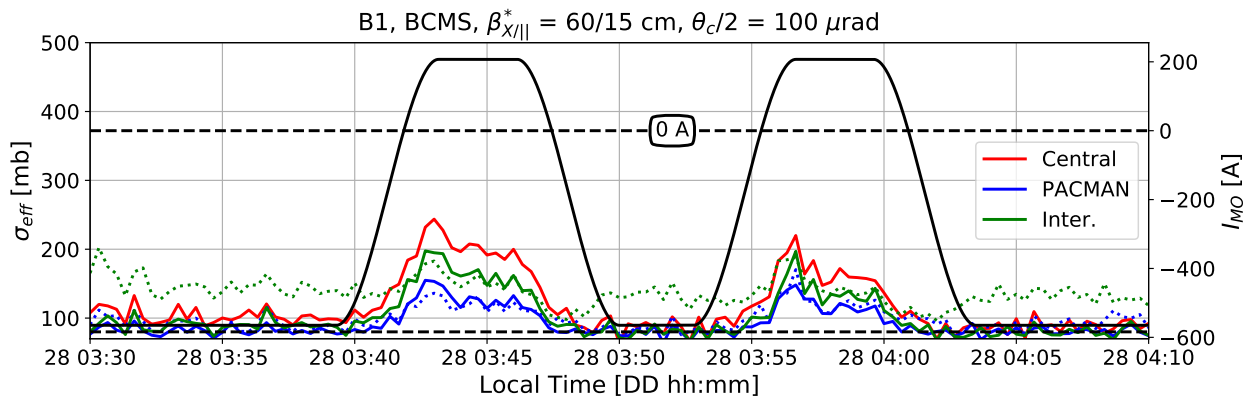


Figure 4.22: Evolution, in time, of the effective cross-section of a collection of bunches included in the BCMS train of Beam 1, during the octupoles current scan at $\theta_c/2 = 100 \mu\text{rad}$.

As one can see in these Figures, the octupoles are not strong enough to mitigate completely the BBLR interactions in this aggressive situation, especially for B2, for which the effective cross-section of the central bunch is already at a level of about 300 mb before the polarity change. The fact that the octupoles seem weaker than with round optics is perfectly understood, as with flat optics, only 25 % of them are enhanced by the ATS scheme (compared to 50 % with round optics, with the same telescopic index). The relative tune spread increase is therefore reduced and the mitigation of the BBLR interactions is then more difficult. In order to gain more in terms of BBLR compensation, one could power the wire compensators, gaining additional tune spread and further reducing the effect of the BBLR interactions. However, no time was left during this experiment to perform such a test. Moreover, with the crossing bumps rotations, the wires would be installed in the *wrong* plane. This inversion would not change the octupolar components, but other RDTs would be affected. Nevertheless, this confirms the possibility of operating the machine

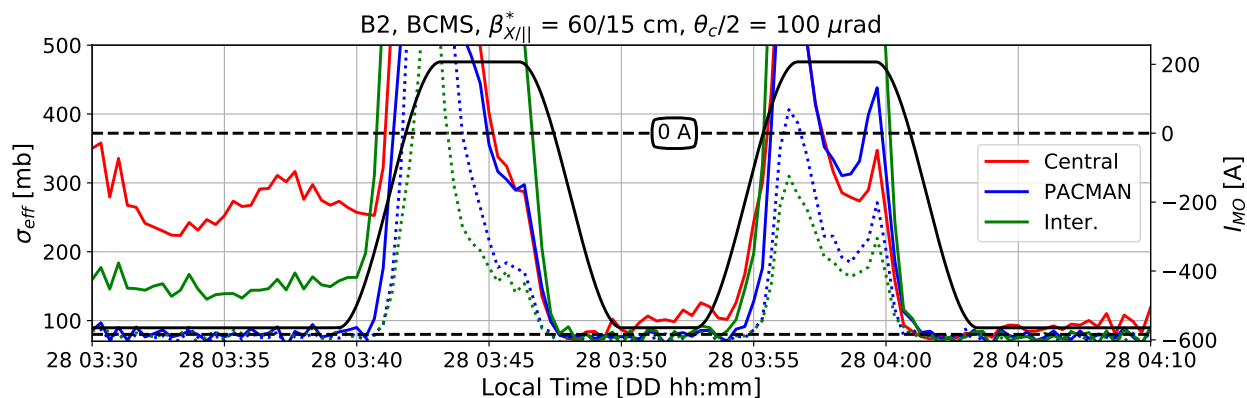


Figure 4.23: Evolution, in time, of the effective cross-section of a collection of bunches included in the BCMS train of Beam 2, during the octupoles current scan at $\theta_c/2 = 100 \mu\text{rad}$.

with flat optics, and wire compensators, in the HL-LHC era. This is considered as a back-up option in case the crab cavities development would fail.

4.4 CONCLUSIONS

During the 2017-2018 LHC Run 2, in parallel to the wire demonstrators experiments, a complementary experimental program was carried out in order to demonstrate the feasibility of deploying the ATS scheme with high tele-index in the LHC, for both round and flat optics.

During this experimental program, it was shown that the ATS scheme, by increasing the efficiency of the negative Landau octupoles in the arcs, gives them the possibility to mitigate the BBLR interactions. With round optics, the octupoles were demonstrated to be strong enough to achieve such a mitigation, even in very aggressive configurations in terms of BBLR interactions, going down to a crossing angle of $95 \mu\text{rad}$ without spoiling the beam lifetime. The corresponding simulations with high tele-indexes were not carried out yet for the LHC. In the HL-LHC, simulations have been carried out [138], but did not show a clear effect of the octupoles on the BBLR interactions without the use of the wire compensators. However, the combination of the octupoles with the wires could significantly improve the dynamic aperture.

In the case of flat optics, the relative increase of the octupoles efficiency is known to be reduced compared to the case with round optics. However, encouraging results were obtained in terms of BBLR mitigation. Nevertheless, in order to fully recover from a configuration where the BBLR interactions are strong, the use of the wire compensators would have been needed, but no time was left to try this out and the wires were sitting in the wrong plane, leading to the impossibility to target the compensation of all the RDTs.

These experiments confirmed to the possibility of deploying such schemes for the LHC Run 3, or for the HL-LHC era. For the HL-LHC, the present baseline assumes a round optics ATS scheme in order to reach the wanted β^* (10-15 cm) and the crab cavities in order to cope with the BBLR interactions. The wire compensators would therefore be installed to mitigate the residual BBLR interactions still present, as the normalized crossing angle remains low. Additionally, and in case the crab cavities would not be installed in the HL-LHC eventually, the use of flat optics with the BBLR compensation using the DC wires remains a good machine configuration in terms of luminosity performance.

5 TOWARDS OPERATION WITH THE WIRE COMPENSATORS FOR THE LHC RUN 3

At the end of 2018, the LHC was shut down, for a two years long period during which upgrades were planned to take place in view of the upcoming LHC Run 3. The LHC was planned to be recommissioned in 2021, although it is now foreseen to inject protons in the machine only in 2022, due to the pandemic and its impact on the activities. Once recommissioned, the LHC is foreseen to enter a three years period of physics production before a new long shutdown. This three years period is called LHC Run 3 and is the main focus of this Chapter. After a presentation of the current status of the foreseen operational scenario, we present the numerical implementation of the wire compensators during this run, together with a collection of tracking simulations results for the LHC Run 3 operation with the wires.

After the very positive results obtained during the 2017-2018 LHC experimental program, it was in fact decided to use the wire compensators also in Run 3, equipping Beam 1 with the two unused wire collimators of Beam 2. The objective of the use of wire compensators during the LHC Run 3 is to gain operational experience in view of the HL-LHC era, more than gaining integrated luminosity. It also represents a unique opportunity to draw conclusions about the possible design of the new hardware to be built for the HL-LHC.

5.1 RUN 3: FORESEEN OPERATIONAL SCENARIOS AND PERFORMANCES ESTIMATES

5.1.1 LHC RUN 3: OBJECTIVES AND CHALLENGES

The transition between LHC and HL-LHC has been split in two in order to manage the different technical aspects of this upgrade. The goal of the Long Shutdown 2 (currently on-going in 2021) was to focus on the injector complex. The LIU project has been successfully carried out, and the injectors are now ready for the HL-LHC era. During the Long Shutdown 3 (LS3) (foreseen to take place between 2025 and 2027), the LHC will be upgraded (change of the Inner Triplet, installation of the 11 T dipoles, etc...).

The foreseen restart of the LHC in 2022 coincides with the completion of the LIU project. The LHC injector chain will then be able to deliver bunches with almost twice the brightness of the LHC Run 2 bunches. However, and as mentioned previously, the LHC will be upgraded during LS3. Therefore, in order to cope with the hardware limitations, and to search for solutions for the LHC to be compatible with such beam parameters, the LHC Run 3 Configuration Working Group was formed. A summary of its work can be found in [139].

The beam intensity ramp up in the injectors chain is foreseen to be gradual over the three years period of the LHC Run 3, starting with a nominal bunch intensity of $1.4 \cdot 10^{11}$ protons in the first year, up to $2.1 \cdot 10^{11}$ protons by the end of the last year. The LIU ramp-up will then continue as the LHC shuts down during LS3 in order to be ready to accept bunches with the nominal intensity of $2.3 \cdot 10^{11}$. For Run 3, the BCMS beams are considered as baseline as those beams present several advantages such as a mitigation of the cryo-cooling capacity needed to cope with the heat load generated by the electron cloud effect in the LHC arc. They also feature smaller emittances, and therefore higher brightnesses. However, a combination of BCMS and 8b4e trains is also under investigation in order to mitigate even more these effects [140, 141]. Taking into consideration all the LHC systems limitations, the maximum bunch

intensity acceptable during the LHC Run 3 has been limited to $1.8 \cdot 10^{11}$ protons. Such a bunch population was assumed to be reached by the end of 2022, even though the current delays might have an impact on this plan.

Different physical and technical aspects have to be addressed when planning to inject bunches with an intensity about 50 % higher than the one used in Run 2. Without entering the details, one can mention the emittance blow-up due to Intra-Beam Scattering (IBS) [142] and Synchrotron Radiation (SR) [143, 144], coherent stability [145] (mostly from an impedance [146, 147] point of view) and the heat load generated in the two rings, as already mentioned. Another critical concern for the LHC Run 3 operation is the luminosity lifetime of the Inner Triplets in IR1 and IR5. Simulations have, in fact, shown that some of the quadrupoles coils have been highly irradiated already, bringing them to half of their lifetime [148]. Loosing a quadrupole of one of the Inner Triplets cannot be tolerated as no spare piece was built. Protecting the IT until their replacement during LS3 is, therefore, of primary importance.

As already mentioned in the previous Chapters, two main options in terms of optics are foreseen for the operation of the LHC during Run 3. The first one is the well known round optics. With such a scheme, the only parameter that could possibly be changed in order to reduce the deposited dose on the Inner Triplet is the polarity of the crossing angle in IR1 (vertical crossing). This option has already been tested during Run 2. However, such a scheme would not prevent the IR5 Inner Triplet to be irradiated. The other option is to use flat optics. As mentioned in Chapter 4, the use of flat optics yields an inversion of the crossing plane between IR1 and IR5. By doing so, different parts of the coils will be irradiated, therefore increasing the lifetime of the Inner Triplet. Finally, one critical parameter, regardless the chosen option, is the absolute value of the crossing angle. The higher the crossing angle, the higher the deposited dose in the Inner Triplet. The target for any operational scenario during the next LHC Run 3 would therefore consists in keeping the crossing angle as low as possible without reducing the beam performance. The wire compensators could help on this aspect, allowing to operate with a lower crossing angle, especially at the end of each fill where the crossing angle reaches its maximal value. This aspect is presented in the following Sections.

5.1.2 FIRST PERFORMANCE ESTIMATES

During the Run 3, the LHC is assumed to operate at an energy of 7 TeV [149], in comparison to the 6.5 TeV of the Run 2. At the time of writing, two types of beams are considered for the operation of the machine during the Run 3. The first one is the typical BCMS beams, providing 2736 collisions at the high luminosity IPs, and emittances of 2.5 mm.mrad. In case of issues with electron cloud effects and heat load in the arcs, an alternative mixed filling scheme, composed of BCMS trains and 8b4e ones is also foreseen. Using this second option, the number of collisions in IP1 and IP5 would be reduced down to 2484. However, the baseline configuration remains the BCMS beams. The expected emittances evolution during a fill can be computed from the IBS and SR dynamical models, together with the experimental observations during the LHC Run 2 [150].

Finally, the luminosity is foreseen to be leveled at $2 \cdot 10^{34}$ Hz/cm² by squeezing β^* from about 1 m down to 28 cm. In order to minimize the impact on the Inner Triplet irradiation, the crossing angle is adjusted accordingly. This leveling is foreseen to last for about 11 h. Assuming a burn-off cross-section at 7 TeV of 110 mb, and a turnaround time (time in between two fills) of about 4 h, the optimal fill length should be around 14 h, giving an integrated luminosity of about 1.3 fb^{-1} per day. The corresponding typical profiles for the luminosity, crossing angle, β^* and emittances are displayed in Figure 5.1.

In the case that flat optics would become the preferred option, the leveling is foreseen to start with round optics, with both the β -functions at the IP set to 50 cm [134]. During the leveling, one of the β^* will be gradually reduced down to 15 cm while the other would remain at the same value. The gain in terms of integrated luminosity is expected to be about 1.5 % and more details can be found in [139].

5.1.3 WIRE COMPENSATORS: CHANGE OF LAYOUT

The results of the experiments obtained in 2017 and 2018 and reported in Chapter 3 have demonstrated the possibility to mitigate the BBLR interactions with DC wires, installed on Beam 2. Despite the original choice of settings -

5.1 Run 3: Foreseen Operational Scenarios and Performances Estimates

IBS+SR+Extra Growth H = 0.05 $\mu\text{m}/\text{h}$ & V = 0.10 $\mu\text{m}/\text{h}$ | Leveling at $2.0 \times 10^{34} \text{ Hz}/\text{cm}^2$
 $N_{1,2} = 1.80 \times 10^{11}$ pbb, $\phi/2 = 109 \mu\text{rad}$, nb = 2736, $\beta_0^* = 1.0$ m, $\epsilon_n^{x,y} = 2.50 \mu\text{m}$, $\sigma_{bOff} = 110$ mb, $\sigma_{inel} = 81$ mb

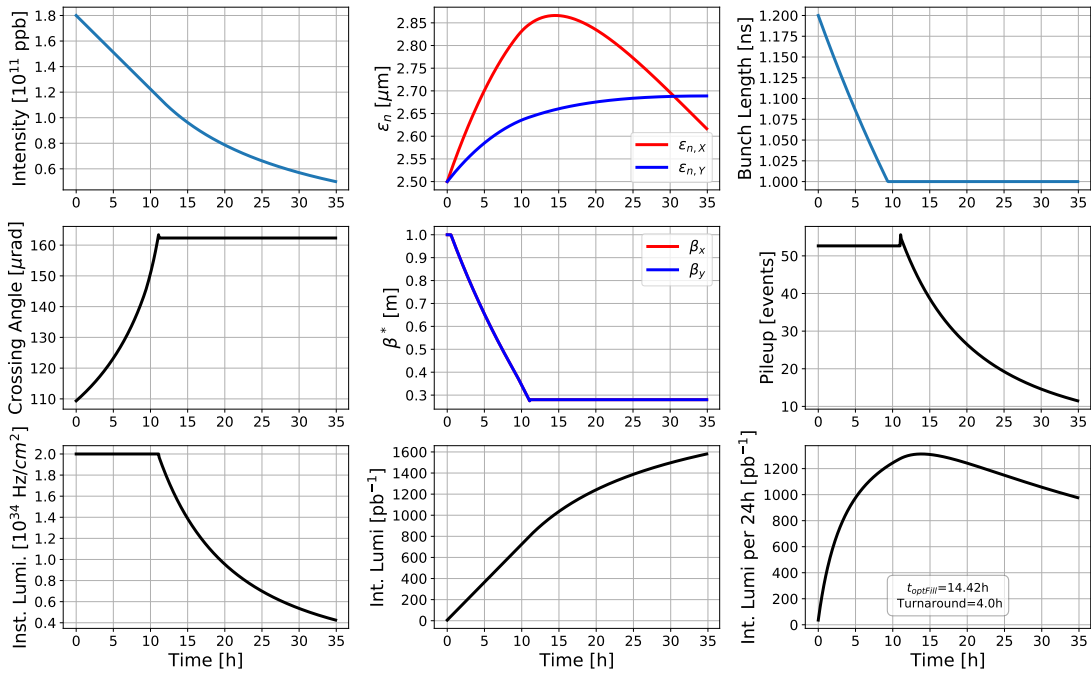


Figure 5.1: First performance estimates for the LHC operation during the next LHC Run 3. From left to right, and from top to bottom: evolution of the beam intensity, horizontal and vertical emittances, bunch length, half crossing angle, β^* , pileup, instantaneous luminosity, integrated luminosity and integrated luminosity per 24 h, as a function of time.

compensating all the RDTs driven by the BBLR - described in Chapter 2, and requiring two wires per IP, the High Intensity experiment showed that we could observe the beneficial effect of the wires in terms of beam losses by using only one wire per IP. Consequently, it was decided to change the wire compensators layout by moving the two unused wire collimators from Beam 2 to Beam 1. The resulting layout is displayed in Figure 5.2, showing an out-of-scale scheme of the LHC rings as foreseen during the LHC Run 3.

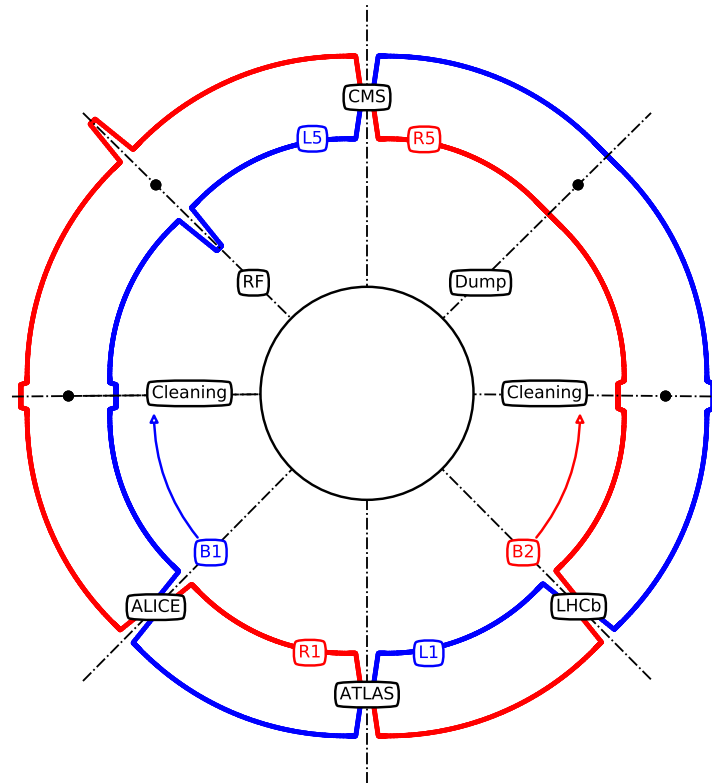


Figure 5.2: Schematic view of the LHC ring configuration during the LHC Run 3. Beam 1 is represented in blue while Beam 2 in red. Two out of the four B2 wire compensators are now installed on B1.

During the LHC Run 2 and the experimental campaign, the wire compensators were considered as demonstrators, and only required an initial validation with a pilot beam when changing configuration, as described in particular in Chapter 3 for the High Intensity experiment. During the LHC Run 3, the wire compensators will be considered as operational devices. The implications of such a statement are important, as it means that the wires will be powered while high intensity beams are circulating in the machine. The most important one is the fact that a wire failure has to trigger a beam dump. Stopping the wires themselves while operating with high intensity beams is not a real problem per se. However, the tune feed-forward system (see, Chapter 3) would remain active after the wire failure, inducing an important tune shift, and an important β -beating wave. This would affect the phase advance between the tertiary collimators and the extraction kickers, potentially leading to important damages in the eventuality of an asynchronous dump (never occurred in the LHC in nominal operation at the time of writing). The different possibilities of wire failures are the following [151]:

- Failure of the power converters.
- Wire overheating: as already mentioned, the heat produced by the Joule effect in the wires is important (about 1 kW) and must be accounted for. It is therefore foreseen to dump the beams in case the jaw temperature exceeds 50°C at the position of the temperature probes.

- Failure of the control card of the wires.
- Electrical circuit opening, for instance, a loss of electrical contact at the wire connector or a damaged cable.

Consequently, a commissioning procedure [152] was prepared and the wires commissioning will be carried out taking into account the aforementioned points.

5.2 NUMERICAL OPTIMIZATION OF THE WIRE COMPENSATORS SETTINGS

As it was done for the LHC Run 2, the technicalities of the implementation of the wires during the next LHC Run 3 are firstly determined numerically. The critical point of this implementation lies in the design of a reliable tune feed-forward system.

During the next LHC Run 3, the wires are planned to be powered at the end of each fill, at the end of the β -leveling ($\beta^* = 30$ cm, $\theta_c/2 = 158$ μ rad). In this configuration, the wire collimators are foreseen to be opened at $8.5 \sigma_{coll}$ [153] and the 2-jaws configuration will consequently be used for the wire powering. The corresponding transverse beam-wire distances are reported in Table 5.1.

Beam	Wire	Dist. from IP [m]	Plane	d_w [mm]
B1	L1	-145.94	V	9.1
	L5	-147.94	H	12.23
B2	R1	145.94	V	9.1
	R5	147.94	H	12.23

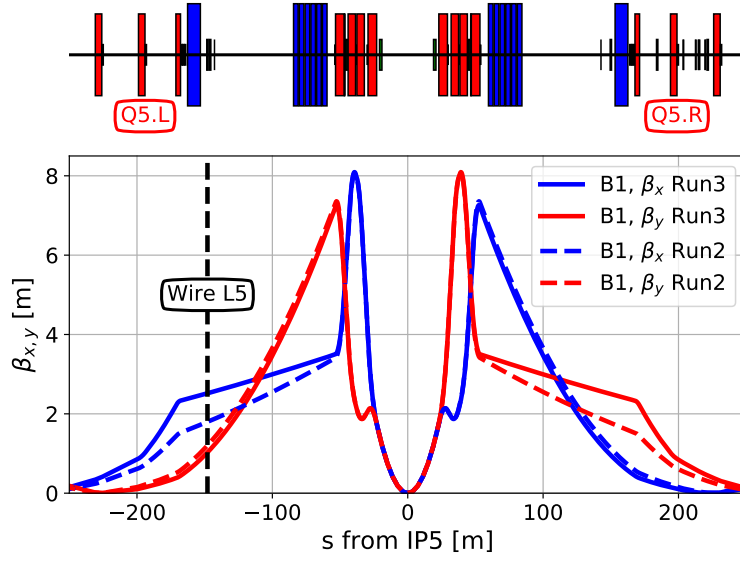
Table 5.1: Wires settings for the next LHC Run 3.

The tune shifts induced by the wires with these settings are presented in Table 5.2 and must be compensated.

Beam	Wire	ΔQ_x	ΔQ_y
B1	IR1	$1.46 \cdot 10^{-2}$	$-6.33 \cdot 10^{-3}$
	IR5	$-8.02 \cdot 10^{-3}$	$5.9 \cdot 10^{-3}$
B2	IR1	$-1.46 \cdot 10^{-2}$	$6.33 \cdot 10^{-3}$
	IR5	$8.02 \cdot 10^{-3}$	$5.91 \cdot 10^{-3}$

Table 5.2: Maximum expected wire induced tune shifts during the next LHC Run 3.

During the LHC Run 2, and as already presented in Chapter 3, this feed-forward made use of the nearby quadrupoles Q4 and Q5 for each wire. The applied strength variation in these quadrupoles was linear with the considered wire current, allowing for a smooth and successful implementation during the experiment. The proximity of these quadrupoles with the wires also allowed to minimize the induced β -beating wave. However, during the next LHC Run 3, the use of higher tele-indexes yields an increase of the β -functions in the arcs. The arc sextupoles become thus more effective and for the same relative β -beating, the impact on the chromaticity is larger. Such effects have been observed numerically while dimensioning a feed-forward system for the wires in Run 3 with the use of MAD-X. Moreover, as one can observe in Figure 5.3, the β -functions at the Q5 location are lower than in the case of the LHC Run 2 and therefore, do not scale linearly with the reduction of β^* . Without this linear scaling, the tune feed-forward system depends on the tele-index. During Run 2, the β^* excursion was negligible or even absent. However, the LHC Run 3 is based on a β^* leveling of the luminosity. Even though the wires are planned to be powered only after this leveling at the moment of writing, having a tele-index independent feed-forward system would be profitable for the future.


 Figure 5.3: Comparison of the β -functions around IP5 for B1, between Run 2 and Run 3.

For these reasons, a new tune feed-forward system is proposed for the next LHC Run 3. This new system profits from the two Q4 quadrupoles, located on each side of the IP. The phase advance between the two is very close to π : the β -beating induced by the correction is thus limited, and so are the chromatic effects. The approach to design such a feed-forward is strictly the same as the one described by the Eq. (3.1 - 3.5). The relation between the Q4 strengths and the wire currents can thus be written:

$$\begin{aligned}
 k_{Q4}^{L1} &\approx 3.486 \cdot 10^{-3} - 2.257 \cdot 10^{-5} \frac{I_{w1}/(350 \text{ A})}{(d_{w1}/(9.1 \text{ mm}))^2} \\
 k_{Q4}^{R1} &\approx -3.486 \cdot 10^{-3} - 6.229 \cdot 10^{-5} \frac{I_{w1}/(350 \text{ A})}{(d_{w1}/(9.1 \text{ mm}))^2} \\
 k_{Q4}^{L5} &\approx 3.486 \cdot 10^{-3} + 1.233 \cdot 10^{-5} \frac{I_{w5}/(350 \text{ A})}{(d_{w5}/(12.23 \text{ mm}))^2} \\
 k_{Q4}^{R5} &\approx -3.486 \cdot 10^{-3} + 3.169 \cdot 10^{-5} \frac{I_{w5}/(350 \text{ A})}{(d_{w5}/(12.23 \text{ mm}))^2},
 \end{aligned} \tag{5.1}$$

where Beam 1 is taken as an example, but similar relations can also be obtained for Beam 2. Figure 5.4 displays graphically the obtained relations for Beam 1. From an operational point of view, one can get an important insight from these relations. The Q4 quadrupoles are in fact not supposed to be trimmed during the operation of the machine. A variation of their current would induce a beam dump. The margin would therefore have to be opened in order to accommodate the current excursion due to the feed-forward system. However from Eq. 5.1, and assuming the wires to be powered at their maximum current (350 A) at their nominal distance (collimators at 8.5σ , see Table 5.1), one can see that the required trims represent less than 1% of the nominal Q4 currents, which is perfectly acceptable from a machine protection point of view.

The triangular markers indicate the values obtained numerically using MAD-X while the solid lines illustrate the analytical expected values, derived in the perturbative approximation. The knobs are perfectly linear with the wire currents, indicating already that the induced β -beating is moderate. A summary of the implementation of this new feed-forward system, in term of tunes and chromatic effects, is presented in Figure 5.5a and Figure 5.5b for

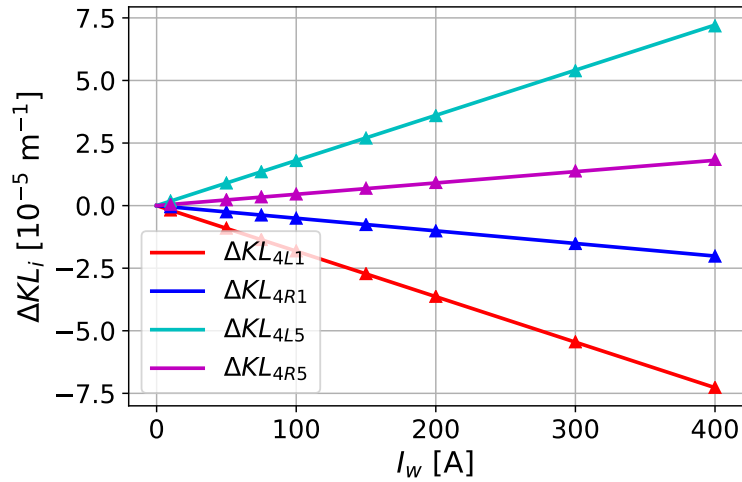


Figure 5.4: Tune feed-forward implementation using the two Q4 quadrupoles in the case of Beam 1: quadrupoles strengths variation as a function of the wires current.

Beam 1 and Beam 2 respectively. The residual tunes and chromaticity offsets are considered within the machine reproducibility.

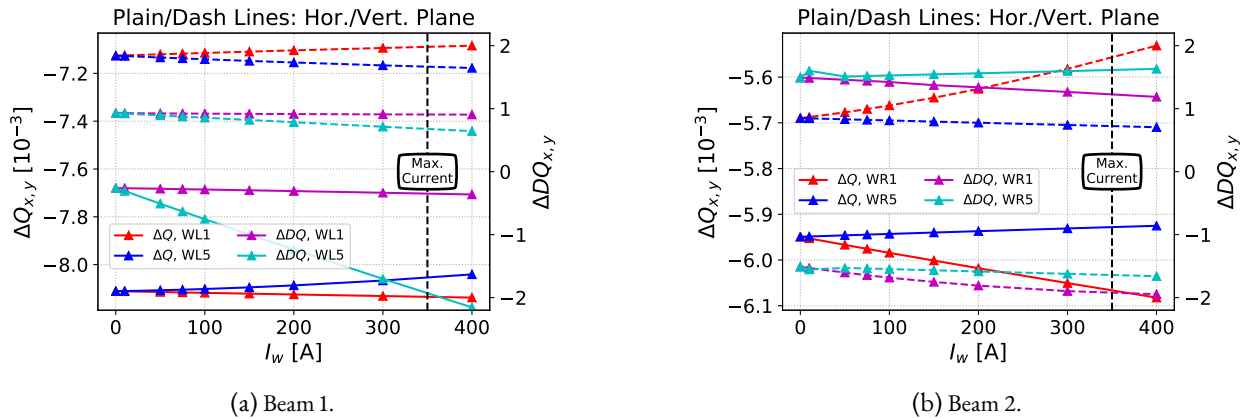


Figure 5.5: Effect of the wire compensators and their feed-forward system for the next LHC Run 3: residual tune shifts as a function of the wires current.

In these Figures, the tunes variations are represented in red and blue for the IR1 and IR5, respectively, while the chromaticities variations are represented in magenta and cyan for the IR1 and IR5, respectively. The solid lines are used for the horizontal plane while the dash lines are used for the vertical one.

Several other aspects (orbit distortion, dispersion shift, etc...) have to be checked in order to fully validate the compatibility of the wire compensators feed-forward system with the nominal operation machine protection concerns. The detailed list of those checks together with detailed figures are reported in [154]. One of the most important check to be verified is the β -beating induced by the wires and their feed-forward system. Figure 5.6 shows the maximum β -beating obtained as a function of the wires current, in the case of Beam 2.

The beating induced by the wires in IR1 is represented in blue while the one induced by the wires in IR5 is drawn in red. The solid and dash lines correspond to the horizontal and vertical planes respectively. The obtained values are low in comparison to the beating induced by the beam-beam interactions and are therefore acceptable. As a comparison, a typical tune trim of about 10^{-2} in both planes induces a maximum β -beating of about 0.5 %.

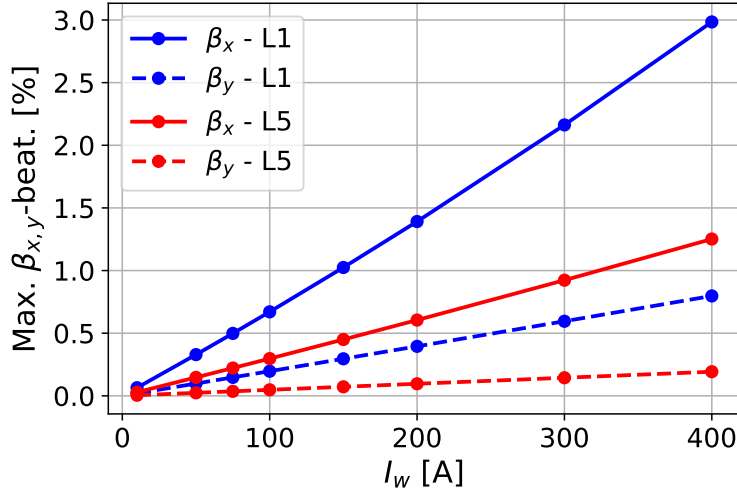


Figure 5.6: Maximum β -beating induced by the wires and their feed-forward system, as a function of the wires current, in the case of Beam 2.

Finally, the location of the maximum β -beating is also important. In the case of the wires and their feed-forward, this maximum is always reached around the considered IP (about 25 cm from the IP), close to the luminous region. In this region, the aperture margin is significant and the effect on the luminosity is expected to be minor (however, it should be quantified numerically, as requested by the Machine Protection Panel). Similar results can be obtained in the case of Beam 1.

In terms of orbit distortion, a maximum orbit shift of about 100 μm is expected around the IPs as well, due to a feed-down effect from the trimmed Q4 quadrupoles (the Q4 quadrupoles are located within the crossing bump). This orbit shift should be significantly mitigated by the LHC closed orbit feedback system. The horizontal and vertical dispersions are also affected, but the effect of the wires and their feed-forward is negligible (a shift of about 4 mm is expected, in comparison to the nominal dispersion that is of the order of a few meters). Moreover, a critical point from a machine protection point of view is the phasing between the tertiary collimators and the extraction kickers, in case of an asynchronous dump. It has therefore been verified that the wires and their feed-forward only affect this phasing by less than 0.1 degrees, which is well within the tolerances.

As mentioned in the motivations for this new tune feed-forward of the wires, it should be ATS independent so that the wires can be used at any time during the β^* -leveling. Figure 5.7 shows the remaining tune shifts (compared to the nominal working point) with respect to the tele-index (wires powered at 350 A, 2-jaws configuration).

This figure shows the example of Beam 1, but the same results are also observed for Beam 2. The obtained remaining tune shifts are within the machine reproducibility, confirming that the tune feed-forward system is ATS independent.

Until now, we dealt with an ideal implementation of the tunes feed-forward system, assuming a perfect alignment of the wires with the beam. However, in the LHC, non-idealities can occur. Other checks have therefore been carried out, especially in the case of a possible misalignment of the wire collimator. For all the types of misalignments (non-centered beam, collimator gap error, 5th-axis), minor effects are expected on all the parameters, apart from the tunes, for which shifts up to about 10^{-3} were observed for important misalignments (order of 1 mm).

Finally, the ramping time of the wire has to be determined such as it does not exceed the Q4 one. An asynchronous ramp of the wires and their tune feed-forward would, in fact, induce an important β -beating wave propagating along the machine, causing possible beam losses, and, eventually, triggering a possible beam dump. The ramp should be within the bandwidth of the LHC orbit feedback system so that possible orbit distortions due to feed-down effects could be mitigated. Consequently, a ramping time of about 1 min was found to be acceptable, as shown in Figure 5.8.

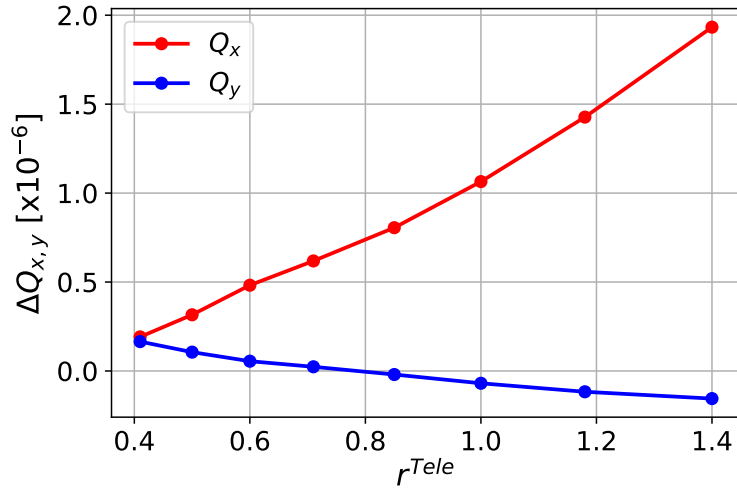


Figure 5.7: Residual tune shifts with the wires on as a function of the tele-index (Beam 1 case).

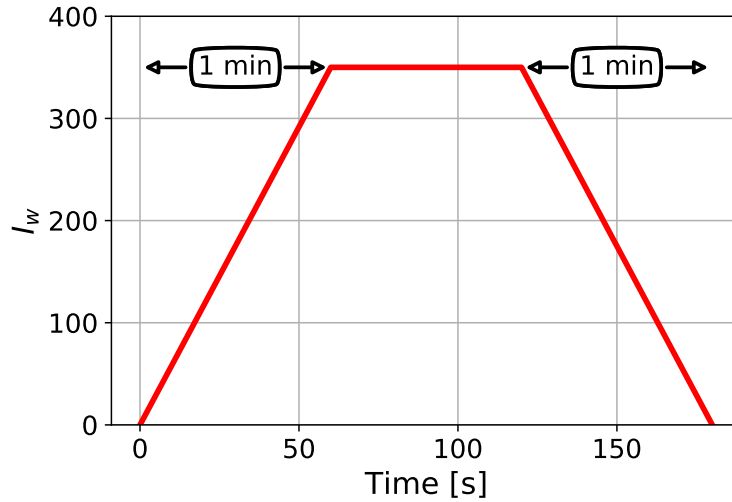


Figure 5.8: Proposal for the wires ramping time.

Using this setup, the next Section describe the work done in terms of tracking simulations for the wire compensators during the LHC Run 3.

5.3 WIRE COMPENSATORS IN THE NOMINAL SCENARIO

In this Section, we explore the potential of the wire compensators within the context of the previously described operational scenario, foreseen for the LHC Run 3. The corresponding parameters are recalled in Table 5.3 (end-of-fill, after the β -leveling). These parameters are used systematically in the following, unless specified otherwise.

The indicated number of turns corresponds, as in the previous chapters, to the the maximum number of turns the particle will do in the machine during the tracking simulations. In the case of the LHC, this corresponds to about 90 sec of actual machine time. It is worth noting that as during the Run 2, the polarity of the octupoles was positive, which is not the favorable situation in terms of BBLR mitigation (see, Chapters 3 and 4). Finally, as in the previous

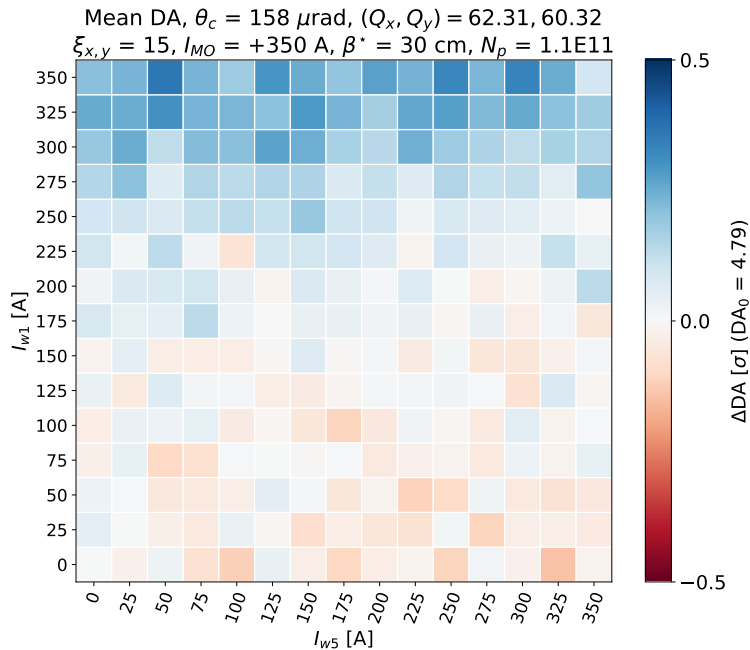
Parameter	Symbol	Reference value
Bunch Intensity	N_b	1.1×10^{11} p
β -function at the IP	β^*	30 cm
Tele-Index	r^{Tele}	3.3
Half crossing-angle	$\theta_c/2$	158 μ rad
Tunes	Q_x, Q_y	62.31, 60.32
Chromaticities	$\xi_{x,y}$	15
Octupole Current	I_{MO}	+350 A
Wire Coll. Opening		$8.5 \sigma_{coll}$
Number of turns		10^6

Table 5.3: Simulations parameters for the nominal operation of the wire compensators in the LHC Run 3

chapters, only Beam 1 is tracked. However, differently than in the previous simulations results, we consider hereby HO collisions and BBLR interactions in all the four IPs.

5.3.1 DYNAMIC APERTURE AND WIRE CURRENTS

The first study to be carried out concerns the only free parameter of the wire compensators during the next LHC Run 3, which is their current. Figure 5.9 thus shows the DA variation with the wire currents.


 Figure 5.9: DA variation as a function of the wire currents for the LHC Run 3. The wire collimators are opened at 8.5σ

The use of the wires can improve the average DA by about 0.35σ but this effect is mostly due to the wires located in IR1. One can in fact observe that the wires in IR5, if powered alone, cannot improve the DA and even seem to degrade it. This difference can be explained by the beam-wire distance, that is larger in the case of the IR5 wires. The DA improvement is maximized by powering the wires in IR1 with 350 A, and the wires in IR5 to 50 or 300 A. This will therefore be the reference study points in the following. With such small DA fluctuations, it is important to

verify that these variations are not due to other effects than the wires, as residual tunes or chromaticities shifts. In this respect, Figure 5.10 shows the variations of the computed tunes and chromaticities during the wires currents scan.

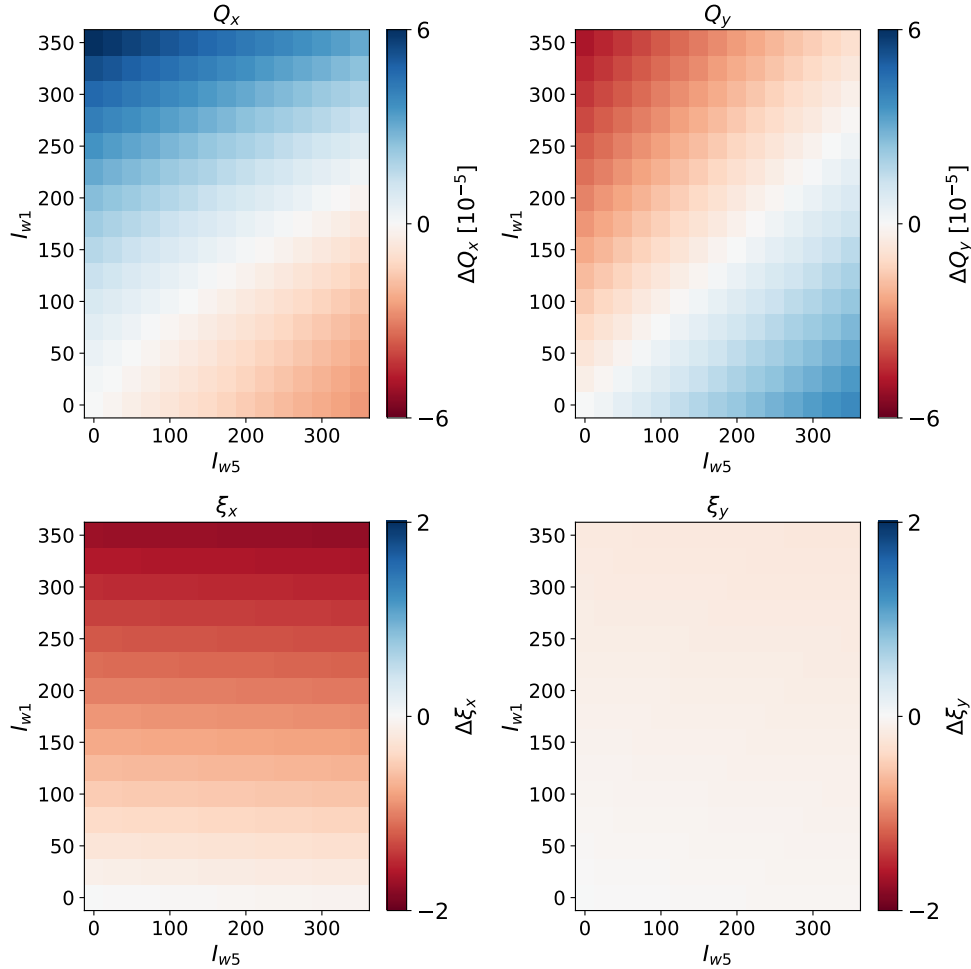


Figure 5.10: Sanity checks for the tracking simulations in the context of the LHC Run 3: tunes and chromaticities as a function of the wires currents.

One can observe a maximum tune shift of about $5 \cdot 10^{-5}$ in both planes. Such shifts are considered to be negligible in terms of DA variation. However, the horizontal chromaticity (shift of about two units) seems correlated to the DA variations observed in Figure 5.9. This observation is consistent from a physics point of view as the DA is improved when the chromaticity is reduced. During the LHC operation, the chromaticities are not corrected, and a shift of 2 units would be tolerated from a machine protection point of view. However, in order to draw conclusions about the beneficial effect of the wires in these simulations, a correction of the chromaticity would be required.

To complete the study displayed in Figure 5.9, one can plot the DA variation in the parameters configuration space, as shown on Figure 5.11.

Several configurations are considered in this Figure. The first one represents the situation without the wires (in red). The average is DA is 4.79σ and the horizontal/vertical asymmetry observed in the simulation for Run 2 is less evident. The second configuration corresponds to the wires powered only in IR5 at 325 A (in blue). One can see that the red and blue lines almost overlap, but that in the case of the wires in IR5 only, some drops are observed, in the horizontal plane and around 45° , reducing the average DA by 0.14σ . The situation with the wires powered only in IR1 (325 A) is represented in green. The DA is mostly improved in the vertical plane (plane where the wires in IR1

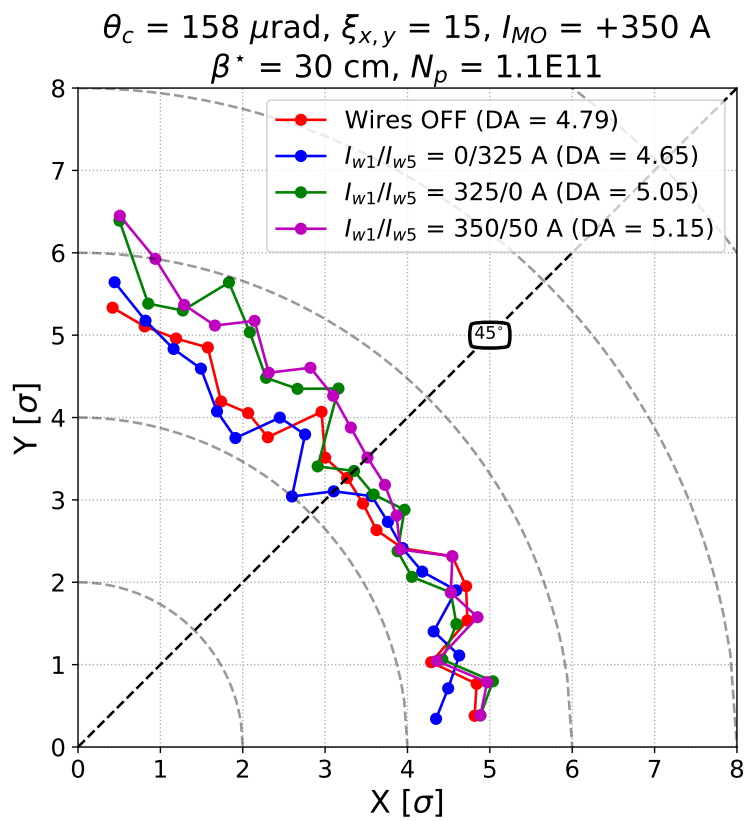


Figure 5.11: Dynamic aperture in the configuration space, for different configurations (no wires, wires in IR1 or IR5 only, and wires in both IRs).

are installed), increasing the average DA by 0.26σ compared to the situation without wires. Finally, the optimal situation observed from Figure 5.9 is shown in magenta and is very similar to the situation with only the wires in IR1 powered. An additional improvement around the 45° line yield an increase of the average DA by 0.36σ , which is the best we can obtain from the scan that was carried out. As observed with the Run 2 simulations, the DA improvement is in general observed for angles higher than 45° . Above the 45° line, the observed DA improvement reaches the order of 1σ , while below, it is close to zero.

The difference between these configurations can also be observed in the tune footprints. Figure 5.12 shows the different tune footprints for the four different situations described previously.

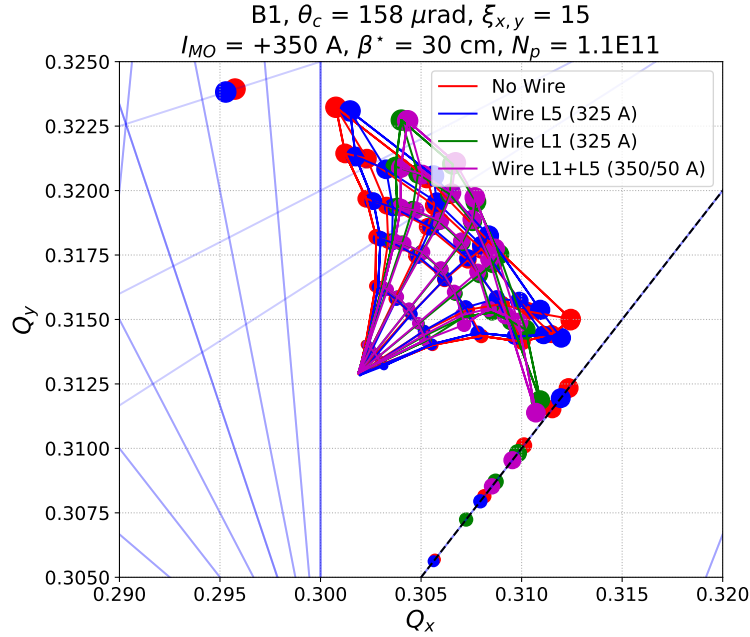


Figure 5.12: Tune footprints, for different configurations (no wires, wires in IR1 or IR5 only, and wires in both IRs).

The color code of the footprint follows the one of Figure 5.11. As for the DA, one can observe that the wires in IR1 are more efficient in terms of footprint effect, especially for the high amplitude particles. The compression of the footprint is slightly improved by adding the wires in IR5 with 50 A. However, like for the DA, the latter do not affect significantly the footprint compression. Some particles are trapped on the diagonal while some others are trapped on the 3^{rd} -integer resonance line. This last observation could be a possible explanation for the slight observed DA degradation.

5.3.2 TUNE SCANS

As for the LHC Run 2, one can study the impact of the tunes on the wires effect on DA. This section reports simulation results for tune scans around the nominal working point. Figures 5.13a and 5.13b show such tune scans with the wires OFF and ON respectively.

In this configuration, the wires improve the DA around the nominal working point and towards the diagonal. The opening of the tune space creates a more comfortable area to accommodate additional non-linear effects such as beam-beam interactions or electron clouds effects, inducing a bunch-by-bunch parameter spread. With or without wires, it seems that - as during the LHC Run 2 - an optimal working point can be found in order to improve the DA of the machine. Typically, moving slightly the working point towards the diagonal ($\Delta Q_x = +0.001 / \Delta Q_y = -0.001$) can improve the DA by about 1σ . The use of the wire could reduce this needed tune shift, therefore remaining as far

5 Towards Operation with the Wire Compensators for the LHC Run 3

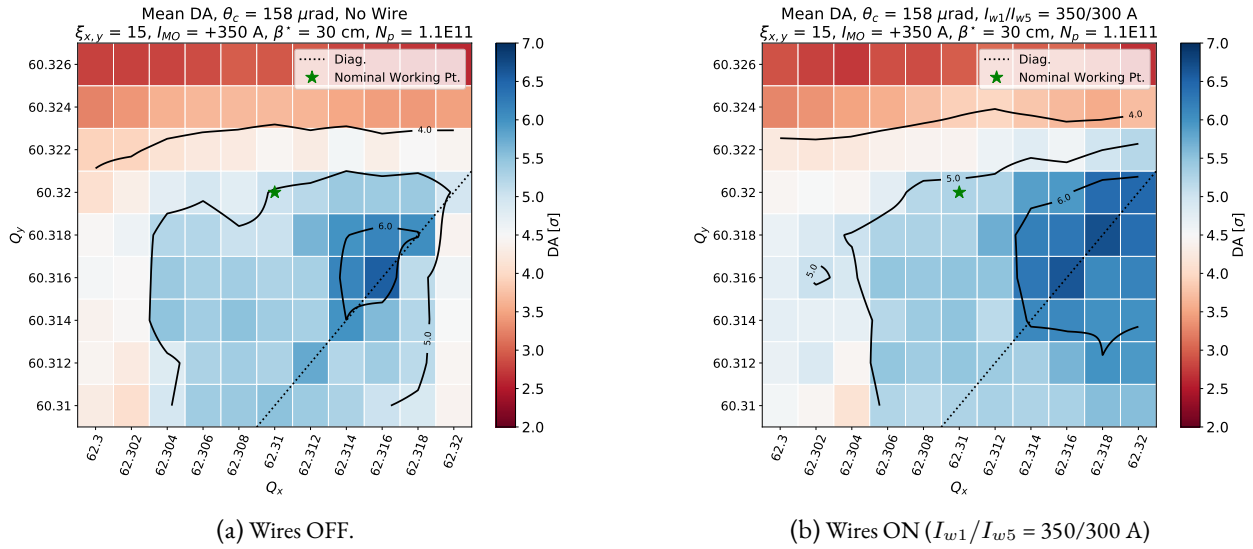


Figure 5.13: Dynamic aperture as a function of the horizontal and vertical tunes, with and without wire compensation, for the LHC Run 3.

as possible from the diagonal, which is always preferable in order to avoid losing high amplitude particles as they cross the diagonal (as seen previously on the footprints).

Finally, similar sanity checks have been led, as in the previous Section, in order to determine if the observed DA fluctuations are due to the wires effect or to possible tunes or chromaticities shifts. In these studies, the final chromaticities do not depend on the working point, except on the diagonal, where a slight shift of about one unit is observed. In terms of tunes, the final tunes computed by MAD-X include the tune shift induced by the beam-beam interactions, as well as the wires and their feed-forward (if present). The tune shift induced by the beam-beam interactions depends on the working point. However, by making the difference between the final tunes computed for the configurations with and without wires, one can observe the residual tunes and chromaticities shifts induced by the β -beating due to the wires and their feed-forward system. Figure 5.14 shows this difference for both horizontal and vertical tunes and chromaticities.

One can see that the residual tune shifts are constant and at the level of 10^{-5} . However, a constant horizontal chromaticity shift of about two units is again observed. Nevertheless, this shift does not depend on the working point, while the DA fluctuations observed in Figure 5.13 do. As for the wire currents study, a correction of the chromaticity in the simulations would be required.

5.3.3 WIRE COMPENSATION AND LANDAU OCTUPOLES

As presented in the introduction of this Chapter, the LHC is foreseen to operate with positive Landau octupoles during the Run 3, even if this would not provide a possible mitigation of the BBLR effects. The baseline current is set to +350 A. This value should ensure a tune spread large enough to keep the beams stable in operation. However, following the experiments carried out during the LHC Run 2 with high tele-indexes (see, Chapter 4), the study of the impact of negative octupoles with the wires is also considered in the case of the Run 3. Moreover, no compensation pattern emerges from Figure 5.9. This seems to exclude the possibility of a resonance compensation mechanism and the beneficial effect of the wires could thus be translated in terms of linear detuning with amplitude, as shown on the previous footprints. In that respect, Figure 5.15 shows the dependency of the average DA on the wires currents (assuming $I_{w1} = I_{w5}$) and the Landau octupoles currents.

Taking into consideration the contribution of the BBLR interactions, the octupoles and the wires, it is possible to overlap the DA scan with the iso-detuning lines corresponding to the three coefficients describing the linear detuning,

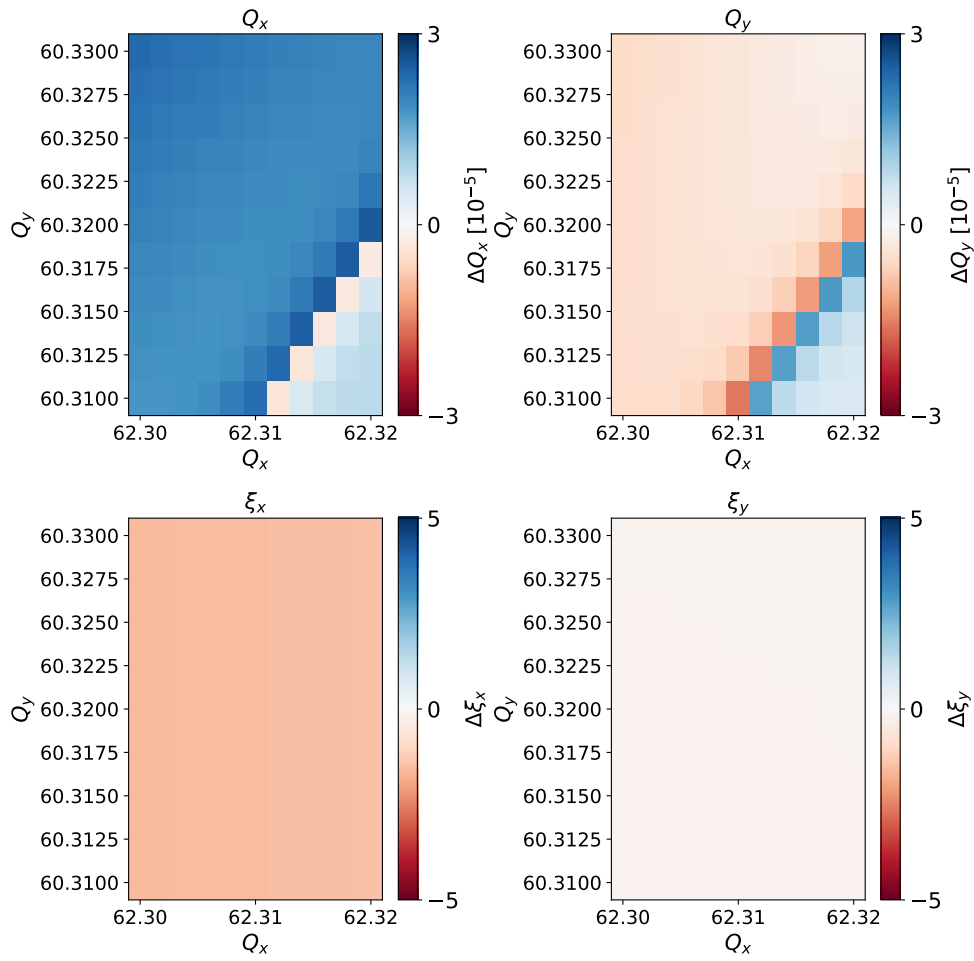


Figure 5.14: Sanity checks for the tracking simulations in the context of the LHC Run 3: computed tunes and chromaticities as a function of the chosen horizontal and vertical tunes.

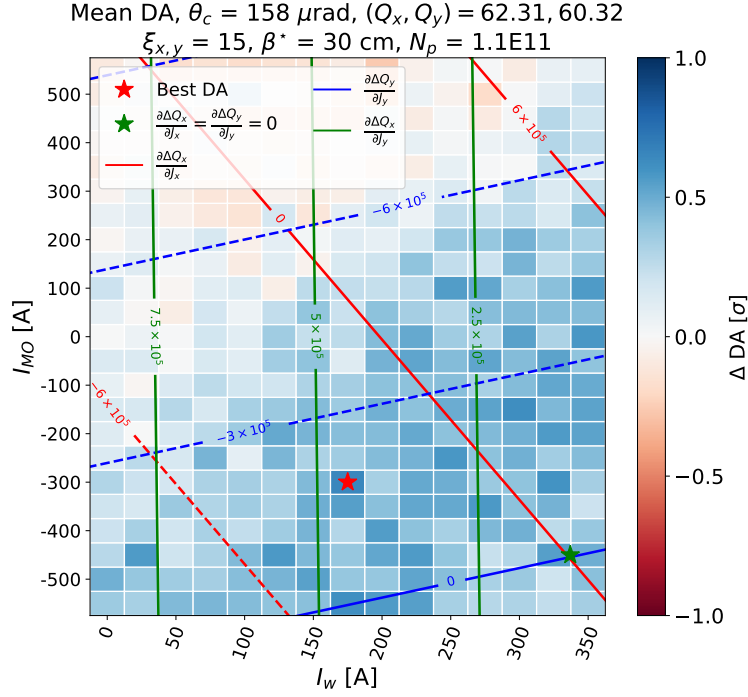


Figure 5.15: DA variation as a function of the wires and the Landau octupoles currents. Iso-detuning lines are also displayed in red (horizontal), blue (vertical) and green (cross anharmonicities). The red star shows the best DA configuration while the green star shows the configuration where both horizontal and vertical detuning cancel out.

namely $a_x = \partial\Delta Q_x/\partial J_x$, $a_y = \partial\Delta Q_y/\partial J_y$ and $a_{xy} = \partial\Delta Q_x/\partial J_y = \partial\Delta Q_y/\partial J_x$ (given in m^{-1}). For the octupoles, those coefficients can be computed, for the LHC, as [155]:

$$\begin{aligned}
 a_x^{MO} &= \frac{7000}{p_0} \left(267065 \frac{I_{MO}^F}{550} - 7859 \frac{I_{MO}^D}{550} \right) \\
 a_x^{MO} &= \frac{7000}{p_0} \left(9789 \frac{I_{MO}^F}{550} - 277203 \frac{I_{MO}^D}{550} \right) \\
 a_{xy}^{MO} &= \frac{7000}{p_0} \left(-102261 \frac{I_{MO}^F}{550} + 93331 \frac{I_{MO}^D}{550} \right),
 \end{aligned} \tag{5.2}$$

where p_0 is the momentum of the particles, express in GeV/c, and the superscripts D and F refer to defocusing and focusing octupoles respectively. For the BBLR interactions and the wires, these coefficients are computed from the detuning expression as given in [112]:

$$\begin{pmatrix} \Delta Q_x \\ \Delta Q_y \end{pmatrix} = -\frac{3\mu_0(IL)_w}{16\pi^2 B\rho} \frac{4\phi_w}{d_w^4} \begin{pmatrix} \beta_x^2 & -2\beta_x\beta_y \\ -2\beta_x\beta_y & \beta_y^2 \end{pmatrix} \begin{pmatrix} J_x \\ J_y \end{pmatrix}, \tag{5.3}$$

where $(IL)_w$ is the integrated current of the considered wire, d_w is the transverse beam-wire distance and $\phi_w = \arctan(y_w/x_w)$ gives the angular position of the wire in the transverse plane. The coefficients are thus obtained by simply differentiating the expression above with respect to the horizontal and vertical amplitudes J_x and J_y , as in Eqs. 5.4:

$$\begin{aligned}
 a_x^w &= -\frac{3\mu_0(IL)_w}{16\pi^2 B\rho} \frac{4\phi_w}{d_w^4} \beta_x^2 \\
 a_y^w &= -\frac{3\mu_0(IL)_w}{16\pi^2 B\rho} \frac{4\phi_w}{d_w^4} \beta_y^2 \\
 a_{xy}^w &= \frac{3\mu_0(IL)_w}{2\pi^2 B\rho} \frac{\phi_w}{d_w^4} \beta_x \beta_y.
 \end{aligned} \tag{5.4}$$

Eq. 5.4 stands for a DC wire, as the wire compensators. However, in this example, we approximate each BBLR interaction to a small wire whose induced linear detuning can be computed with this formula. This assumption remains valid until the beam-beam distance becomes too small (below 1-2 σ_{beam} , see Introduction in Figure 1.21).

As expected from the experimental results presented in Chapter 4, a negative polarity of the octupole current contributes to the mitigation of the BBLR interactions. One can thus determine a compromise between the wires and the octupoles in order to minimize the detrimental effect of the BBLR interactions and optimize the DA of the machine. According to Figure 5.15, there is no configuration for which the three detuning coefficients cancel out together. Such a point can be determined analytically by solving a system of three equations, the three unknowns being the currents of the wires in IR1, in IR5 and the Landau octupoles currents:

$$\begin{cases}
 A_{x1}I_{w1} + A_{x5}I_{w5} + \alpha_x I_{MO}^{D/F} + LR_x = 0 & (5.5a) \\
 A_{y1}I_{w1} + A_{y5}I_{w5} + \alpha_y I_{MO}^{D/F} + LR_y = 0 & (5.5b) \\
 A_{xy1}I_{w1} + A_{xy5}I_{w5} + \alpha_{xy} I_{MO}^{D/F} + LR_{xy} = 0, & (5.5c)
 \end{cases}$$

where the A coefficients are the detuning coefficients from the wires, normalized by their currents, the α coefficients are the detuning coefficients from the octupoles, normalized by their current, the LR coefficients are the ones from the BBLR interactions and $I_{MO}^{D/F} = I_{MO}^D = I_{MO}^F$ in the case of the LHC. From this system of equations, one gets:

$$\begin{aligned}
 I_{MO}^{D/F} &= \frac{-LR_x(A_{xy1}A_{y5} - A_{xy5}A_{y1}) - LR_y(A_{x1}A_{xy5} - A_{x5}A_{xy1}) + LR_{xy}(A_{x1}A_{y5} - A_{x5}A_{y1})}{A_{x1}A_{xy5}\alpha_y - A_{x1}A_{y5}\alpha_{xy} - A_{x5}A_{xy1}\alpha_y + A_{x5}A_{y1}\alpha_{xy} + A_{xy1}A_{y5}\alpha_x - A_{xy5}A_{y1}\alpha_x} \\
 I_{w1} &= \frac{-LR_x(A_{xy5}\alpha_y - A_{y5}\alpha_{xy}) - LR_y(A_{x5}\alpha_{xy} - A_{xy5}\alpha_x) + LR_{xy}(A_{x5}\alpha_y - A_{y5}\alpha_x)}{A_{x1}A_{xy5}\alpha_y - A_{x1}A_{y5}\alpha_{xy} - A_{x5}A_{xy1}\alpha_y + A_{x5}A_{y1}\alpha_{xy} + A_{xy1}A_{y5}\alpha_x - A_{xy5}A_{y1}\alpha_x} \\
 I_{w5} &= \frac{LR_x(A_{xy1}\alpha_y - A_{y1}\alpha_{xy}) + LR_y(A_{x1}\alpha_{xy} - A_{xy1}\alpha_x) - LR_{xy}(A_{x1}\alpha_y - A_{y1}\alpha_x)}{A_{x1}A_{xy5}\alpha_y - A_{x1}A_{y5}\alpha_{xy} - A_{x5}A_{xy1}\alpha_y + A_{x5}A_{y1}\alpha_{xy} + A_{xy1}A_{y5}\alpha_x - A_{xy5}A_{y1}\alpha_x}.
 \end{aligned} \tag{5.6}$$

Evaluating these expressions, one finds out that the needed currents to reach such a configuration are way out of the limits of the wires power supplies:

$$\begin{cases}
 I_{MO} = -380A & (5.7a) \\
 I_{w1} = -2742A & (5.7b) \\
 I_{w5} = 6817A. & (5.7c)
 \end{cases}$$

Moreover, using such settings would yield an unpredictable machine configuration from the physics point of view.

Nevertheless, one can consider the configuration where both $\partial\Delta Q_x/\partial J_x$ and $\partial\Delta Q_y/\partial J_y$ vanish (green star in Figure 5.15). With such a configuration, a DA improvement of 0.5 σ is observed. However, the DA seems more related to the vertical detuning (blue lines). Moreover, one can observe better points in terms of DA. A gain of 0.7 σ is for instance observed with the wires powered at 175 A and the octupole current set to -300 A, while clearly the

detuning coefficients do not cancel out. These different configurations are studied in terms of footprint, as shown on Figure 5.16.

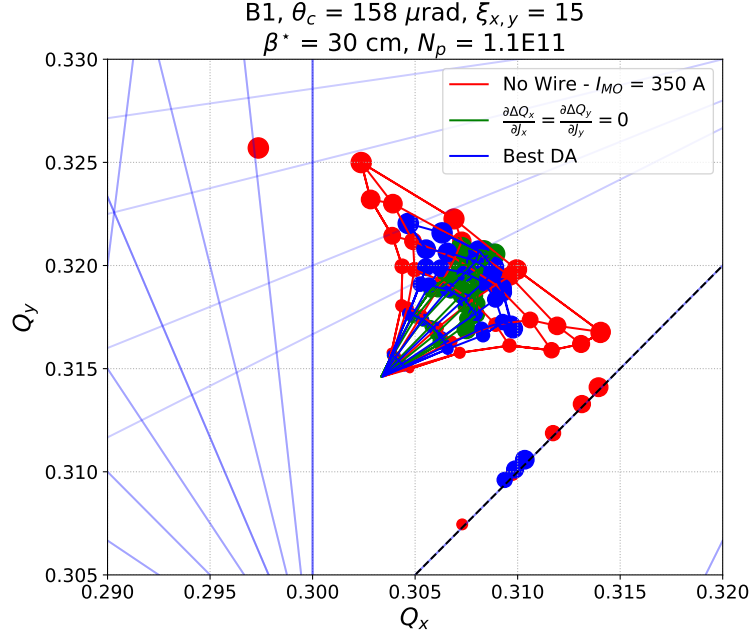


Figure 5.16: Tune footprints without compensation, for the linear detuning cancellation, and for the best DA configuration.

The use of the wires together with negative octupoles improves the compression of the tune footprint. As expected - since two of the three detuning coefficients cancel out - the green footprint shows an almost perfect compression, even if the footprint seems twisted, due to the residual cross anharmonicities. The best configuration in terms of DA is represented in blue. The compression seems less efficient than in the green footprint case. The observed better DA could possibly be explained by the fact that in the case of the green footprint, particles are compressed on a resonance line. However, this resonance is of 10^{th} order and it seems unlikely that a difference in the beam losses could be observed experimentally between the two configurations.

OCTUPOLE JUMP

During the operation of the LHC, the operators might have to revert the polarity of the octupoles while the beams are separated. In this configuration, there is no head-on collision and the only tune spread is thus the one induced by the octupoles. This can lead to coherent instabilities when the current of the octupoles is reduced down to zero before the polarity inversion. A possible solution to cope with this issue would be to use the wires in order to introduce some additional tune spread. Since the octupolar component of the wires is strong, one can dimension a knob driving the currents of the wires as a function of the one of the octupoles in order to maintain a constant detuning.

Reverting the octupoles polarity results in the inversion of the triangular shape of the footprint. One can define a scalar that would quantify this triangular shape. In that respect, we define a RMS-like linear detuning, written as:

$$\Delta Q_{RMS} = \frac{1}{\sqrt{2}} \sqrt{\left(\frac{\partial \Delta Q_x}{\partial J_x}\right)^2 + \left(\frac{\partial \Delta Q_y}{\partial J_y}\right)^2}. \quad (5.8)$$

Figure 5.17 then shows this quantity as a function of the wires and octupoles currents, assuming that the wires are powered with the same current.

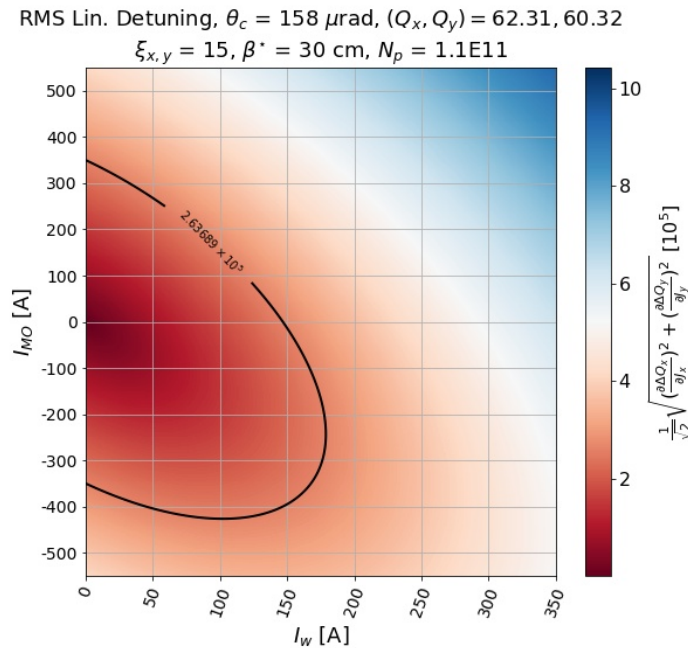


Figure 5.17: RMS-like detuning due to the wires and the Landau octupoles.

In this Figure, the black line gives the relation we are searching, giving the needed wire current in order to maintain a constant detuning while transitioning the octupoles from +350 A to -350A. Such a designed knob would be completely non-linear and impossible to design technically for the operation of the machine. However, it is possible to simplify the problem, as shown in Figure 5.18.

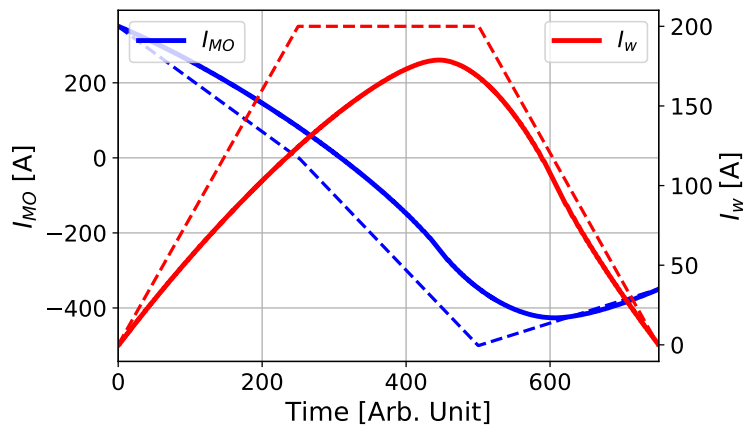


Figure 5.18: Knob proposal to maintain the detuning constant while inverting the octupoles polarity: wires and Landau octupoles currents as a function of time.

In this Figure, one can see the evolution in time (arbitrarily chosen) of the currents for the wires (in red) and the octupoles (in blue). These values correspond to the iso-detuning line drawn in Figure 5.17. As mentioned, the knob is complex and can be simplified, as illustrated with the dashed lines. The detuning does not have to stay exactly constant in order to avoid any instability. The proposed knob consists therefore in piece-wise linear ramps for both

the octupoles and wires currents. Using these ramps, one can compute the residual RMS-like detuning, as shown in Figure 5.19.

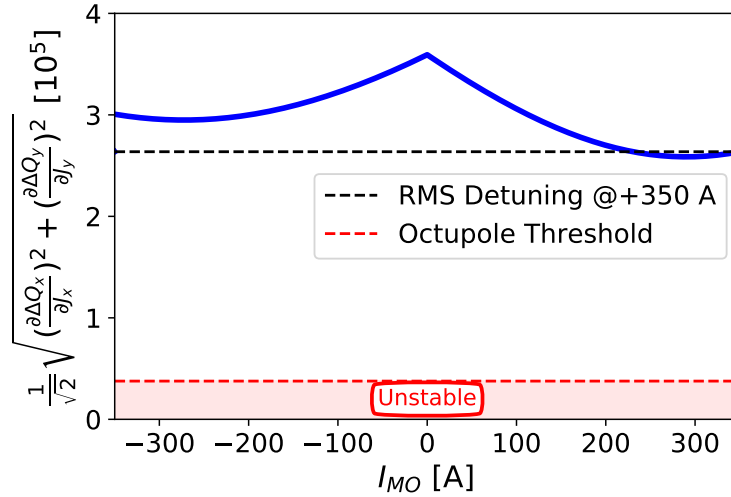


Figure 5.19: Residual RMS-like while inverting the octupoles polarity, with the use of the wires.

During the ATS experimental program described in Chapter 4, the octupole threshold for the coherent stability has been estimated to be about ± 50 A. One can see that the use of the proposed knob allows the operators to invert the polarity of the octupoles without reducing the detuning enough to trigger beam instabilities. By doing so, even with separated beams, it should be possible to cross the zero current line of the octupoles without experiencing issues.

5.3.4 BUNCH INTENSITY AND CROSSING ANGLE

As mentioned previously, using the current baseline parameters, the crossing angle is set to $158 \mu\text{rad}$ at the end of the luminosity leveling. This crossing angle corresponds to the limit value below which the DA is lower than 5σ and the beam lifetime is therefore significantly degraded. Figure 5.20 shows the evolution of the DA as a function of the bunch intensity and the half crossing angle, without the use of the wire compensators.

With a bunch population of $1.1 \cdot 10^{11}$ p, simulations confirm that the crossing angle cannot be reduced further down than the foreseen $158 \mu\text{rad}$. However, one can observe in the Figure that the luminosity limit of $2 \cdot 10^{34}$ Hz/cm² is quite far from the 5σ iso-DA line. Figure 5.21 shows the results of the same DA scan, but with the additional use of the wires, powered with 350 A in IR1, and 300 A in IR5. This configuration corresponds to one of the best DA configurations determined from Figure 5.9.

One can observe that in comparison with Figure 5.20, the wires could allow a slight reduction of crossing angle by about $10 \mu\text{rad}$ after the end of the β -leveling, leading to a possible marginal increase of the luminosity.

In this Section, we showed the potential of the wires compensators, used together with the baseline parameters. However, these parameters are still under discussion at the time of writing, and one can carry out additional studies, changing them, in a reasonable range, in order to explore the full potential of the BBLR wire demonstrators.

5.4 EXPLORING THE POTENTIAL OF THE WIRE COMPENSATORS

Among all the possible parameters, the most interesting from a BBLR compensation point of view are the Landau octupoles current and the beam-wire distances. The first one has been discussed in the previous Section. It has in fact been shown that negative octupoles would help the BBLR mitigation process. The second one is dealt with in this Section. The possibility of tighter collimation settings is, in fact, under investigation for the LHC Run 3 [156].

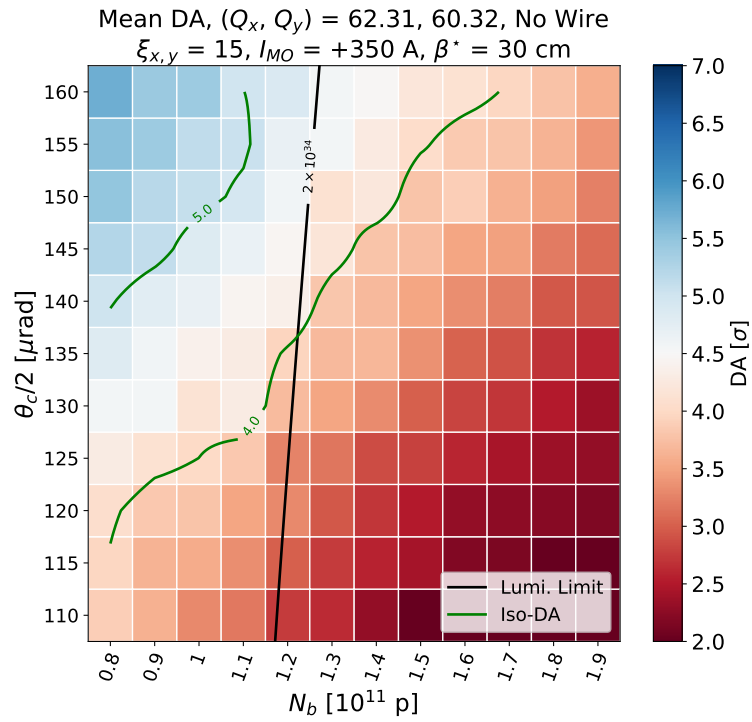


Figure 5.20: Dynamic aperture as a function of the half the crossing angle and the bunch population, at the end of the β -leveling, without the use of the wire compensation.

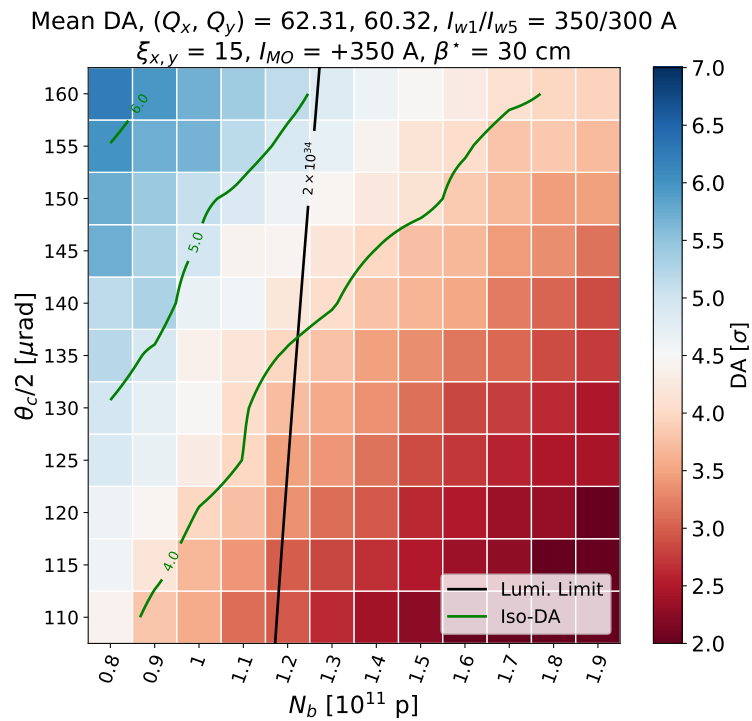


Figure 5.21: Dynamic aperture as a function of the half the crossing angle and the bunch population, at the end of the β -leveling, with the use of the wire compensators.

In this Section, we therefore explore the possibility to close the wire collimators down to $7.5 \sigma_{coll}$, which would reduce slightly the transverse beam-wire distance, as shown in Table 5.4.

Collimator Opening	Wire IR1	Wire IR5
$7.5 \sigma_{coll}$	8.39 mm	11.15 mm
$8.5 \sigma_{coll}$	9.1 mm	12.23 mm

Table 5.4: Beam-wire distances as a function of the collimator opening.

One can thus reproduce the wire current scan presented in Figure 5.9, with negative octupoles, and the wire collimators closed at $7.5 \sigma_{coll}$. The corresponding results are presented in Figure 5.22.

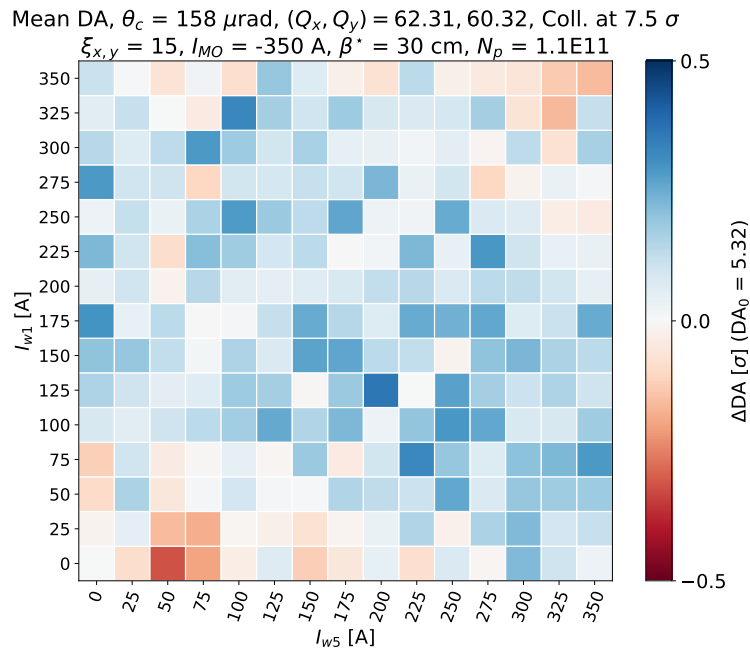


Figure 5.22: Dynamic aperture variation as a function of the wire currents, with negatives octupoles and reduced wire collimators gap.

The first point to be noticed from this figure is the fact that the DA_0 , corresponding to the DA value without wires, has improved from 4.79 to 5.32σ , simply by inverting the octupoles polarity. With the use of the wires, in this configuration with reduced beam-wire distances, the DA is maximized when powering the wires in IR1 with 125 A, and the ones in IR5 with 200 A. In this configuration, the average DA gain is 0.36σ , which is comparable to the nominal scenario. However, the absolute DA would thus be brought to 5.68σ , while, using the baseline parameters, the DA with the wires on reached 5.15σ .

This optimal configuration is used for the study of the DA as a function of the half crossing angle and the bunch population. Figure 5.23 shows the results of this study, to be compared to the ones displayed in Figures 5.20 and 5.21.

In this configuration, it would be possible to reduce the crossing angle from the initial $158 \mu\text{rad}$ down to $145 \mu\text{rad}$, without degrading the DA below the 5σ limit. Assuming a systematic use of the wires at the end of the β -leveling, for about 3 hours, and maintaining the crossing angle at $145 \mu\text{rad}$ until the end of the fill, the integrated luminosity gain would roughly reach 2 %.

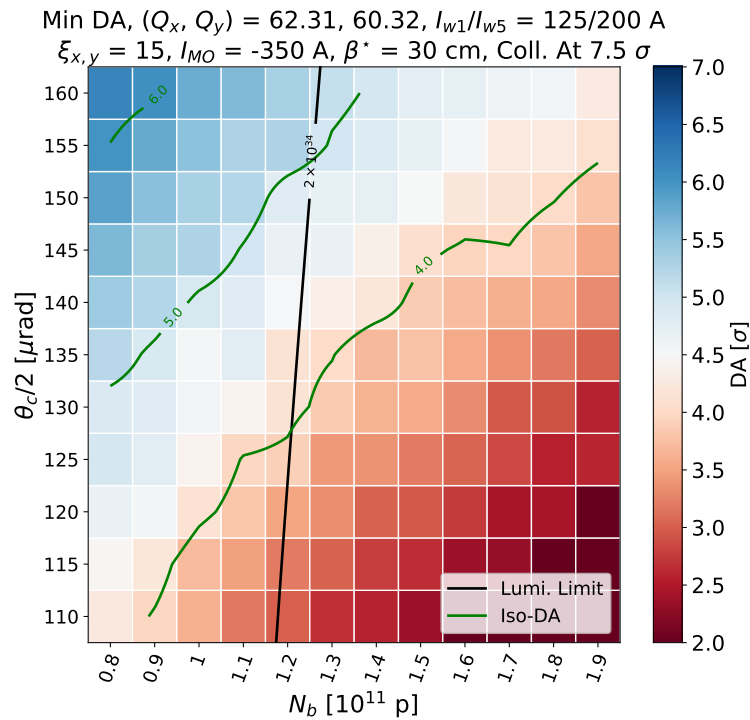


Figure 5.23: Dynamic aperture as a function of the half the crossing angle and the bunch population, at the end of the β -leveling, with negative octupoles, and reduced wire collimators gap.

5.5 HARDWARE NON-IDEALITIES AND CONSEQUENCES FOR THE HL-LHC ERA

The goal of this Section is to use tracking simulations in order to highlight some hardware limitations for the LHC Run 3, and to draw conclusions in view of the HL-LHC era. These limitations have already been mentioned from the experiments, but tracking simulations can give a quantitative insight.

5.5.1 EFFECT OF A MISALIGNMENT OF THE WIRES ON THE DYNAMIC APERTURE

The first issue to be dealt with is the 5^{th} -axis alignment of the wire collimators. As it has already been discussed, the overall structure of the wire collimator can be moved in the plane orthogonal to the one of installation. The correct alignment of this axis is of prime importance in order to avoid the introduction of additional components in the magnetic field induced by the wires. However, the impact of a misalignment on the beam losses was not studied experimentally. Dynamic aperture studies can quantify this impact. In that respect, Figure 5.24 shows the evolution of the DA as a function of a horizontal displacement of the wires in IR1, and of a vertical displacement of the wires in IR5. The settings are the same as the ones used in the previous section, corresponding to an end-of-fill situation, with the wire collimators open at 8.5σ , and powered with their maximal current, using the 2-jaws powering configuration.

One can see that the average DA does not evolve significantly for a misalignment lower than 1 mm for both wire collimators. However, for larger misalignment, DA can shrink by 0.5 to 1σ , which would jeopardize the beneficial effect of the wires. The effect of a misalignment of the wires in IR5 is less important, due to the larger beam-wire distance. In case of misalignment, the angle between the wires and the beam will therefore be smaller than for the wires in IR1 with the same absolute misalignment. The DA decrease due to the misalignment is enlarged in the case of a reduced wire collimators gap down to 7.5σ .

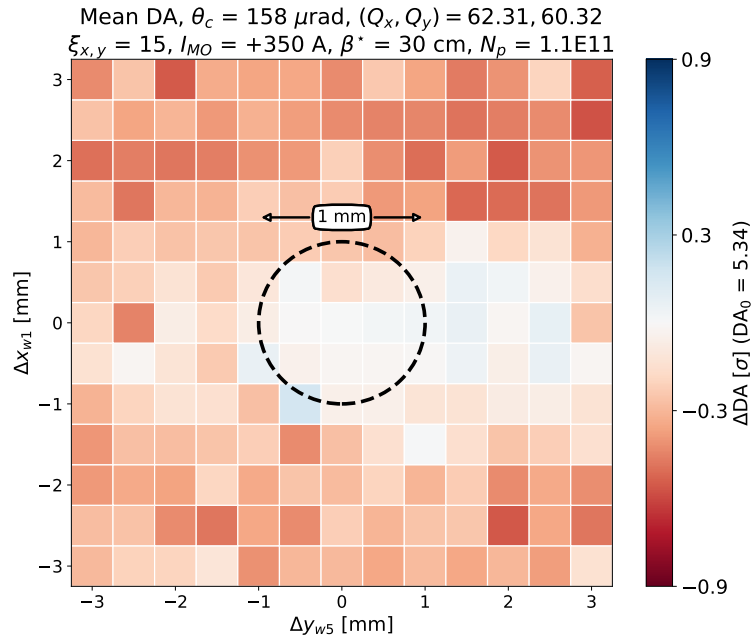


Figure 5.24: Dynamic aperture as a function of a horizontal and vertical 5th-axis misalignment.

The alignment of the 5th-axis should be done with the best possible precision. However, this study shows that an alignment with a precision below 0.5 mm could be enough in order to preserve the wire compensators beneficial effect.

5.5.2 ALIGNING THE WIRES WITHOUT THE USE OF THE BPMs

During the LHC Run 2, the alignment of the wires was done using the BPMs embedded into the wire collimators. This was helpful in order to reach precise alignments. However, in the present design of the new wire compensators for HL-LHC, the question about embedding BPMs was raised, as for the moment, the wires are not foreseen to be housed inside a collimator. This section therefore tries to evaluate the possibility to align the wires without the use of local BPMs.

From the previous Section, the target would be to be able to align the wires with a precision lower than 0.5 mm. The goal of this study is therefore to determine if one could evaluate such a misalignment by monitoring the tunes. In the following, we move the 5th-axis of each wire collimators of Beam 1 (similar results can be obtained for Beam 2) and we record the expected induced tune shift. This test is done at top energy, with a single individual bunch ($N_b = 1.1 \cdot 10^{11}$), in order to remain compatible with the LHC conditions. The tunes are matched to the nominal values, and the feed-forward system of the wires is switched off. Figure 5.25a and 5.25b show the expected tune shifts, computed with MAD-X, for a misalignment of the wires in IR1 and IR5 respectively.

The tune shift induced by such a misalignment can reach up to $4 \cdot 10^{-3}$ in the case of IR1, for a misalignment of 3 mm. However, this effect is significantly reduced with the wires in IR5 since they are located further away from the beam. Moreover, in the previous section, the requirement in terms of precision was set to half a millimeter. One can observe that for such values, the induced tune shift is very small (order of 10^{-5}). The typical limit of the tunes measurements in the LHC is of the order of 10^{-4} [157]. Aligning the wire collimators' 5th-axis using tune measurements seems therefore difficult, or impossible. One would have to close significantly the collimators in order to observe a visible effect on the tunes. This could be done during the machine commissioning, using pilot beams allowing the collimators gaps to be reduced from a machine protection point of view. However, embedding BPMs in the wire collimators, or in the early design stage for the HL-LHC era would be the best and most reliable option.

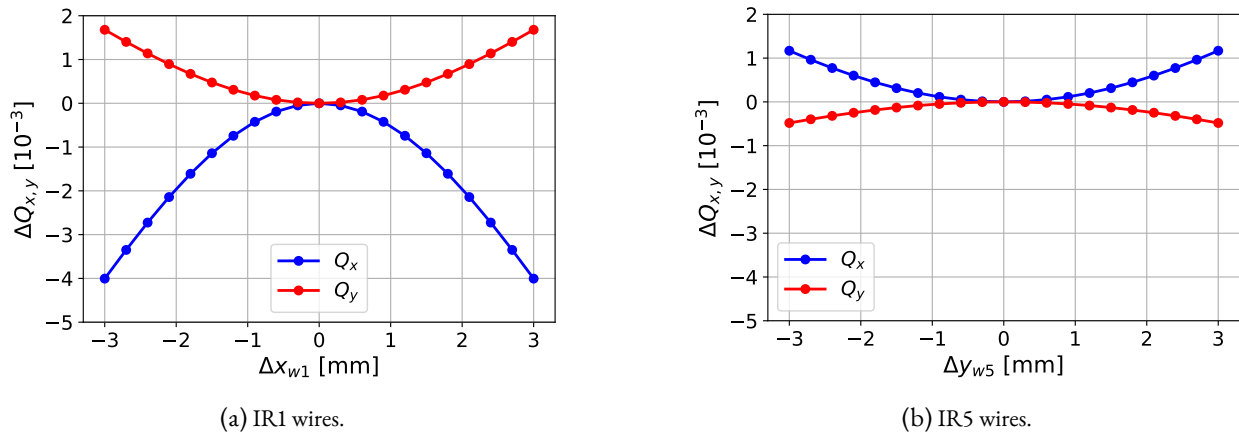


Figure 5.25: Effect of a misalignment of the 5th-axis on the horizontal (in blue) and the vertical (in red) tunes (2-jaws powering configurations, collimators opened at 8.5σ).

5.6 CONCLUSIONS

In this Chapter, we gave an overview of the possible use of the wire compensators during the LHC Run 3, that would represent a unique opportunity to gain experience in operating the LHC with such devices. The foreseen plan (at the time of writing) is to power the wires on both beams systematically at the end of each fill, after the β -leveling.

Through a rich collection of simulations, the positive effect of the wires on the machine dynamic aperture has been demonstrated. However, this improvement has been shown to be limited with the present baseline parameters. With a wire collimator opening of 8.5σ , it seems in fact that an improvement of about 0.4σ DA can be obtain. The effect of the wires on the tune footprint is limited as well.

As discussed in the previous chapter, an important parameter that could be discussed is the current - and more specifically, the polarity - of the Landau octupoles. In the present baseline for the LHC Run 3, the octupoles current is set to 350 A, which does not correspond to a BBLR mitigation regime. A possible way to improve the wire effect during Run 3 would be to invert this polarity in order to operate with the octupoles powered at -350 A. In addition, it has been shown that the wires could be used while reverting the polarity of the octupoles in order to maintain a constant tune spread, avoiding triggering beam instabilities.

Moreover, the possibility to close the wire collimators down to 7.5σ was also discussed. Combined with negative octupoles, this configuration could improve the BBLR mitigation using the wires. It has in fact been shown that a crossing angle reduction would even be possible. Despite the fact that the primary goal of operating the LHC in Run 3 with the wires is to gain experience, a performance gain could also be observed in that case.

Finally, this set of simulations confirmed experimental observations concerning the present hardware. The in-jaw configuration of the wires is not ideal. We showed that the DA is sensitive to a possible misalignment of the wires, and a reasonable target would be a 0.5 mm precision. For the HL-LHC era, it is presently foreseen to abandon this in-jaw configuration in favor of a moving structure inside the vacuum chamber. However, we showed that the presence of BPMs close to the wires would ease significantly the alignment procedure.

6 CONCLUSIONS AND PERSPECTIVES

In the search for new physics, modern colliders, such as the LHC or the HL-LHC, are trying to reach higher and higher integrated luminosity in order to decrease the statistical errors of the measurements, and to possibly achieve new discoveries. Consequently, the beams intensities are constantly increased, and new challenges are then met in terms of beam physics. One of the main performance limitations when colliding two intense beams is the possible interactions between the two beams, when they are located close from each other, right before, or after, entering in collisions. These Beam-Beam Long-Range interactions are known to have a detrimental effect on the beam lifetime, and, consequently, on the possible luminosity reach. Compensating their effect is therefore of prime importance.

In the early 2000's, and for the first time, the idea of using DC wires to mitigate BBLR interactions was proposed, based on the observation of the similarity between the forces induced by such a wire, and a beam. In 2015, S. Fartoukh proposed a rationale for the choice of settings of the wire compensators. This was based on a semi-analytical work consisting in compensating all the BBLR-driven Resonance Driving Terms. This approach relies on a close proximity between the wires and the beams, which is not reachable in practice. However, these results motivated the construction and the installation of demonstrators in the LHC.

During the 2017-2018 LHC run, we carried out a two years long experimental campaign in the LHC, using the freshly installed demonstrators. In a first experiment, we used a low intensity beam, composed by only two bunches. With this configuration, the wires could be brought closer to the beam. After identifying a clear BBLR signature, the wires were turned on and off repeatedly, while reducing the beams crossing angle. The results of this proof of concept showed for the first time a clear evidence of a possible mitigation of the BBLR interactions using wires and motivated a second set of experiments with a setup closer to the nominal LHC operation. In this second set of experiments, both beams were composed of several trains of bunches. Consequently, for machine protection reasons, the wires were located further away from the beam and their effect was reduced. In order to increase their effective strength, the two wires housed in the collimators were powered in series, doubling their octupolar strength. Results showed a possible reduction of beam losses by powering the wires, even at lower crossing angle. Through this experimental campaign, we showed that it was possible to achieve a partial, but still beneficial, compensation in conditions different from the original proposal from S. Fartoukh, but also compatible with the nominal LHC operation.

These very positive results yielded a change of layout during the Long Shutdown 2, as a preparatory step for the last LHC run before the HL-LHC era. It was, in fact, decided to equip Beam 1 with wires as well, using two of the wire collimators originally installed for Beam 2. The results of the experiments, together with an important numerical tracking campaign, proved that the wire compensators - initially built as demonstrators, for a proof-of-concept - were worth being used as operational devices. It is now foreseen to power the wires routinely at the end of each fill during the next LHC run in order to gain experience in operating the machine with such devices, in view of the HL-LHC era. The tracking simulations allowed us to determine operational scenarios for the upcoming Run 3 with the wire compensators.

Additionally, we addressed, in this Thesis, another aspect of the BBLR mitigation that is of prime importance for the Run 3. The efficiency of the Landau octupoles present in the machine is significantly increased by using optics with higher telescopic indexes. Through a set of experiments, we showed that these octupoles could mitigate the BBLR interactions effect, when their polarity is reverted from positive to negative. These experiments included both round and flat optics, two possible options for the future operation of the (HL)-LHC. Through these experiments,

we manage to demonstrate that a combination of octupoles and wire compensators, with high tele-indexes, could improve significantly the efficiency of the compensation.

Due to the residual crossing angle and corresponding BBLR interactions, on the longer term, it has now been decided to reserve space for the wire compensators in the HL-LHC and they are considered as a complementary solution to the crab cavities. The wire compensators could recover - at least, partially - the loss of luminosity. In the HL-LHC, the crossing angle, and therefore the normalized beam-beam separation, are foreseen to be larger than in the LHC, further improving the beam-wire approximation. The potential of the wire compensators would therefore be exploited at its best, as it was shown in the simulation work described in [52].

Finally this experimental campaign, together with the simulations results, also showed the limitations of the current hardware. The *in-jaw* configuration of the wires should be avoided in the future, as collimator jaws are bulky and can limit the movement of the wires and the additional distance between the wire and the edge of the jaw adds up with the already important beam-wire distance, reducing the efficiency of the compensators. Finally, we saw that it was necessary to have local beam diagnostics (typically, BPMs) around the wires in order to ease their alignment with the beam.

From the early 2000's to nowadays, the idea of compensating the BBLR interactions with DC wires evolved significantly: this Thesis contributed in the advancement of this research topic. From elegant mathematical optimizations of the wires' settings, we managed to adapt them as much as possible to be compatible with the operation of such a complex collider that is the LHC. We proved that, despite the technical constraints, the wire compensators can mitigate successfully the BBLR interactions in a rich collections of configurations. The future of the wire compensators at CERN will start in 2022 with the restart of the LHC. During the three years of foreseen operation, the goal will be to gain as much as possible experience, operating these devices in order to be ready for the HL-LHC era. With its large normalized beam-beam separation and its very high intensity beams, the HL-LHC could present the best conditions for the wire compensators to show their best potential.

Appendices

A LUMINOSITY AND CROSSING ANGLE

In the Introduction, we derived an expression for the luminosity in the case of two Gaussian bunches colliding purely head-on. However, we also saw that in the case of the (HL)-LHC, the collisions were achieved with a crossing angle in order to separate the two beams after they collide. The impact of the crossing angle on the luminosity was presented in the Introduction, but this Appendix presents the full derivation of the final formula.

Let us start from the overlap integral expressed in Eq. 1.4, giving the luminosity of only one collision:

$$\mathcal{L}_{SB} = N_1 N_2 f_{rev} K \int_{S_c} \rho_1(\mathbf{x}, t) \rho_2(\mathbf{x}, t) d^3 \mathbf{x} dt, \quad (\text{A.1})$$

where K is the kinematic factor as discussed in the Introduction.

In the following, we consider a crossing angle in the horizontal plane, but the same results can be obtained for a vertical crossing. We denote θ_c this crossing angle. A change of variable is necessary (in addition to the usual $t = s/c$) in order to compute the overlap integral in presence of a crossing angle, as shown in Figure A.1.

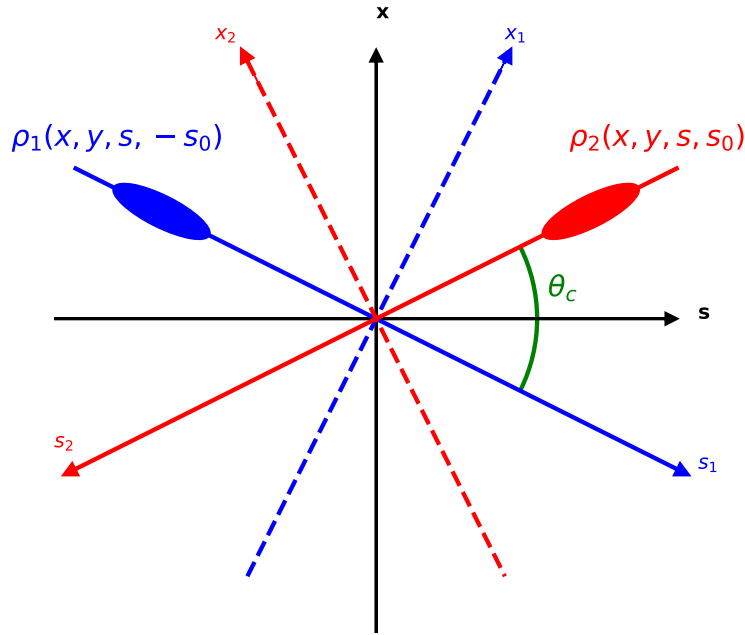


Figure A.1: Rotated reference system for collisions in presence of a crossing angle.

The new systems (x_1, s_1) and (x_2, s_2) are related to the initial (x, s) as:

$$\begin{aligned} x_1 &= x \cos\left(\frac{\theta_c}{2}\right) - s \sin\left(\frac{\theta_c}{2}\right) \\ s_1 &= s \cos\left(\frac{\theta_c}{2}\right) + x \sin\left(\frac{\theta_c}{2}\right), \end{aligned} \quad (\text{A.2})$$

A Luminosity and Crossing Angle

and:

$$\begin{aligned} x_2 &= x \cos\left(\frac{\theta_c}{2}\right) + s \sin\left(\frac{\theta_c}{2}\right) \\ s_2 &= s \cos\left(\frac{\theta_c}{2}\right) - x \sin\left(\frac{\theta_c}{2}\right). \end{aligned} \quad (\text{A.3})$$

The two bunches are assumed to be Gaussian in all dimensions, as described in Eqs. 1.7. All the densities are therefore uncorrelated in all planes, and the bunches are assumed to be equal ($\sigma_{1xy} = \sigma_{2xy}$). As the velocities of the two bunches are not collinear anymore, the K kinematic factor is now equal to $2 \cos(\theta_c/2)c$, and the integral can be written:

$$\mathcal{L}_{SB} = 2 \cos\left(\frac{\theta_c}{2}\right) N_1 N_2 f_{rev} \iiint\limits_{S_{\mathcal{L}}} \rho_{1x}(x_1) \rho_{1y}(y_1) \rho_{1s}(s_1 - s_0) \rho_{2x}(x_2) \rho_{2y}(y_2) \rho_{2s}(s_2 + s_0) dx dy ds ds_0. \quad (\text{A.4})$$

We substitute the expressions of the densities to get:

$$\begin{aligned} \mathcal{L}_{SB} &= \frac{2N_1 N_2 f_{rev}}{(\sqrt{2\pi})^6 \sigma_s^2 \sigma_x^2 \sigma_y^2} \cos\left(\frac{\theta_c}{2}\right) \iiint\limits_{S_{\mathcal{L}}} e^{-\frac{x_1^2}{2\sigma_x^2}} e^{-\frac{y_1^2}{2\sigma_y^2}} e^{-\frac{s_1^2}{2\sigma_s^2}} e^{-\frac{-s_0^2}{\sigma_s^2}} \\ &\quad e^{-\frac{x_2^2}{2\sigma_x^2}} e^{-\frac{y_2^2}{2\sigma_y^2}} e^{-\frac{s_2^2}{2\sigma_s^2}} e^{-\frac{s_0^2}{\sigma_s^2}} dx dy ds ds_0. \end{aligned} \quad (\text{A.5})$$

One can thus substitute the expression of the new variables as a function of (x, y, s) and integrate over y and s_0 , using:

$$\int_{-\infty}^{+\infty} e^{-(at^2+bt+c)} dt = \sqrt{\frac{\pi}{a}} e^{-\frac{b^2-ac}{4a}}, \quad \forall a > 0, \forall b, c \in \mathbb{R}, \quad (\text{A.6})$$

and get:

$$\mathcal{L}_{SB} = \frac{N_1 N_2 f_{rev}}{4\pi^2 \sigma_s \sigma_x^2 \sigma_y} \cos\left(\frac{\theta_c}{2}\right) \iint\limits_{S_{\mathcal{L}}} e^{-\frac{x^2 \cos^2(\theta_c/2) + s^2 \sin^2(\theta_c/2)}{\sigma_x^2}} e^{-\frac{x^2 \sin^2(\theta_c/2) + s^2 \cos^2(\theta_c/2)}{\sigma_s^2}}. \quad (\text{A.7})$$

As x and $\sin(\theta_c/2)$ are both small, we drop all the terms $s^k \sin^l(\theta_c/2)$ and $x^k \sin^l(\theta_c/2)$, for $k + l \geq 4$. Moreover, we approximate $\sin(\theta_c/2)$ to $\theta_c/2$. After integration, we obtain:

$$\mathcal{L}_{SB} = \frac{N_1 N_2 f_{rev}}{4\pi \sigma_x \sigma_y} \frac{1}{\sqrt{1 + \frac{\sigma_x}{\sigma_s} \tan\left(\frac{\theta_c}{2}\right)^2}} \frac{1}{\sqrt{1 + \frac{\sigma_s}{\sigma_x} \tan\left(\frac{\theta_c}{2}\right)^2}}. \quad (\text{A.8})$$

Assuming that the RMS bunch length is much larger than the transverse beam size (which is a valid assumption for the (HL)-LHC), and considering N_b collisions in the considered IP, the final formula for the luminosity is obtained, as in the Introduction:

$$\mathcal{L} = \frac{N_1 N_2 f_{rev} N_b}{4\pi \sigma_x \sigma_y} \frac{1}{\sqrt{1 + \frac{\sigma_s}{\sigma_x} \tan\left(\frac{\theta_c}{2}\right)^2}}. \quad (\text{A.9})$$

The impact of the crossing angle is shown in Figure 1.6 in the Introduction.

B LIST OF THE LHC FILLS FOR THE EXPERIMENTAL CAMPAIGN

We report in this Appendix the fully detailed list of the LHC fills considered for the experimental campaign. Table B.1 reports this list together with the beams intensities at injection and energies, the wire collimators opening, the reason of the beam dump, the date of the fill and some eventual comments.

Fill #	Nb (B1) [p]	Nb (B2) [p]	Energy [GeV]	Gap [σ_{coll}]	Date	Dump Reason	Comments
5898	$5.5 \cdot 10^{12}$	$3 \cdot 10^{11}$	6500	6	01/07/2017	RF Interlock	No Data Taken
5900	$5.5 \cdot 10^{12}$	$3 \cdot 10^{11}$	6500	6	01/07/2017	Manual	Wires in IR5 only
6434	$1.8 \cdot 10^{13}$	$2 \cdot 10^{11}$	6500	5.5	29/11/2017	PS Interlock	No Data Taken
6435	$1.8 \cdot 10^{13}$	$2 \cdot 10^{11}$	6500	5.5	29/11/2017	Manual	
6797	$1.8 \cdot 10^{13}$	$3 \cdot 10^{11}$	6500	5.5	14/06/2018	B1 instability	No Data Taken
6798	$1.8 \cdot 10^{13}$	$3 \cdot 10^{11}$	6500	5.5	14/06/2018	B1 instability	Wire Alignment
6799	$1.55 \cdot 10^{13}$	$2 \cdot 10^{11}$	6500	5.5	14/06/2018	Manual	Not conclusive
6972	$1.55 \cdot 10^{13}$	$2.4 \cdot 10^{11}$	6500	5.5	24/07/2018	Manual	Test Wires IR1
7169	$1.55 \cdot 10^{13}$	$2.4 \cdot 10^{11}$	6500	5.5/6	14/09/2018	Manual	Crossing Angle Reduction
7385	$1.55 \cdot 10^{13}$	$2.4 \cdot 10^{11}$	450/6500	8.5	29/10/2018	Manual	Validation fill
7386	$1.6 \cdot 10^{13}$	$1.6 \cdot 10^{13}$	6500	8.5	29/10/2018	Manual	Compensation with trains

Table B.1: List of the LHC fills considered for the experimental campaign

ACRONYMS

ALICE	A Large Ion Collider Experiment
ATLAS	A Toroidal LHC ApparatuS
BBES	Beam-Beam Encounter Schedule
BBLR	Beam-Beam Long-Range
BCMS	Batch Compression Merging and Splitting
BCT	Beam Current Transformer
BLM	Beam Loss Monitor
BLN	Brookhaven National Laboratory
BPM	Beam Position Monitor
CMS	Compact Muon Solenoid
DA	Dynamic Aperture
DAFNE	Double Annular Factory for Nice Experiments
dBLM	diamond Beam Loss Monitor
DC	Direct Current
FBCT	Fast Beam Current Transformer
FCC	Future Circular Collider
HL-LHC	High-Luminosity Large Hadron Collider
HO	Head-On
INFN	Istituto Nazionale di Fisica Nucleare
IP	Interaction Point
IR	Insertion Region
ISR	Intersection Storage Rings
IT	Inner Triplet
LEP	Large Electron-Positron collider
LHC	Large Hadron Collider
LHCb	Large Hadron Collider beauty
LIU	LHC Injector Upgrade
MD	Machine Development
PS	Proton Synchrotron
PU	Pick-Up
RDT	Resonance Driving Term
RF	Radio Frequency
RHIC	Relativistic Heavy Ion Collider
SC	Synchrotron
SPS	Super Proton Synchrotron
SSC	Superconductive Super Collider

GLOSSARY

$(IL)_w$	Wire integrated current
$B\rho$	Magnetic rigidity
$J_{x,y}, \phi_{x,y}$	Action-angle variables
$N_{1,2}$	Bunch intensity in protons
$Q_{x,y}$	Horizontal and vertical betatronic tunes
Φ_w	Piwinski angle
β^*	Betatronic function at the IP
β_r, γ_r	Lorentz relativistic factors
$\beta_{x,y}$	Horizontal and vertical betatronic functions
$\delta = \Delta p/p_0$	Momentum deviation
ϵ_0	Permittivity of free space
\mathcal{L}	Instantaneous luminosity
\mathcal{L}_{int}	Integrated luminosity
μ_0	Permeability of free space
$\mu_{x,y}$	Horizontal and vertical betatronic phase advances
σ_{eff}	Effective cross section
$\sigma_{x,y,s}$	Transverse and longitudinal normalized beam sizes
θ_c	Crossing angle
$\epsilon_N = \beta_r \gamma_r \epsilon_g$	Normalized beam emittance
ϵ_g	Geometrical beam emittance
$\xi_{x,y}$	Horizontal and vertical chromaticities
c_{pq}	(p, q) Resonance Driving Term
d_w	Physical beam-wire distance
d_{bb}	Physical beam-beam separation
f_{RF}	RF Frequency
f_{rev}	Revolution frequency
h	Harmonic number
$l = m_x + m_y = p + q$	Resonance order
$r/r_w/r^*$	β aspect ratio
r^{Tele}	Telescopic Index
r_p	Classical proton radius
c	Speed of light

BIBLIOGRAPHY

1. *The Synchrocyclotron*. 2012. URL: <https://cds.cern.ch/record/1997556>.
2. *The Proton Synchrotron*. 2012. URL: <https://cds.cern.ch/record/1997189>.
3. E. Mobs. *The CERN accelerator complex - 2019. Complexe des accélérateurs du CERN - 2019*. General Photo. 2019. URL: <https://cds.cern.ch/record/2684277>.
4. K. Johnsen. “CERN Intersecting Storage Rings (ISR)”. *Proc. Natl. Acad. Sci. U. S. A.* 70, 1973. National Academy of Sciences Autumn Meeting (October 1972): Symposium: New Accelerators, 619–626. 8 p. URL: <https://cds.cern.ch/record/2318386>.
5. *The Super Proton Synchrotron*. 2012. URL: <https://cds.cern.ch/record/1997188>.
6. “First proton-antiproton collisions in the CERN SPS collider”. *Phys. Lett. B* 107:CERN-SPS-81-27-EA, 1981, 306–309. 8 p. DOI: [10.1016/0370-2693\(81\)90836-4](https://doi.org/10.1016/0370-2693(81)90836-4). URL: <https://cds.cern.ch/record/135712>.
7. L. Di Lella and C. Rubbia. “The Discovery of the W and Z Particles”. *Adv. Ser. Dir. High Energy Phys.* 23, 2015, pp. 137–163. DOI: [10.1142/9789814644150_0006](https://doi.org/10.1142/9789814644150_0006). URL: <https://cds.cern.ch/record/2103277>.
8. R. W. Assmann, M. Lamont, and S. Myers. “A Brief History of the LEP Collider”. *Nucl. Phys. B, Proc. Suppl.* 109:CERN-SL-2002-009-OP, 2002, 17–31. 15 p. DOI: [10.1016/S0920-5632\(02\)90005-8](https://doi.org/10.1016/S0920-5632(02)90005-8). URL: <https://cds.cern.ch/record/549223>.
9. O. S. Brüning et al. *LHC Design Report, Vol. I, The Main Ring*. CERN Yellow Reports: Monographs. CERN, Geneva, 2004. DOI: [10.5170/CERN-2004-003-V-1](https://doi.org/10.5170/CERN-2004-003-V-1). URL: <https://cds.cern.ch/record/782076>.
10. A. Team. *Diagram of an LHC dipole magnet. Schéma d’un aimant dipôle du LHC*. 1999. URL: <https://cds.cern.ch/record/40524>.
11. V. Baglin. “The LHC vacuum system: Commissioning up to nominal luminosity”. *Vacuum* 138, 2017, 112–119. 8 p. DOI: [10.1016/j.vacuum.2016.12.046](https://doi.org/10.1016/j.vacuum.2016.12.046). URL: <http://cds.cern.ch/record/2270074>.
12. D. Boussard et al. *The LHC Superconducting RF System*. Technical report LHC-Project-Report-316. CERN-LHC-Project-Report-316. Geneva: CERN, 1999. URL: <https://cds.cern.ch/record/410377>.
13. T. C. Committee. *HL-LHC Parameters V7.1.1*. 2020. URL: https://espace.cern.ch/HiLumi/TCC/_layouts/15/WopiFrame.aspx?sourcedoc=/HiLumi/TCC/SiteAssets/HL_LHC_Parameter_Table.xlsx&action=default.
14. S. D. Fartoukh et al. *LHC Abort Gap Filling by Proton Beam*. Technical report LHC-Project-Report-763. CERN-LHC-Project-Report-763. revised version submitted on 2004-09-23 11:55:00. 2004, 4 p. URL: <https://cds.cern.ch/record/790609>.
15. M. Benedikt, P. Collier, V. Mertens, J. Poole, and K. Schindl. *LHC Design Report, Vol. III, The LHC Injector Chain*. CERN Yellow Reports: Monographs. CERN, Geneva, 2004. DOI: [10.5170/CERN-2004-003-V-3](https://doi.org/10.5170/CERN-2004-003-V-3). URL: <https://cds.cern.ch/record/823808>.
16. G. Apollinari et al. *High-Luminosity Large Hadron Collider (HL-LHC): Technical Design Report V. 0.1*. CERN Yellow Reports: Monographs. CERN, Geneva, 2017. DOI: [10.23731/CYRM-2017-004](https://doi.org/10.23731/CYRM-2017-004). URL: <https://cds.cern.ch/record/2284929>.
17. H. Damerau et al. *LHC Injectors Upgrade, Technical Design Report*. Technical report CERN-ACC-2014-0337. 2014. URL: <https://cds.cern.ch/record/1976692>.

Bibliography

18. M. Vretenar et al. *Linac4 design report*. Vol. 6. CERN Yellow Reports: Monographs. CERN, Geneva, 2020. DOI: [10.23731/CYRM-2020-006](https://doi.org/10.23731/CYRM-2020-006). URL: <https://cds.cern.ch/record/2736208>.
19. *ATLAS: technical proposal for a general-purpose pp experiment at the Large Hadron Collider at CERN*. LHC Tech. Proposal. CERN, Geneva, 1994. URL: <https://cds.cern.ch/record/290968>.
20. J. G. Layter. *The CMS muon project: Technical Design Report*. Technical Design Report CMS. CERN, Geneva, 1997. URL: <https://cds.cern.ch/record/343814>.
21. *ALICE: Technical proposal for a Large Ion collider Experiment at the CERN LHC*. LHC Tech. Proposal. CERN, Geneva, 1995. URL: <https://cds.cern.ch/record/293391>.
22. *LHCb: letter of intent*. Technical report CERN-LHCC-95-5. LHCC-I-8. Geneva: CERN, 1995. URL: <https://cds.cern.ch/record/290868>.
23. B. Salvachua et al. “Validation of Off-momentum Cleaning Performance of the LHC Collimation System”. In: *Proceedings of the 7th International Particle Accelerators Conference, Busan, Korea*. CERN-ACC-2016-220. 2016, WEPMW007. 3 p. DOI: [10.18429/JACoW-IPAC2016-WEPMW007](https://doi.org/10.18429/JACoW-IPAC2016-WEPMW007). URL: <https://cds.cern.ch/record/2207405>.
24. T. Kramer. “LHC Beam Dump System: Analysis of beam commissioning, performance and the consequences of abnormal operation”. Presented 05 Oct 2011. PhD thesis. Institut für Hochspannungstechnik und Systemmanagement Technische Universität, Graz, 2011. URL: <https://cds.cern.ch/record/1392619>.
25. C. Bracco, R. W. Assmann, S. Redaelli, and R. Robert-Demolaize. *Scenarios for Beam Commissioning of the LHC collimation system*. Technical report LHC-PROJECT-Report-1013. CERN-LHC-PROJECT-Report-1013. 2007. URL: <https://cds.cern.ch/record/1056681>.
26. *Design Report Tevatron 1 project*. Technical report FERMILAB-DESIGN-1984-01. 1984. URL: <https://cds.cern.ch/record/1478620>.
27. M. Benedikt et al. *FCC-ee: The Lepton Collider: Future Circular Collider Conceptual Design Report Volume 2. Future Circular Collider*. Technical report CERN-ACC-2018-0057. 2. Geneva: CERN, 2018. DOI: [10.1140/epjst/e2019-900045-4](https://doi.org/10.1140/epjst/e2019-900045-4). URL: <https://cds.cern.ch/record/2651299>.
28. W. Herr and B. Muratori. “Concept of luminosity”. In: *Proceedings of the CERN Accelerator School CAS 2006: Intermediate Accelerator Physics*. 2006. DOI: [10.5170/CERN-2006-002.361](https://doi.org/10.5170/CERN-2006-002.361). URL: <https://cds.cern.ch/record/941318>.
29. M. A. Furman. *The Møller Luminosity Factor*. Technical report LBNL-53553, CBP Note-543. Lawrence Berkeley National Laboratory, 2003.
30. B. Muratori. *Luminosity and luminous region calculations for the LHC*. Technical report LHC-PROJECT-NOTE-301. Geneva: CERN, 2002. URL: <https://cds.cern.ch/record/691967>.
31. M. A. Furman and M. Zisman. “Luminosity”. In: *Handbook of Accelerators Physics and Engineering*. Forst. World Scientific, 1999. Chap. 4.1, pp. 277–281.
32. M. Crouch, B. D. Muratori, and R. B. Appleby. “Analytical Approach to the Beam-Beam Interaction with the Hourglass Effect”. In: *Proceedings of the 6th International Particle Accelerator Conference, Richmond, VA, USA, 3 - 8 May 2015, pp.MOPJE082*. CERN-ACC-2015-0181. 2015, 4 p. URL: <https://cds.cern.ch/record/2113428>.
33. F. Ruggiero and F. Zimmermann. “Luminosity Optimization near the Beam-Beam Limit by Increasing Bunch Length or Crossing Angle”. *Phys. Rev. Spec. Top. Accel. Beams* 5: CERN-SL-2002-005-Rev-AP, 2002. revised version number 1 submitted on 2002-06-13 14:28:50, 061001. 16 p. DOI: [10.1103/PhysRevSTAB.5.061001](https://doi.org/10.1103/PhysRevSTAB.5.061001). URL: <http://cds.cern.ch/record/540249>.

34. W. Herr and J. Miles. *Optimizing the LHC Interaction Region to Obtain the Highest Possible Luminosity*. Technical report LHC-Project-Report-40. CERN, 1996. URL: <https://cds.cern.ch/record/309213>.
35. S. Papadopoulou et al. “Impact of Non-Gaussian Beam Profiles in the Performance of Hadron Colliders. Modeling and Measurements of Bunch Profiles at the LHC”. *Phys. Rev. Accel. Beams* 23:arXiv:1806.07317. 10, 2018, 101004. 21 p. DOI: [10.1103/PhysRevAccelBeams.23.101004](https://doi.org/10.1103/PhysRevAccelBeams.23.101004). URL: <https://cds.cern.ch/record/2631511>.
36. S. Papadopoulou et al. “Modelling and measurements of bunch profiles at the LHC”. *J. Phys. : Conf. Ser.* 874:FERMILAB-CONF-17-155-AD. CERN-ACC-2017-329. 1, 2017, 012008. 6 p. DOI: [10.1088/1742-6596/874/1/012008](https://doi.org/10.1088/1742-6596/874/1/012008). URL: <http://cds.cern.ch/record/2275963>.
37. G. Sterbini. “An Early Separation Scheme for the LHC Luminosity Upgrade”. Presented on 27 Nov 2009. PhD thesis. Ecole Polytechnique Fédérale de Lausanne, 2009. URL: <https://cds.cern.ch/record/1229215>.
38. F. Ruggiero. *Nominal LHC Parameters*. 7th LTC Meeting. 2003. URL: <https://lhc-data-exchange.web.cern.ch/ruggiero.pdf>.
39. S. Chatrchyan et al. “A New Boson with a Mass of 125 GeV Observed with the CMS Experiment at the Large Hadron Collider”. *Science* 338:6114, 2012, 1569–1575. 16 p. DOI: [10.1126/science.1230816](https://doi.org/10.1126/science.1230816). URL: <https://cds.cern.ch/record/1529911>.
40. G. Aad et al. “Observation of a new particle in the search for the Standard Model Higgs boson with the ATLAS detector at the LHC. Observation of a new particle in the search for the Standard Model Higgs boson with the ATLAS detector at the LHC”. *Phys. Lett. B* 716:arXiv:1207.7214. CERN-PH-EP-2012-218, 2012, 1–29. 29 p. DOI: [10.1016/j.physletb.2012.08.020](https://doi.org/10.1016/j.physletb.2012.08.020). URL: <https://cds.cern.ch/record/1471031>.
41. R. Aaij et al. *First observation of the decay $\Lambda_b^0 \rightarrow \eta_c(1S)pK^-$* . Technical report arXiv:2007.11292. LHCB-PAPER-2020-012. Geneva: CERN, 2020. URL: <https://cds.cern.ch/record/2724728>.
42. J. Adam et al. “Enhanced production of multi-strange hadrons in high-multiplicity proton–proton collisions. Multiplicity-dependent enhancement of strange and multi-strange hadron production in proton-proton collisions at $\sqrt{s} = 7$ TeV”. *Nature Phys.* 13:CERN-EP-2016-153, 2016. In Press, 535–539. 17 p. DOI: [10.1038/nphys4111](https://doi.org/10.1038/nphys4111). URL: <https://cds.cern.ch/record/2189682>.
43. N. Mokhov et al. “Energy deposition studies for the High-Luminosity Large Hadron Collider inner triplet magnets. Energy Deposition Studies for the High-Luminosity Large Hadron Collider Inner Triplet Magnets”. *Phys. Rev. Spec. Top. Accel. Beams* 18:FERMILAB-PUB-15-095-APC. FERMILAB-PUB-15-095-APC, 2015, 24 pp, 051001. 10 p. DOI: [10.1103/PhysRevSTAB.18.051001](https://doi.org/10.1103/PhysRevSTAB.18.051001). URL: <https://cds.cern.ch/record/2006710>.
44. N. Mokhov and I. Rakhno. “Mitigating radiation loads in Nb3Sn quadrupoles for LHC upgrades”. *Phys. Rev. Spec. Top. Accel. Beams* 9:physics/0608001, 2006. 13 pages, 12 figures, 1 table Report-no: Fermilab-FN-0789-AD Subj-class: Accelerator Physics, 101001. 13 p. DOI: [10.1103/PhysRevSTAB.9.101001](https://doi.org/10.1103/PhysRevSTAB.9.101001). URL: <https://cds.cern.ch/record/976091>.
45. L. Rossi and O. Brüning. “Introduction to the HL-LHC Project”. *Adv. Ser. Dir. High Energy Phys.* 24, 2015, pp. 1–17. DOI: [10.1142/9789814675475_0001](https://doi.org/10.1142/9789814675475_0001). URL: <https://cds.cern.ch/record/2130736>.
46. S. Fartoukh and F. Zimmermann. “The HL-LHC accelerator physics challenges”. *Adv. Ser. Dir. High Energy Phys.* 24, 2015, pp. 45–96. DOI: [10.1142/9789814675475_0004](https://doi.org/10.1142/9789814675475_0004). URL: <https://cds.cern.ch/record/2132265>.
47. K. Ohmi. “Study of beam-beam interaction with a large Piwinski angle at LHC”. In: *CARE-HHH-APD Workshop on Finalizing the Roadmap for the Upgrade of the CERN and GSI Accelerator Complex*. 2008. DOI: [10.5170/CERN-2008-005.23](https://doi.org/10.5170/CERN-2008-005.23). URL: <https://cds.cern.ch/record/1133119>.
48. S. Fartoukh et al. “Compensation of the long-range beam-beam interactions as a path towards new configurations for the High Luminosity LHC”. *Phys. Rev. Spec. Top. Accel. Beams* 18:CERN-ACC-2015-0095, 2015, 121001. 23 p. DOI: [10.1103/PhysRevSTAB.18.121001](https://doi.org/10.1103/PhysRevSTAB.18.121001). URL: <https://cds.cern.ch/record/2052448>.

Bibliography

49. R. Calaga. “Crab Cavities for the LHC Upgrade”. In: *Proceedings of the Chamonix 2012 Workshop on LHC Performances*. 2012, 10 p. DOI: [10.5170/CERN-2012-006.363](https://doi.org/10.5170/CERN-2012-006.363). URL: <https://cds.cern.ch/record/1493034>.
50. R. Calaga et al. “Crab Cavity Development”. *Adv. Ser. Dir. High Energy Phys.* 24, 2015, pp. 137–156. DOI: [10.1142/9789814675475_0007](https://doi.org/10.1142/9789814675475_0007). URL: <https://cds.cern.ch/record/2130793>.
51. R. Calaga. *Overview of Crab Cavities for HL-LHC*. International Review of the Crab Cavity Performance for HiLumi, 3-5 April, CERN. 2017. URL: https://indico.cern.ch/event/590988/contributions/2489578/attachments/1437189/2212211/HLLHC_Review_02042017_Calaga.pdf.
52. K. Skoufaris et al. “Numerical optimization of DC wire compensation in HL-LHC”. In: *Proceedings of the 10th International Particle Accelerator Conference, Melbourne, Australia*. CERN-ACC-2019-081. 2019, MOPMP053. 4 p. DOI: [10.18429/JACoW-IPAC2019-MOPMP053](https://doi.org/10.18429/JACoW-IPAC2019-MOPMP053). URL: <https://cds.cern.ch/record/2695241>.
53. R. Bruce et al. *Parameters for HL-LHC aperture calculations and comparison with aperture measurements*. Technical report CERN-ACC-2014-0044. Geneva: CERN, 2014. URL: <https://cds.cern.ch/record/1697805>.
54. G. Skripka and G. Iadarola. *Beam-induced heat loads on the beam screens of the inner triplets for the HL-LHC*. Technical report CERN-ACC-NOTE-2018-0009. 2018. DOI: [10.17181/CERN.I7WJ.TNS9](https://doi.org/10.17181/CERN.I7WJ.TNS9). URL: <https://cds.cern.ch/record/2305245>.
55. S. Bidon et al. “Normal Conducting Separation Dipoles for the LHC Beam Cleaning Insertions”. *IEEE Trans. Appl. Supercond.* 14:LHC-Project-Report-714. CERN-LHC-Project-Report-714. 2, 2004, 437–440. 5 p. DOI: [10.1109/TASC.2004.829690](https://doi.org/10.1109/TASC.2004.829690). URL: <https://cds.cern.ch/record/732321>.
56. D. Missiaen. *Realignment around CMS*. 363rd LHC Machine Committee, CERN, Geneva, Switzerland. 2018.
57. A. Ribes Metidieri and X. Buffat. *Studies of PACMAN effects in the HL-LHC*. Technical report CERN-ACC-NOTE-2019-0037. 2019. URL: <https://cds.cern.ch/record/2690083>.
58. D. Ritson and W. Chou. “Minimizing the Pacman Effect on the Closed Orbit”. *Part. Accel.* 59, 1998, pp. 157–167. URL: <https://cds.cern.ch/record/1120304>.
59. S. Fartoukh. *An Achromatic Telescopic Squeezing (ATS) Scheme For The LHC Upgrade*. Technical report CERN-ATS-2011-161. 2011, 3 p. URL: <https://cds.cern.ch/record/1382077>.
60. M. Pojer et al. “LHC Operational Experience of the 6.5 TeV Proton Run with ATS Optics”. CERN-ACC-2018-166, 2018, MOPMF050. 4 p. DOI: [10.18429/JACoW-IPAC2018-MOPMF050](https://doi.org/10.18429/JACoW-IPAC2018-MOPMF050). URL: <https://cds.cern.ch/record/2646065>.
61. S. Fartoukh. “Achromatic telescopic squeezing scheme and application to the LHC and its luminosity upgrade”. *Phys. Rev. Spec. Top. Accel. Beams* 16:CERN-ACC-2013-0289, 2013, 111002. 33 p. DOI: [10.1103/PhysRevSTAB.16.111002](https://doi.org/10.1103/PhysRevSTAB.16.111002). URL: <https://cds.cern.ch/record/1636178>.
62. J.-P. Koutchouk et al. *A more robust and flexible lattice for LHC*. Technical report LHC-Project-Report-107. CERN-LHC-Project-Report-107. 1997, 3 p. URL: <http://cds.cern.ch/record/327771>.
63. J. Gareyte, J.-P. Koutchouk, and F. Ruggiero. *Landau damping dynamic aperture and octupole in LHC*. Technical report LHC-Project-Report-91. CERN-LHC-Project-Report-91. revised version number 1 submitted on 2003-08-21 14:12:02. Geneva: CERN, 1997. URL: <https://cds.cern.ch/record/321824>.
64. W. Herr. “Introduction to Landau Damping”. In: *Proceedings of CERN Accelerator School: Advanced Accelerator Physics Course, Trondheim, Norway, 18-29 Aug 2013*. arXiv:1601.05227. 2014, 27 p. DOI: [10.5170/CERN-2014-009.377](https://doi.org/10.5170/CERN-2014-009.377). URL: <https://cds.cern.ch/record/1982428>.

65. S. Papadopoulou et al. “Monitoring and modelling of the LHC emittance and luminosity evolution in 2018”. In: *Proceedings of the 10th International Particle Accelerator Conference, Melbourne, Australia*. CERN-ACC-2019-114. 2019, WEPTS046. 4 p. DOI: [10.18429/JACoW-IPAC2019-WEPTS046](https://doi.org/10.18429/JACoW-IPAC2019-WEPTS046). URL: <http://cds.cern.ch/record/2693256>.
66. W. Herr. “Beam-beam interactions”. In: *Proceedings of the CERN Accelerator School: Intermediate Accelerator Physics*. 2006. DOI: [10.5170/CERN-2006-002.379](https://doi.org/10.5170/CERN-2006-002.379). URL: <https://cds.cern.ch/record/941319>.
67. M. Bassetti and G. Erskine. *Closed expression for the electrical field of a two-dimensional gaussian charge*. Technical report CERN-ISH-TH/80-06. CERN, 1980.
68. U. Dorda. “Compensation of long-range beam-beam interaction at the CERN LHC”. Presented on 02 Jun 2008. PhD thesis. Technischen Universität Wien, Fakultät für Physik, 2008. URL: <https://cds.cern.ch/record/1114782>.
69. D. Rice and U. Cornell. “Error Sources and Effects”. In: *Handbook of Accelerators Physics and Engineering*. Ed. by A. W. Chao, K. H. Mess, M. Tigner, and F. Zimmermann. Second. World Scientific, 2012. Chap. 4.7.1, pp. 346–347.
70. R. Alemany et al. *Head-on beam-beam tune shifts with high brightness beams in the LHC*. Technical report CERN-ATS-Note-2011-029 MD. 2011. URL: <https://cds.cern.ch/record/1359945>.
71. M. A. Furman. *Results of coherent dipole beam-beam interaction studies for SSC lattices*. Technical report SSC-062. 1986.
72. W. Herr. “Beam-beam effects in the LHC”. *Part. Accel.* 50:CERN-SL-94-92-AP. LHC-NOTE-301. CERN-LHC-Note-301, 1994, 69–81. 14 p. URL: <https://cds.cern.ch/record/272882>.
73. J. Rossbach and P. Schmüser. “Basic course on accelerator optics”. In: CERN-1994-001. CAS - CERN Accelerator School : 5th General Accelerator Physics Course, 1992, pp. 17–88.
74. F. C. Iselin. *The MAD Program, Physical Methods Manual*. Version 8.13. 1992. URL: http://mad8.web.cern.ch/mad8/doc/phys_guide.pdf.
75. A. Wolski. “Electromagnetic Fields in Accelerator Components”. In: *Beam dynamics in high energy particle accelerators*. Imperial College Press, 2014. Chap. 1, pp. 3–57. DOI: [10.1142/p899](https://doi.org/10.1142/p899). URL: <https://cds.cern.ch/record/1622200>.
76. *MAD-X*. <http://madx.web.cern.ch/madx/>.
77. A. Wolski. “Hamiltonian for a Particle in an Accelerator Beam Line”. In: *Beam dynamics in high energy particle accelerators*. Imperial College Press, 2014. Chap. 2, pp. 59–80. DOI: [10.1142/p899](https://doi.org/10.1142/p899). URL: <https://cds.cern.ch/record/1622200>.
78. W. Herr. “Mathematical and Numerical Methods for Non-linear Beam Dynamics”. In: *Proceedings of the 2018 CERN–Accelerator–School course on Numerical Methods for Analysis, Design and Modelling of Particle Accelerators, Thessaloniki, Greece*. 2020. URL: <https://arxiv.org/abs/2006.09052>.
79. A. Wolski. “Linear Transfer Maps for Common Components”. In: *Beam dynamics in high energy particle accelerators*. Imperial College Press, 2014. Chap. 3, pp. 83–125. DOI: [10.1142/p899](https://doi.org/10.1142/p899). URL: <https://cds.cern.ch/record/1622200>.
80. H. M. Ewen. “Modelling and correction of the non-linear transverse dynamics of the LHC from beam-based measurements”. PhD thesis. Herford College, University of Oxford, 2014. URL: <https://cds.cern.ch/record/1951379>.
81. V. Shiltsev et al. “Compensation of Beam-Beam Effects in the Tevatron with Electron Beams”. *Phys. Rev. ST Accel. Beams* 2, 1999, p. 071001. DOI: [10.1103/PhysRevSTAB.2.071001](https://doi.org/10.1103/PhysRevSTAB.2.071001).

Bibliography

82. V. Shiltsev et al. “Compensation of Beam-Beam Effects in Tevatron Collider with Electron Beams”. In: *IEEE PAC99*. 1999.
83. G. Stancari and V. Shiltsev. “Beam-Beam Compensation Studies in the Tevatron with Electron Lenses”. In: *ICFA Mini-Workshop on Beam-beam Effects in Hadron Colliders*. FermiLab. 2013.
84. Y. Papaphilippou and F. Zimmermann. “Estimates of Diffusion due to Long-range Beam-beam Collisions”. *Phys. Rev. Spec. Top. Accel. Beams* 5:LHC-Project-Report-600. CERN-LHC-Project-Report-600. 7, 2002, 074001. 22 p. DOI: [10.1103/PhysRevSTAB.5.074001](https://doi.org/10.1103/PhysRevSTAB.5.074001). URL: <https://cds.cern.ch/record/574079>.
85. J.-P. Koutchouk. *Principle of a correction of the long-range beam-beam effect in LHC using electromagnetic lenses*. Technical report LHC-PROJECT-NOTE-223. revised version number 1 submitted on 2000-11-20 10:24:42. Geneva: CERN, 2000. URL: <https://cds.cern.ch/record/692058>.
86. R. Calaga et al. “Long-range beam-beam experiments in the Relativistic Heavy Ion Collider”. *Phys. Rev. ST Accel. Beams* 14, 9 2011, p. 091001. DOI: [10.1103/PhysRevSTAB.14.091001](https://doi.org/10.1103/PhysRevSTAB.14.091001). URL: <https://link.aps.org/doi/10.1103/PhysRevSTAB.14.091001>.
87. C. Milardi et al. *Dafne Lifetime Optimization with Compensating Wires and Octupoles*. 2008. arXiv: [0803.1544](https://arxiv.org/abs/0803.1544) [physics.acc-ph].
88. F. Zimmermann. “10 Years of wire excitation experiments in the CERN SPS”. In: *Proceedings of ICFA Mini-Workshop on Beam-Beam Effects in Hadron Colliders*. arXiv:1410.3654. 2014, 153–166. 14 p. DOI: [10.5170/CERN-2014-004.153](https://doi.org/10.5170/CERN-2014-004.153). URL: <http://cds.cern.ch/record/1955353>.
89. F. Zimmermann et al. “Experiments on LHC Long-Range Beam-Beam Compensation and Crossing Schemes at the CERN SPS in 2004”. In: *Proceedings of the 21st IEEE Particle Accelerator Conference, Knoxville, TN, USA*. LHC-Project-Report-844. CERN-LHC-Project-Report-844. 2005, 4 p. DOI: [10.1109/PAC.2005.1590528](https://doi.org/10.1109/PAC.2005.1590528). URL: <https://cds.cern.ch/record/872262>.
90. A. Rossi et al. “Progress with Long-Range Beam-Beam Compensation Studies for High Luminosity LHC”. In: *Proceedings of 8th International Particle Accelerator Conference*. CERN-ACC-2017-158. 2017, TUPVA115. 4 p. DOI: [10.18429/JACoW-IPAC2017-TUPVA115](https://doi.org/10.18429/JACoW-IPAC2017-TUPVA115). URL: <https://cds.cern.ch/record/2289671>.
91. G. Robert-Démolaize. “Design and Performance Optimization of the LHC Collimation System”. Presented on 20 Nov 2006. PhD thesis. Université Joseph Fourier, Grenoble, 2006. URL: <http://cds.cern.ch/record/1004869>.
92. R. W. Assmann et al. *The final collimation system for the LHC*. Technical report LHC-PROJECT-Report-919. CERN-LHC-Project-Report-919. revised version submitted on 2006-09-15 14:36:59. 2006, 4 p. URL: <http://cds.cern.ch/record/972336>.
93. A. Goldblatt et al. “Design and Performance of Coronagraph for Beam Halo Measurements in the LHC”. In: *Proceedings of the International Beam Instrumentation Conference, Barcelona, Spain*. 2017, MOPG74. 4 p. DOI: [10.18429/JACoW-IBIC2016-MOPG74](https://doi.org/10.18429/JACoW-IBIC2016-MOPG74). URL: <https://cds.cern.ch/record/2313940>.
94. O. Aberle. *Status of “Wire in jaw collimator” production*. Workshop on Simulations and Measurements of Long-Range Beam-Beam Effects in the LHC, Lyon. 2015. URL: https://indico.cern.ch/event/456856/contributions/1968796/attachments/1195437/1738664/TCTW_design.pdf.
95. F. Carra. *TCTW Collimator Design*. Workshop on Simulations and Measurements of Long-Range Beam-Beam Effects in the LHC, Lyon. 2015. URL: https://indico.cern.ch/event/456856/contributions/1968796/attachments/1195437/1738664/TCTW_design.pdf.
96. A. Garcia-Tabares Valdivieso. “Optics-measurement-based Beam Position Monitor Calibration”. Presented 08 Nov 2019. PhD thesis. Universidad Complutense de Madrid, 2019. URL: <https://cds.cern.ch/record/2701414>.

97. A. Dallocchio et al. “LHC Collimators with Embedded Beam Position Monitors: A New Advanced Mechanical Design”. In: *Proceedings of the 2nd International Particle Accelerator Conference, San Sebastian, Spain, 4 - 9 Sep 2011*. CERN-ATS-2011-228. 2011, 4 p. URL: <https://cds.cern.ch/record/1402570>.
98. A. Wolski. “Methods for Analysis of Single Particle Dynamics”. In: *Beam dynamics in high energy particle accelerators*. Imperial College Press, 2014. Chap. 11, pp. 331–391. DOI: [10.1142/p899](https://doi.org/10.1142/p899). URL: <https://cds.cern.ch/record/1622200>.
99. D. Pellegrini et al. “Multiparametric response of the HL-LHC Dynamic Aperture in presence of beam-beam effects”. In: *8th International Particle Accelerator Conference*. CERN-ACC-2017-323. 1. 2017. DOI: [10.1088/1742-6596/874/1/012007](https://doi.org/10.1088/1742-6596/874/1/012007). URL: <https://cds.cern.ch/record/2276047>.
100. D. Banfi, J. Barranco Garcia, T. Pieloni, and A. Valishev. “Weak-strong beam-beam simulations for HL-LHC”. In: *5th International Particle Accelerator Conference*. CERN-ACC-2014-0104. 2014. URL: <https://cds.cern.ch/record/1742126>.
101. *SixTrack: Single Particle Tracking Code Treating Transverse Motion with Synchrotron Oscillations in a Symplectic Manner*. <http://sixtrack.web.cern.ch/SixTrack/>.
102. E. Todesco and M. Giovannozzi. “Dynamic aperture estimates and phase space distortions in nonlinear betatronic motion”. *Phys. Rev. E* 53:CERN-SL-95-90-AP. 4B, 1995, 4067–4076. 26 p. DOI: [10.1103/PhysRevE.53.4067](https://doi.org/10.1103/PhysRevE.53.4067). URL: <https://cds.cern.ch/record/292371>.
103. L. H. A. Leunissen, H. Grote, and F. Schmidt. *LHC Dynamic Aperture Including the Beam-Beam Force*. Technical report LHC-Project-Report-405. CERN-LHC-Project-Report-405. 2000, 4 p. URL: <https://cds.cern.ch/record/462634>.
104. T. Pieloni, D. Banfi, and J. Barranco Garcia. “Dynamic Aperture Studies for HL-LHC with beam-beam effects”. CERN-ACC-NOTE-2017-0035, 2017. URL: <https://cds.cern.ch/record/2263345>.
105. D. Kaltchev. “Fourier Coefficients of Long-Range Beam-Beam Hamiltonian via Two-Dimensional Bessel Functions”. In: *Proceedings of the 9th International Particle Accelerator Conference (IPAC18), Vancouver, BC, Canada*. 2018. URL: <https://accelconf.web.cern.ch/ipac2018/papers/thpak108.pdf>.
106. A. Poyet. “Compensation of the Long-Range Beam-Beam Interaction in the LHC”. Presented 07 Sep 2017. MA thesis. Grenoble INP Phelma, 2017. URL: <https://cds.cern.ch/record/2320490>.
107. G. Sterbini et al. *MD2202: compensating long-range beam-beam effect in the LHC using DC wires*. Technical report CERN-ACC-NOTE-2019-0052. 2019. URL: <https://cds.cern.ch/record/2703495>.
108. A. Poyet et al. “MD3263: Beam-Beam Long-Range Compensation using DC Wires in the LHC”. CERN-ACC-NOTE-2019-0053, 2019. URL: <https://cds.cern.ch/record/2703503>.
109. A. Poyet. “First Experimental Evidence of a Beam-Beam Long-Range Compensation Using Wires in the Large Hadron Collider”, To be published.
110. L. Ponce, K. Fuchsberger, S. Jackson, and J. Wenninger. “Tune and orbit feedbacks”. In: *Proceedings of 6th Evian Workshop on LHC beam operation*. 2016, 53–58. 6 p. URL: <https://cds.cern.ch/record/2294515>.
111. D. Pellegrini et al. “Multiparametric response of the LHC Dynamic Aperture in presence of beam-beam effects”. *J. Phys. : Conf. Ser.* 874:CERN-ACC-2017-330. 1, 2017, 012006. 6 p. DOI: [10.1088/1742-6596/874/1/012006](https://doi.org/10.1088/1742-6596/874/1/012006). URL: <https://cds.cern.ch/record/2275962>.
112. Y. Papaphilippou. *Proposal for the experimental scenario*. Workshop on simulations and measurements of the long-range effects in the LHC, Lyon, France. 2015. URL: https://indico.cern.ch/event/456856/contributions/1968793/attachments/1196177/1740660/BBLR_LYON_2015.pdf.
113. F. Antoniou et al. “Can we predict luminosity?” In: *Proceedings of 7th Evian Workshop on LHC beam operation*. 2017, 125–132. 8 p. URL: <http://cds.cern.ch/record/2293678>.

Bibliography

114. L. Adamczyk. *Measurement of the total cross section in proton proton collisions at $\sqrt{s} = 7$ TeV with the ALFA sub-detector of ATLAS*. Technical report ATL-PHYS-PROC-2015-125. Geneva: CERN, 2015. URL: <https://cds.cern.ch/record/2062926>.
115. G. Antchev et al. “Luminosity-independent measurements of total, elastic and inelastic cross-sections at $s = 7$ TeV”. *EPL (Europhysics Letters)* 101, 2013. DOI: [10.1209/0295-5075/101/21004](https://doi.org/10.1209/0295-5075/101/21004).
116. A. Garcia et al. *LHC Beam Loss Monitors*. Technical report.
117. E. B. Holzer. *The LHC BLM System: Overview and Experience*. 7th DITANET Topical Workshop on Beam Losses Monitoring. https://indico.cern.ch/event/154172/contributions/1399480/attachments/163416/230527/eholzer_LHC_BLM_1_v2.pdf. 2011.
118. A. Gorzawski et al. *Fast loss analysis with LHC diamond detectors in 2017*. Technical report. 2018. URL: <https://cds.cern.ch/record/2320644>.
119. J. Gras et al. *The 2010 LHC DC BCT measurement system and its main sources of uncertainties*. Technical report LHC-Project-Note-432. CERN-LHC-Project-Note-432. Geneva: CERN, 2010. URL: <https://cds.cern.ch/record/1300775>.
120. D. Belohrad et al. *The 2010 LHC ring Fast BCT measurement system and its main sources of uncertainties*. Technical report LHC-Project-Note-433. CERN-LHC-Project-Note-433. Geneva: CERN, 2010. URL: <https://cds.cern.ch/record/1300776>.
121. B. Salvachua et al. *Lifetime Analysis at High Intensity Colliders Applied to the LHC*. Technical report CERN-ACC-2013-0072. 2013, 3 p. URL: <https://cds.cern.ch/record/1574586>.
122. W. Hofle et al. *Controlled Transverse Blow-up of High Energy Proton Beams for Aperture Measurements and Loss Maps*. Technical report CERN-ATS-2012-128. 2012, THPPR039. 3 p. URL: <https://cds.cern.ch/record/1459854>.
123. F. Zimmermann. “Electron cloud effects in the LHC”. In: *Proceedings E-CLOUD’02: Mini Workshop on Electron Cloud Simulations for Proton and Positron Beams*. 2002. DOI: [10.5170/CERN-2002-001.47](https://doi.org/10.5170/CERN-2002-001.47). URL: <https://cds.cern.ch/record/585562>.
124. K. Paraschou et al. “Analysis on bunch-by-bunch beam losses at 6.5 TeV in the Large Hadron Collider”. In: *Proceedings of 10th International Particle Accelerator Conference*. CERN-ACC-2019-068. 2019, MOPMP029. 4 p. DOI: [10.18429/JACoW-IPAC2019-MOPMP029](https://doi.org/10.18429/JACoW-IPAC2019-MOPMP029). URL: <https://cds.cern.ch/record/2696125>.
125. S. Fartoukh et al. *Round telescopic optics with large telescopic index*. Technical report CERN-ACC-2018-0032. Geneva: CERN, 2018. URL: <https://cds.cern.ch/record/2643258>.
126. S. Fartoukh et al. *Combined ramp and telescopic squeeze*. Technical report CERN-ACC-2020-0028. Geneva: CERN, 2020. URL: <https://cds.cern.ch/record/2742895>.
127. H. Damerou et al. *RF Manipulations for Higher Brightness LHC-Type Beams*. Technical report CERN-ACC-2013-0210. 2013, 3 p. URL: <https://cds.cern.ch/record/1595719>.
128. H. Damerou et al. “LIU: exploring alternative ideas”. In: *Proceedings of the Review of LHC and Injector Upgrade Plans Workshop*. 2014. DOI: [10.5170/CERN-2014-006.127](https://doi.org/10.5170/CERN-2014-006.127). URL: <https://cds.cern.ch/record/1977365>.
129. O. Dominguez et al. *Electron cloud studies for alternative train configurations and bunch spacings at the HL-LHC*. Technical report. 2013. URL: <https://cds.cern.ch/record/1559716>.
130. G. Iadarola et al. *Beam-induced heat loads on the LHC arc beam screens with different beam and machine configurations: experiments and comparison against simulations*. Technical report CERN-ACC-NOTE-2019-0057. 2019. URL: <https://cds.cern.ch/record/2705513>.

131. M. Benedikt. "LHC Pilot Bunches from the CERN PS Booster". In: *Proceedings of the 20th IEEE Particle Accelerator Conference, Portland, OR, USA*. LHC-Project-Report-653. CERN-LHC-Project-Report-653. 2003, 4 p. URL: <https://cds.cern.ch/record/620370>.
132. B. Salvachua. "Beam Diagnostics for Studying Beam Losses in the LHC". In: *Proceedings of the 8th International Beam Instrumentation Conference (IBIC 2019), Malmo, Sweden, 2019*, TUAO01. 7 p. DOI: [10.18429/JACoW-IBIC2019-TUAO01](https://doi.org/10.18429/JACoW-IBIC2019-TUAO01). URL: <http://cds.cern.ch/record/2750959>.
133. S. Fartoukh. *Towards the LHC Upgrade using the LHC well-characterized technology*. Technical report sLHC-PROJECT-Report-0049. CERN-sLHC-PROJECT-Report-0049. Geneva: CERN, 2010. URL: <https://cds.cern.ch/record/1301180>.
134. S. Fartoukh et al. *About flat telescopic optics for the future operation of the LHC*. Technical report CERN-ACC-2018-0018. Geneva: CERN, 2018. URL: <https://cds.cern.ch/record/2622595>.
135. S. Fartoukh et al. "An Alternative High Luminosity LHC with Flat Optics and Long-Range Beam-Beam Compensation". In: *Proceedings of the 6th International Particle Accelerator Conference, Richmond, VA, USA*. CERN-ACC-2015-0180. 2015, 4 p. URL: <https://cds.cern.ch/record/2113269>.
136. J. M. Coello De Portugal - Martinez Vazquez et al. *MD2148: Flat optics*. Technical report CERN-ACC-NOTE-2018-0051. 2018. URL: <https://cds.cern.ch/record/2632141>.
137. S. Fartoukh et al. *First High-Intensity Beam Tests with Telescopic Flat Optics at the LHC*. Technical report CERN-ACC-2019-0052. Geneva: CERN, 2019. URL: <https://cds.cern.ch/record/2687343>.
138. K. Skoufaris. "Numerical optimization of DC wire parameters for mitigation of the long range beam-beam interactions in HL-LHC", 2021. To be published.
139. N. Karastathis et al. "Report from the Run-III Configuration Working Group". In: *Proceedings in 9th LHC Operations Evian Workshop, 30 Jan. - 1 Feb. 2019, Evian, France*. 2019. URL: https://indico.cern.ch/event/751857/contributions/3259414/attachments/1782259/3080238/nkarast_proceedings.pdf.
140. G. Ferlin et al. "Cryogenics experience during Run 2 and impact of LS2 on the next run". In: *Proceedings in 9th LHC Operations Evian Workshop, 30 Jan. - 1 Feb. 2019, Evian, France*. 2019. URL: https://indico.cern.ch/event/751857/contributions/3259379/attachments/1783039/3019939/JACoW_LaTeX_template_evian_gf_.pdf.
141. G. Iadarola et al. "Electron cloud and heat loads in Run 2". In: *Proceedings in 9th LHC Operations Evian Workshop, 30 Jan. - 1 Feb. 2019, Evian, France*. 2019. URL: https://indico.cern.ch/event/751857/contributions/3259379/attachments/1783039/3019939/JACoW_LaTeX_template_evian_gf_.pdf.
142. T. Mertens. "Intrabeam scattering in the LHC". Presented 17 Jun 2011. PhD thesis. Universidade Do Porto, 2011. URL: <https://cds.cern.ch/record/1364596>.
143. V. Baglin et al. "Synchrotron Radiation in the LHC Vacuum System". In: *Proceedings of the 2nd International Particle Accelerator Conference, San Sebastian, Spain*. CERN-ATS-2011-245. 2011, 4 p. URL: <https://cds.cern.ch/record/1407539>.
144. E. Buratin. "Electron Cloud and Synchrotron Radiation characterization of technical surfaces with the Large Hadron Collider Vacuum Pilot Sector". Presented 10 Dec 2020. PhD thesis. 2020. URL: <https://cds.cern.ch/record/2746058>.
145. C. Tambasco et al. "Impact of Incoherent Effects on the Landau Stability Diagram at the LHC". In: *Proceedings of the 8th International Particle Accelerator Conference, Copenhagen, Denmark*. CERN-ACC-2017-150. 2017, TUPVA031. 4 p. DOI: [10.18429/JACoW-IPAC2017-TUPVA031](https://doi.org/10.18429/JACoW-IPAC2017-TUPVA031). URL: <https://cds.cern.ch/record/2289679>.
146. D. Amorim et al. *MD3318 - Impedance Contribution of Secondary and Tertiary Collimators*. Technical report CERN-ACC-NOTE-2020-0033. 2020. URL: <https://cds.cern.ch/record/2720699>.

Bibliography

147. S. Antipov et al. “Low-Impedance Collimators for HL-LHC”. In: *Proceedings of the 9th International Particle Accelerator Conference, Vancouver, Canada*. CERN-ACC-2018-147. 2018, WEYGBE4. 4 p. DOI: [10.18429/JACoW-IPAC2018-WEYGBE4](https://doi.org/10.18429/JACoW-IPAC2018-WEYGBE4). URL: <https://cds.cern.ch/record/2648423>.
148. F. Cerutti et al. *LHC triplet lifetime versus operational scenario in ATLAS and CMS*. 225th LHC Machine Committee, CERN, Geneva, Switzerland. 2015.
149. E. Todesco et al. “Training of the Main Dipoles Magnets in the Large Hadron Collider Toward 7 TeV Operation. Training of the Main Dipoles Magnets in the Large Hadron Collider Toward 7 TeV Operation”. *IEEE Trans. Appl. Supercond.* 28:3, 2018, 4006905. 5 p. DOI: [10.1109/TASC.2018.2799570](https://doi.org/10.1109/TASC.2018.2799570). URL: <http://cds.cern.ch/record/2311400>.
150. F. Antoniou et al. “Building a Luminosity Model for the LHC and HL-LHC”. In: *Proceedings of the 6th International Particle Accelerator Conference, Richmond, VA, USA*. CERN-ACC-2015-283. 2015, TUPTY020. 4 p. URL: <https://cds.cern.ch/record/2141831>.
151. A. Rossi. *Machine Protection Aspects of BBLR operation in Run 3*. 193rd Machine Protection Panel Meeting. 2020. URL: https://indico.cern.ch/event/927406/contributions/3899416/attachments/2061683/3458595/BBLR_19062020_MPP.pdf.
152. A. Rossi et al. *LHC Long Range Beam-Beam Compensator Wire (BBCW) Commissioning and Revalidation after Failure Recovery*. Technical report. CERN, 2020.
153. N. Fuster-Martinez. *Options for IR collimators settings in Run 3*. 249th LHC Collimation Working Group. 2020. URL: https://indico.cern.ch/event/891653/%20contributions/3760722/attachments/2000412/%203338999/Run3_TCT_XRP_CWG.pdf.
154. A. Poyet. *Wire compensation feed-forward in Run 3*. 193rd Machine Protection Panel Meeting. 2020. URL: https://indico.cern.ch/event/927406/contributions/3899418/attachments/2060462/3456063/MPP_RUN3_FF_190620_v2.pdf.
155. N. Mounet. “The LHC Transverse Coupled-Bunch Instability”. Presented 2012. PhD thesis. Ecole Polytechnique Fédérale de Lausanne, 2012. DOI: [10.5075/epfl-thesis-5305](https://doi.org/10.5075/epfl-thesis-5305). URL: <https://cds.cern.ch/record/1451296>.
156. R. Bruce. *Machine Configuration Options (and Limits)*. LHC Performance Workshop, Chamonix, France. 2018. URL: https://indico.cern.ch/event/676124/contributions/2767832/attachments/1591277/2518560/2018.01.29--Chamonix_2018_LHC_Configuration_169.pdf.
157. A. Boccardi et al. *First Results from the LHC BBQ Tune and Chromaticity Systems*. Technical report LHC-Performance-Note-007. CERN-LHC-Performance-Note-007. Geneva: CERN, 2009. URL: <http://cds.cern.ch/record/1156349>.